AD-A045 319 AIR FORCE AERO PROPULSION LAB WRIGHT-PATTERSON AFB OHIO F/G 20/4
A CASCADE IN UNSTEADY FLOW.(U)
DEC 76 F R OSTDIEK
UNCLASSIFIED AFAPL-TR-76-115 NL

1 OF 3
ADA
045319

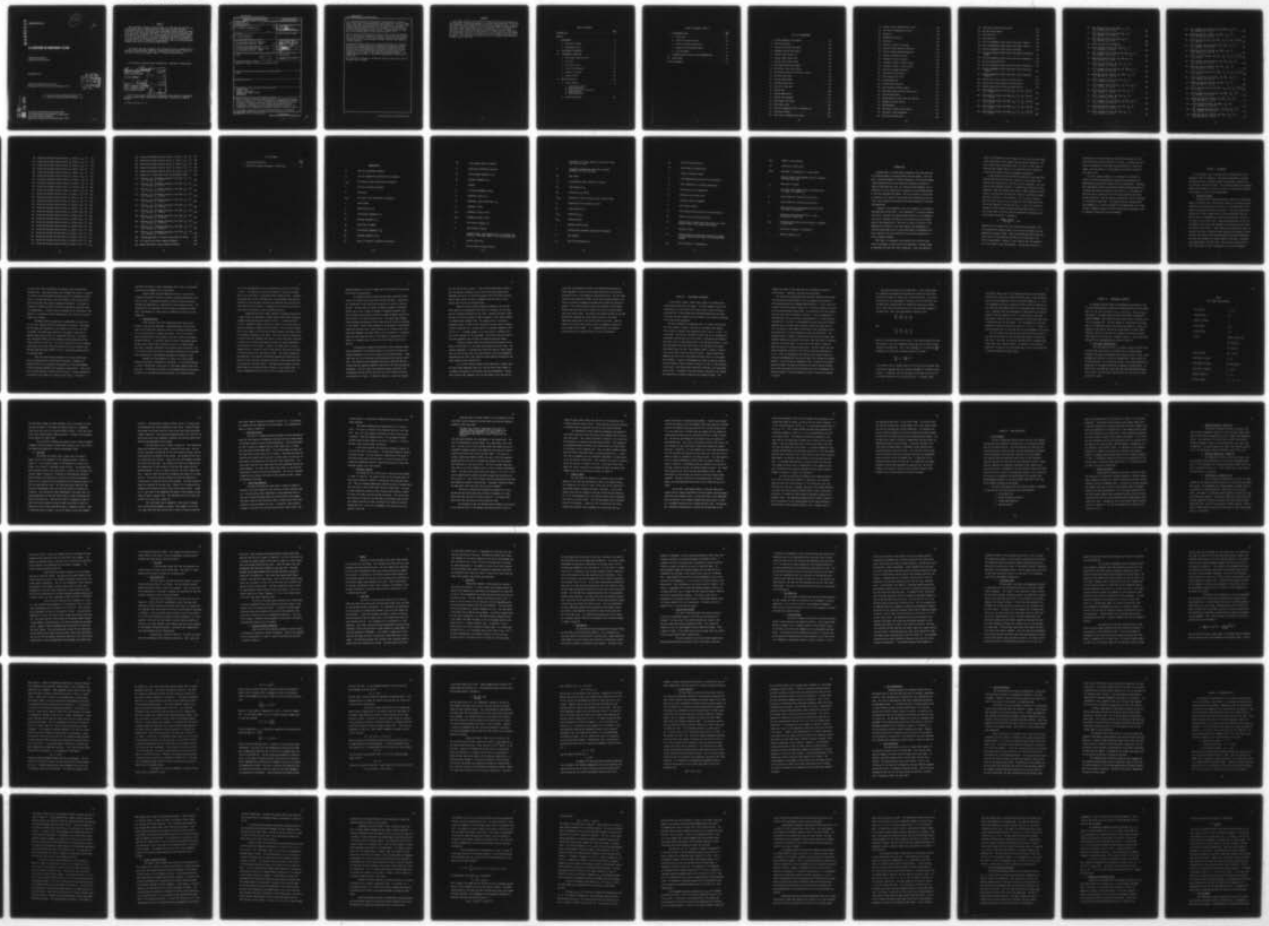

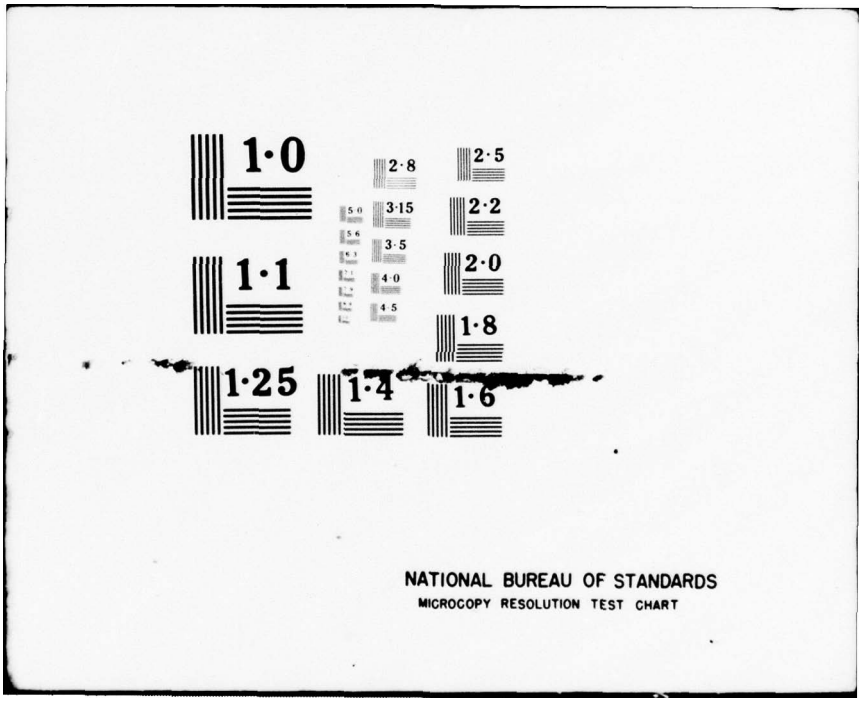
1·0
1·1
1·25
1·4
1·6
1·8
2·0
2·2
2·5
2·8
3·15
3·5
4·0
4·5
5·0
5·6
NATIONAL BUREAU OF STANDARDS
MICROCOPY RESOLUTION TEST CHART

AD A045319

AFAPL-TR-76-115

A CASCADE IN UNSTEADY FLOW

COMPONENTS BRANCH
TURBINE ENGINE DIVISION

DECEMBER 1976

DDC
RECEIVED
OCT 19 1977
A

TECHNICAL REPORT AFAPL-TR-76-115
Final Report for Period November 1969 through June 1975

Approved for public release; distribution unlimited.

DDC FILE COPY

AIR FORCE AERO-PROPULSION LABORATORY
AIR FORCE WRIGHT AERONAUTICAL LABORATORY
AIR FORCE SYSTEMS COMMAND
WRIGHT-PATTERSON AIR FORCE BASE, OHIO 45433

NOTICE

When Government drawings, specifications, or other data are used for any purpose other than in connection with a definitely related Government procurement operation, the United States Government thereby incurs no responsibility nor any obligation whatsoever; and the fact that the government may have formulated, furnished, or in any way supplied the said drawings, specifications, or other data, is not to be regarded by implication or otherwise as in any manner licensing the holder or any other person or corporation, or conveying any rights or permission to manufacture, use, or sell any patented invention that may in any way be related thereto.

This report has been reviewed by the Information Office, (ASD/OIP) and is releasable to the National Technical Information Service (NTIS). At NTIS it will be available to the general public, including foreign nations.

This technical report has been reviewed and is approved for publication.

FRANCIS R. OSTDIEK
Project Engineer/AFAPL

FOR THE COMMANDER

JAMES L. RADLOFF, Major USAF
Chief, Components Branch
Turbine Engine Division

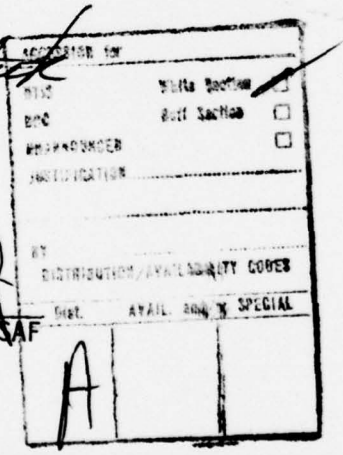

Copies of this report should not be returned unless return is required by security considerations, contractural obligations, or notice on a specific document.

UNCLASSIFIED

SECURITY CLASSIFICATION OF THIS PAGE *(When Data Entered)*

REPORT DOCUMENTATION PAGE

READ INSTRUCTIONS BEFORE COMPLETING FORM

1. REPORT NUMBER: AFAPL-TR-76-115	2. GOVT ACCESSION NO.
3. RECIPIENT'S CATALOG NUMBER	
4. TITLE *(and Subtitle)*: A Cascade in Unsteady Flow.	5. TYPE OF REPORT & PERIOD COVERED: Final Report. Nov 69 - Jun 75
	6. PERFORMING ORG. REPORT NUMBER
7. AUTHOR(s): Francis R. Ostdiek	8. CONTRACT OR GRANT NUMBER(s)
9. PERFORMING ORGANIZATION NAME AND ADDRESS: Air Force Aero Propulsion Laboratory, Wright-Patterson AFB, OH 45433	10. PROGRAM ELEMENT, PROJECT, TASK AREA & WORK UNIT NUMBERS: Element-62203F, Project-3066, Task Area 04, Work Unit-18
11. CONTROLLING OFFICE NAME AND ADDRESS: Air Force Aero Propulsion Laboratory/TBC, Wright-Patterson AFB, OH 45433	12. REPORT DATE: Dec [redacted] 1976
	13. NUMBER OF PAGES: 256
14. MONITORING AGENCY NAME & ADDRESS *(if different from Controlling Office)*: Same	15. SECURITY CLASS. *(of this report)*: Unclassified
	15a. DECLASSIFICATION/DOWNGRADING SCHEDULE

16. DISTRIBUTION STATEMENT *(of this Report)*

Approved for public release; distribution unlimited.

17. DISTRIBUTION STATEMENT *(of the abstract entered in Block 20, if different from Report)*

Same

18. SUPPLEMENTARY NOTES

19. KEY WORDS *(Continue on reverse side if necessary and identify by block number)*

UNSTEADY FLOW
CASCADES (FLUID FLOW)
SUBSONIC WIND TUNNEL TESTING
AERODYNAMICS

20. ABSTRACT *(Continue on reverse side if necessary and identify by block number)*

The flow velocity in an axial compressor, with a distorted inlet pressure profile or rotating stall cells, is unsteady in both magnitude and direction with the unsteadiness in direction having a more abrupt effect on airfoil performance. The objective of this research was to obtain pressure distributions and pressure histories on both surfaces of an airfoil in a cascade while it is undergoing a sinusoidal variation in angle of attack.

A low speed, 80-150 fps, wind tunnel was constructed with a stationary

DD FORM 1 JAN 73 1473 EDITION OF 1 NOV 65 IS OBSOLETE

UNCLASSIFIED

SECURITY CLASSIFICATION OF THIS PAGE *(When Data Entered)*

011 570

20. five-blade cascade in a three by ten inch test section. The wind tunnel inlet, which included guide vanes, was forced to oscillate by a motor driven crank about an axis transverse to the cascade axis. The vanes guided the flow along the instantaneous axis of the inlet and thus achieved a variable flow direction of $\pm$ 5 3/4° at any frequency in the 0-16 hz range while the flow magnitude was nearly constant. The mean cascade air angle was 30° and the mean angle of attack was varied from 6 to 14°.

The 2.81 inch chord airfoils were biconvex circular arc with 10% thickness and 12° turning and were spaced at 2.3 inches. Each surface contained ten static pressure ports. These signals along with tunnel side wall statics and upstream velocity were recorded on FM Tape, digitized, and reduced on a digital computer.

The pressure fluctuations over most of both surfaces were near sinusoidal and the cyclic average showed little dependence on frequency or velocity. The pressure fluctuation decreased in amplitude along the chord on the pressure surface and changed phase on the suction surface near mid-chord. The pressures on both surfaces were adjusted by slow-moving waves and showed only a small change in phase angle with increased frequency. The unsteady pressure profiles are in excellent agreement with theory near the leading edge.

This wind tunnel represents a new method of obtaining experimental data for unsteady flows in cascades.

FOREWORD

This report contains the results of a dissertation which was prepared for the Mechanical Engineering Department of The Ohio State University. The effort was performed in the Computer Branch of the Turbine Engine Division of the Air Force Aero Propulsion Laboratory, Air Force Systems Command, Wright-Patterson AFB, Ohio, under Project 3066, Task 04, and Work Unit 18. A low speed atmospheric inlet cascade wind tunnel was constructed to obtain a flow which has a sinusoidal variation in flow direction. A stationary five-blade cascade was studied while varying flow velocity, oscillation frequency and mean angle of attack. This effort was conducted by Francis R. Ostdiek during the period November 1969 to June 1975.

TABLE OF CONTENTS

		Page
INTRODUCTION		1
Chapter		
I.	BACKGROUND	4
	A. Analytical Studies	4
	B. Experimental Work	8
II.	PRELIMINARY EXPERIMENTS	13
III.	EXPERIMENTAL APPARATUS	17
	A. Wind Tunnel Specifications	17
	B. Flow Path	21
	C. Oscillating Inlet	23
	D. Inlet Crank Mechanism	23
	E. Stationary Cascade	24
	F. Exhaust Plenum	26
IV.	DATA ACQUISITION	30
	A. Overall Method	30
	1. Channel Description 2. Wind Tunnel Test 3. Analog to Digital Conversion 4. Data Reduction 5. Data Correlation	
	B. System Performance	58

TABLE OF CONTENTS (Cont'd)

	Page
V. EXPERIMENTAL DATA	60
A. Inlet Flow	61
B. Airfoil Pressure Profiles	64
C. Airfoil Pressure Correlations	72
D. Comparison to Whitehead Theory	73
E. Lift and Moment	74
VI. INTERPRETATION OF RESULTS AND RECOMMENDATIONS	80
VII. CONCLUSIONS	86
LIST OF REFERENCES	88

LIST OF ILLUSTRATIONS

1. Typical Compressor Flow Angles 93
2. Flat Plate Airfoil 93
3. Fluidic Wind Tunnel Flow Path 94
4. Assembled Fluidic Wind Tunnel 94
5. Fluidic Tunnel Flow at 0° 95
6. Fluidic Tunnel Flow at 90° 95
7. Fluidic Tunnel Flow at 180° 96
8. Oscillatory Wind Tunnel Model 96
9. Oscillatory Tunnel Test Set-up 97
10. Oscillatory Tunnel with Hot Wire in Place 97
11. One Inch Chord Vanes 98
12. Two Inch Chord Vanes 98
13. Preliminary Vane Test 99
14. Test Cell Filter Wall 99
15. Control Room 100
16. Cascade Nomenclature 100
17. Cascade Flow Schematic 101
18. Wind Tunnel Side Plates 101
19. Oscillatory Inlet 102
20. Partially Assembled Tunnel on Assembly Jig 102
21. Stationary Cascade 103
22. Rear View of Assembled Wind Tunnel 103

23. Quarter View of Assembled Wind Tunnel 104
24. Top View of Assembled Wind Tunnel 104
25. Stanchion 105
26. Assembled Wind Tunnel 105
27. Gear Case 106
28. Biconvex Circular Arc Cascade 106
29. Pressure Surface Machining Operation 107
30. Suction Surface Machining Operation 107
31. Pressure Transducer Clusters 108
32. Transducer Cluster Side View 108
33. Transducer Cluster in Right Trunion 109
34. Transducer Cluster in Left Trunion 109
35. Auxiliary Transducer Mounting 110
36. Flow Control Valve Outlet 110
37. Flow Control Valve Inlet 111
38. Plenum Muffler Box 111
39. Variable Area Flow Path 112
40. Data Acquisition Block Diagram 113
41. Data Acquisition, Step One and Step Two 114
42. Tape Recording Room 115
43. Data Acquisition, Step Three and Step Four 116
44. Keyboard and Video Display 117
45. DBN Breadboard 117
46. Electronic Low-Pass Filter Design 118
47. Electronic Filter Breadboard 119
48. One Cycle Pressure Data 120

49. Eight Cycle Average Pressure Data 121

50. Hot Wire Probe Support 122

51. Clean Hot Wires 122

52. Dirty Hot Wires 123

53. Hot Film Anemometer Output Versus Flow Angle, Channel 1 . . 124

54. Hot Film Anemometer Output Versus Flow Angle, Channel 2 . . 125

55. Hot Wire Anemometer Output Versus Flow Angle 126

56. Hot Film Anemometer Output Versus Flow Angle and Reynolds Number 127

57. Hot Film Anemometer Output Versus Flow Total Temperature . 128

58. Hot Wire Angle Definition 129

59. Hot Wire Anemometer Output Versus Flow Angle Calibration . 130

60. Hot Wire Anemometer Output Versus Mass Flow Calibration, Channel 1 131

61. Hot Wire Anemometer Output Versus Mass Flow Calibration, Channel 2 132

62. Pressure Data Using 5-Terms of Fourier Series 133

63. Pressure Data Using 10-Terms of Fourier Series 134

64. Pressure Data Using 15-Terms of Fourier Series 135

65. Inlet Velocity History, Run 3730, $\alpha_m = 6°$, $V_N = 150$ fps, $f_t = 1.43$ hz 136

66. Inlet Velocity History, Run 3850, $\alpha_m = 8°$, $V_N = 150$ fps, $f_t = 1.43$ hz 137

67. Inlet Velocity History, Run 3970, $\alpha_m = 10°$, $V_N = 150$ fps, $f_t = 1.43$ hz 138

68. Inlet Velocity History, Run 4060, $\alpha_m = 12°$, $V_N = 150$ fps, $f_t = 1.43$ hz 139

69. Inlet Pressure History, Run 7490, $\alpha_m = 10°$, $V_N = 150$ fps, $f_t = 0.2$ hz 140

70. Inlet Pressure History, Run 7520, α_m = 10°, V_N = 150 fps, f_t = 6.14 hz 141

71. Inlet Pressure History, Run 7570, α_m = 10°, V_N = 150 fps, f_t = 16.21 hz 142

72. Inlet Pressure History, Run 7020, α_m = 6°, V_N = 150 fps, f_t = 0.2 hz 143

73. Airfoil Pressure Port Designation 144

74. Airfoil Pressure History, Run 7020, α_m = 6°, V_N = 150 fps, f_t = 0.2 hz 145

75. Time Increment Pressure Profile, Run 7020, α_m = 6°, V_N = 150 fps, f_t = 0.2 hz 146

76. Normalized Pressure Profile, Run 7020, α_m = 6°, V_N = 150 fps, f_t = 0.2 hz 147

77. Airfoil Pressure History, Run 7100, α_m = 6°, V_N = 150 fps, f_t = 16.2 hz 148

78. Time Increment Pressure Profiles, Run 7100, α_m = 6°, V_N = 150 fps, f_t = 16.2 hz 149

79. Normalized Pressure Profiles, Run 7100, α_m = 6°, V_N = 150 fps, f_t = 16.2 hz 150

80. Airfoil Pressure History, Run 7110, α_m = 6°, V_N = 110 fps, f_t = 0.2 hz 151

81. Time Increment Pressure Profiles, Run 7110, α_m = 6°, V_N = 110 fps, f_t = 0.2 hz 152

82. Normalized Pressure Profiles, Run 7110, α_m = 6°, V_N = 110 fps, f_t = 0.2 hz 153

83. Airfoil Pressure History, Run 7190, α_m = 6°, V_N = 110 fps, f_t = 16.2 hz 154

84. Time Increment Pressure Profiles, Run 7190, α_m = 6°, V_N = 110 fps, f_t = 16.2 hz 155

85. Normalized Pressure Profiles, Run 7190, α_m = 6°, V_N = 110 fps, f_t = 16.2 hz 156

86. Airfoil Pressure History, Run 7220, α_m = 8°, V_N = 150 fps, f_t = 0.2 hz 157

87. Time Increment Pressure Profiles, Run 7220, $\alpha_m = 8°$, $V_N = 150$ fps, $f_t = 0.2$ hz 158

88. Normalized Pressure Profiles, Run 7220, $\alpha_m = 8°$, $V_N = 150$ fps, $f_t = 0.2$ hz 159

89. Airfoil Pressure History, Run 7360, $\alpha_m = 8°$, $V_N = 150$ fps, $f_t = 16.2$ hz 160

90. Time Increment Pressure Profiles, Run 7360, $\alpha_m = 8°$, $V_N = 150$ fps, $f_t = 16.2$ hz 161

91. Normalized Pressure Profiles, Run 7360, $\alpha_m = 8°$, $V_N = 150$ fps, $f_t = 16.2$ hz 162

92. Airfoil Pressure History, Run 7370, $\alpha_m = 8°$, $V_N = 110$ fps, $f_t = 0.2$ hz 163

93. Time Increment Pressure Profiles, Run 7370, $\alpha_m = 8°$, $V_N = 110$ fps, $f_t = 0.2$ hz 164

94. Normalized Pressure Profiles, Run 7370, $\alpha_m = 8°$, $V_N = 110$ fps, $f_t = 0.2$ hz 165

95. Airfoil Pressure History, Run 7450, $\alpha_m = 8°$, $V_N = 110$ fps, $f_t = 16.2$ hz 166

96. Time Increment Pressure Profiles, Run 7450, $\alpha_m = 8°$, $V_N = 110$ fps, $f_t = 16.2$ hz 167

97. Normalized Pressure Profiles, Run 7450, $\alpha_m = 8°$, $V_N = 110$ fps, $f_t = 16.2$ hz 168

98. Airfoil Pressure History, Run 7490, $\alpha_m = 10°$, $V_N = 150$ fps, $f_t = 0.2$ hz 169

99. Time Increment Pressure Profiles, Run 7490, $\alpha_m = 10°$, $V_N = 150$ fps, $f_t = 0.2$ hz 170

100. Normalized Pressure Profiles, Run 7490, $\alpha_m = 10°$, $V_N = 150$ fps, $f_t = 0.2$ hz 171

101. Airfoil Pressure History, Run 7570, $\alpha_m = 10°$, $V_N = 150$ fps, $f_t = 16.2$ hz 172

102. Time Increment Pressure Profiles, Run 7570, $\alpha_m = 10°$, $V_N = 150$ fps, $f_t = 16.2$ hz 173

103. Normalized Pressure Profiles, Run 7570, $\alpha_m = 10°$, $V_N = 150$ fps, $f_t = 16.2$ hz 174

104. Airfoil Pressure History, Run 7710, α_m = 10°, V_N = 110 fps, f_t = 1.43 hz 175

105. Time Increment Pressure Profiles, Run 7710, α_m = 10°, V_N = 110 fps, f_t = 1.43 hz 176

106. Normalized Pressure Profiles, Run 7710, α_m = 10°, V_N = 110 fps, f_t = 1.43 nz 177

107. Airfoil Pressure History, Run 7780, α_m = 10°, V_N = 110 fps, f_t = 16.2 hz 178

108. Time Increment Pressure Profiles, Run 7780, α_m = 10°, V_N = 110 fps, f_t = 16.2 hz 179

109. Normalized Pressure Profiles, Run 7780, α_m = 10°, V_N = 110 fps, f_t = 16.2 hz 180

110. Airfoil Pressure History, Run 7790, α_m = 10°, V_N = 82 fps, f_t = 0.2 hz 181

111. Time Increment Pressure Profiles, Run 7790, α_m = 10°, V_N = 82 fps, f_t = 0.2 hz 182

112. Normalized Pressure Profiles, Run 7790, α_m = 10°, V_N = 82 fps, f_t = 0.2 hz 183

113. Airfoil Pressure History, Run 7920, α_m = 12°, V_N = 150 fps, f_t = 0.2 hz 184

114. Time Increment Pressure Profiles, Run 7920, α_m = 12°, V_N = 150 fps, f_t = 0.2 hz 185

115. Normalized Pressure Profiles, Run 7920, α_m = 12°, V_N = 150 fps, f_t = 0.2 hz 186

116. Airfoil Pressure History, Run 8000, α_m = 12°, V_N = 150 fps, f_t = 16.1 hz 187

117. Time Increment Pressure Profiles, Run 8000, α_m = 12°, V_N = 150 fps, f_t = 16.1 hz 188

118. Normalized Pressure Profiles, Run 8000, α_m = 12°, V_N = 150 fps, f_t = 16.1 hz 189

119. Airfoil Pressure History, Run 8100, α_m = 12°, V_N = 110 fps, f_t = 0.2 hz 190

120. Time Increment Pressure Profiles, Run 8100, α_m = 12°, V_N = 110 fps, f_t = 0.2 hz 191

121. Normalized Pressure Profiles, Run 8100, $\alpha_m = 12°$, $V_N = 110$ fps, $f_t = 0.2$ hz 192

122. Airfoil Pressure History, Run 8180, $\alpha_m = 12°$, $V_N = 110$ fps, $f_t = 16.2$ hz 193

123. Time Increment Pressure Profiles, Run 8180, $\alpha_m = 12°$, $V_N = 110$ fps, $f_t = 16.2$ hz 194

124. Normalized Pressure Profiles, Run 8180, $\alpha_m = 12°$, $V_N = 110$ fps, $f_t = 16.2$ hz 195

125. Comparison of Steady Pressure Profile to Steady Cascade Data 196

126. Unsteady Pressure Phase Angle, Variable Velocity, $\alpha_m = 6°$ 197

127. Unsteady Pressure Phase Angle, Variable Velocity, $\alpha_m = 8°$ 198

128. Unsteady Pressure Phase Angle, Variable Velocity, $\alpha_m = 10°$ 199

129. Unsteady Pressure Phase Angle, Variable Velocity, $\alpha_m = 12°$ 200

130. Unsteady Pressure Phase Angle, Variable Frequency, $\alpha_m = 12°$ 201

131. Normalized Average Pressure Versus f_t, Group 1, $\alpha_m = 6°$ 202

132. Normalized Average Pressure Versus f_t, Group 2, $\alpha_m = 6°$ 203

133. Normalized Average Pressure Versus f_t, Group 3, $\alpha_m = 6°$ 204

134. Normalized Average Pressure Versus f_t, Group 4, $\alpha_m = 6°$ 205

135. Normalized Average Pressure Versus f_t, Group 5, $\alpha_m = 6°$ 206

136. Normalized Unsteady Pressure Versus f_t, Group 1, $\alpha_m = 6°$ 207

137. Normalized Unsteady Pressure Versus f_t, Group 2, $\alpha_m = 6°$ 208

138. Normalized Unsteady Pressure Versus f_t, Group 3, $\alpha_m = 6°$ 209

139. Normalized Unsteady Pressure Versus f_t, Group 4, $\alpha_m = 6°$ 210

140. Normalized Unsteady Pressure Versus f_t, Group 5, $\alpha_m = 6°$ 211

141. Normalized Average Pressure Versus f_t, Group 1, $\alpha_m = 8°$ 212
142. Normalized Average Pressure Versus f_t, Group 2, $\alpha_m = 8°$ 213
143. Normalized Average Pressure Versus f_t, Group 3, $\alpha_m = 8°$ 214
144. Normalized Average Pressure Versus f_t, Group 4, $\alpha_m = 8°$ 215
145. Normalized Average Pressure Versus f_t, Group 5, $\alpha_m = 8°$ 216
146. Normalized Unsteady Pressure Versus f_t, Group 1, $\alpha_m = 8°$ 217
147. Normalized Unsteady Pressure Versus f_t, Group 2, $\alpha_m = 8°$ 218
148. Normalized Unsteady Pressure Versus f_t, Group 3, $\alpha_m = 8°$ 219
149. Normalized Unsteady Pressure Versus f_t, Group 4, $\alpha_m = 8°$ 220
150. Normalized Unsteady Pressure Versus f_t, Group 5, $\alpha_m = 8°$ 221
151. Normalized Average Pressure Versus f_t, Group 1, $\alpha_m = 10°$ 222
152. Normalized Average Pressure Versus f_t, Group 2, $\alpha_m = 10°$ 223
153. Normalized Average Pressure Versus f_t, Group 3, $\alpha_m = 10°$ 224
154. Normalized Average Pressure Versus f_t, Group 4, $\alpha_m = 10°$ 225
155. Normalized Average Pressure Versus f_t, Group 5, $\alpha_m = 10°$ 226
156. Normalized Unsteady Pressure Versus f_t, Group 1, $\alpha_m = 10°$ 227
157. Normalized Unsteady Pressure Versus f_t, Group 2, $\alpha_m = 10°$ 228
158. Normalized Unsteady Pressure Versus f_t, Group 3, $\alpha_m = 10°$ 229
159. Normalized Unsteady Pressure Versus f_t, Group 4, $\alpha_m = 10°$ 230
160. Normalized Unsteady Pressure Versus f_t, Group 5, $\alpha_m = 10°$ 231
161. Normalized Average Pressure Versus f_t, Group 1, $\alpha_m = 12°$ 232
162. Normalized Average Pressure Versus f_t, Group 2, $\alpha_m = 12°$ 233
163. Normalized Average Pressure Versus f_t, Group 3, $\alpha_m = 12°$ 234
164. Normalized Average Pressure Versus f_t, Group 4, $\alpha_m = 12°$ 235
165. Normalized Average Pressure Versus f_t, Group 5, $\alpha_m = 12°$ 236

166. Normalized Unsteady Pressure Versus f_t, Group 1, $\alpha_m = 12°$ 237

167. Normalized Unsteady Pressure Versus f_t, Group 2, $\alpha_m = 12°$ 238

168. Normalized Unsteady Pressure Versus f_t, Group 3, $\alpha_m = 12°$ 239

169. Normalized Unsteady Pressure Versus f_t, Group 4, $\alpha_m = 12°$ 240

170. Normalized Unsteady Pressure Versus f_t, Group 5, $\alpha_m = 12°$ 241

171. Comparison of Experimental Data with Whitehead Theory . . . 242

172. Pressure, Lift, and Moment Hysteresis, Run 7020, $\alpha_m = 6°$, $V_N = 150$ fps, $f_t = 0.2$ hz 243

173. Pressure, Lift, and Moment Hysteresis, Run 7220, $\alpha_m = 8°$, $V_N = 150$ fps, $f_t = 0.2$ hz 244

174. Pressure, Lift, and Moment Hysteresis, Run 7490, $\alpha_m = 10°$, $V_N = 150$ fps, $f_t = 0.2$ hz 245

175. Pressure, Lift, and Moment Hysteresis, Run 7500, $\alpha_m = 10°$, $V_N = 150$ fps, $f_t = 1.42$ hz 246

176. Pressure, Lift, and Moment Hysteresis, Run 7510, $\alpha_m = 10°$, $V_N = 150$ fps, $f_t = 4.42$ hz 247

177. Pressure, Lift, and Moment Hysteresis, Run 7520, $\alpha_m = 10°$, $V_N = 150$ fps, $f_t = 6.14$ hz 248

178. Pressure, Lift, and Moment Hysteresis, Run 7530, $\alpha_m = 10°$, $V_N = 150$ fps, $f_t = 8.08$ hz 249

179. Pressure, Lift, and Moment Hysteresis, Run 7540, $\alpha_m = 10°$, $V_N = 150$ fps, $f_t = 10.34$ hz 250

180. Pressure, Lift, and Moment Hysteresis, Run 7550, $\alpha_m = 10°$, $V_N = 150$ fps, $f_t = 12.01$ hz 251

181. Pressure, Lift, and Moment Hysteresis, Run 7560, $\alpha_m = 10°$, $V_N = 150$ fps, $f_t = 14.09$ hz 252

182. Pressure, Lift, and Moment Hysteresis, Run 7570, $\alpha_m = 10°$, $V_N = 150$ fps, $f_t = 16.21$ hz 253

183. Time-Average Center of Pressure Versus Angle of Attack . . 254

184. Lift Coefficients Versus Reduced Frequency 255

185. Moment Coefficients Versus Reduced Frequency 256

LIST OF TABLES

		Page
1.	Cascade Specifications	18
2.	Normalized Unsteady Aerodynamic Coefficients	79

NOMENCLATURE

A	Hot wire correlation constant
A_ω	Hot wire temperature coefficient of resistance
$a_{n,k}$	kth Fourier cosine coefficient for Channel n
B	Hot wire correlation constant
b	Half-chord
$b_{n,k}$	kth Fourier sine coefficient for Channel n
c	Chord length
C_L	Coefficient of Lift
$\overline{C}_L$	Time-average component of C_L
$\tilde{C}_L$	Unsteady component of C_L
C_M	Coefficient of Moment
$\overline{C}_M$	Time-average component of C_M
$\tilde{C}_M$	Unsteady component of C_M
CP	Center of pressure, fraction of half-chord

$\overline{CP}$	Time-average center of pressure
C_p	Normalized differential pressure
$\overline{C}_p$	Time-averaged component of C_p
$\tilde{C}_p$	Unsteady component of C_p
D	Diameter
E_c	Calculated anemometer output
E_f	Anemometer output at T_f
E_o	Anemometer output normalized to T_o
E_t	Anemometer output
E_{60}	Anemometer output at 60°F
E_{80}	Anemometer output at 80°F
f_t	Oscillation frequency, hz
g	Gravitational constant
i	Incidence angle, angle between inlet air direction and tangent to blade mean camber line at leading edge, deg.
k	Specific heat ratio
K	Hot wire angle correction factor

L	Aerodynamic lift force normal to the airfoil chord for a one inch span
M	Aerodynamic moment about the point of maximum thickness for a one inch span
M_N	Mach number
p_n	Instantaneous static pressure of nth port
$\bar{p}_n$	Time-average of p_n
Δp_n	Variation of p_n from $\bar{p}_n$
$\Delta p_{n,k}$	Differential static pressure using k Fourier terms
P_n	Normalized static pressure of port n
$\bar{P}_n$	Time-averaged of P_n
$\Delta P_{n,1}$	Normalized $\Delta p_{n,1}$
p_{ref}	Plenum pressure
q	Measured velocity head
Q	Velocity head, pressure drop across the cascade
R	Gas constant
R_f	Hot wire resistance at T_f

R_w	Hot wire resistance at T_w
r/L	Crank radius to length ratio
S	Pressure conversion factor
T_f	Fluid temperature during hot wire calibration
T_o	Total temperature or reference temperature
T_w	Calculated hot wire temperature
T_N	Normalized oscillation time
u	Turbulent velocity component
U	Free stream velocity
U_o	Free stream velocity during hot wire calibration
U_e	Effective hot wire cooling velocity
V_N	Nominal tunnel velocity which would exist at a fixed pressure ratio if the cascade were removed
V	Velocity, ft/sec
V_C	Velocity normal to the airfoil chord which a change in inlet direction would induce if the cascade were removed
V_{ax}	Axial velocity in a turbomachine

ΔV_{ax}	Change in axial velocity
x/c	Fraction of airfoil chord
XFUN	Amplitude of fundamental of a data channel
α	Angle of attack, angle between inlet air direction and blade chord, deg.
α_m	Mean angle of attack
β	Air angle, angle between inlet air direction and line normal to cascade axis
β_1	Angle between air direction and Hot Wire 1
β_2	Angle between air direction and Hot Wire 2
γ	Blade chord angle, angle between blade chord and line normal to cascade axis
θ_1	Protractor reading when Hot Wire 1 is near perpendicular to the flow
θ_{ref}	Protractor reading when hot wire probe is installed in wind tunnel
ω	Oscillation frequency in radians/sec
$\bar{\omega}$	Reduced frequency, $\omega b/V$

INTRODUCTION

Unsteady flows in turbine engine compressors have been receiving an increasing amount of attention during the past decade. There has been a continuing demand for higher performance aircraft which undergo violent maneuvers and this has forced the designer to consider all types of flows which may exist in a turbine engine compressor and, in particular, to give a great deal of attention to the unsteady aspects of the flow throughout the engine. This has resulted in a great deal of research on all aspects of the problem, both experimental and analytic, which ranges from considering the whole compressor to detailed flow mechanisms.

In general, the throughflow in an axial compressor is unsteady in both magnitude and direction. This unsteadiness is caused by rotating stall cells, stationary distorted pressure profiles at the compressor inlet face, secondary flow effects at the hub and casing, and blade wakes of the preceding row. The result is often a variation in both magnitude and direction of the flow; however, the unsteadiness in direction would seem to have a more abrupt effect on performance and, thus, research in this area would have a more direct application in future compressor designs.

Most flows in a compressor are turbulent and in the strictest sense are unsteady, but the scale of the turbulence is several orders of magnitude less than the airfoil dimensions. Also, the operating

point of the compressor varies slowly and in this case the wave length of the disturbance is much greater than the airfoil dimensions. However, between these two extremes there is a class of flows with disturbances wave lengths from 0.01 to 5 times the airfoil dimensions which can have drastic effects on compressor performance.

In the present work the variable flow caused by a distorted total pressure profile at the inlet face, which has a wave length on the order of the circumference of the face, will be considered. This variation in total pressure results in a variable axial velocity into the compressor. When the constant rotor speed is added vectorially, there results a relative flow into the rotor which has a variation in magnitude and a variation in flow direction. This is shown in Figure 1 where the axial velocity, V_{ax}, corresponds to the minimum total pressure on the compressor face and then ΔV_{ax} is a result of a positive increment in total pressure and the resulting angle chance is $\Delta\beta$. It can be shown that for typical aircraft operational requirements, the total pressure distortion is bounded by

$$0 < \frac{P_{T,Max} - P_{T,Min}}{P_{T,\ Avg}} < 0.40$$

Depending on the average inlet axial velocity and blade angles, the flow direction can change as much as 10-15° from the average, and the magnitude can change by $\pm$20%. These are extreme cases which would certainly lead to flow separation and should not be considered in an initial investigation. However, it does indicate that the problem is not in the range of small perturbations. Although the problem of a

stationary total pressure distortion pattern has been used to illustrate flow with a variable direction in a rotor, a rotating stall cell could be considered to create much the same problem in a stator row. Indeed, the rotor wakes of a large diameter fan could be included in this type of flow.

In a basic research program, it is desirable to consider the effects of variable magnitude and variable direction separately to quantitatively assess their effects on airfoil performance. Therefore, this experimental research was directed towards obtaining pressure distributions and pressure histories on one airfoil of a stationary cascade which had an oncoming flow of oscillating direction but nearly constant amplitude. Then the pressure fluctuations could be attributed to a directional change only. The oncoming flow has unsteady components embedded in it and the assumption of two-dimensional flow is made so that a staggered cascade of airfoils can be used to represent a row of compressor blades that has been unwrapped.

CHAPTER I. BACKGROUND

In this chapter, some of the past work on unsteady flow will be reviewed to show its relevance to the present experimental investigation which involves a turbulent stream of sinusoidally varying direction through a stationary cascade. The literature abounds with unsteady laminar work and while it may give us clues as to the proper investigative direction, it will not be reviewed here.

A. Analytical Studies

Unsteady airfoil flows have been the subject of a considerable amount of analytical work starting from a paper by von Karman and Sears (1938) who used the theory of thin airfoils in two-dimensional flow to analyze the non-uniform motion of an airfoil. This work assumes small motions and a lightly loaded airfoil so that the oncoming flow, the airfoil which is represented by a vorticity distribution, and the airfoil wake all lie on the X-axis. Generalized expressions for the lift and moment on the airfoil were obtained for translatory and rotational oscillation of the airfoil. Sears (1940) later extended this work, and using the same basic linearized theory, analyzed the unsteady lift generated on an isolated airfoil moving through an upstream disturbance. The flows were assumed to be steady potential flows with a transverse gust superimposed on the mean flow. Kemp and Sears (1953) used this first-order theory of small fluctuations to study the aerodynamic

interference between a stator and a rotor in a turbomachine. The study was limited to cascades of blades wherein the effects of the unsteady parts of the circulation of other blades was neglected while the steady-state parts were retained. The blades were modeled as lightly loaded thin airfoils in an incompressible inviscid fluid. Later, Kemp and Sears (1955) added the effects of a viscous wake which was modeled as an inviscid shear flow but the presence of vorticity in the oncoming flow was neglected.

Horlock (1968) added a chordwise gust to the Sears theory and thus was able to consider gusts with components parallel and perpendicular to the undisturbed flow. He obtained an estimate of the unsteady flow effects of this type of flow on a rotor blade. Henderson and Horlock (1972) continued this approach for airfoils in a cascade in an inviscid flow and made provisions for the nearby blades. This study was done for a cascade where the blade spacing was small compared to the wavelength of the disturbance. Highly cambered blades were used but the lift coefficient was kept low by choosing a low pitch-chord ratio. The flow was assumed to be inviscid, and incompressible and the equations of continuity and momentum were averaged across the pitch.

Henderson and Daneshyar (1972) used unsteady thin airfoil theory to analyze the fluctuating lift of a rigid cascade of airfoils. They replaced the reference blade by a continuous vorticity distribution and the neighboring blades by concentrated vortices. Inviscid incompressible flow with small disturbances was assumed. Osborne (1973a) (1973b) provides an extension to the previous work on thin airfoils.

His work is restricted to subsonic flow, low reduced frequency, and small perturbations with the resulting restrictions. A subsequent note by Kemp (1973) provides some closed form expressions for lift and moment for Osborne's theory.

Fleeter (1973) used the thin-airfoil assumptions to consider small unsteady compressible perturbations on a basic uniform two-dimensional compressible flow. His results agreed with potential flow results for both isolated airfoils and cascaded airfoils in incompressible flow.

Graham (1970) used similarity rules to analyze a thin two-dimensional wing at subsonic speeds which encountered gusts at an angle to the leading edge. This is a linear analysis in which airfoil thickness, incidence, camber and gust velocities are all assumed small. Graham observes that the validity of linearization is vital to the analysis of turbulent flows, since without it, Fourier analysis cannot be used and the problem becomes intractable. This observation is particularly applicable to cascade flows with a large incidence and turning angle since the mean flow, the airfoil, and the vortex sheet which is shed from the trailing edge no longer lie close to one axis. In addition, if a flow has a variable direction it must have some vorticity in the stream which impinges on the cascade. This effect has been neglected in the linearized thin airfoil approach.

Schorr and Reddy (1971) analyzed a cascade with a basic steady state flow over which unsteady normal velocity fluctuations were superimposed. An incompressible inviscid flow is assumed with a thin airfoil

and only small flow disturbances are allowed so that linearization becomes valid. They make the point that unsteady flow, due to a cascade of airfoils oscillating about some pivot point in an otherwise uniform flow, is not the same case as the flow through a rigid set of airfoils when the upstream flow contains unsteady disturbances. The former is important in flutter work while the latter more nearly describes flows in turbomachinery. In either case, the problem can be linearized if the analysis is restricted to small perturbations, thin airfoils, and small camber and incidence.

Whitehead (1960) considered the incompressible inviscid case of flat plate cascades with small amplitudes of vibration. The blades and the wakes were regarded as vortex sheets and in one of the cases considered, the blades were operating in the wakes of some kind of periodic obstruction similar to a compressor blade row. In further work, Whitehead (1974a) uses the unsteady velocity potential and considers vorticity in the flow. This line of analysis has led to computer calculations of the flow field and some results of this analysis have been provided (Whitehead 1974b) for use in the present program and will be presented later.

There are some analyses presented in the past several years which use turbulent flow as the point of departure. McDonald and Shamroth (1971) did an analytical investigation of the time-dependent integral turbulent boundary layer equations of mean motion. Their solution involved choosing a velocity profile family, a velocity-temperature relationship, and a model for turbulent shear stress. The model is

presently restricted to small disturbances and is used to investigate some shock wave-boundary layer interactions.

Rannie (1974) used one-dimensional flow in a duct and the linearized equations of motion to consider upstream disturbances sinusoidal in time. He obtained solutions of acoustic-type waves moving upstream and downstream at a speed which is not necessarily sonic. The interaction of the compressor can thus change the oncoming disturbed flow. Consideration is being given to extending the analysis to two-dimensions.

B. Experimental Work

There has been very little experimental work that is even similar to the present experiment. Some experimental work has been done on flat plates with impulsive starts or oscillating motions parallel to the direction of a steady flow stream. This will certainly cause a marked change in the boundary layer but it does not simulate a variable direction. In addition, there has been a considerable amount of work using airfoils which oscillate in pitch in a steady stream. This work is certainly applicable to helicopter rotors and flutter, but it is not the fluid flow case of an oncoming stream which has a variable flow direction and is not generally applicable to compressor flows.

Consider the flow schematic in Figure 2 of a flow of mean velocity U and angle α directed on a flat plate. If the flow direction, α, varies, the pressure at any point P in the upper boundary layer will also vary. If the flow at the point is accelerated because of the angle variation, the accelerations would be neither in the same direction,

nor of the same magnitude as the case where the airfoil is oscillated in pitch. In addition, an airfoil oscillating in pitch may be doing work on the fluid while a stationary airfoil cannot do work. Therefore, the energy level of the fluid particles in the boundary layer would be different for the two cases and both the separation point and the pressure profile will be affected. Consequently, an airfoil oscillating in pitch does not simulate a flow of variable direction.

Commerford and Carta (1974) simulated an unsteady direction on a single airfoil by generating a Karman vortex street from a transverse cylinder mounted upstream and below an airfoil. A three-inch chord, 5% thick, symmetrical double circular arc airfoil was selected and five pressure transducers connected to each surface. The tests were conducted at a Mach number of 0.25 and the cylinder diameter was chosen to give a disturbance wavelength of one chord. The flow field thus created has a vertical velocity component which varies in both directions, requiring a little care in airfoil positioning to obtain the proper magnitude of the fluctuation at the airfoil. However, this would not be a serious drawback unless a cascade of airfoils were used in which case the velocity direction would vary from blade to blade. The results showed that the amplitude of the pressure fluctuation exceeded the theoretical prediction of Sears and had a chordwise variation in phase angle which was not predicted by the Sears theory. The phase angle decreases from the leading edge to mid-chord and then increases to the trailing edge. It must be remembered that this test was for an isolated airfoil at a

reduced frequency of 3.9, but a comparison can be made with the present data and will be done below.

An unsteady flow wind tunnel was described by Horlock (1974) in which the tunnel test section has flexible side walls. These walls are constrained to form traveling sine waves by a system of cams and springs. The wavy walls can travel in phase to produce a transverse (Sears) gust or out of phase to produce a streamwise (Horlock) gust. The sine waves must be made to travel at a speed different from the air flow or there is no flow variation at all. This means that unsteady flow disturbances convected at free stream velocity cannot be simulated in this tunnel. Holmes (1973) reported on an experiment in the Horlock tunnel with pressure taps on both surfaces of an isolated airfoil and found good agreement with Kemp (1952) at zero incidence to a transverse gust, but also found the airfoil to be subject to separation at incidence to a streamwise gust so that thin airfoil theory could not be applied.

Satyanarayana, Henderson and Gostelow (1974) reported on additional experiments in the Horlock tunnel on a cascade of airfoils for reduced frequencies less than 0.1 based on free stream velocity. These tests were run for a transverse non-convected gust with various solidities. They found that the unsteady pressure was sinusoidal near the leading edge but departed completely from that as the trailing edge was approached. They also found that separation always occurred on the instantaneous suction surface but that the airfoil pressure profiles were smooth at all times. In addition, there was a phase lag between

the lift and the gust velocity. Their pressure measurements indicate that the pressure difference across the trailing edge remained zero throughout the cycle, but that the pressure level itself may fluctuate. Some of these results are not in agreement with the results in the present test and will be discussed later.

There are several research programs underway at the present which feature an instrumented rotor blade in a rotating rig with some sort of disturbance mechanism at the inlet. Henderson and Bruce (1974) describe a facility designed to obtain response of rotor blade elements in incompressible unsteady flow. The unsteady flow is produced by segmented screens in front of the inlet which has been shown to produce a nearly sinusoidal axial velocity profile at reduced frequencies from 0.27 to 4.11. A midspan segment of one rotor blade is mounted to obtain direct readings of lift and moment. Preliminary data was found to have some agreement with the Sears and Henderson-Daneshyar models.

O'Brien and Moses (1974) have placed miniature pressure transducers on the blades of a low speed single-stage axial-flow rotor. The research compressor is equipped with distortion-inducing screens immediately in front of the rotor, and with the help of hot wire anemometers downstream of the rotor, they intend to study pressure fluctuations and other changes during rotating stall.

In a similar fashion, Peacock (1974) describes a lightly loaded single stage compressor which has 1.90 inch chord rotor blades instrumented at midspan to yield dynamic pressure measurements. Distortion screens of 90° segmental area are positioned at the inlet and he

found that the magnitude and shape of the generated distortion was highly dependent, not only on the screen position but also upon the operational point on the compressor characteristic map. The non-linear response of the compressor blades, due to the distortion pattern, produced a disturbance propagating upstream which changed the distortion pattern. This supports Rannie's analytical approach to the problem. Peacock found that the plots of normal force versus incidence angle could have several peaks. The primary peak always occurred at the same spot but the secondary dip always seems to occur in the region immediately downstream of the trailing edge of the gauze. Both the primary and tertiary peaks could be made to disappear by choosing a short enough screen segment. It is recognized that the upstream vorticity may have a profound effect on airfoil performance.

CHAPTER II. PRELIMINARY EXPERIMENTS

In preliminary studies, several small models of candidate wind tunnel designs were built and tested. The first schemes involved jets intersecting in a test section with one or more of the jets having a pulsating flow. These schemes were discarded because the flow direction across the test section was not constant at any instant and because of the high mixing turbulence.

The third candidate was patterned after a bi-stable fluidic amplifier and is shown in Figure 3 with part of the upper cover removed. Air was drawn in through a two-dimensional nozzle into a 1 1/2 by 1 1/2 inch throat. The flow was switched to either side of the centerbody by alternately blocking each leg of the tunnel. Blockage was performed by pulsing an array of high pressure jets in the upstream direction. These jets were made by drilling small holes in the one-fourth inch copper tube placed across the leg. The assembled tunnel is shown in Figure 4 with a plate glass cover over the test section. Sewing needles were hammered into the floor of the tunnel and small pieces of silk thread were attached. A series of photographs was taken to show one complete cycle and three of them are shown in Figures 5, 6 and 7 at 90° intervals in the cycle. This device gave directional variations up to the design angle of $\pm 40°$. The general flow angle pattern indicated by the threads was supported by a potential mapping using conductive paper. The

temporal variation in flow angle was not sinusoidal but tended to switch rapidly. Therefore, this device was discarded.

The fourth wind tunnel model that was built differed significantly from the previous three because it did not depend on fluid mixing or jet interaction with the consequent nonuniformities. In this case, the location of the fluid source relative to a fixed test section was varied by oscillating the whole wind tunnel. An oscillating inlet was simulated with a small metal box shown in Figure 8. It has a connection for high pressure air at one end and a two-dimensional 1 x 6 inch nozzle at the other end. The flow is straightened with soda straws and the whole mechanism was oscillated using an electric motor and crank with the axis of rotation at the middle of the throat of the convergent section. Oscillation was in a plane transverse to the flow contraction. The assembled tunnel is shown in Figure 9 with the crank at the lower left. The metal housing and plexiglas structure at the right forms a rotatable table for a hot wire probe. An end view of the tunnel in Figure 10 shows the hot wire in position during test. The test results gave the design directional variation of 24° and was smooth and continuous at 1.4 hz. Also, the magnitude of the velocity was constant within $\pm$1%. Since this performance met the original goals, this concept was adopted. However, it was felt that an atmospheric inlet in the full size tunnel would give better flow quality and would be an easier design problem. Also, guide vanes would be utilized rather than flow straighteners and would be located in the two-dimensional nozzle to minimize the moment of inertia.

Since the guide vanes would create wakes, a short investigation was conducted to determine the required area contraction ratio downstream of the vanes for smooth flow in the test section. An inviscid calculation for two streamtubes of different initial velocities, but the same static pressure which go through the same static pressure ratio, can be used to simulate the flow in the vane wake compared to the main flow. Then, the steady Bernoulli equation gives

$$\frac{W_2^2}{2} - \frac{W_1^2}{2} = \frac{p_1}{\rho_1} - \frac{p_2}{\rho_2}$$

and

$$\frac{V_2^2}{2} - \frac{V_1^2}{2} = \frac{p_1}{\rho_1} - \frac{p_2}{\rho_2}$$

where W is the mainstream velocity and V is the velocity behind the vane and stations 1 and 2 are immediately behind the vane and after an area contraction respectively. Now, if we assume $\frac{V_1}{W_1} = 0.1$ so that the $(\frac{V_1}{W_2})^2$ disappears, and using the continuity equation, we obtain:

$$\frac{V_2}{W_2} = [1 - (\frac{A_2}{A_1})\ ]^{1/2}$$

This velocity ratio is greater than 0.9 for any area ratio greater than 2.29 and this approach does not include entrainment or turbulent mixing effects. In addition, the trailing edges of the vanes can be beveled and further smooth the final velocity profile. To support these

conclusions, model tests of the proposed guide vanes were performed. Three 120° arc vanes were stacked 0.375 inch apart in the contracting part of the two-dimensional inlet of wind tunnel Model No. 3. A hot wire anemometer was used to traverse the test section to determine if the individual blade wakes could still be observed after flow contraction. Individual tests were performed for vane widths of one and two inches as shown in Figures 11 and 12. Several sets of vanes were fabricated so that the radius of curvature of these curved vanes could be varied from one to eight inches. This corresponds to a flow area contraction, based on the vane exit area, of 1.4 to 11.1. Figure 13 shows the tunnel with its top plate and hot wire anemometer in position.

The test results show that the vane wakes could not be found in the test section except for the vane with the smallest inside radius (one inch). Even then, the wake was characterized by increased turbulence rather than a velocity defect. Therefore, one of the design guidelines for the full size wind tunnel was to use an inlet which had a flow area contraction greater than 2.

CHAPTER III. EXPERIMENTAL APPARATUS

An unsteady flow wind tunnel was designed and constructed at the Air Force Aero-Propulsion Laboratory at Wright-Patterson Air Force Base, Ohio, for the tests performed for this dissertation. Almost two years were spent in its design and construction and another six months in system shakedown. This tunnel can now be used to test a variety of airfoils in unsteady flow. The test complex was constructed in the basement of the Laboratory and the wind tunnel was housed in a closed room adjacent to the control room and was an atmospheric in-draft tunnel. Therefore, the wall of the test cell opposite the tunnel was used to hold a bank of air filters and is shown in Figure 14. The control room and some of the instrumentation are shown in Figure 15.

A. Wind Tunnel Specifications

This wind tunnel was built to simulate a typical variable flow direction that may be seen in the compressor of a turbine engine. Therefore, the operating parameters were chosen with this in mind. Each parameter was fixed by a variety of considerations, some of which will be discussed here. As in any design process, it was often necessary to change part of the specification due to mechanical considerations. In these cases, the change was always made with the aforementioned objective in mind. The wind tunnel specifications for this series of tests are given in Table I.

TABLE I

WIND TUNNEL SPECIFICATIONS

Test Section	3" x 10"
Cascade Angle, β	30°
Number of Blades	5
Chord Length	2.81"
Blade Spacing	2.3"
Airfoil	Double Circular Arc, 10% Thickness, 12° Turning
Velocity Range	82 - 150 fps
Mean Angle of Attack	6 - 14°
Delta Angle of Attack	$\pm$5 3/4° Nominal
Oscillation Frequency	0 - 16 hz
Reduced Frequency	0 - .15
Reynolds Number	1.2 - 2.2 x 10^5

The test section was kept as small as possible to reduce dynamic forces without seriously compromising aerodynamic performance. A blade chord length of approximately three inches is desirable to ease the static port machining problem and to negate machining inaccuracies and small scale flow irregularities. A solidity of 1.25 is in the range of compressor design practice and this fixed the blade spacing at 2.3 inches. The minimum number of airfoils that can be considered for a cascade to obtain good periodicity is five and was chosen for this test. This is a compromise that could be made in a first experiment because the aerodynamic results would be compared on a steady to unsteady basis to obtain relative changes in the same wind tunnel. A larger number of blades obviously increases the dynamic forces during operation and was, therefore, avoided. A cascade with more airfoils can be considered for future designs. The cascade angle and turning angle of the airfoils were both chosen at minimum values to ease design of the flow path. The airfoil shape was chosen to be a double circular arc so that it could be manufactured in-house with consequent closer engineering control on surface finish, static hole location and finish, and overall dimensional accuracy, and to minimize manufacturing lead times. Also, one of the objectives of this first series of tests was to demonstrate the capabilities of this wind tunnel and, thus, need not be directed towards a particular compressor application. A similar airfoil was tested by Commerford and Carta (1974) and will be used as a comparison.

The velocity is low for several reasons. First of all, the

objective was to study unsteady flow and this could be done most easily by keeping the flow in the incompressible range. Secondly, one of the correlation parameters for unsteady flow work is reduced frequency, $\omega b/V$. The range of this parameter can be increased by reducing the velocity. On the other hand, at 82 fps, the dynamic head is only 0.0542 psid or 1.5 inches of water. The pressure variations on the airfoil were expected to be much less than that so the velocity could not be allowed to go lower without serious measurement problems.

In addition, the velocity could not be allowed to go much lower without encountering a non-linearity in the cascade total pressure loss. This loss (Johnsen and Bullock 1965) is relatively constant for large blade-chord Reynolds numbers but increases rapidly when the Reynolds number is less than 10^5. The loss, expressed as a fraction of the freestream velocity head, for a double circular arc cascade varies from .042 at $Re = 1.18 \times 10^5$ to .032 at $Re = 2.16 \times 10^5$. These Reynolds numbers correspond to freestream flow velocities of 110 and 150 fps respectively and are the endpoints of the data presented in this report. This represents a test to test change in loss for this cascade of 1%. The change in loss was subsequently determined from the test data to be 1.6% for the test program velocity range.

The mean angle of attack of 6-14° is large enough to obtain a performance variation versus angle of attack. When the cyclic variation of 5.75° is added, the total operating range for the airfoil was 0.25°-19.75°. This corresponds to an incidence range of -5.25° to +13.75°.

The oscillatory change in angle of attack, $\pm 5.75°$, was chosen to simulate the variation in flow angle that would be seen in a compressor blade row as the result of a pressure defect ($\Delta P_T/P_T = 0.15$) that could easily occur during normal flight operations. A range of this parameter can be chosen for future tests.

The oscillation frequency was chosen so that a range of reduced frequency could be attained in which other research, e.g., Carta (1967) has shown the unsteadiness to have an aerodynamic effect.

B. Flow Path

The cascade flow angles used in these tests are shown in Figure 16 and a flow schematic of the complete cascade is shown in Figure 17. A five-bladed cascade is held between two circular side plates, all of which is stationary during the test. The cascade inlet, which includes circular inlet guide vanes, a contracting flow path, and suitable support structures, is mounted on large bearings concentric with the tunnel side plates and is forced to oscillate sinusoidally about an axis transverse to the cascade axis and through the center airfoil by a motor-driven crank. The inlet guide vanes guide the flow along the instantaneous inlet axis and thus achieve a variable flow direction. Area contraction occurs downstream of the guide vanes in a plane perpendicular to the oscillation plane in order to maintain the desired flow direction. Each of the airfoils is mounted on a pair of small end plates recessed into the circular side plates so that the blades can be set at any blade-chord angle, γ, between 4 and 24°. Thus, a fixed mean angle of attack, α_M, can be chosen for any test between

26 and 6°. The variation in angle of attack, ±5.75°, is fixed by the crank mechanism but can be changed for future tests. Figure 18 shows the cascade side plates with two of the airfoil end plates and mating clamps in position. The traversing mechanism shown at the left will be used during future test sequences to measure the velocity profile both upstream and downstream of the cascade.

The oscillatory inlet is shown in Figure 19. This picture was taken while determining the center of gravity of the inlet. The two circular openings form housings for the inlet support bearings and also allow insertion and removal of the cascade. The cascade and the inlet are supported on two trunions. These are eight inch diameter cylinders which serve two functions. The cascade side plates are clamped across the inboard ends of the cylinders to form the flow channel and the outside diameter is used as a bearing seat for the inlet support bearings. Figure 20 shows the partially assembled wind tunnel in an assembly jig. The airfoils and one cascade side plate are mounted on a trunion which is inserted into the inlet opening. The other trunion is ready for insertion in the near side. Figure 21 is a close-up of the cascade with the pressure ports visible on the center airfoil. Figure 22 is a rear view of the assembled wind tunnel on the assembly jig and Figure 23 gives a quarter view. The convergent part of the inlet can be seen in the top view in Figure 24.

This wind tunnel has an atmospheric inlet and will exhaust into a large settling chamber or plenum. This chamber is a 41 inch I.D. pipe, nine feet long, and one end is shown in Figure 25 with the

wind tunnel support stanchion positioned in front of it. The trunions are clamped onto the stanchion in the two saddles. The assembled wind tunnel is shown in Figure 26.

C. Oscillating Inlet

The inlet is a welded and bolted aluminum structure designed to guide the flow along an instantaneous flow path and to be strong enough to withstand stresses caused by high accelerations. The 26 guide vanes are 150° circular arc segments and are 0.091 inches thick, 2 inches wide, and spaced 0.380 inches apart. The trailing edges are sharp and the vanes have an outer radius of 5.15 inches. This makes the area contraction ratio (guide vanes to the test section) equal to 4.50 and 2.75 when based on the guide vane inlet and exit areas respectively. The guide vanes along with the plates which form the convergent section are welded together. The inlet also contains two plates in line with the cascade and at either end which are adjustable. The inlet is carefully aligned with the cascade side plates during assembly to make a smooth and continuous flow path.

D. Inlet Crank Mechanism

The gear case below the inlet shown in Figure 27 houses an eccentric drive cam connected to the inlet by a 20 inch floating crank rod. The oscillating inlet represented a large unbalanced force so two sets of counter-rotating steel discs were housed in the gearbox. They were driven by the timing belt shown in Figure 26 and flats were machined on them to balance the inlet. In addition, they served as flywheels to maintain the rotating speed constant within $\pm$1/2%. The

electric motor is an additional flywheel and helped maintain close speed tolerance.

The cranking mechanism was designed with an L/r value of 25.73. This gives a variation from sinusoidal motion of less than 3/4%. Thus, the inlet angular oscillation is quite close to being sinusoidal. Power was obtained from a 7 1/2 horsepower Reliance variable speed DC motor shown at the left in Figure 25. It drives the main crank through another timing belt.

During early testing, the pressure transducers showed a 34 cycle carrier wave on their output. The amplitude seemed to increase from week to week. This was traced to a combination of 40 teeth in the timing belt pulleys and 28 rollers in the main bearing and the problem was completely solved by frequent application of heavy duty machinery grease to the main bearing.

E. Stationary Cascade

The cascade has five airfoils and a close-up during assembly is shown in Figure 28. The center airfoil has ten pressure ports on each surface spaced at intervals of one-fourth inch along the chord line. They are arranged symmetrically about the point of maximum thickness which puts a port 0.240 inches from the leading edge. The ports on each surface were placed on four different span positions located 0.75 and 1.00 inches from each cascade side plate. This can be seen most clearly in Figure 21, and was done to avoid downstream interference effects from hole to hole, including fluid injection from the transmission line. Using this arrangement, the closest axial hole spacing is one inch.

Since the data of primary interest in this program was to be the airfoil static pressures, the ports were given special attention. Willmarth (1971) says that,

> "At best, very little is known about the errors in unsteady pressure measurement that are caused by the connection of the transducer to a static hole in a plane surface when there is a fluid flowing over the surface."

This description matches the requirements in the present test. The error is determined by the hole depth, size, edge shape, burrs, and dirt. The hole size of 0.063 inch was chosen high enough to give an acceptable frequency response even though the error may be as much as 0.009 Q according to Garlin and Slizinger (1964). The results of Livesey, Jackson and Southern (1962), who used a similarity approach, showed that the error due to the depth and diameter for the present test conditions is less than 0.010 Q. The burrs and edge shape were taken care of by using a method similar to that of Franklin and Wallace (1970). The static holes were drilled and reamed in the airfoil billet prior to machining the surfaces and were plugged with hard brass rod using a push fit. The airfoil surfaces were then machined and the plugs were removed by hydraulic back-pressure. Subsequent inspection showed the edge radius to be less than 10% of the hole diameter.

The airfoil surfaces were machined by clamping the billets between two face plates and using a grinding attachment on a lathe. These operations are shown in Figures 29 and 30. The leading edge radius was 0.025 inch and the trailing edge was sharp.

The cascade axis was set vertical during assembly by using pins in two leveling holes in the cascade side plates and can be seen in

Figure 28 spaced three inches fore and aft of the cascade axis and slightly above the center airfoil. These pins were also used to define a reference plane to optically set the hot wire probe protractor.

The differential airfoil pressure transducers were mounted in two clusters external to the flow path on the outboard side of the cascade side plates. The clusters are shown in Figures 31 and 32 with the wiring harness and reference pressure tubes attached. The transducers are sandwiched between stainless steel plates which are fixed solidly to the center airfoil clamping ring. Thus, the whole assembly rotates when the airfoil blade-chord angle is changed between tests. In addition, this arrangement puts the transducer diaphragms in a plane parallel to the plane of crank motion. The transducers are shown in position inside the trunions in Figures 33 and 34. During some of the tests, tunnel wall static pressures were recorded and these transducers were clamped to the top of the cluster as shown in Figure 35.

F. Exhaust Plenum

The wind tunnel was mounted on a stanchion which was bolted securely to the floor and positioned in front of an exhaust plenum. This plenum was a 41 inch I.D. pipe, 9 feet long and was connected to the building exhaust system at the rear of the tank. A sonic flow control valve was also located at the rear of the tank and consisted of a 3 1/2 inch diameter hole in the plenum end wall with an aluminum cone used as the valve pintle. The cone was powered with an electric aircraft flap actuator. During the first airflow tests, the noise produced was extremely loud throughout the building and the flow

control valve with its shock wave was blamed. A muffler was designed and built according to Lyon and Shahady (1974) that would be a tortuous path for the acoustic noise but would not be a serious pressure drop. A 12 inch steel pipe, 14 inches long, was welded onto the plenum end plate around the valve hole on the outlet side and is shown in Figure 36. The annulus thus formed with the exhaust pipe was packed with polyurethane foam. Thus, most of the acoustic noise on the outlet side was reflected at least once before transmission through the exhaust pipe wall. Similarly, a 10 inch diameter by 20 inch long aluminum pipe with 3/8 inch walls was placed over the inlet side of the valve and is shown in Figure 37, mounted on the plenum end wall. This pipe protruded into a welded aluminum box placed inside the exhaust plenum and shown in Figure 38. Polyurethane foam was cemented to the outside of the pipe, inside of the box, and exhaust plenum end plate. The largest flow velocity on the inlet side was approximately 95 fps. After installation of this system, the noise on the inlet side was almost inaudible. Outside of the test cell and downstream of the exhaust plenum, the valve-generated noise could still be heard but was not a hazard.

During 1974 a considerable amount of data was taken which covered the full range of operation of the wind tunnel and one progress report was given (Ostdiek 1974). During early 1975, it was determined that the pressure in the exhaust plenum varied during tests in close to a sinusoidal fashion and was in phase with the inlet. The pressure was a maximum at maximum angle of attack and the amplitude of the

variation was between 2 and 10% of the dynamic head, depending on the cascade mean angle of attack, α_M, and on the oscillation frequency. At 1.4 hz, the amplitude was 10% at $\alpha_M = 6°$ and decreased progressively to 4% at $\alpha_M = 14°$. At all blade settings the amplitude decreased with increasing frequency so that at f = 12 hz the amplitude was only 50% of the above values. This pressure variation was observed at the front face of the plenum and at several axial stations with no large change. Since the plenum had a sonic valve at the outlet, the flow rate into the plenum had to be varying. It should be emphasized that although the amplitude of the pressure variation was 10% of the dynamic head and could, therefore, have a large effect on the airfoil pressure measurements, the absolute flow variation into the plenum was quite small. The maximum amplitude was 0.5 inches of water and since the flow through the sonic valve is proportional to the stagnation pressure, the absolute flow variation through the wind tunnel, assuming leakage is constant, is always less than $\pm$0.3%.

The flow variation was attributed to two different effects. First, the loss across any cascade is a function of the incidence angle and since this angle varies by 11 1/2° during one cycle, the flow rate will also vary. Secondly, the ends of the cascade represent a variable flow area during oscillation and will cause a flow variation which is in phase with that caused by changing incidence and is probably larger. The adjustable cascade end walls shown in Figure 17 can be set parallel to the cascade blades and the area variation is then minimized if the blade-chord angle is zero. However, most of

the testing was done with γ in the 16-24° range. The problem could be solved by constructing a plenum chamber with a much larger volume, but this was discarded due to time limitations. The problem could also be solved by keeping the flow rate constant by building another variable area flow path which was out of phase with the cascade. This was done and is shown in Figure 39 located above the wind tunnel and exhausting directly into the plenum. A fence was attached to the inlet and oscillated beneath an adjustable curved ramp which was positioned prior to each test series. This auxiliary valve proved to be satisfactory and the back pressure variation was subsequently found to be only 1-2% of the dynamic head. A comparison of the pressure profiles before and after this fix showed that the plenum pressure variation had attenuated the pressures near the suction surface trailing edge in the early tests reported (Ostdiek 1974). A better set of pressure profiles can now be presented.

CHAPTER IV. DATA ACQUISITION

A. Overall Method

It must be recognized from the outset that this test presents some peculiar data acquisition problems that are not normally encountered in wind tunnel testing. Since the pressures and velocities are fluctuating rapidly during the test, the data system must be designed to take simultaneous and continuous readings of all data channels. This requires that each measuring station have its own transducer-amplifier combination rather than the usual approach of using a single pressure transducer and sequential switching to each channel with a long settling time. Consequently, the inter-channel accuracy for these tests will not be as high as for stationary cascades. Also, there must be provision to reconstruct the analog signals with accurate time-phasing between channels so that the unsteady components of the flow can be properly analyzed and correlated.

The overall data acquisition and reduction scheme is presented in Figure 40 and is divided into four discrete operations:

1. Wind Tunnel Test
2. Analog to Digital Conversion
3. Primary Data Reduction
4. Data Correlation

Each of these operations will be described in detail in the following paragraphs. This method of data acquisition was chosen because most of the tape recording and playback system and the digital computer with interface equipment was in operation for a J-85 turbojet engine control test which required on-line acquisition of engine operating parameters but did not require accurate inter-channel time phasing. It was found that this equipment could be used concurrently for this cascade test by the addition of a shaft encoder, DBN Pulse Network, transducers, test cell amplifiers and low-pass filters. In addition, all the computer software and a number of new operational techniques were added to establish a complete data handling system for this unsteady aerodynamics test. A considerable amount of difficulty was experienced in the initial tests in using this data system, but it is now operational and can easily be used for future tests.

1. Channel Description

Twenty-eight data channels were used to record test data and consisted of a differential reference pressure, a reference temperature, twenty-four channels of dynamic differential pressures, and two channels of hot-wire anemometer data. In addition to the data channels, two channels were used to record a shaft encoder output and another channel for a time code generator. All of the data channels and the two shaft encoder channels were transmitted from the test cell via an instrumentation cable to the FM recording station approximately three hundred feet away. Consequently, some of the analog signals required line-driver amplifiers. The time code generator was located at the recording station.

a. Reference Pressure - Channel 21

The pressure difference from the wind tunnel inlet total pressure (barametric pressure) to the wind tunnel exhaust pressure in the plenum was measured with a Bell & Howell electromanometer system. This consisted of a ±5 psid Type 4-336-001 Force Balance Pressure Transducer, a Type 1-169 Servo Amplifier, and a Type 1-168 DC Amplifier. The plenum pressure was used as the reference pressure for all the differential pressure transducers used in this test.

b. Reference Temperature - Channel 22

The temperature of the air at the wind tunnel inlet was recorded by Stow Laboratories Inc. Electronic Thermometer Model 911 PL. This instrument has a platinum resistance element and an output of 10.00 millivolts per °F. A Bell & Howell Type 1-168 DC Amplifier was used as a line-driver.

c. Flow Velocity - Channels 23, 24

The air velocity was measured at a station 3.0 inches upstream of the cascade centerline and with an X-array hot-wire anemometer system. The anemometers were Thermo Systems Inc. Model 1050 and the sensor was a Thermo Systems Inc. Model 1240-T1.5 Cross Flow X Probe. This sensor is a platinum coated tungsten wire 0.050 inch long and 0.00015 inch diameter. The hot wire sensor was chosen rather than the more rugged hot film sensor because of the vortex street formed behind the film. This will be discussed in another section. A Bell & Howell 1-168 DC Amplifier was used on the output of each of the anemometers as a line-driver.

d. Differential Pressure - Channels 1-20, 25-28

Twenty-four channels of differential pressure data was recorded. This included ten static ports on each surface of the airfoil (Ch 1-20), three tunnel wall static pressures (Ch 25, 27, 28), and the plenum pressure (Ch 26). The average plenum pressure (Ch 21) was used as the reference pressure for all of these transducers. This meant that Channel 26 was a measurement of the dynamic variation of the plenum pressure. All of the differential pressures were sensed with $\pm$0.5 psid variable reluctance pressure transducers and included C. J. Enterprises Model CJVRM $\pm$.5 psid and Celesco Industries Inc. Model P109D $\pm$.5 psid. These transducers are large (1 7/16 x 1 3/16 x 13/16 inches) and therefore must be external to the airfoil. Thus, they have a low frequency response due to the volume, but were chosen because of their high output. The maximum dynamic head in these experiments was about five inches of water and it is desirable to measure accurately at 5% of this range or 0.25 inch of water. Most commercially available transducers of the strain gage type would have less than 0.5 millivolt output and, thus, would make an extremely difficult measurement problem. On the other hand, the variable reluctance transducers have an output of 2-3 millivolts.

A Natel Model No. 2088 Carrier Amplifier System was used with the pressure transducers with a Model 2088-2A Carrier Oscillator providing 2.500 vrms excitation at 6 KHz. The transducer output was connected to a Model No. 2088-1A Carrier Amplifier Demodulator which had a full scale output of $\pm$5.0 vdc. These transducer-amplifier

combinations gave excellent results for both steady and dynamic tests even at the small differential pressures required for these tests. A later inspection of some of the data shows that signal was still usable even though only 1% of the full scale range was being used.

e. Shaft Encoder

The analog data signals are time-correlated by recording two pulse trains on the same tape with the analog data. These pulses are produced by a Norden Optical Incremental Shaft Encoder, Model OADC/23/1024P/INC. It is mechanically coupled to the main drive shaft on the right side as shown in Figure 25. The pulse trains are binary square waves with a zero level less than 0.4 volts and a one level greater than three volts. The encoder used in this test produced 1024 pulses per revolution so that the smallest angular resolution was limited to 360/1024 = 0.352 degrees. The other channel of the encoder was an index pulse (one square wave per revolution) of 0.176 degrees duration. This is used to obtain the same mechanical reference position for all tests and was set to correspond to maximum angle of attack which is at top dead center of the crank mechanism.

The two encoder pulse trains, together with the time code, were initially multiplexed together on one tape track. However, tests on February 27, 1974 could not be reproduced because of noise and stray pulses on these channels. They were subsequently assigned to individual tape tracks and playback capability improved. Two Ithaco Model 255 AC Amplifiers were initially used as line-drivers for the shaft encoder pulses so that the on condition was between the desired

four and five volts. Later tests showed that this overloaded the tape recording system electronics and the line-drivers were removed. This dropped the recorded signal to two volts but it could then be amplified during playback to be compatible with the digital equipment. This further improved playback capability.

These particular channels proved to be quite troublesome and for definite reasons. They were the only data channels transmitted from the test cell to the remote FM recording station which contained digital information. That is, the information in these channels was contained in the number of pulses rather than the signal level. Consequently, electrical noise produced by a broad spectrum of equipment from low speed motors up to radio frequency equipment added pulses to these channels and could completely disrupt the flow of information.

One of the most difficult noise problems was a spike of 2 μsec duration which appeared on all transmission lines in a seemingly random manner with a maximum of four volts p-p. This spike was quite repeatable with most of its power at 3.3 mHz. It could even be detected as a 20 volt p-p pulse on the H-beams which support the building. This pulse had very little effect on the analog signals because a large number of data points per cycle tend to average out occasional spikes. However, digital equipment detects and counts it along with the "good" pulses. This was particularly ruinous for the index pulse channel which had one "good" pulse per wind tunnel inlet oscillation. The fix for this and several similar problems was tie all the shields (bleed wires) in the instrumentation cable together and connect them

to an electrical buss-bar ground. This reduced the voltage level of these spikes to less than 0.1 volt and subsequent filtering during playback kept these spikes from being counted.

f. Time Code

A Systron-Donner Model 8120 Time Code Generator was used to record real test time on the FM tape. This signal is subsequently used to search the tape for the desired test.

2. Wind Tunnel Test

The first step in the data acquisition process is to perform the test and record it on FM tape. The test required several people and several pieces of auxiliary equipment. Thus, the test had to be scheduled up to two weeks in advance and contributed to the slow progress during the initial facility shakedown.

These tests were conducted with a written test plan and objective. During 1974-1975, approximately twenty test days were scheduled for data purposes with numerous short tests for observation. The important tests among these with results and problems are discussed in Chapter V. Each of the data tests required a crew of four people: (1) a facilities technician to operate a 2000 hp exhauster; (2) a test operator in the test cell and control room with hands-on control of the test; (3) a data recorder in the control room; and (4) an operator at the remotely located FM recorder. Continuous voice communication was required among the last three people.

The data path is shown in Figure 41. The test cell amplifiers and transducers have already been described. Their output was

wired into a tape recording system approximately three hundred feet from the test cell and is shown in Figure 42. The first step there was to convert the analog signals to FM signals by means of a Vidar Corporation 205 Voltage Controlled Oscillator. These FM signals were then multiplexed with seven data channels on one tape track. The tape recorder was an Ampex FR1600 with an ES-200 electronic package for either AM or FM capability. Since there were twenty-eight analog channels, this made four tape tracks. Each of the shaft encoder pulse trains was recorded on a track and the time code was on another track making a total of seven tracks. The tape recorder was run at 120 ips for approximately fifteen seconds for each test point. Even at the slowest powered wind tunnel frequency of 1.4 hz, this allowed recording of more than twenty complete cycles.

This part of the data system required two to three months of initial shakedown and was then plagued by the extra pulses in the encoder lines for several more months. In addition, building power transients have been suspected as the cause of the occasional overnight loss of from two to six instrumentation amplifiers. This part of the system is presently being upgraded to allow easier calibration and continuity check-out of all channels.

3. Analog to Digital Conversion

After a set of tests had been performed, the data stored on FM tape was converted to digital information. Some of the equipment for this transcription is shown in Figure 42 and the data flow path is shown in Figure 41.

a. Method

Each test run was assigned a four digit number ending in zero during the test phase. This designation followed the test data throughout the data handling process. The test numbers were separated by ten to allow intermediate steps to be assigned unique test numbers. In particular, a limitation in the FM tape system allowed playback of only fourteen channels at once and, thus, two passes were required and two new test numbers were attached to the data. Several descriptors for the data including test date, time, frequency, and barometric pressure were recorded on the digital tape during this conversion to aid in identifying the data.

b. Data Path

The test run start and stop times were set into the time code reader and search units (Systron-Donner Models 8130 and 8140) to find the desired test information. The information was demultiplexed in two passes of fourteen data channels each using Vidar Model 302 Discriminators. These discriminators had 4300 hz low-pass filtering which was much too high for these tests, so the signals were then low-pass filtered at 63 hz. This frequency will be explained in a later paragraph. The filters used were four-pole Butterworth low-pass active electronic filters and consisted of seven channels of Ithaco Model 411 and seven channels of FRO Model 1. The former is commercially available and the latter was built in-house and is described later in this report. The digitizing process was initiated from a keyboard shown in Figure 44 and was controlled as follows. The tape search unit would

not allow data transfer until it approached the specified test time interval from the zero time end. The DBN pulse network then issued read commands to the digital computer at the rate of 256 commands per test oscillation for a total of 10-15 oscillations when the process was terminated manually. The number of pulses from a high frequency oscillator between each read was recorded and immediately tabulated and displayed on the video unit shown in Figure 44 to insure that the proper inter-channel time phasing was maintained.

c. Data Rate

Twenty-eight channels of analog data was recorded real-time during testing. The shaft encoder was purchased before the specific data demands were established and consequently was specified so that it could accommodate the maximum desirable digitizing rate for this kind of test. This was judged to be 1024 points per cycle. A power of two was chosen since it makes the digital programming easier and allows shorter machine times for data reduction. The oscillating inlet was designed for a maximum frequency of 30 hz. This then makes a gross data rate of 860,160 points/second. The digital computer used for this data transmission is an IBM 1800 Processor Controller which is the same as the IBM 1130 except it has an increased capability for process I/O (i.e., analog in/digital out). In addition, it has a video display for on-line viewing of selected data. It is known that the data rate of 11 bit resolution must be well under 21 KHz. This is partially determined by the software problem of filling an array, checking to see if the tape drive has finished with the last write,

and starting the new array write to the tape. Obviously, the digitizing rate would have to be slowed down considerably. The single largest improvement was obtained by recording at an FM tape speed of 120 ips and doing the playback at the slow speed of 7 1/2 ips which is a speed ratio of 16. In addition, only 14 analog channels could be digitized at one time because of the tape recording system limitations. Also, the first series of tests were planned for low oscillation frequencies with an upper limit of 16 hz. All of these considerations reduced the data rate to 14,336 conversions/second which was still marginal (later testing showed the maximum reliable rate to be about 5,000 conversions/second). The IBM 1800 has a background working area of approximately 25,600 storage locations. Each data value takes two storage locations and, since there are 28 analog channels, the maximum permissible number of points per wind tunnel oscillation is 256. This was accomplished by using a DBN pulse network which counted the shaft encoder pulses and issued a read command to the digitizer every fourth pulse after the first index pulse. This network was designed and built in-house by a co-worker (Herren 1974) and a breadboard of the resulting network is shown in Figure 45.

d. Data Quality

The discriminators were equipped with low-pass filters but the lowest value available was 4300 hz. This corresponds to a real-time cutoff of 68.8 Khz which is much too high. Seven channels of Ithaco Model 411 active filters were available, but there was insufficient time to procure an additional seven channels. Therefore, seven

channels of FRO Model 1 active four-pole Butterworth filters were built in-house according to the design procedure of Al-Nasser (1971). A schematic and table of design value is presented in Figure 46 and the filters are shown in Figure 47 as built on a phenolic board. An Applied Dynamics Model AD-5 analog computer with 120 amplifiers and integrators was available in the control room as part of a different test. These amplifiers were wired into the breadboard circuit to provide the active components. A -3 db cut-off of 63 hz was chosen as the design point. This translates to a real-time cut-off of 1008 hz. This value is a compromise and is below the maximum frequency (1250 hz) of the Natel amplifiers but is higher than the twentieth harmonic (600 hz) of the wind tunnel design frequency. The change in gain was not measurable at an equivalent 320 hz which is the maximum frequency used in the data reduction for this dissertation. The phase lag for all channels fell in a narrow band of values.

e. Transmission Problems

This step in the data acquisition process proved to be the most troublesome because of difficulty in pin-pointing the problems. The read rate of the digital computer was slowed to less than half speed during early transmission tests. This caused the computer to miss the read commands from the DBN pulse network. After a number of tests, it was found that the out-of-range signal was coming from an unused channel from a different test.

The noise problems in the shaft encoder channels have been mentioned previously and were solved in this phase of the work.

In addition, the equipment in this control room was very sensitive to temperature and it was determined by trial and error that it would operate reliably only if the control room temperature was kept below 77°F. The solution to these problems was time consuming because it required transmitting and re-transmitting large batches of data. This was partially relieved by doing a statistical analysis of the timing of each run immediately after its transmission, and displaying the results on the video monitor shown in Figure 44. If the results were unsatisfactory, the tape could be backspaced and the test data transmitted again. This part of the data acquisition process is now operating satisfactorily.

4. Data Reduction

The data stored on digital tape during the digitizing process was reduced to values of the physical test parameters by digital computation. This involved not only a large computer programming effort but also careful calibration of all of the transducers to obtain consistent and accurate results.

a. N-Cycle Average

The digital computer working area restricted each data channel to 256 points per wind tunnel oscillation. From a purely mathematical viewpoint, this is enough to obtain a finite Fourier series of 128 terms, but this must be tempered by a few aerodynamic considerations. The objective of this complete test series is to obtain pressure histories of selected points on both surfaces of an airfoil while it is undergoing a continuous variation in angle of attack. In this

flow field, any point on the airfoil will have a periodic pressure variation plus secondary flow variations caused by free stream turbulence, static hole oscillation, system vibrations, and other non-linear and aperiodic viscous interactions. These secondary flow variations will have a much smaller amplitude than the periodic variations and may even be in the electrical noise range of the transducer amplifier combination. Although they are of interest, they do not fit into the objectives of the present research and are left for later investigations. At the present, the research is directed towards determining the "average" pressure, p(t), on the airfoil without considering cycle-to-cycle variations which may occur. To accomplish this, the digital data from eight successive inlet oscillations was averaged together at each of the 256 time slices per cycle. This was done for all of the processed data including the calibration runs. Thus, an average cycle of 2048 data points per channel was created and subsequently analyzed. The effect of this averaging technique can be seen by comparing Figures 48 and 49. Each of these shows the pressure variation for all of the airfoil static ports. The normalized time span corresponds to one complete wind tunnel oscillation and the average pressures for the complete oscillation are listed in the center of the plot. Both figures are made from the same test run except Figure 48 is made from only one cycle which is 256 data points per cycle, while Figure 49 is made from eight cycles including the one used for Figure 48. This averaging technique has obviously smoothed the pressure traces but not at the expense of destroying it. The average pressures have changed by a

maximum of 0.002 psi and the shape of the curve is still the same. The eight-cycle average is a more realistic presentation of the data. This operation should also help the reader understand the need for obtaining an accurate pulse count in the analog to digital conversion described in the preceeding section. Missing read pulses in the first of the eight cycles would result in a data skew in all succeeding cycles and an inaccurate average cycle.

b. Calibration Data

The pressures, velocities, and temperature recorded in these tests are first obtained as millivolt or microvolt signals from a transducer. This signal is then processed by several different electronic packages including as many as five amplifiers, several filters, and three tape heads before it is available to the digital computer data reduction program. It would be quite impractical to calibrate all of these devices for each set of runs to obtain a set of scale factors. Therefore, all the equipment was calibrated end-to-end at a low signal level and a high signal level for each small set of runs (usually eight to ten). Pressure differentials and electrical signals were artificially applied and the amplifier outputs were recorded on FM tape like a dynamic run and also recorded on a data sheet. The data sheet values were later punched on cards to be read by the digital computer. Thus, the high and low endpoints of the multi-step data acquisition path were assigned physical values and all other digital data could then be reduced. The shape of each calibration curve was established by bench test prior to the wind

tunnel test and the end-to-end calibration was used only to establish the curve endpoints.

The electronic thermometer and the reference differential pressure transducer had linear calibration curves but it was found that the ±0.5 psid variable reluctance transducers exhibit a typical S-curve output when passing through zero pressure input. The deviation of the output from a best straight line was less than 1% of full scale. However, some of the tests were run with a dynamic head of only 0.057 psid which is a small part of the transducer range so that the deviation was as much as 3% of test full scale. This necessitated using two straight line segments for the calibration curves for most of the airfoil and tunnel wall static transducers. A slight further improvement can be obtained with a third or fourth order curve fit. A Meriam Model 34FB2, 0-10 inches of water with 0.001 inch increments, Micromanometer was used as a pressure standard in the test cell for both the reference pressure transducer and the airfoil transducers. Frequent checks of the reference pressure were performed during testing. A mercury barometer was used for barometric pressure.

The connection of the static pressure ports on the airfoil and wind tunnel side walls has been discussed in Chapter III and consisted of two transmission lines. The first included the passageway in the airfoil and a short connecting tube and was 0.063 inches in diameter and 1.85 inches long. The second included connecting tubes and an equivalent length for the transducer internal volume

and was 0.069 inch in diameter and 1.82 inches long. The response of this type of transmission line was analyzed by Gerlack, Johnson, and Astleford (1970) using an inviscid linearized approach. Their experimental results showed remarkable agreement with their theory over a wide range of frequencies. Their analysis was programmed and used to calculate both the pressure amplitude ratio and phase angle from the test port to the transducer diaphragm. The value of the amplitude ratio varied from 1.0 at 0 hz to 1.256 at 320 hz and was stored in the digital computer in tabular form. The phase angle reached a maximum of -3.4 degrees at 320 hz and was neglected for these tests since it would represent a change of only 0.17 degrees on the fundamental of the tunnel oscillation.

Calibration of the equipment for velocity measurement was much more difficult and time consuming than the pressure transducer calibrations. The calibrator consisted of a settling chamber of 2.825 inches O.D. with screens, converging nozzle with a throat diameter of 0.6505 inch, and suitable controls and probe insertion parts. The calibrator was connected to the building air supply and exhausted to the atmosphere. Thus, using isentropic relationships, the throat velocity could be calculated as:

$$V = \left[\frac{2k}{k-1} R\, g\, T_o\right]^{1/2} \left[1 - \left(\frac{P_o}{P+\Delta P/S}\right)^{\frac{k-1}{1}}\right]^{1/2}$$

Each of the wires of the x-array sensor is calibrated over the complete velocity range at each of the endpoints of the angular range. The flow

direction of the calibration scheme was determined optically by inserting a lapped cylinder into the calibrator exit throat. The cylinder had an adjustable mirror mounted on one end perpendicular to the axis of the cylinder. A light beam from an auto-collimator, located ten feet in front of the calibrator, was then used to (a) align the mirror by rotating the cylinder and (b) locate the tunnel axis by moving the auto-collimator. A hot wire probe support is shown in Figure 50. A circular dial and a pointer with two location pins are clamped to the shaft. Since the auto-collimator is located on the calibrator flow axis, it is then used to optically align the plane of the two location pins with the flow axis and record the dial reading. The reading, when wire No. 1 is perpendicular to the flow, is defined as θ_1. Thus, aided by the optical equipment, the hot wire probe can be removed from the calibrator and installed in the wind tunnel with known angular reference to the test hardware and the absolute flow angle in the cascade can then be recorded during test. Similarly, the probe can be re-inserted in the calibrator and calibration checks can be performed at the same angular settings as before.

Hot wire calibrations were performed frequently over the past three years of this project and were beset by several problems. The calibrator was initially hooked to the shop air supply available in the test cell. The hot wire data from the first series of wind tunnel tests performed in June 1974 were not usable because the hot wire sensors were coated with small dirt particles after the tests. Figures 51 and 52 show a 40X magnification of the sensors

before testing and after several hours of air flow. Subsequent investigations reveal that the sensors and supports were coated with oil and consequently picked up foreign particles passing through the tunnel and thus making the data unusable. The sensor became coated with oil during calibration from oil entrained in the shop air supply. In fact, a pool of oil was found in the calibrator settling chamber during disassembly. The oil film on the sensors apparently reached a stable thickness during calibration with the clean but oily air since the calibration curves were repeatable. The complete calibration system was subsequently moved to another building which had a clean air supply from a Gardner Denver Company Model RL126DL oil free air compressor. This removed one source of oil and dirt contamination, but it was found that the sensor still required frequent cleaning during wind tunnel testing.

At the initiation of this project, two types of velocity sensors were available; a hot film sensor and a hot wire sensor. The hot film sensor is a platinum film on a quartz rod of 0.002 inch in diameter. This sensor is very rugged but has a high enough sensitivity to easily measure the flows expected in this wind tunnel. On the other hand, a hot wire is not only very sensitive to flow changes, but is also susceptible to damage through handling and foreign object impingement and to contamination by fluid-borne particles. The first attempts at velocity measurement were made using the more rugged hot film. However, a great deal of difficulty was experienced in obtaining smooth or repeatable curves when plotting anemometer output versus

mass velocity. Further investigation showed that if the mass flow was held constant and the probe was rotated slowly in the calibrator, the output was very irregular. These anemometer output curves versus index angle are shown in Figures 53 and 54 for Wire No. 1 and No. 2 respectively. For Wire No. 1, which is the outermost wire in the x-probe, two distinct jumps in the curve occurred at approximately 38 and 135°. The indentation at 88° occurred only for increasing β. For decreasing β this part of the curve was smooth and continuous. The results for Wire No. 2 show similar jumps at 48 and 130°, but the peak of the curve is flattened off because of the Wire No. 1 support interference. These curves represent neither best nor worst cases, but are typical of many plots that were made. They can be compared to the curve of Figure 55 which is a typical trace for a hot wire and was made using the same equipment. In an attempt to determine whether all of the flow irregularities could be attributed to probe support interferences, a probe with two hot films (0.001 and 0.002 inch in diameter) mounted parallel to each other and 0.040 inch apart was tested with the same results as the x-array films. If the probe support interferred, its effect was small compared to the observed variations. Collis and Williams (1959) observe that the exponent, n, in the empirical relationship

$$N_u = A + B\ Re^n$$

changes at Reynolds numbers greater than 44 or thereabouts. They believe this occurs when vortices are shed from the rear of the cylindrical wire. A further experiment was then performed to see if the hot film behavior could thus be explained. The 0.001 inch diameter film

was exposed to a free stream and slowly rotated through 120° at several different velocities. The results are shown in Figure 56. The probe was rotated in alternate directions for each successive velocity and the arrows indicate increasing or decreasing β. The curve for Reynolds number of 19 is quite smooth but the other curves become more erratic for increasing Reynolds number. The erratic behavior occurred first when the flow was not perpendicular to the wire. This could seem reasonable since the effective path over the wire will increase when the film is yawed, thus increasing the effective Reynolds number. However, the angle of the onset of erratic flow did not change linearly with cos β as the velocity was increased. This agrees with the results of Hanson (1966) who found that the critical Reynolds number based on the normal velocity component was nearly constant at low angles but decreased with increasing yaw angle when the angle was in the 40 to 70° range. In addition, in the Reynolds number range of 37 to 74, the erratic behavior occurred only when the angle β was receding from 90°. It should be emphasized that even though the wire was rotated slowly, this effect was found repeatedly. This hysteresis effect was left for later investigation. The overall results agree with the vortex argument of Collis and Williams. Therefore, the problem could be and was solved by using hot wires with a diameter of 0.00015 inch. This kept the wire Reynolds number below ten for the wind tunnel tests which is below the vortex shedding range.

The output of a hot wire anemometer is usually fitted with a King's Law empirical curve.

$$Nu = A + B\, R_e^{0.5}$$

The hot wire calibration data were reduced following the methods of Bearman (1971), Bradshaw (1971), Champagne, Sleicher, and Wehrmann (1967), and Champagne and Sleicher (1967) using the following relationship:

$$\frac{E_f^2}{T_\omega - T_f} = A + B\, U^{0.5}$$

Where E_f is data taken at temperature T_f, and T_ω is the wire temperature. An equivalent output, E_o, at a suitable reference temperature, T_o, was then obtained

$$E_o^2 = E_f^2 \cdot \frac{T_\omega - T_o}{T_\omega - T_f}$$

The wire temperature, T_ω, is defined as suggested by the manufacturer, Thermo Systems Inc. (1973),

$$\frac{R_\omega}{R_f} = 1 + A_\omega\,(T_\omega - T_f)$$

R_ω/R_f is then the overheat ratio. A value of 1.5 was used for these experiments. The value of A_ω was determined by taking hot wire data over a temperature range from 63.2 to 81.3°F at a constant mass flow rate of 9.25 lb/ft^2-sec. The test values are presented in Figure 57 and A_ω is the slope of the best straight line curve fit of the data. Sensor 1240-9028 had a coefficient of 0.00182/°F giving a wire operating temperature of 807°R. Since the x-array hot wire probe was used to measure flow direction as well as velocity, the angle dependence was determined by calibration. Figure 58 defines the angles between

the wires and flow. It was assumed throughout this work that the angle between the wires was 90°.

$$\beta_2 + \beta_1 = 90$$

This was done in order to keep the equations from getting messy. This assumption does not change the results since the data are fitted with a curve over the usable range.

The hot wire sensors available for this program were found to have irregularities in the output curves for flow angles in the 40-50° range which were similar to those observed for hot films but not as severe. Since this is the usual range chosen for x-arrays, it was necessary to choose a calibration range of β_1 between 60 and 80 where the calibration curve was smooth for both wires. These data are presented in Figure 59. Hinze (1959) recommends an angular correlation of the form

$$U_e^2 = U_o^2 (\sin^2 \beta + K^2 \cos^2 \beta)$$

where U_e and U_o are the effective and free stream velocities and K is an experimentally determined parameter. The heat dissipated in the wire (Nusselt No.) is proportional to E^2 and from King's Law we obtain

$$E^2 \alpha V^n$$

and since Collis and Williams find n = 0.5 in this Reynolds number range, we have

$$E^8 \alpha V^2$$

Therefore, the data for Wire No. 1 were fitted with a curve of the form

$$E^8 = E_o^8 (\sin^2 \beta_1 + K_1^2 \cos^2 \beta_1)$$

in the angle range of 60 to 80°. Other exponents were tried but the eighth power gave the best fit. The percentage change from this curve and the data points is defined as

$$D = \frac{E_t - E_c}{E_{80}-E_{60}} \times 100$$

and was found to be 3.3%. This represents a change in velocity of only 0.003% at 100 fps since a wire is not very sensitive to angle change at high incidence angles. This relationship was used throughout these tests for the outermost wire of the x-array and proved to be quite adequate. The cosine multiplier, K, was found to be constant over the calibration velocity range of 50 to 200 fps and its value is 0.73 which differs markedly from values in the literature. However, it should be remembered that this value was obtained to correlate a raw unscaled anemometer output rather than the velocity and, therefore, should be different.

Friehe and Schwartz (1968) discuss deviations from the cosine law and find that a good fit for data in a yaw range up to 60° could be obtained using a linear equation in $\cos^{1/2}$ where α is the yaw angle. However, the second wire of the x-array in the present tests was operated in a β-range of 10-30° which is a yaw angle of 80-60 and thus outside the range of the Friehe and Schwartz data. As the wire passes through $\beta = 0$ the wire is parallel to the flow and, intuitively, the output curve should pass through an inverted spike. Thus, the data could not be satisfactorily fitted with either a square or a square root function since it must pass through zero. The data

were fitted for $10° < \beta_2 < 30°$ with

$$E_2 = B \sin \beta_2 + C$$

where B and C are functions of mass velocity. Equations of this form matched the data quite well for a range of mass velocities of 4-14 lb/ft^2-sec and was used throughout the tests for the inner wire of the x-array. However, each of the hot wires was calibrated over the complete velocity range at both endpoints of the β-range. This produced anemometer output versus mass velocity curves as in Figures 60 and 61, and each curve was fitted with a fourth order equation over the mass velocity range from 3.5 to 14. The reader should note that both correlations for effect of change in β are for constant mass velocity (i.e., a vertical line on Figures 60 or 61) whereas in the data reduction algorithm the anemometer outputs, which represent horizontal lines, are known and thus there is no straightforward interpolation scheme. The flow speed and direction are determined by a trial and error process. Computational time is minimized by specifying the mass flow as a function of anemometer output for Wire No. 1

$$\rho V = F = F(E)$$

and the reverse for Wire No. 2

$$E = E(F)$$

In summary, the hot wire bench calibration data were (a) corrected to the reference temperature, (b) curve fitted for yaw angle variation, and (c) curve fitted for velocity variation while the test data was (a) scaled from computer voltage to test cell

voltage, (b) phase and amplitude corrected, (c) corrected to the reference temperature, and (d) iterated on to obtain speed and direction.

c. Fourier Analysis

The test data was scaled using the various calibration curves and techniques discussed in the preceding paragraphs and then a Fourier analysis was performed on each data channel to not only obtain such useful information as average values and phase angles, but also to perform the last phases of data reconstruction and smoothing. The analysis was performed by using the Fast-Fourier Transform techniques which have been in wide use in acoustic research in the past decade. See, for example, the papers by Cooley and Tukey (1965), Helms (1967) and Brigham and Morrow (1967). The transform used for the test data was written by Brenner (1969) and is based on the work by Cooley and Tukey. This transform operates on a data array of NN + 1 points to give all of the Fourier coefficients up to NN/2. In the present case, NN is 256. There are frequency-dependent amplitude gains and phase angle changes introduced into the data from the airfoil static pressure port transmission lines and from the low-pass filters used during the A/D conversion. The corrections for these effects were made to the proper Fourier coefficients after the first Fourier transform after the method of Helms. Also, the shaft encoder index pulse was set according to the mechanical position of the crank mechanism. This precedes the corresponding aerodynamic angle of attack at the cascade by a delta time, VLAG, equal to the inlet transport time

$$VLAG = 343 \times f_t/V_t$$

This correction makes all the cascade data a function of a calculated aerodynamic angle of attack. After all corrections had been made to the data, the Fourier coefficients were stored and the inverse transform was performed to obtain a set of corrected data. The data could be quite effectively smoothed during this operation. That is, only the Fourier coefficients which contained aerodynamic rather than noise information were retained. The rest were set to zero. Figure 49 was previously discussed and represents a data reconstruction using the first twenty terms of both the sine and cosine terms. This can be compared to Figures 62, 63 and 64 which represent the same test run but were reconstructed using the first five, ten, and fifteen terms respectively. A consideration of an asymmetric repetitive sawtooth shows that it can be quite adequately fitted using the first ten terms of the series. Indeed, a good representation of a single square wave can be made using only twenty terms, but these cases represent requirements which are more severe than a temporal pressure variation if the turbulent components are not required. However, it was decided to include twenty terms so that any sharp pressure variations due to separation could be indicated even though an investigation of airfoil separation is left for later research. The data reconstructed in this manner were used for the plots which appear in this report. The instantaneous lift and moment of the airfoil were calculated and also Fourier analyzed to obtain the Fourier coefficients but, of course, the inverse transform was not needed and the calculated data remained unchanged.

d. Data Presentation

A computer program which reduced the data from the digitized values to the calculated data bank of pressures, temperature, velocity, lift, and moment was constructed for this experimental program. This deck of approximately 3500 cards represented many months of programming effort. It included provision for making machine plots in eight different formats and the printed output of all the data points and/or Fourier analysis results as desired. In addition, the calculated data array of 28 channels by 256 points was stored on disk for future use. The IBM 1800 computer was used for all debugging and shakedown of the complete data acquisition chain because it could be dedicated completely to this project as required. In addition, it could be operated outside of normal laboratory duty hours. However, the machine time for the reduction of one test was 20 to 30 minutes on this machine so the majority of the production runs were performed on an IBM 370 which reduced the required time by a factor of about 50.

5. Data Correlation

The reduced data array for all twenty-eight channels of test data was stored on disk in the IBM 1800. Thus, machine plots could be remade or the data could be plotted with a new format. In addition, particular values from all of the tests could be cross-plotted. This feature proved to be quite valuable. Most of the difficulty in this step was introduced by using two different computer systems which write in completely different formats. Most of the programming for this part of the data handling was done by a co-worker and is described in detail by High (1974).

B. System Performance

The data acquisition system was assembled over a three year time period and represents a considerable investment in time and equipment. Therefore, periodic checks were made to give some estimation of the accuracy of the system in transmitting data.

The initial runs were considered successful if a recognizable signal could be obtained after data reduction. However, rapid improvement was made to an accuracy plateau of $\pm$2%. Further improvement was then obtained by maintaining reasonably constant temperatures during testing in both the control room and FM recording station. While these temperature variations did not affect the level of the analog channels as much as the encoder channels, their effect on system accuracy was quite pronounced.

Later, during one set of checkout runs, the airfoil pressure transducers were not required. Therefore, these twenty channels were ganged together to a 4.6 volt wave generator phase-locked to the wind tunnel crank. The output of this generator contained all frequencies up to the tenth harmonic. A total of sixty-two test runs were recorded and extended over one hour and forty-five minutes test period with calibration runs at the beginning and end. This test period was allowed to be over twice as long as any other test period to check on the drift of the complete data system. The deviation of each channel during the entire test period was less than 1% of the amplitude, whereas the channel-to-channel deviation during each run was less than 2%. The final calibration runs were calculated using the machine values

from initial calibration runs and were found to agree with the input within $\pm$0.4%. The single channel drift of less than 1% was certainly acceptable while the inter-channel deviation of 2% is an indication of the complete system linearity. This percentage was determined by comparing the calculated fundamental amplitude for each channel. This fundamental is thus composed of data at all voltage levels between $\pm$4.6 volts and is affected by frequencies up to the tenth harmonic.

A further improvement has been made by changing the A/D conversion from eight to eleven bit resolution and the inter-channel deviation is now less than 1 1/2% of the maximum test range used in these tests. Still greater accuracy can be attained by replacing the two channels (14 and 19) which consistently established the deviation range and by carefully scaling all of the channels to use the full voltage range of the A/D converter.

This method of data acquisition has a slow turn-around time because of the amount of work required after the wind tunnel tests had been run. A group of eight to ten wind tunnel tests, which took about thirty minutes to perform, required from two to twenty hours for A/D conversion, cycle averaging, and preparation of the input cards before the data could be reduced. Consequently, the minimum turn-around time for the results of one day of testing was one week.

This complete data acquisition system has been debugged and the complete system has been used for three major blocks of test data. An overall accuracy of 1-2% has been demonstrated and further improvements can be made if necessary. Therefore, the system is immediately available for future tests.

CHAPTER V. EXPERIMENTAL DATA

The construction and operation of a wind tunnel requires attention to a multitude of small details if consistent and accurate aerodyamic data are to be obtained. Shakedown periods of several months to years are not uncommon and this wind tunnel was no exception. Some of the difficulties encountered during the first fifteen months of tunnel operation have been discussed along with the fixes used. There remains a great deal of work to be done to completely define the operating points of this tunnel, but some aerodynamic data can now be presented. All of the pressure data used in this report was taken on February 21, 1975 when a total of 120 test runs was conducted. The velocity data were taken on November 26-27, 1974. The range of test variables presented in this dissertation are as follows:

1. Mean angle of attack 6 - 12°
2. Cascade pressure drop 1.5 - 5 in H_2O
3. Oscillating frequency 0.2 - 16 hz

These data were reduced during the weeks following the tests with the major portion being done on March 12, 1975. Since the field of unsteady flow in cascades is rather new and this is a unique test, there is no standard data presentation format. Therefore, detailed data from selected runs will be presented in several different plots and enough runs will be selected to indicate the trends in the data changes.

In particular, the runs at the end points of the test variables will be presented. In addition, several cross-correlations of selected values will be made which will include the results of all the data runs.

A. Inlet Flow

This wind tunnel is unique because of its ability to generate a variable direction flow. The difficulties in using hot wire equipment in the relatively dirty basement atmosphere where the test cell is located have been discussed previously. During the February 21 test runs, the wires were again contaminated from an excessive amount of humidity in the basement and dirt outside the test area. Therefore, velocity data from runs made on November 26-27, 1974 will be shown. It should be noted that these runs were made before the fix for a variable plenum pressure was made so that the fluctuation in magnitude may not be accurate, but it seems a variable cascade back pressure would have little if any effect on the measured flow angle upstream of the cascade. The velocity and direction history for one period of the tunnel oscillation at a low frequency are shown in Figures 65, 66, 67, and 68 for mean angles of attack of 6, 8, 10, and 12° respectively, and at a constant total to static cascade pressure drop of 0.182 psid. This would correspond to a velocity of 150 fps if the cascade was not there. The start of the plot (THETA = 0) corresponds to the inlet being at maximum angle of attack. The data were taken 1.7 inches in front of the leading edge at which point the flow had undergone considerable adjustment in direction. The fluctuation in flow magnitude was less

than ±2 1/2% which corresponds to ±5% change in Q. The average velocity increased with increased turning angle as expected. The flow direction can be seen to vary quite regularly. The variation of approximately ±7 1/2° is greater than the design of ±5 3/4° and the average angle of attack is smaller than if no cascade were present, but this can be the result of interactions with the cascade and remains to be investigated further. However, it does show that the wind tunnel generates a smooth and controllable variation in flow direction with only a small variation in the magnitude of the velocity. The incidence angle is much more regular than that shown by Peacock (1974) but that test utilizes distortion screens which produce static pressure variations of 50% of Q and total pressure variation of 100% of Q. The incidence variation of Commerford and Carta (1974) is also irregular.

The turbulence level in the wind tunnel was obtained at both 1.4 and 10 hz oscillation frequencies. The hot wire probe was traversed from mid-tunnel to one-fourth inch from the wall. A boundary layer probe was not available so that the wall flow could not be investigated. A 1.3 to 2.5% rms turbulence level, $\sqrt{u^2}/V_N$, was found at the high oscillation frequency with a linear increase from the 1.3% value at the center of the tunnel to 2.5% close to the wall. These values were reduced by approximately 10 to 30% by reducing the oscillation frequency to 1.4 hz. Using this data, it was concluded that the test section flow was probably turbulent for all of the data runs.

The circular side plates of the wind tunnel had wall static ports along the leading edge line and trailing edge line of the cascade.

These were situated in the flow passages between the blades and can be seen in Figure 21. During cascade tests, dynamic pressure data were taken on each of the two ports along the leading edge which are one and one half passageways from the center airfoil. They were identified in the data as an upper wall static (top of the picture) and a lower wall static. In Figure 21, the flow approaches the cascade from the left at 30° above the horizontal. In addition, one of the leveling holes used for cascade alignment was fitted with a static port by drilling the plug for the hole and was identified as the upstream wall static. This port was located about three-fourths of a chord length upstream of the center airfoil and close to the airfoil axis. This position can also be identified in Figure 21; however, the photo was taken before drilling the static hole in the alignment hole plug.

The results during tunnel operation at 10° mean angle of attack are shown in Figures 69, 70, and 71 for frequencies of 0.2, 6.14, and 16.21 hz respectively which covers the range from steady state to maximum oscillation rate. The plots show one oscillation period and a suitable pressure range. The pressure variation is largest for the upstream position and is $\pm$7% of Q at steady state and $\pm$9% at maximum frequency. It is out of phase with the velocity head variations shown earlier and is also larger (7% versus 5%). The wall pressure variations at the cascade leading edge, on the other hand, are in the $\pm$4-6% range. Thus, much of the variation in tunnel side wall pressure may be due to a change in velocity magnitude with the total head relatively constant. The plenum pressure variation is also shown in

these figures and is small as previously discussed. Similar data for a 6° angle of attack is shown in Figure 72 and shows a phase change for the upper wall static pressure. This illustrates the cascade end wall problem which caused some of the variable back pressure. This effect occurred primarily at low angles of attack and did not have a large effect on the other two pressure traces which still have the same shape and amount of fluctuation. This problem can be solved by a variable end wall bleed similar to the fix used for the variable back pressure problem but, due to the scope of the required effort, is left for a later program. The unsteady flow in this inlet is an exceedingly complex flow problem and more experimental and analytical work is planned.

B. Airfoil Pressure Profiles

The range of test variables was specified at the beginning of this chapter and in general was done by maintaining a constant pressure drop across the cascade (measured from the atmosphere to the plenum) and taking data at 8-10 frequency settings. A new pressure drop was then chosen and the frequency settings were repeated. The tunnel flow was then terminated and a new mean angle of attack setting was made, and the above procedure was then repeated. In this manner, a series of frequency runs was made at each of four mean angles of attack. The pressure drops were chosen to correspond to nominal tunnel velocities, V_N, of 150 and 110 fps. This is defined as the velocity which would exist if no cascade were present. At one blade setting, $\alpha_M = 10°$, two additional sets of runs at pressure drops corresponding to 134 and 82

fps were accomplished. The detailed pressure profile data from the runs at each end of the frequency groups are presented in Figures 74 to 124.

The pressure port numbering system was established early in the program and was maintained throughout the data reduction and is used on the plots that follow. The key to the port location is given in Figure 73 with the ports from 1-10 on the pressure surface and those from 11-20 on the suction surface.

Figure 74 shows the time history of each pressure port on the airfoil during one complete oscillation of the inlet at $\alpha_M = 6°$, $f_t = 0.2$, and $V_N = 150$. Normalized times, T_N, of 0 and 1.0 correspond to maximum angle of attack. The average pressure, $\bar{p}_n$, for each port is listed in the center of the figure and only the variation from this average is plotted. The group of plots on the left of the figure is for the pressure surface and those on the right for the suction surface. It can be noted that the leading edge pressure is a maximum on the pressure surface for a maximum angle of attack and is the reverse on the suction surface as expected. On the pressure surface, the magnitude of the oscillation decreases along the chord starting from the leading edge and the pressure is constant at the trailing edge. On the other hand, the pressure fluctuations on the suction surface decrease from a maximum at the leading edge to zero at mid-chord and then increase from zero at mid-chord to the trailing edge. The fluctuations near the leading edge are out of phase with those near the trailing edge on this surface. Since $f_t = 0.2$ hz, this is quasi-steady

operation, but the same variations will be observed for higher frequencies and other velocity and α_M values.

Commerford and Carta (1974) in their isolated airfoil test case at higner reduced frequencies have shown a gradual reduction in pressure fluctuation along the chord to zero at the trailing edge, and a decrease in phase angle from the leading edge to mid-chord and then an increase but not a change in phase. The large phase shift on the suction surface in the present test, as well as the increase in fluctuation magnitude, may be due to a cascade effect. The change in phase angle will be discussed later. However, when this change in phase angle was first noted in mid-1974, a short investigation was conducted to determine if a vortice or region of backflow was being induced by the unsteady flow in the corner formed by an airfoil and the side wall. The side wall and both surfaces of the airfoil were painted with lines of pigmented oil. The oil streaks thus obtained indicated there were no unusual flow patterns in the corner. However, a more thorough investigation should be done in the future.

Fleeter (1975) also obtained a chordwise reduction in pressure fluctuation for a cascade in supersonic flow. The cascade rig is described by Novick, et al (1975) and variable incidence was obtained by mechanical oscillation of the upstream wedge to change the shock angle.

Figure 75 presents the data as instantaneous pressure profiles for the pressure surface on the left and suction surface on the right. The profiles are shown for sixteen time slices in each of two

oscillations of the inlet, with the pressure zero point displaced one division for each succeeding time slice. The inlet position is indicated for reference as a cosine curve versus time in the middle of the plot. Two symbols are used to identify the curves at each half-cycle with the proper zero point on the y-axis. The x-axis is proportional to the airfoil chord and each curve consists of the ten values of pressure on that surface connected by straight lines. This plot will be used to demonstrate the inter-relationships of various pressure fluctuations.

A third presentation of the same data is given in Figure 76. During data analysis, each pressure channel, n, was Fourier analyzed and the average value, $\overline{p}_n$, along with the first twenty terms of the Fourier series were retained.

$$p_n = \overline{p}_n + \sum_{k=1}^{20} (a_{n,k} \cos 2\pi\, k\, T_N + b_{n,k} \sin 2\pi\, k\, T_N)$$

The average for one period, $\overline{p}_n$, is normalized

$$\overline{P}_n = (\overline{p}_N - p_{ref})/Q$$

and is shown in the upper part of the plot to give an average pressure profile for the complete cycle for each airfoil surface. The normalization factor is the total-to-static pressure drop across the cascade previously defined. The fundamental of the pressure fluctuation is obtained from the finite Fourier series as

$$\Delta p_{n,1} = ((a_{n,1})^2 + (b_{n,1})^2)^{1/2}$$

and normalized

$$\Delta P_{n,1} = (\Delta p_{n,1} - p_{ref})/Q$$

and shown in the lower half of the plot. The $\overline{P}_n$ profile is similar to what would be expected in a stationary cascade. The curves can reasonably be extended to join up at the reference pressure at the trailing edge and thus satisfy a mean Kutta condition. The $\Delta P_{n,1}$ curves show a gradual decrease on the pressure surface as previously discussed but the suction surface curve "bounces off" the x-axis where it changes phase. The large fluctuation of $\Delta P_{11,1}$ near the trailing edge requires that a sharp change in pressure be made in the remaining 11% of the chord to satisfy the classical Kutta condition of zero pressure differential. A change of frequency to 16.2 hz is shown in Figures 77, 78, and 79. A comparison of Figures 77 and 74 shows that the frequency change has caused a phase shift along the chord on the pressure surface which indicates a pressure wave traveling down the surface. The average pressure curves in Figure 79 are almost identical to those in Figure 76, while the fluctuating Component $\Delta P_{n,1}$ has changed considerably with smaller fluctuations at both the leading and trailing edges.

Figures 80 through 85 give data for $\alpha_M = 6°$ and $V_N = 109$ fps. The same trends can be identified in this data as for the higher velocity.

The data for $\alpha_M = 8°$ are given in Figures 86 through 97 and for $\alpha_M = 10°$ in Figures 98 through 112. Four different nominal velocity settings were used at $\alpha_M = 10°$ and the results for the lowest one, 82 fps, are shown in Figures 110, 111, and 112. The pressure histories

and time slices are not as regular as they are for higher velocities. However, the pressure variations being measured were quite small. For example, full scale on Figure 110 is 0.44 inches of water. The data was shown to agree in general with the data at higher velocities but with a lot of scatter. Even so, the normalized curves in Figure 112 are smooth and in good agreement with the previous curves. Thus, data could be obtained at this and lower velocities if more than eight cycles were averaged to cancel out the noise.

The data for $\alpha_M = 12°$ is shown in Figures 113 through 124. In this set of data it can be noted that ΔP_{20} at the suction surface no longer has a sinusoidal shape (Figures 113, 119). This is confirmed by Figures 114 and 120 which show abrupt changes in the pressure profiles and we can conclude that the leading edge is separating for part of the cycle. The separation is not affected by changing velocity (compare Figure 115 to 121) but is affected by changing frequency (compare Figure 115 to 118 and 121 to 124). However, this same effect can be seen by comparing data for non-separated cases. The problems of unsteady cascade flow are formidable at best and the problem of separated unsteady flow will be left for a later investigation.

The fundamental pressure fluctuations, $\Delta P_{n,1}$, have changed with angle of attack. This can be seen by comparing Figures 79, 91, 103, and 118. In particular, the fluctuations at the leading and trailing edges of the suction surface have decreased with increasing α_M and increased loading. In fact, at the highest loading, Figure 118

shows that both the average and fluctuating pressure profiles will require little adjustment to meet at the trailing edge.

Satyanarayana, Henderson, and Gostelow (1974) found that, for a cascade in their fluctuating wall wind tunnel, the instantaneous static pressure difference tended to zero at the trailing edge. This was obvious in the present tests only for high loading. The high fluctuating pressure component on the suction surface with virtually no pressure fluctuation on the pressure surface has been previously noted for low angle of attack.

The average pressure profiles were compared to data obtained for another double circular arc airfoil in a steady flow wind tunnel to determine if the tunnel, cascade, and data acquisition system were giving realistic results. This tie to past experience is necessary to establish credibility of this experiment since it represents an unusual method of testing. However, the objective of this first series of tests was to determine if a variable flow direction in a low frequency range had any qualitative effect on airfoil performance. If the results confirmed the initial postulation that there would be unsteady effects and that they would be different than oscillating airfoils, then detailed tests would have to be carried out to establish the steady performance of the cascade as well as the inlet and wake flow patterns.

Experimental data were obtained (Rockenback 1973) for a steady cascade with a higher Mach number (0.317 versus 0.13), lower thickness (9% versus 10.2%), less turning (10° versus 12°), and higher space-

chord ratio (0.833 versus 0.819). The normalized pressure profiles are shown in Figure 125 for the only comparable geometric case and correspond to $\alpha_m = 5°$ for the steady cascade and $\alpha_m = 6°$ for the present work. The profiles are quite similar in shape with the higher loaded airfoil having larger negative pressure coefficients as expected. Note that in both cases the pressure profiles near the trailing edge require rapid adjustment for zero static pressure difference at the edge. This comparison indicates that the results from the unsteady wind tunnel are reasonable; however, detailed steady state evaluation will be done in future testing.

The chordwise changes in phase angle of the pressure profiles on each surface were noted earlier. A consideration of the phase angles of the pressure fundamentals, $\Delta P_{n,1}$, show that (Figure 126) there is a change in phase angle on both surfaces. On the pressure surface the phase angle decreases smoothly from the leading edge to the trailing edge while on the suction surface it increases slowly from the leading edge to midchord, and then jumps as previously noted. The results are similar for $\alpha_m = 8, 10, 12°$ and are shown in Figures 127, 128, and 129 respectively. The phase change on the pressure surface is only 150° rather than 180°. This jump occurs at smaller x/c for increased α_m at about the same chordwise position as the minimum flow area. The change in velocity has little effect on the phase angles on the pressure surface where the wave travels down the airfoil. On the suction surface the pressure wave would lag by 180° as the frequency approaches zero due to the reference frame chosen. On this surface,

near the leading edge, a pressure wave which leads the oncoming flow moves from midchord to the leading edge. The speed of these waves seem to be unaffected by change in tunnel velocity, V_N, and can be estimated from the plots. The speed of the anticipatory wave on the suction surface ranges from 45 to 70 fps for V_N = 150 fps and from 45 to 200 fps for V_N = 109. The wave speed on the pressure surface increases with loading and ranges from 20 to 60 fps. A phase angle plot for variable frequency and constant flow velocity is shown in Figure 130 and shows that the suction surface wave speed is a function of f_t since it keeps the same shape and is probably induced by the oncoming flow. The wave speed on the pressure surface is about the same for all the frequencies chosen. It is dependent on α_m and may be an acoustic or vorticity phenomena since it travels at 2-6% of sonic velocity. Further study on both of these waves should be done.

C. Airfoil Pressure Correlations

The normalized average pressures for one angle of attack, α_m = 6°, and for various velocities and oscillation frequencies are shown in Figures 131 through 135. Each figure has a plot for two adjacent pressure ports on the suction surface on the upper half of the plot and the corresponding ports on the pressure surface on the lower half of the plot. The first plot starts with the leading edge group and the fifth plot has the trailing edge group. The data is plotted against reduced frequency. The data collapses to nearly a straight line for each pressure port indicating that the average normalized pressures on the airfoil have only a second-order

dependence, if any, on velocity or oscillation frequency. This is true for the entire set of tests and will become apparent when discussing lift and moment.

The normalized fundamental pressure amplitude, $\Delta P_{n,1}$, is shown in a similar manner for $\alpha_m = 6°$ in Figures 136 through 140. $\Delta P_{n,1}$ decreases with increasing $\bar{\omega}$ from the leading edge to midchord and can be fitted with a second order curve which is concave up. From midchord to the trailing edge the curve fit is concave down as it is for the entire pressure surface except the trailing edge where the fluctuation is close to zero. The data follows this pattern for the other values of α_m. Data correlation with reduced frequency is excellent except for the suction surface trailing edge.

A similar set of data is presented in Figures 141 through 150, Figures 151 through 160, and Figures 161 through 170 for $\alpha_m = 8$, 10, and 12° respectively. Three sets of velocity data were used for $\alpha_m = 10°$. All of the data follows the same pattern and is remarkably consistent.

D. Comparison to Whitehead Theory

A theoretical calculation for the unsteady conditions of this wind tunnel and for this cascade at $\alpha_m = 6°$ was obtained (Whitehead 1974). The theory is for unsteady flow through an infinite two-dimensional cascade of flat plate blades at zero mean incidence. A complex unsteady potential with a vorticity disturbance convected at the mainstream velocity impinges on the cascade. Since this is a flat plate, the fluctuating pressure profile is chosen as the

pressure jump across the blade and is normalized

$$\Delta P = \frac{\Delta p}{V_N \, V_C/2g}$$

The results are plotted against chord position and are shown as the solid lines in Figure 171 for two reduced frequencies. The pressure jumps obtained in the present tests at $\alpha_m = 6°$ and $V_N = 150$ fps, are also shown and the agreement is excellent near the leading edge. The theory indicates a slight increase in $\overline{\Delta P}$ with increased f_t whereas the reverse was found experimentally. Near the trailing edge the agreement is not as good. The experimental data passes through a minimum near midchord as previously noted and diverges from the theory near the trailing edge. However, this could result from viscous and wake effects and also from the large trailing edge average pressure differential for light loads which this airfoil exhibits. Airfoils without this characteristic may provide better agreement. For comparative purposes, data at $\alpha_m = 10°$ was also plotted. In this case, the loading has reduced the variation at the trailing edge but the data still passes through a midchord minimum. Even though some modification may be necessary to satisfactorily explain this phenomena, it is encouraging to find that the experimental data are in agreement with theory near the leading edge where the potential flow predominates.

E. Lift and Moment

The instantaneous values of pressure on the airfoil surface can be used to calculate the lift or normal force, L, and moment, M, about the airfoil center. The moment and lift calculations were made

AD-A045 319 AIR FORCE AERO PROPULSION LAB WRIGHT-PATTERSON AFB OHIO F/G 20/4
A CASCADE IN UNSTEADY FLOW.(U)
DEC 76 F R OSTDIEK
UNCLASSIFIED AFAPL-TR-76-115 NL

2 OF 3
ADA
045319

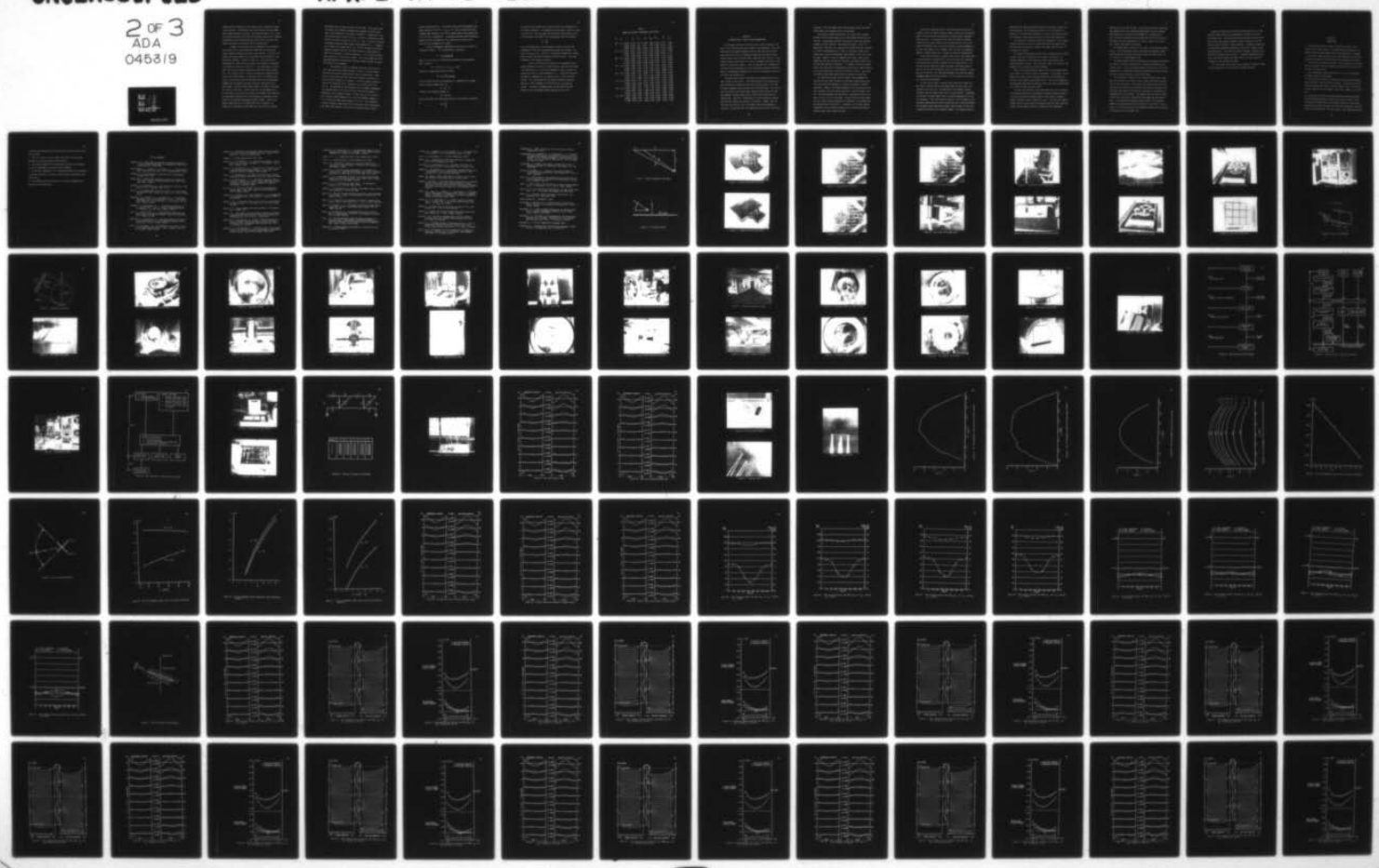

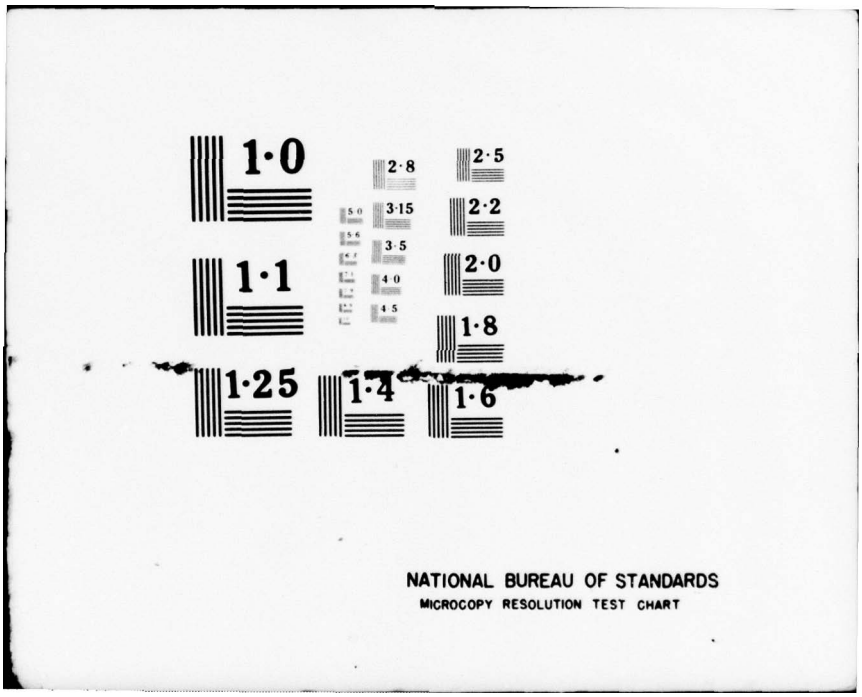
1·0
1·1
1·25
1·4
1·6
1·8
2·0
2·2
2·5
2·8
3·15
3·5
4·0
4·5
5·0
5·6
6·3
NATIONAL BUREAU OF STANDARDS
MICROCOPY RESOLUTION TEST CHART

assuming that the pressure at each static port was constant to midway to the next port. The pressures near the leading and trailing edges were assumed constant to the edge. No attempt was made to fit a curve to the pressure profile since the trailing edge pressure varies sharply. Nevertheless, these calculated values can be used to study the aerodynamic hysteresis of the airfoil due to unsteady flow.

A nominal flow direction can be calculated as the direction which would exist if the cascade were removed and the directional change convected through the inlet at local velocity. A plot of lift, moment, and pressure against this calculated flow direction at a low oscillation frequency is shown in Figure 172. Each static port is represented by a small plot and the plots are arranged to correspond to the physical location on the airfoil. The leading edge is at the upper left with the pressure surface port below the suction surface port. The string of plots is broken at midchord and continued below so that the trailing edge is at the right side in the middle of the figure. Each plot was made from 256 data values for the fluctuating component and the symbols are used to indicate direction of flow angle change. The port identification number is printed in the upper left corner of each plot. Similar plots for lift and moment for a one inch span of the airfoil are given at the bottom of the figure and any aerodynamic hysteresis will be indicated by a separation of the curves for increasing and decreasing angle of attack. There is an angular range from $\pm 2°$ to $0°$ wherein the lift is constant. An inspection of the pressure loops shows this to be due to a pressure

adjustment near the suction surface trailing edge. On the other hand, the moment varies smoothly throughout the complete cycle which indicates a rapid movement of the center of pressure. A comparison of this figure with Figures 173 and 174 for α_m = 8 and 10°, respectively, shows that the flat spot has moved to -2° to -4°. Thus, it occurs at the same instantaneous angle of attack range of approximately 8°-6°. A comparison of Figures 174 through 182 for α_m = 10° and increasing oscillation frequency indicates that this flat spot occurs at a higher angle of attack for increasing α than for decreasing α. This is the most significant hysteresis in this series of tests. The trailing edge flow field adjustment mechanism involved here should be studied further to successfully explain this phenomena.

The hysteresis curves are markedly affected by the choice of inlet flow phase angle because the data is taken in a cyclic fashion. The wrong choice would cause hysteresis even at steady state. Therefore, we should take particular note of the change in hysteresis as the oscillation frequency is increased. This can be done by comparing Figures 174 through 182 for an increase of f_t in steps from 0.2 to 16.2 hz. The amplitude of the fluctuating lift and moment fundamentals have changed and the lift curve still has a flat spot but there is remarkably little hysteresis change. In fact, for α_m = 6, 8, and 10°, the lift phase angle changed by 14° or less for frequency changes of 0.2 to 16 and the moment phase angle by 9° or less. This represents a reduced frequency range from 0.001 to 0.108 where other investigators have found large hysteresis loops while oscillating airfoils rather

than oscillating the flow. The absolute values of both parameters were always between +17° and -3°. For α_m = 12°, where we previously noted a leading edge separation, the lift and moment phase angle changes were 19.7° and 15.6°, respectively. The maximum calculated phase difference between the lift and moment for this complete set of tests was 9°. Thus, the lift and moment are in phase.

A set of aerodynamic coefficients for this set of airfoils is presented in Table 2. A lift coefficient is defined as

$$C_L = \frac{L}{c\rho\ V_N\ V_C/2g\cdot 144}$$

where L is in lb and V_C is the velocity induced by the perturbation and is given by

$$V_C = V_N\ [\sin \alpha_m - \sin (\alpha_m - 5.75)]$$

Similarly, a moment coefficient is defined

$$C_M = \frac{M}{c^2\ \rho\ V\ V\ /4g\cdot 144}$$

The lift coefficient can be represented as a combination of a steady part, $\overline{C}_L$, and an unsteady part, $\tilde{C}_L$

$$C_L = \overline{C}_L + \tilde{C}_L$$

Similarly, the normalized moment is

$$C_M = \overline{C}_M + \tilde{C}_M$$

We can also define the time-average position of the center of pressure as

$$\overline{CP} = \frac{\overline{C}_M}{\overline{C}_L}$$

The data from the present set of tests show $\overline{CP}$ to be independent of oscillation frequency. Its dependence on mean angle of attack is shown in Figure 183. Using the phase and fluctuation relationships of the lift and moment, the range of the instantaneous center of pressure

$$CP = \frac{C_M}{C_L}$$

can be calculated and is also presented in Table 2 with only the fundamentals of the lift and moment being taken into account. The ends of the range, $CP_{1,+}$ and $CP_{1,-}$, correspond to maximum and minimum angle of attack and are in fractions of the half-chord. This range decreases as the frequency increases.

A plot of both steady and unsteady lift components versus reduced frequency are given in Figure 184 which shows that the steady lift coefficient, $\overline{C}_L$, is primarily dependent on angle of attack as expected with only a slight dependence on f_t. Figure 185 shows that the moment is dependent on α_m, velocity, and f_t in much the same fashion. This illustrates that the average individual pressures have only a small dependence on velocity and f_t as pointed out earlier. It should be remembered that the calculated lift and moment are from incremental average pressure on the airfoil.

TABLE 2

NORMALIZED UNSTEADY AERODYNAMIC COEFFICIENTS

V_N	α_M	$\bar{\omega}$	$\bar{C}_L$	$\tilde{C}_{L,1}$	$\bar{C}_M$	$\tilde{C}_{M,1}$	$CP_{1,+}$	$\overline{CP}$	$CP_{1,-}$
150	6.0	0.0010	2.372	1.339	-0.204	1.282	0.290	-0.121	-1.439
		0.0396	2.338	1.251	-0.211	1.229	0.284	-0.127	-1.325
		0.0795	2.338	0.920	-0.204	1.012	0.248	-0.123	-0.858
110	6.0	0.0013	2.332	1.502	-0.187	1.195	0.263	-0.113	-1.666
		0.0541	2.340	1.238	-0.161	1.085	0.258	-0.097	-1.131
		0.1081	2.232	0.860	-0.185	0.823	0.206	-0.116	-0.734
150	8.0	0.0010	2.866	1.205	0.225	1.227	0.357	0.110	-0.603
		0.0395	2.804	1.056	0.199	1.134	0.345	0.100	-0.535
		0.0788	2.818	0.855	0.242	0.996	0.337	0.121	-0.384
110	8.0	0.0013	2.808	1.272	0.193	1.125	0.323	0.097	-0.607
		0.0541	2.689	1.082	0.162	1.016	0.312	0.084	-0.532
		0.1083	2.737	0.766	0.191	0.836	0.293	0.098	-0.327
150	10.0	0.0010	3.485	1.163	0.689	1.161	0.398	0.278	-0.203
		0.0396	3.431	1.028	0.671	1.078	0.390	0.275	-0.165
		0.0795	3.419	0.866	0.710	0.903	0.376	0.292	-0.076
110	10.0	0.0096	3.376	1.176	0.617	1.071	0.370	0.257	-0.207
		0.0539	3.383	1.068	0.617	0.973	0.357	0.256	-0.154
		0.1084	3.353	0.717	0.625	0.750	0.337	0.262	-0.048
150	12.0	0.0010	3.883	1.252	1.104	1.115	0.432	0.399	-0.004
		0.0395	3.891	1.137	1.098	0.979	0.413	0.397	0.043
		0.0790	3.773	0.988	1.086	0.776	0.391	0.405	0.111
110	12.0	0.0013	4.028	1.081	1.018	1.037	0.402	0.355	-0.006
		0.0540	3.968	0.912	1.002	0.903	0.390	0.355	0.032
		0.1083	3.878	0.740	0.991	0.663	0.358	0.359	0.104

CHAPTER VI

INTERPRETATION OF RESULTS AND RECOMMENDATIONS

A wind tunnel has been built which gives a nearly sinusoidal variation in flow direction with small change in flow magnitude. Tests were conducted at low reduced frequencies and the data show that the pressures around the airfoil are adjusted through pressure waves on both surfaces which travel at a much slower speed than sonic velocity. These induced pressure waves affect the airfoil performance and should be considered in theoretical studies. Since the assumption of incompressible flow implies that adjustment to a flow disturbance by means of acoustic waves is instantaneous throughout the field, this assumption may have to be altered for unsteady flow.

Sinusoidal type pressure fluctuations were obtained over most of both surfaces of the airfoil. The pressure traces on the pressure surfaces show small fluctuations due to the turbulent nature of the flow and depart somewhat from sinusoidal near the leading edge. This may be due to shifting of the leading edge stagnation point during the cycle. The smoothest pressure traces were on the suction surface near the leading edge. The flow is accelerated as it flows around the leading edge and this reduces the turbulent fluctuations. However, when the flow nears the trailing edge, the boundary layer has developed and vorticity is being shed into the stream making the pressure traces more

irregular. Also, the length of the finite Fourier series (20 terms) allows some of the turbulent noise to be retained.

The pressure profiles obtained for this airfoil show a smooth approach to the trailing edge only for high loadings and then only in the mean. Instantaneous pressure differentials at 89% chord position reached 0.10 Q but these are also reduced by loading. This is in opposition to the data for a single airfoil (Homes 1973) and a cascade of airfoils (Satyanarayana et al 1974) in a wavy-wall tunnel which showed static pressure differentials which tended to zero at the trailing edge. However, it must be remembered that those airfoils were symmetrical and that the wavy-wall may have a noticeable effect on the trailing edge pressure fluctuations. For example, during the present tests it was found that a variable back pressure had a larger effect on the suction surface than it did on the pressure surface. Thus, great care must be taken when establishing the cascade exit conditions.

The normalized average pressures showed little dependence on velocity and oscillation frequency and provided average pressure profiles which would be expected in a steady flow cascade for similar conditions. However, the reduced frequencies for these tests are low and a deviation from this might be observed if tests at higher $\bar{\omega}$ are run. The crank mechanism was designed for a maximum oscillation frequency of 30 hz at $\pm 5.75°$ amplitude. The next series of tests should be run at higher reduced frequencies to determine if the average and unsteady pressures are affected. In addition, still higher reduced frequencies can be obtained by reducing the oscillation amplitude so that the stress levels remain the same.

During these additional tests, the flow velocity can also be increased so that the reduced frequency remains constant but the Reynolds number increases and thus investigate any Reynolds number dependence which may exist. It was shown earlier that the change in Reynolds number had only a small effect on the cascade pressure loss, but the pressure fluctuations near the trailing edge may be quite dependent on R_e since that appears to be a boundary layer and vorticity phenomena. However, a larger range in R_e is required to make that determination.

On the pressure surface, a pressure wave travels from leading edge to trailing edge at a speed (2-6% of sonic velocity) which increases with increasing α_m and does not depend on free stream velocity. The unsteady pressure amplitude steadily decreases from leading edge to near zero at the trailing edge for any set of flow conditions. At any point on the airfoil, this amplitude decreases with increased reduced frequency except past mid-chord where it first increases to a maximum at $\bar{\omega} \simeq 0.05$ and then decreases.

On the suction surface, a pressure wave leads the incident flow and travels from mid-chord to the leading edge and would seem to be induced by the inlet flow. The amplitude of the unsteady pressure decreases from the leading edge to zero at near mid-chord. Downstream of mid-chord, the phase angle shifts by 150-180° depending on oscillation frequency. This shift occurs at smaller x/c for increased α_m and coincides approximately with the minimum flow area of the blade channel. The unsteady pressure amplitude increases from mid-chord to the trailing edge and decreases with increased loading. The unsteady pressure

amplitude at any chord position decreases with increased $\bar{\omega}$ except past mid-chord where, like the pressure surface, it first increases to a maximum at $\bar{\omega} \simeq 0.05$ and then decreases as it did on the pressure surface. This increase is small and may be peculiar to the tunnel operation.

The similarity of the phase angle and $\bar{\omega}$ dependence of the unsteady pressure variations on the two surfaces past mid-chord suggests that the flow should be analyzed as channel flow rather than as airfoil in the middle of a stream.

The steady lift and moment increase with increased angle of attack and also show a small increase for an increase in velocity. The unsteady components, on the other hand, show a small decrease with increasing angle of attack. They also vary slightly with velocity, and decrease with increasing oscillation frequency.

There are no large hysteresis loops in the lift and moment curves as was shown in oscillating airfoil experiments. The unsteady lift and moment are in-phase, have a decreasing amplitude with increasing f_t, but show little change in phase angle with f_t. This can be compared to the decreasing amplitude but increasing phase lag found by Satyanarayana et al (1974) in their wavy-wall tunnel.

The lift curve does have a flat spot wherein the lift is constant. This occurred during each cycle between calculated incidence angles of +2° and 0° (the actual incidence angle is lower) where a cascade is normally expected to have a smooth lift curve. This flat spot seems to connect two lift curves which are otherwise smooth and occurs when the suction surface pressure profile is undergoing rapid adjustment,

especially near the trailing edge. The pressures near the leading edge vary smoothly during this transition which seems to rule out leading edge separation or stagnation point movement as a probable cause. Thus, the trailing edge activity indicates that the lift flat spot may be caused by the wake adjustment for a lightly loaded airfoil with a small leading edge radius of curvature.

The average center of pressure lies close to mid-chord and changes with α_m. The instantaneous center of pressure moves through a large range during each oscillation and moves so that the step in the lift still results in a smooth moment curve.

The average pressure profiles obtained during unsteady flow testing are similar to profiles obtained from a stationary cascade test of a similar airfoil. Also, the unsteady pressure profiles are in excellent agreement with a theoretical prediction (Whitehead 1974) near the leading edge but differ markedly at the trailing edge.

It is difficult to obtain a truly variable direction and a great deal of work remains to be done to fully explain and define the operation of this wind tunnel. The pressures and velocities not only vary cyclically with time but also have non-linear phase relationships with each other which makes it difficult for the observer to establish any phenomenological flow patterns. The oncoming flow direction is established by the inlet but is adjusted by the cascade near the leading edge. A three-dimensional mapping should be done in the future to establish the pressure and velocity variations in the inlet. This, of course, will then provide one of the boundary conditions for an analytical description of the cascade flow.

Future work should also include flow visualization tests in the cascade to help establish the time sequence of events in the flow during each cycle. The present tests have shown that the suction surface trailing edge pressure undergoes large fluctuations while the pressure surface pressure is nearly constant. Therefore, the position of the dividing streamline downstream of the airfoil probably varies during each cycle. This would also imply a temporal variation of the position of the wake and its profile. A traverse mechanism has been built into the wind tunnel side plate and will be used to map the cascade exit flow including the wakes.

This wind tunnel can be used to test compressor cascades of other airfoil shapes and will provide useful unsteady flow data.

CHAPTER VII

CONCLUSIONS

1. This wind tunnel gives a nearly sinusoidal variation in flow direction with a small change in flow magnitude and represents a new method of obtaining experimental data for unsteady flows in cascades.

2. The airfoil average pressures show little dependence on velocity or frequency and agree with data obtained from a stationary wind tunnel.

3. The pressure fluctuations over most of both surfaces of the airfoil was near sinusoidal with the smoothest fluctuations on the suction surface near the leading edge.

4. The instantaneous pressure differential at the trailing edge was not smooth except at high loading.

5. On the pressure surface the unsteady pressure amplitude decreased along the chord to zero at the trailing edge. A pressure wave, which lags the oncoming flow, travels from the leading to the trailing edge. The wave speed, which lies between 20 and 60 fps, depends on α_m but not on V.

6. On the suction surface the unsteady pressure amplitude decreases from the leading edge along the chord to zero near mid-chord. Here, the fluctuation changes phase and increases toward the trailing edge. A pressure wave which anticipates the flow angle change moves from mid-chord to the leading edge. This wave speed is near freestream velocity.

A pressure wave downstream of mid-chord travels from mid-chord to the trailing edge.

7. Thus, as a result of 5 and 6 above, the airfoil pressures were adjusted by slow-moving waves on both surfaces.

8. The steady components of lift and moment increase with increasing α_m but are independent of test oscillation frequency.

9. The unsteady components of lift and moment decrease with increasing α_m and with increasing f_t and have a small change in phase angle with increasing f_t.

10. The unsteady pressure profiles are in excellent agreement with theory near the leading edge.

LIST OF REFERENCES

Bearman, P. W., "Corrections for the Effect of Ambient Temperature Drift on Hot-Wire Measurements in Incompressible Flow," DISA Information, No. 11 (May 1971).

Bisplinghoff, R. L., Ashley, H., and Halfman, R. L., "Aeroelasticity," Addison-Wesley Publishing Co., Inc., Cambridge, Mass. (1955).

Bradshaw, P., "An Introduction to Turbulence and Its Measurement," Pergamon Press (1971).

Brenner, N. M., "Fast Fourier Transform of Externally Stored Data," IEEE Trans. on Audio and Electroacoustics, Vol. AU-17, No. 2 (July 1969), 128-132.

Bringham, E. O. and Morrow, R. E., "The Fast Fourier Transform," IEEE Spectrum, Vol. 4 (December 1967), 63-70.

Carta, F. O., "Unsteady Normal Force on an Airfoil in a Periodically Stalled Inlet Flow," Journal of Aircraft, Vol. 4, No. 5 (1967), 416-421.

Champagne, F. H., Sleicher, C. A., and Wehrmann, O. H., "Turbulence Measurements with Inclined Hot-Wires. Part 1. Heat Transfer Experiments with Inclined Hot-Wire," J. Fluid Mech., Vol. 28, Part 1 (1967), 153-175.

Champagne, F. H. and Sleicher, C. A., "Turbulence Measurements with Inclined Hot-Wires. Part 2. Hot-Wire Response Equations," J. Fluid Mech., Vol. 28, Part 2 (1967), 177-182.

Collis, D. C. and Williams, M. J., "Two-Dimensional Convection from Heated Wires at Low Reynolds Numbers," Journal of Fluid Mech., Vol. 6 (1959), 357-384.

Commerford, G. L. and Carta, F. O., "Unsteady Aerodynamic Response of a Two-Dimensional Airfoil at High Reduced Frequency," AIAA Journal, Vol. 12, No. 1 (1974), 43-48.

Cooley, J. W. and Tukey, J. W., "An Algorithm for the Machine Calculation of Complex Fourier Series," Math. of Comput., Vol. 19, No. 90 (April 1965), 297-301.

Fleeter, S., "Fluctuating Lift and Moment Coefficients for Cascaded Airfoils in a Nonuniform Compressible Flow," Journal of Aircraft, Vol. 10, No. 10 (1973), 93-98.

Fleeter, S., Private Communication (April 1975).

Franklin, R. E. and Wallace, J. M., "Absolute Measurements of Static Hole Error Using Flush Transducers," J. Fluid Mech., Vol. 42, Part 1 (1970), 33-48.

Friehe, C. A. and Schwartz, W. H., "Deviations from the Cosine Law for Yawed Cylindrical Anemometer Sensors," Trans. ASME, Journal of Applied Mechanics (December 1968), 655-662.

Fung, Y. C., "Introduction to the Theory of Aeroelasticity," Galcit Aeronautical Series, John Wiley & Sons, Inc., New York (1955).

Garlin, S. M. and Slezinger, I. I., "Wind Tunnels and Their Instrumentation," Izdatel stvo "Nauka," Moskva (1964) NASA TTF-346, Translated from Russian by Israel Program for Scientific Translations, Jerusalem (1966).

Geising, J. P., "Vorticity and Kutta Condition for Unsteady Multienergy Flows," Trans. ASME, Journal of Applied Mechanics, Vol. 36 (1969), 608-613.

Gerlack, C. R., Johnson, J. E., and Astleford, W. J., "Instrumentation for Monitoring Dynamic Flow Parameters in Engines," AFAPL-TR-70-14 (1970).

Graham, J. M. R., "Similarity Rules for Thin Airfoils in Non-Stationary Subsonic Flows," J. Fluid Mech., Vol. 43, Part 4 (1970), 753-766.

Hanson, A. R., "Vortex Shedding from Yawed Cylinders," AIAA Journal, Vol. 4 (1966), 738.

Helms, H. D., "Fast Fourier Transform Method of Computing Difference Equation and Simulating Filters," IEEE Trans. on Audio and Electroacoustics, Vol. AU-15, No. 2 (June 1967).

Henderson, R. E. and Bruce, E. P., "Effect of Blade Row Geometry on Axial Flow Rotor Unsteady Response to Inflow Distortions," Unsteady Flows in Jet Engines, SQUID Workshop (July 1974), F. O. Carta, ed, 115-149.

Henderson, R. E. and Daneshyar, H., "Theoretical Analysis of Fluctuating Lift on the Rotor of an Axial Turbomachine," Aeronautical Research Council, Great Britain, R&M No. 3684 (1972).

Henderson, R. E. and Horlock, J. H., "An Approximate Analysis of the Unsteady Lift on Airfoils in Cascade," Trans. ASME, Journal of Engineering for Power, Vol. 94 (1972), 233-240.

Herren, P. C., Jr., Unpublished Work, Private Communication (1974).

High, R. C., Unpublished Work, Private Communication (1974).

Hinze, J. O., "Turbulence," Chapter 2, Principle of Methods and Techniques in the Measurement of Turbulent Flows, McGraw-Hill Book Company (1959).

Holmes, D. W., "Lift and Pressure Measurements in an Aerofoil in Unsteady Flow," 18th ASME International Gas Turbine Conference, Washington DC, ASME Paper No. 73-GT-41 (April 8-12, 1973).

Horlock, J. H., "Fluctuating Lift Forces on Airfoils Moving Through Transverse and Chordwise Gusts," Trans. ASME, Journal of Basic Engineering, Vol. 90 (1968), 494-500.

Horlock, J. H., "An Unsteady Flow Wind Tunnel," The Aeronautical Quarterly, Vol. XXV (May 1974), 81-90.

Johnsen, I. A. and Bullock, R. O., Editors, "Aerodynamic Design of Axial-Flow Compressors," NASA SP-36 (1965)

Kemp, N. H., "On the Lift and Circulation of Airfoils in Some Unsteady-Flow Problems," Journal of the Aeronautical Sciences, Vol. 19 (1952), 713-714.

Kemp, N. H., "Closed-Form Lift and Moment for Osborne's Unsteady Thin Airfoil Theory," AIAA Journal, Vol. 11, No. 9 (1973), 1358-1360.

Kemp, N. H. and Sears, W. R., "Aerodynamic Interference Between Moving Blade Rows," Journal of the Aeronautical Sciences, Vol. 20 (1953), 585-597.

Kemp, N. H. and Sears, W. R., "The Unsteady Forces Due to Viscous Wakes in Turbomachines," Journal of the Aeronautical Sciences, Vol. 22 (1955), 478-483.

King, L. V., "On the Convection of Heat from Small Cylinders in a Stream of Fluid. Determination of Convection Constants of Small Platinum Wires with Application to Hot-Wire Anemometry." Phil. Trans. A (1914), 214, 373-432.

Kreyszig, E., "Advanced Engineering Mathematics," John Wiley & Sons, Inc. New York (1962).

Livesey, J. L., Jackson, J. D., and Southern, C. J., "The Static Hole Error Problem," Aircraft Engineering (1962), 34, 43-47.

Lyon, C. A. and Shahady, P. A., Private Communiction (1974).

Martin, R. J., "Characteristic Distortion Intensities," Unpublished Work, Private Communication (1972).

McCroskey, W. J. and Philippe, J. J., "Unsteady Viscous Flow on Oscillating Airfoils," AIAA Journal, Vol. 13 (1975), 71-79.

McDonald, H. and Shamroth, S. J., "An Analysis and Application of the Time-Dependent Turbulent Boundary-Layer Equations," AIAA Journal, Vol. 9, No. 8 (1971), 1553-1560.

Nasser, Al-, Farouk, "Tables Speed Design of Low-Pass Active Filters," EDN Electronic Design News (March 15, 1971), 23-32.

Naumann, H. and Yeh, J., "Lift and Pressure Fluctuations of a Combined Airfoil Under Periodic Gusts and Applications in Turbomachinery," ASME Gas Turbine and Fluids Engineering Conference, San Francisco, California, Paper No. 72-GT-30 (March 26-30, 1972).

Novick, A. S., Jay, R. L., Sinnet, G. T., and Fleeter, S., "An Experimental Investigation of Unsteady Airfoil Motion in a Supersonic Stream," Presented at the Symposium on Unsteady Aerodynamics, Tucson, Arizona (March 18-20, 1975).

O'Brien, W. F., Jr. and Moses, H. L., "On-Rotor Studies of Rotating Stall," Unsteady Flows in Jet Engines, SQUID Workshop (July 1974), F. O. Carta, ed. 99-104.

Osborne, C., "Unsteady Thin-Airfoil Theory for Subsonic Flow," AIAA Journal, Vol. 11, No. 2 (1973), 205-209.

Osborne, C., "Compressible Unsteady Interactions Between Blade Rows," AIAA Journal, Vol. 11, No. 3 (1973), 340-346.

Ostdiek, F. R., "A Cascade in Unsteady Flow--A Progress Report," Unsteady Flows in Jet Engines, SQUID Workshop (July 1974), F. O. Carta, ed, 347-376.

Peacock, R. E., "Unsteady Response of Compressor Rotors to a 90° Circumferential Pressure Distortion," Unsteady Flows in Jet Engines, SQUID Workshop (July 1974), F. O. Carta, ed, 193-210.

Rannie, W. D., "The Response of an Axial Compressor to Unsteady Disturbances," Unsteady Flows in Jet Engines, SQUID Workshop (July 1974), F. O. Carta, ed, 63-74.

Rochenbach, R., "NACA, Circular Arc Airfoil Test Data," Private Communication (1973).

Satyanarayana, B., Henderson, R. E., and Gostelow, J. P., "A Comparison Between Experimental and Theoretical Fluctuating Lift on Cascades at Low Frequency Parameters," ASME Gas Turbine Conference, Zurick, Switzerland, ASME Paper No. 74-GT-78, (March 30 - April 4, 1974).

Schlichting, H., "Boundary layer Theory," Mc-Graw-Hill Series in Mechanical Engineering, McGraw-Hill Book Company, Inc., New York (1960).

Schorr, B. and Reddy, K. C., "Inviscid Flow Through Cascades in Oscillatory and Distorted Flow," AIAA Journal, Vol. 9, No. 10 (1971), 2043-2050.

Sears, W. R., "Some Aspects of Non-Stationary Airfoil Theory and Its Practical Application," Journal of the Aeronautical Sciences, Vol. 8 (1940-41), 104-114.

Shaw, R., "The Influence of Hole Dimensions on Static Pressure Measurements," J. Fluid Mech., Vol. 7, Part 4 (1960), 550-564.

Shapiro, A. H., "The Dynamics and Thermodynamics of Compressible Fluid Flow," Vol. I, The Ronald Press Company, New York (1953).

Spotts, M. F., "Design of Machine Elements," Prentice-Hall, Inc., Englewood Cliffs, New Jersey (1948).

Thermo Systems Inc., "Anemometry" (1973).

von Karman, T. and Sears, W. R., "Airfoil Theory for Non-Uniform Motion," Journal of the Aeronautical Sciences, Vol. 5, No. 10 (1938), 379-390.

Whitehead, D. S., "Force and Moment Coefficients for Vibrating Aerofoils in Cascade," Aeronautical Research Council, Great Britain, R&M No. 3254 (1960).

Whitehead, D. S., "The Basis of a Field Method for the Calculation of Unsteady Flow in Cascades," Unsteady Flows in Jet Engines, SQUID Workshop (July 1974), F. O. Carta, ed, 211-222.

Whitehead, D. S., Private Communication (November 1974).

Willmarth, W. W., "Unsteady Force and Pressure Measurements," Annual Review of Fluid Mechanics," Vol. 3 (1971), 161.

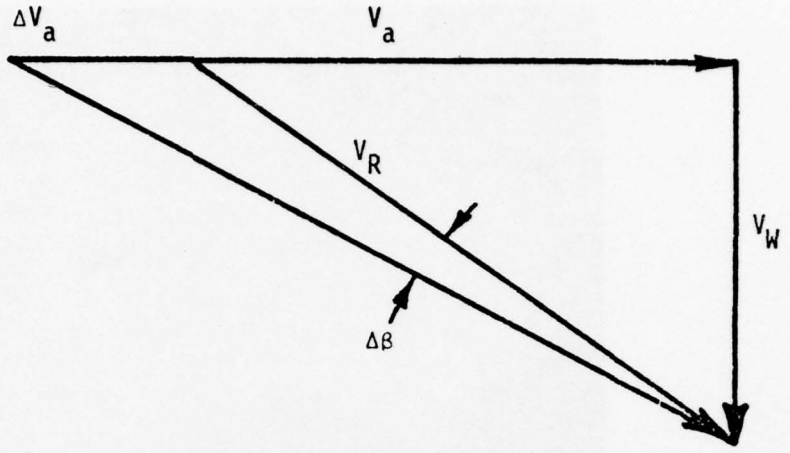

Figure 1. Typical compressor flow angles

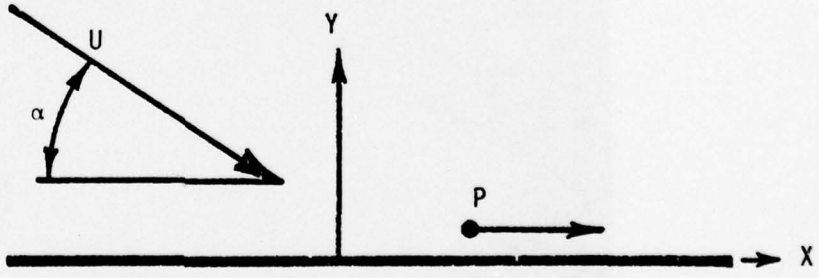

Figure 2. Flat plate airfoil

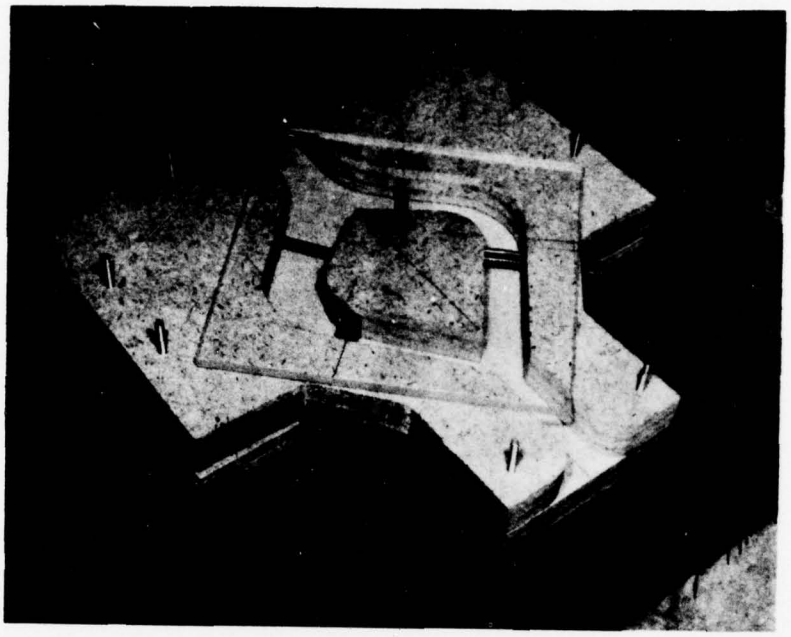

Figure 3. Fluidic wind tunnel flow path

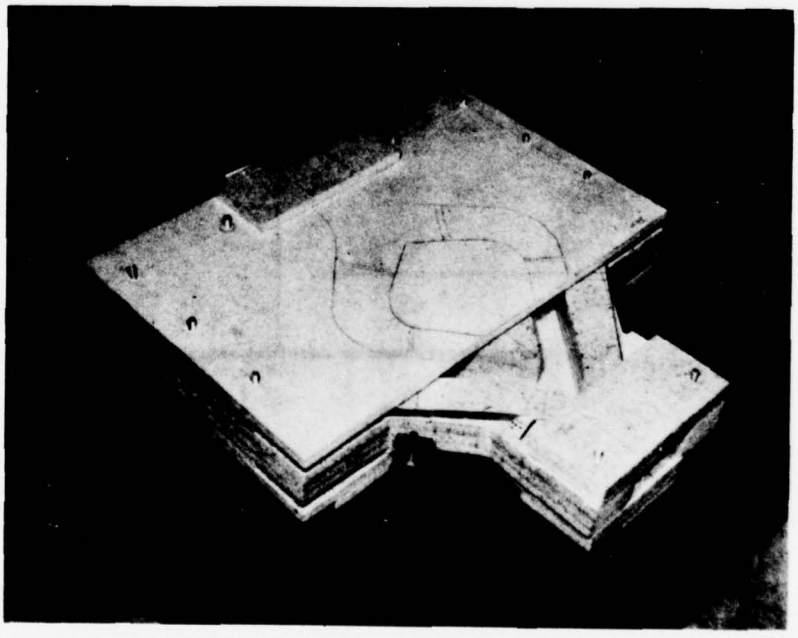

Figure 4. Assembled fluidic wind tunnel

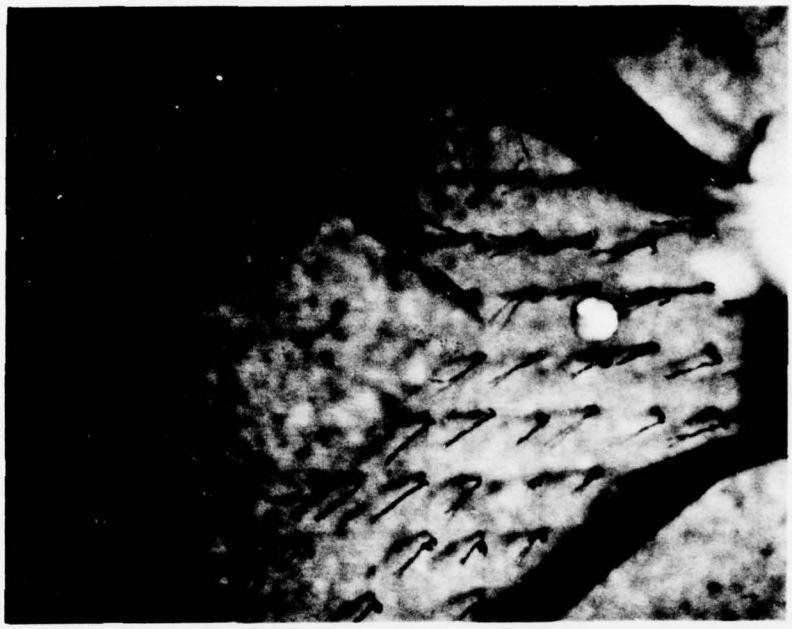

Figure 5. Fluidic tunnel flow at 0°

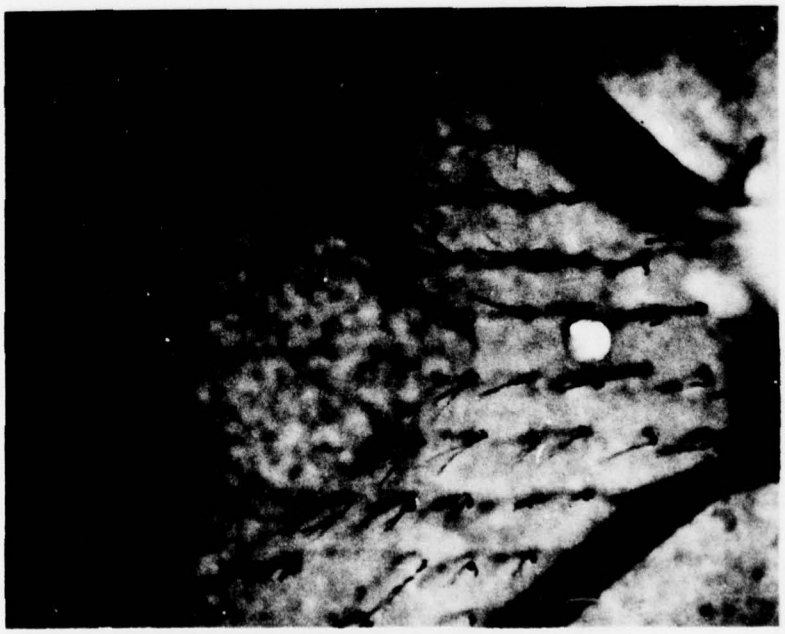

Figure 6. Fluidic tunnel flow at 90°

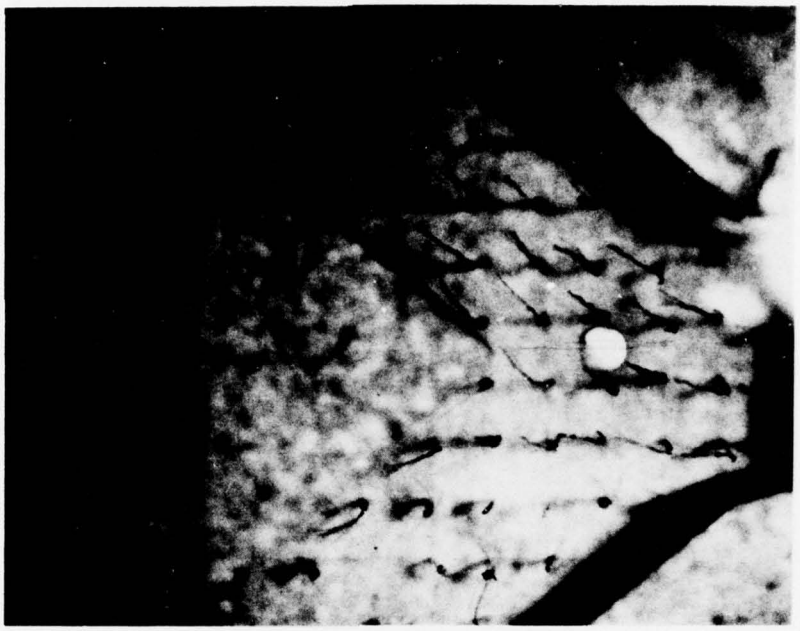

Figure 7. Fluidic tunnel flow at 180°

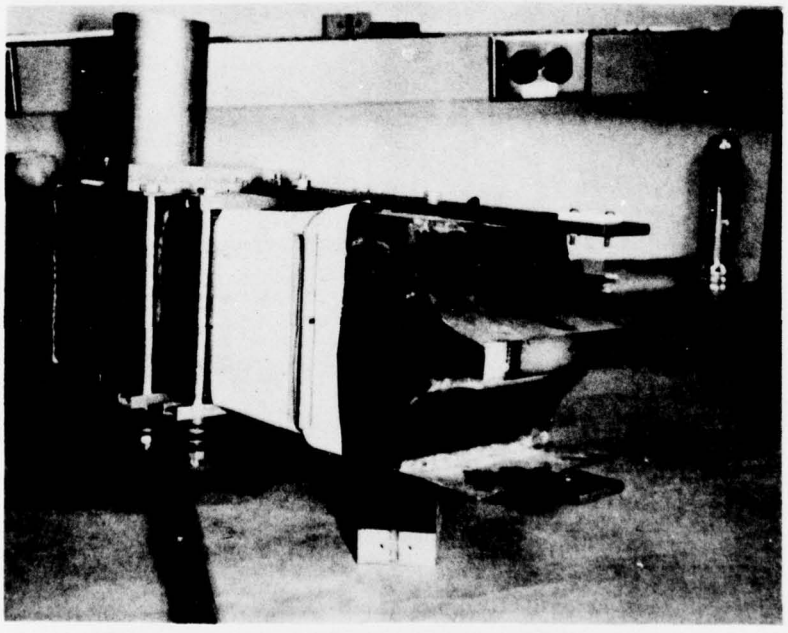

Figure 8. Oscillatory wind tunnel model

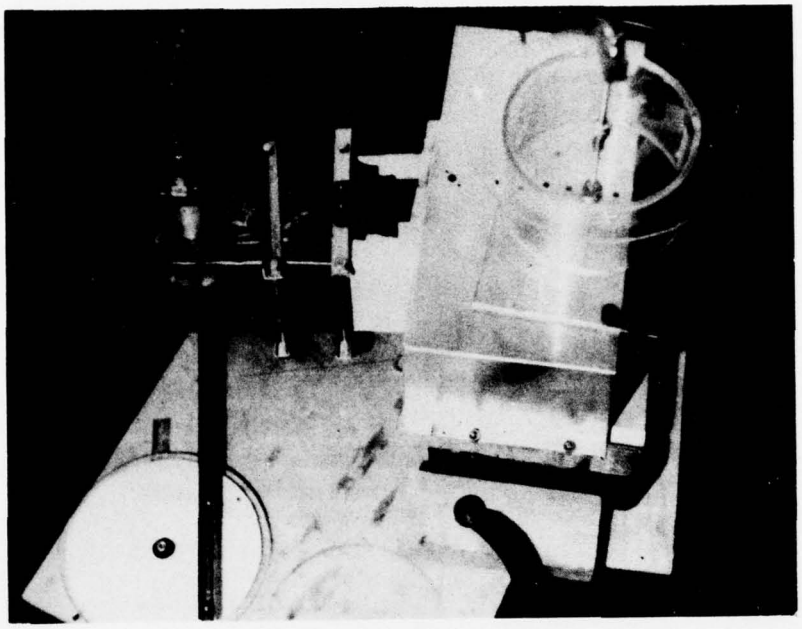

Figure 9. Oscillatory tunnel test set-up

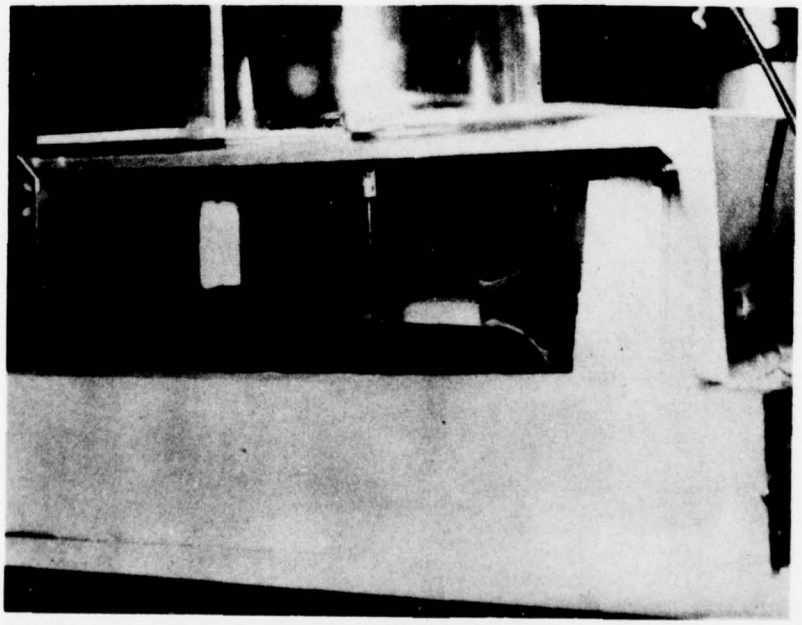

Figure 10. Oscillatory tunnel with hot wire in place

Figure 11. One inch chord vanes

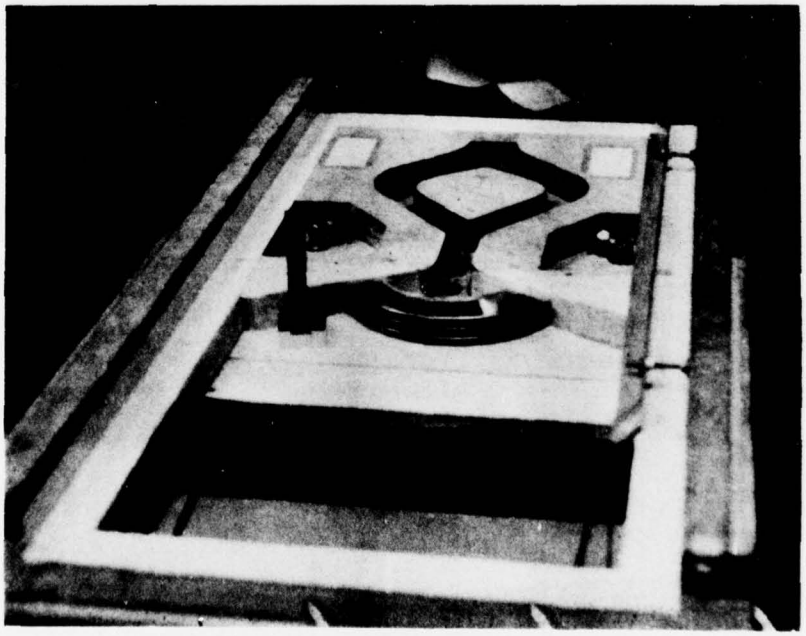

Figure 12. Two inch chord vanes

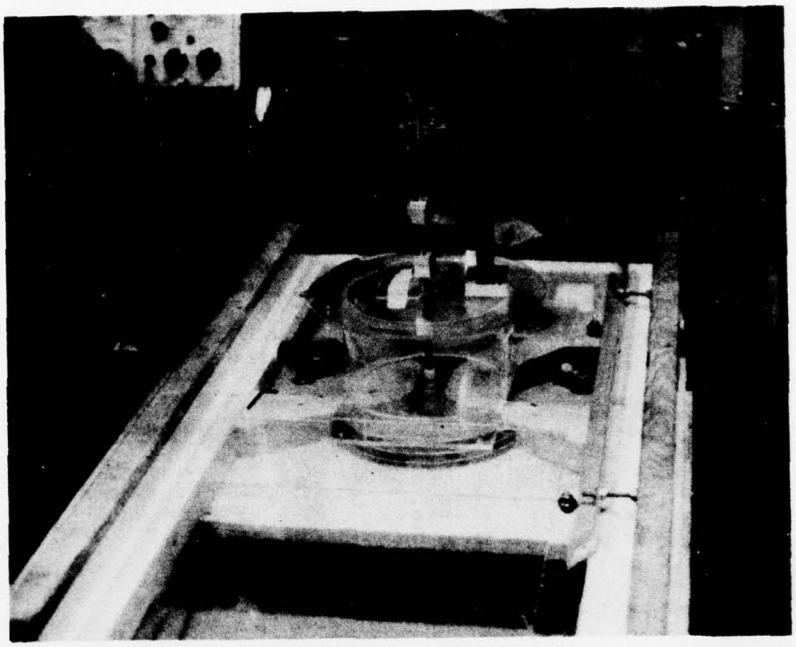

Figure 13. Preliminary vane test

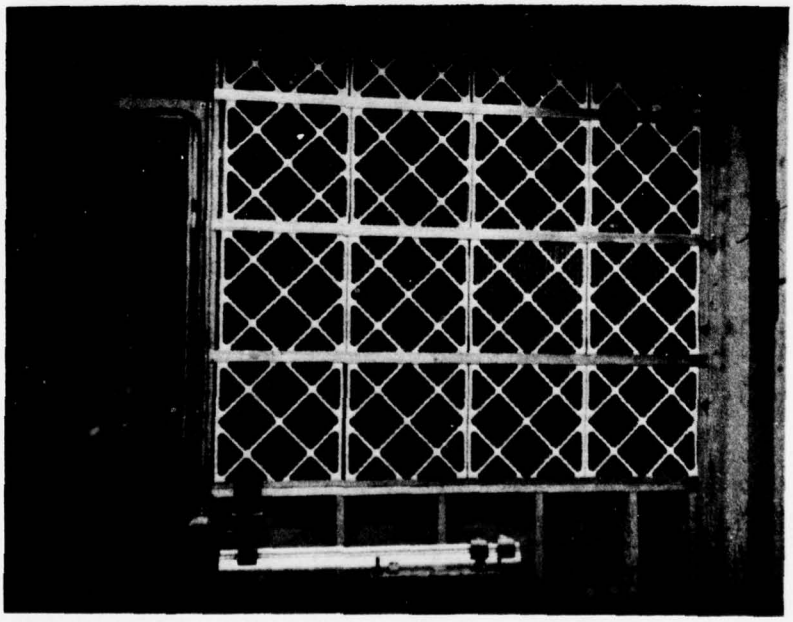

Figure 14. Test cell filter wall

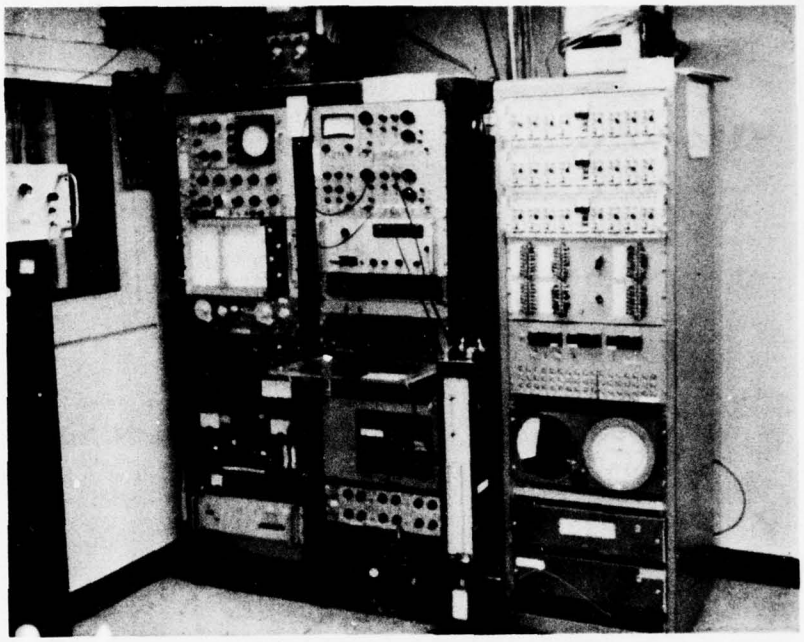

Figure 15. Control room

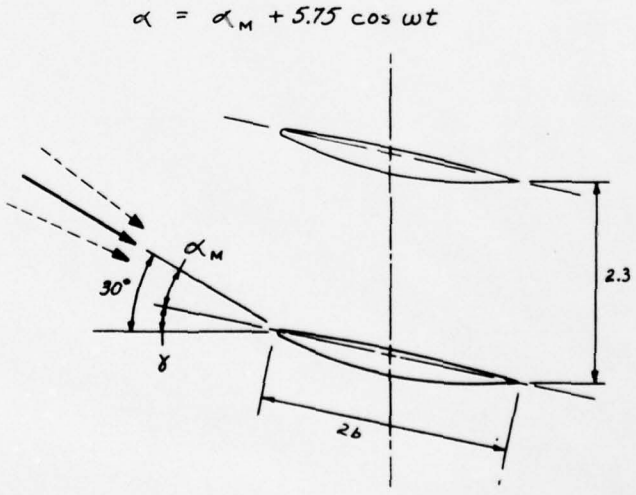

Figure 16. Case de nomenclature

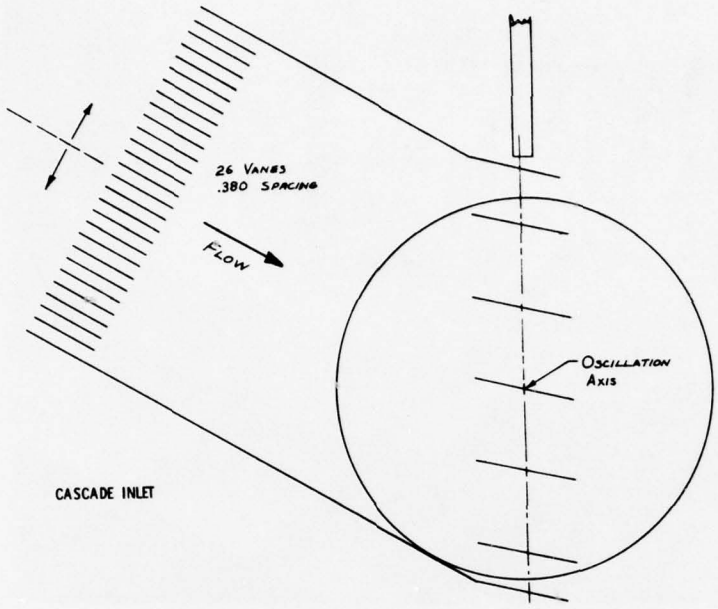

Figure 17. Cascade flow schematic

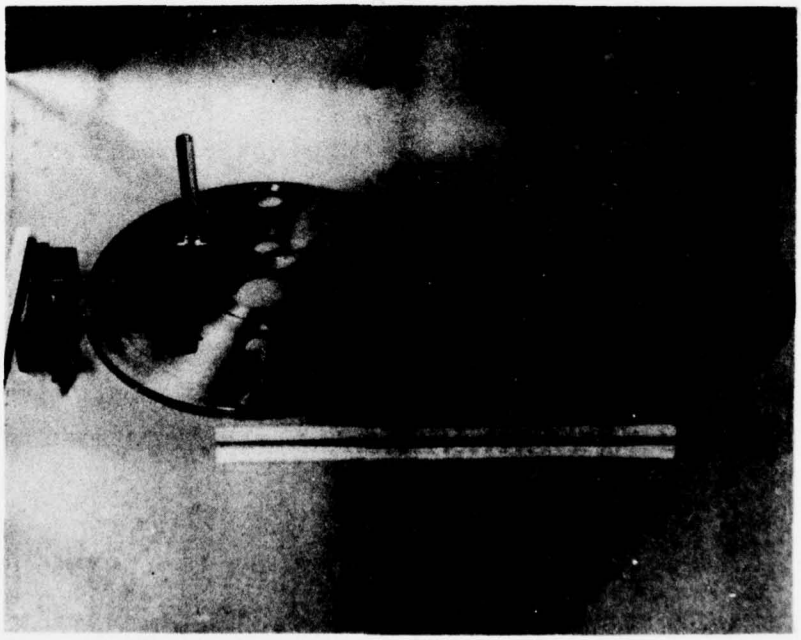

Figure 18. Wind tunnel side plates

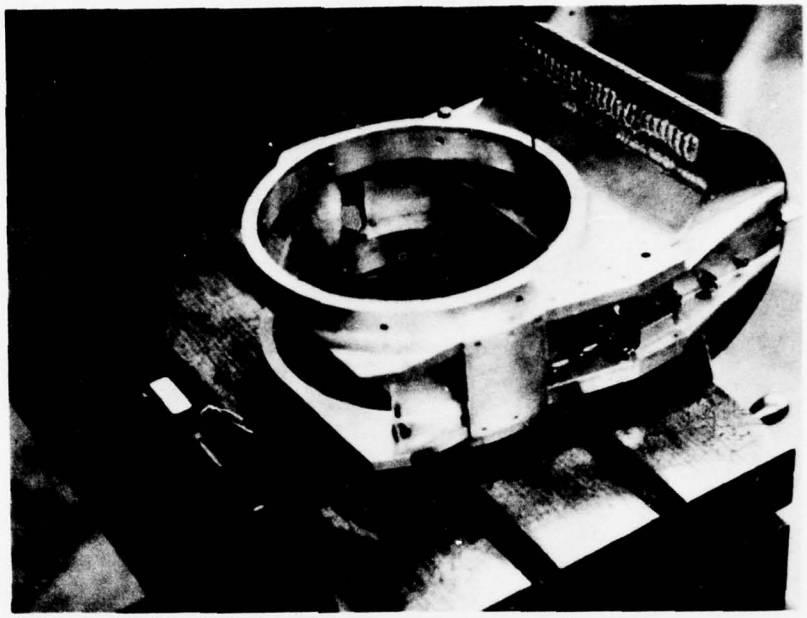

Figure 19. Oscillatory inlet

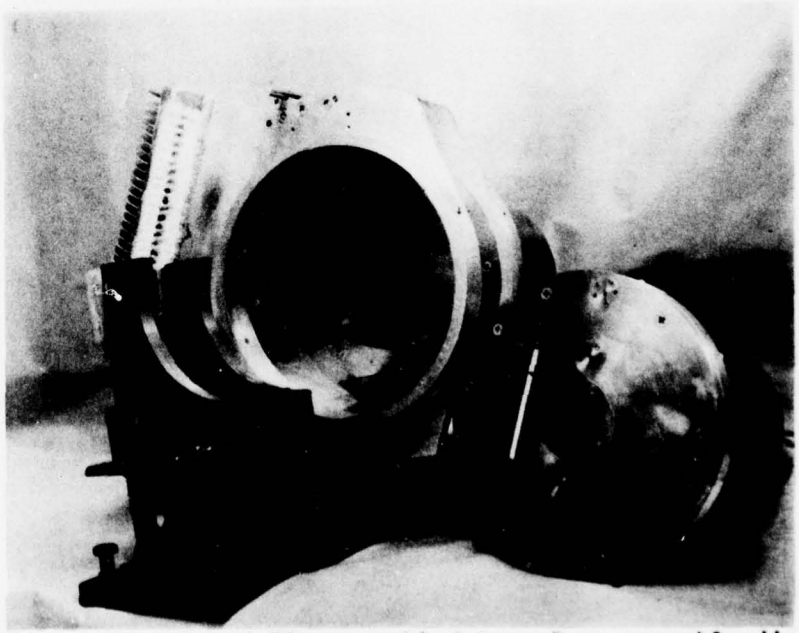

Figure 20. Partially assembled tunnel on assembly jig

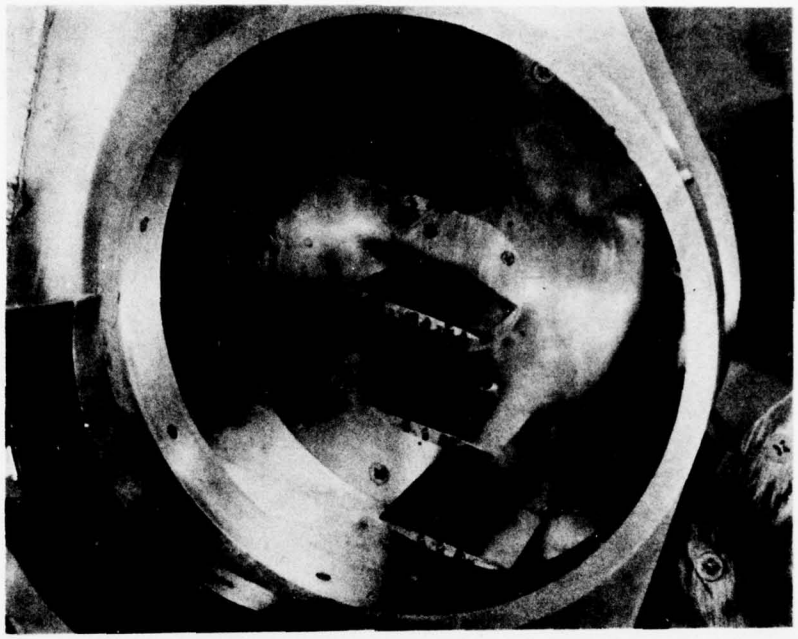

Figure 21. Stationary cascade

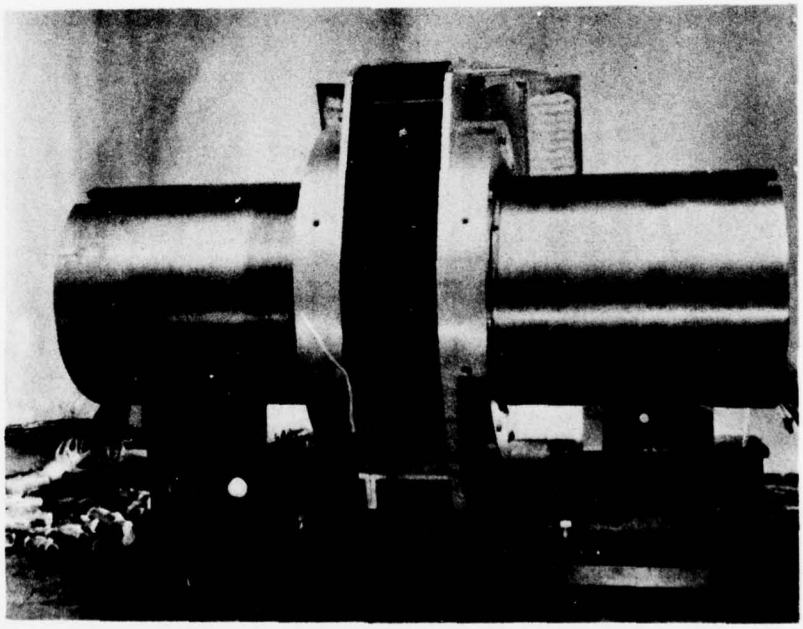

Figure 22. Rear view of assembled wind tunnel

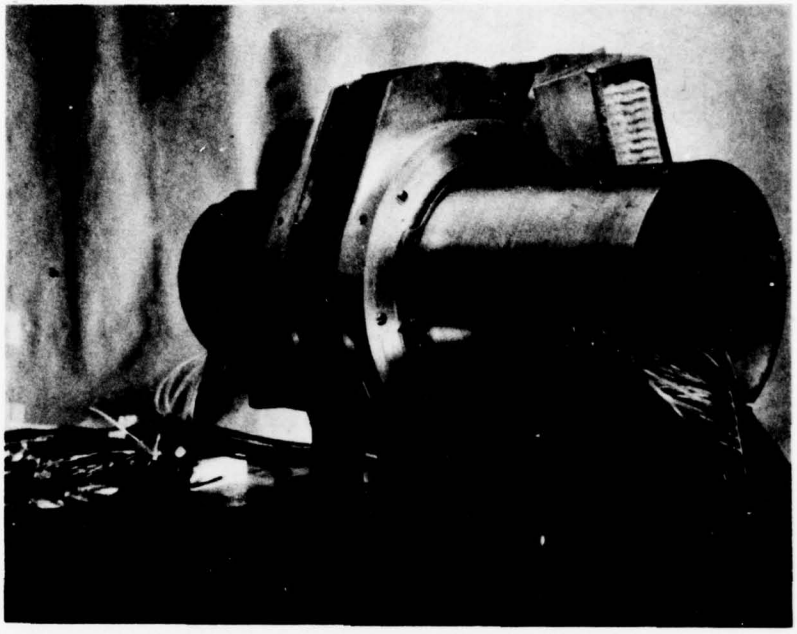

Figure 23. Quarter view of assembled wind tunnel

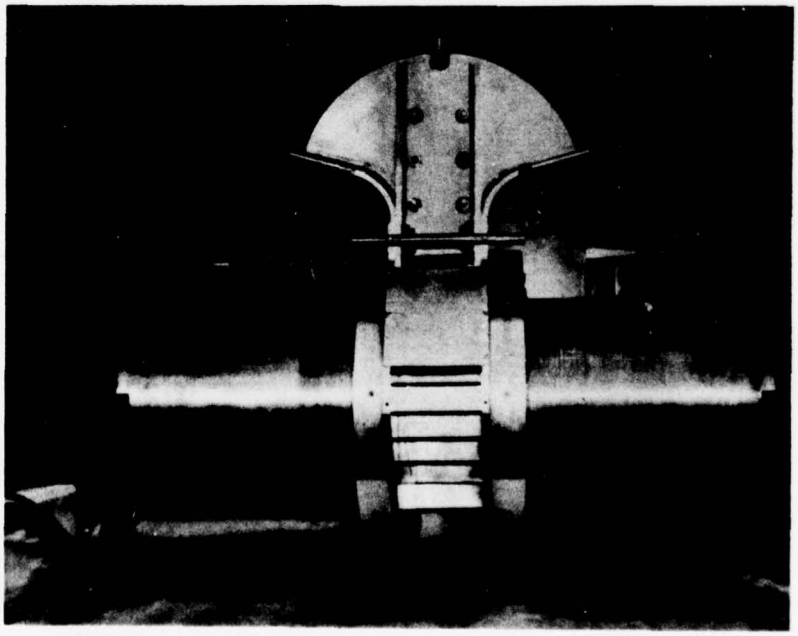

Figure 24. Top view of assembled wind tunnel

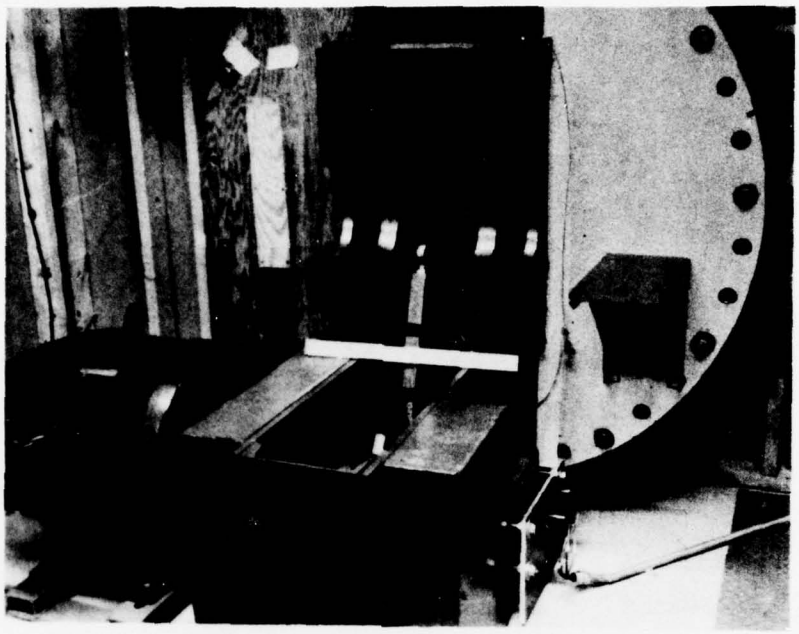

Figure 25. Stanchion

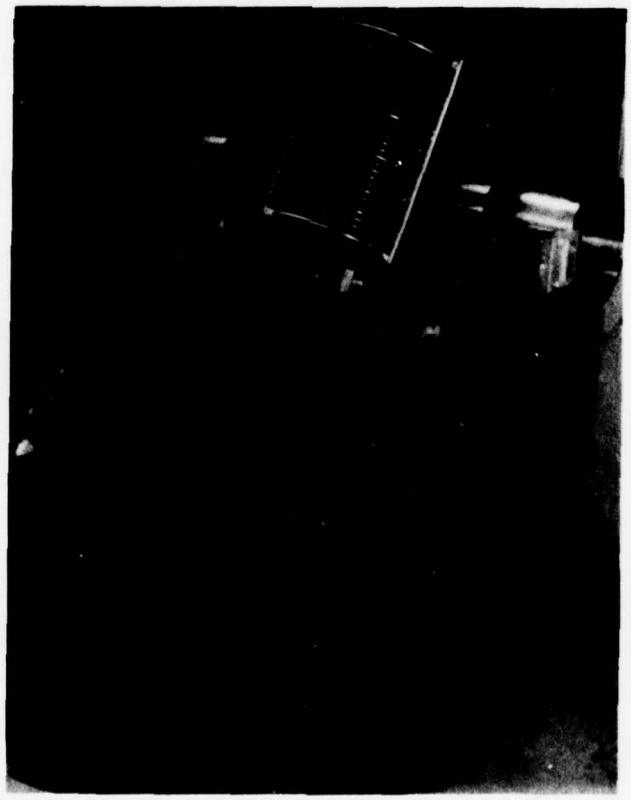

Figure 26. Assembled wind tunnel

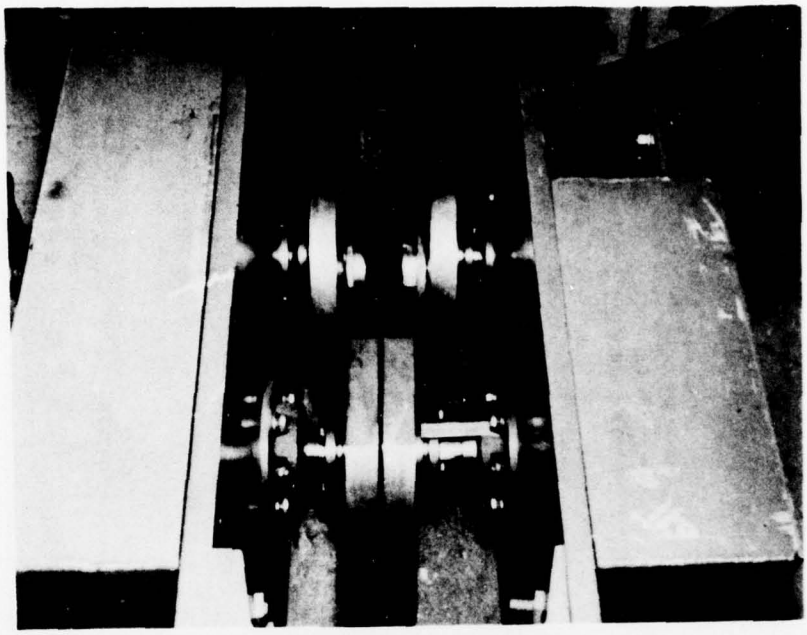

Figure 27. Gear case

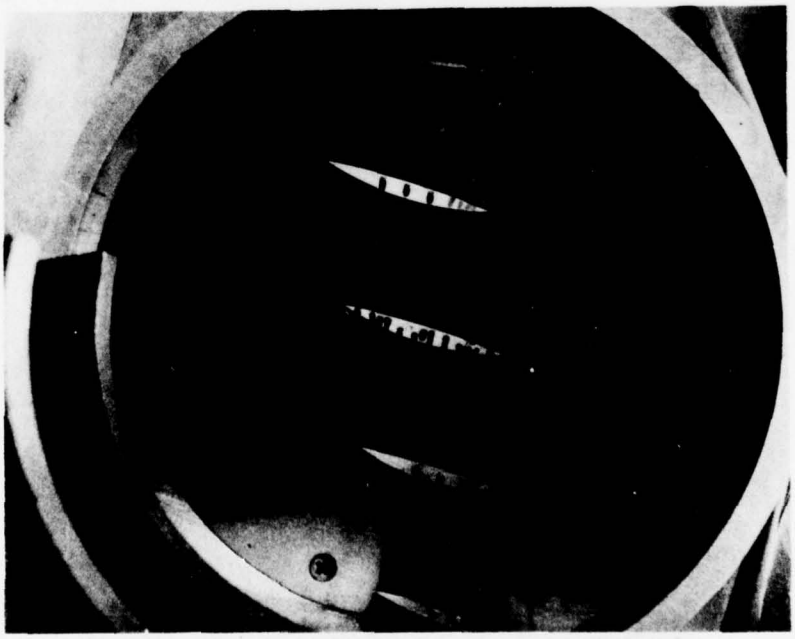

Figure 28. Biconvex circular arc cascade

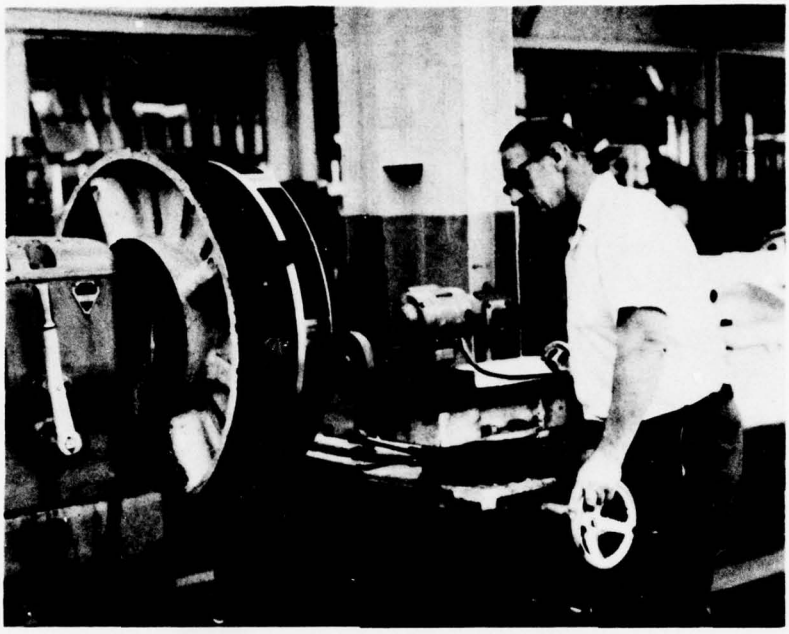

Figure 29. Pressure surface machining operation

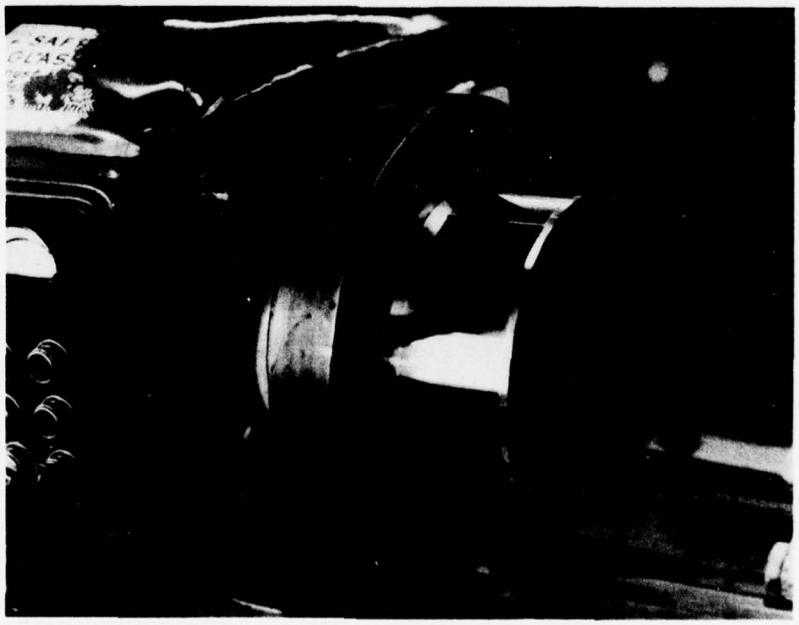

Figure 30. Suction surface machining operation

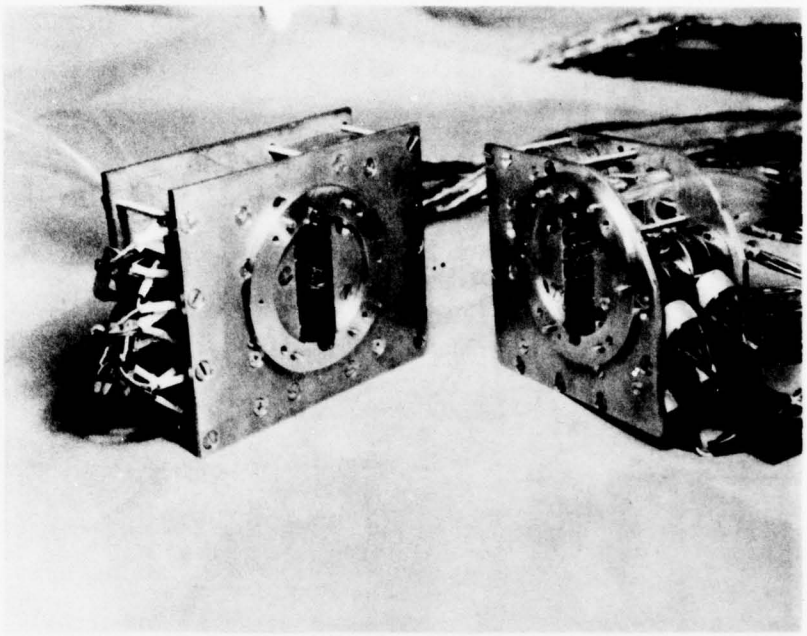

Figure 31. Pressure transducer clusters

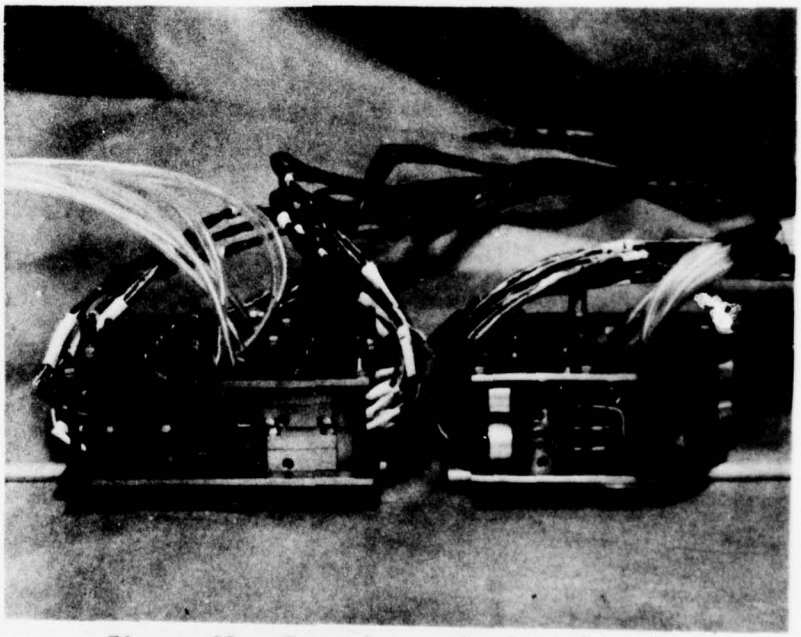

Figure 32. Transducer cluster side view

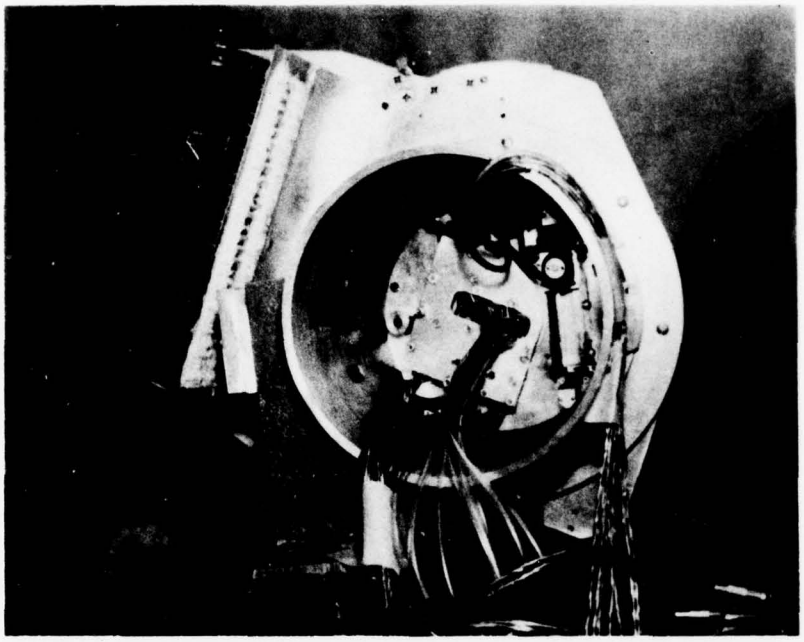

Figure 33. Transducer cluster in right trunion

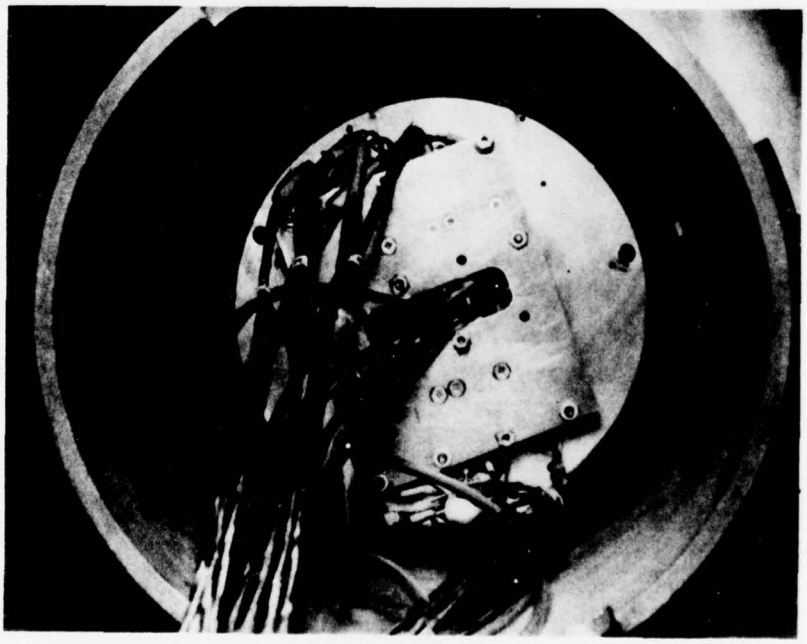

Figure 34. Transducer cluster in left trunion

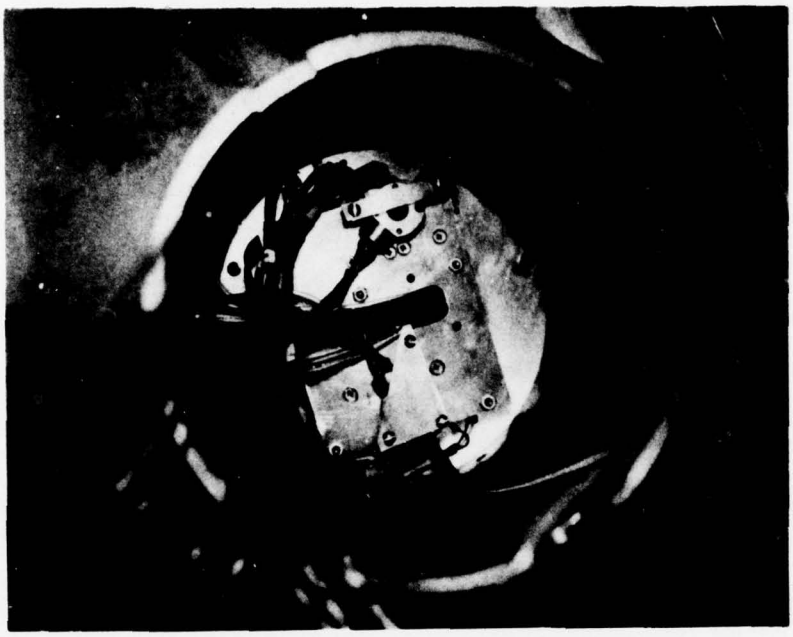

Figure 35. Auxiliary transducer mounting

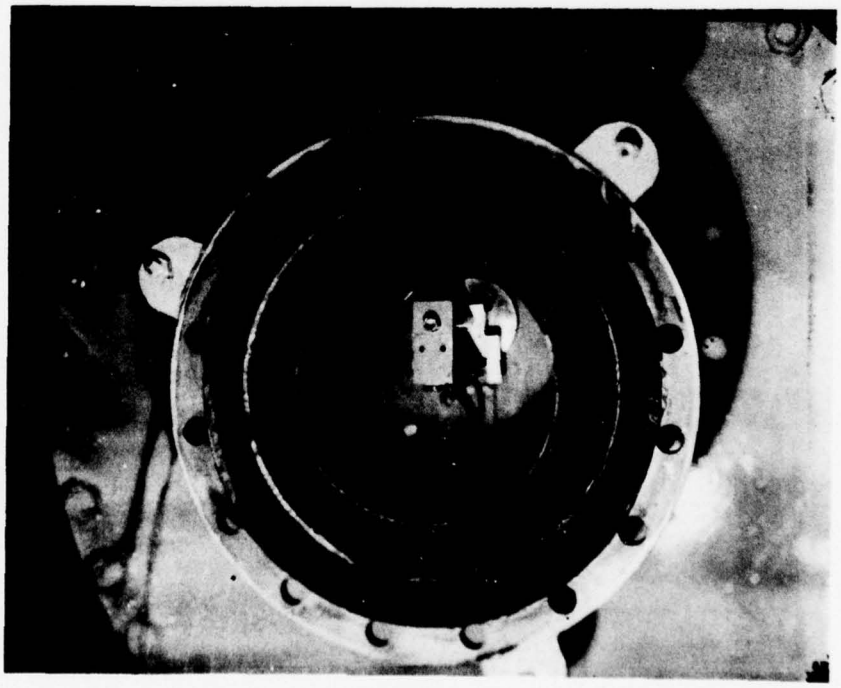

Figure 36. Flow control valve outlet

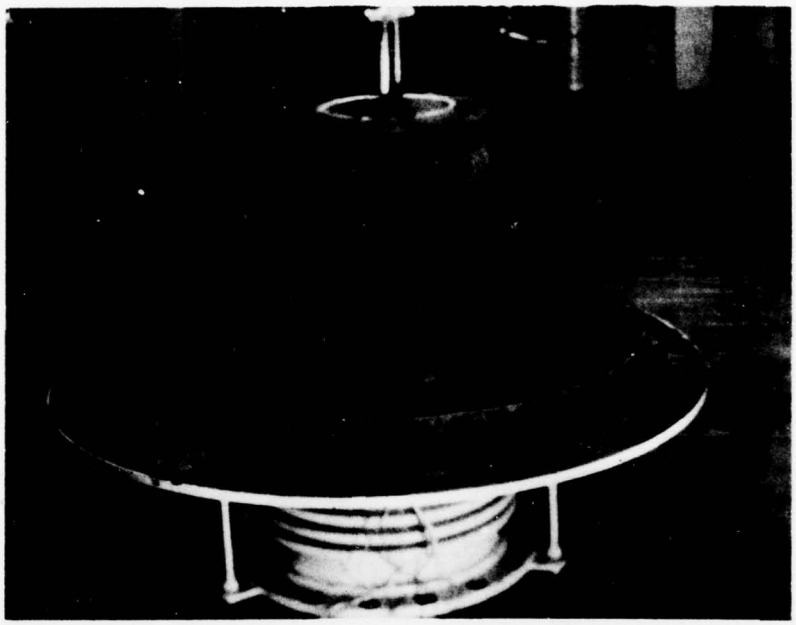

Figure 37. Flow control valve inlet

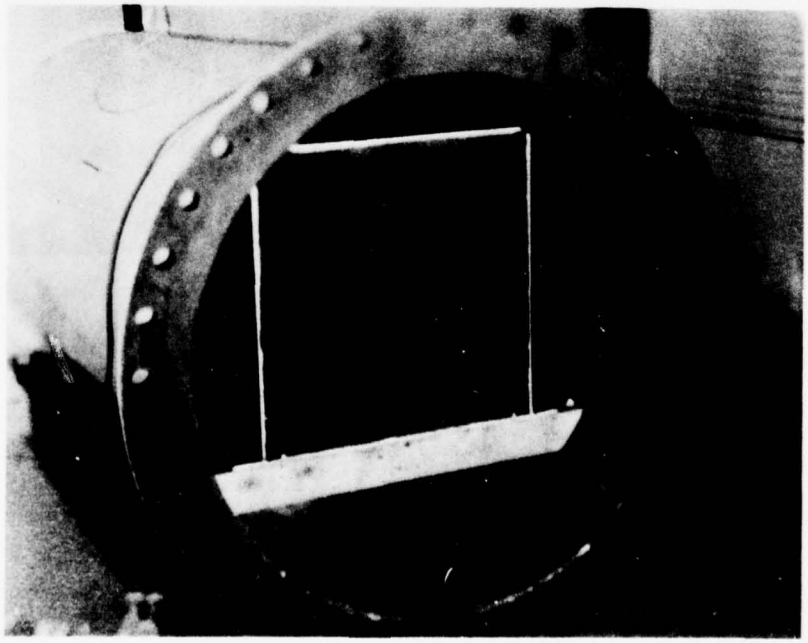

Figure 38. Plenum muffler box

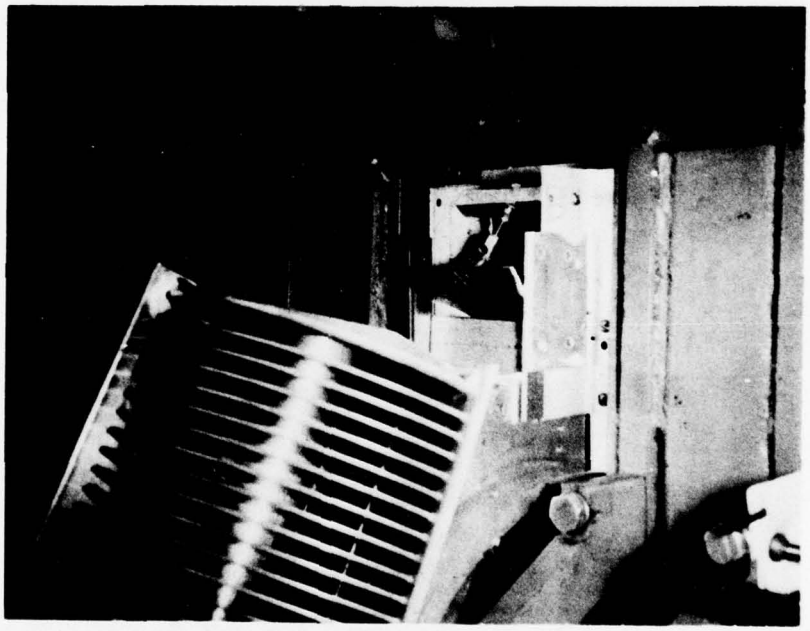

Figure 39. Variable area flow path

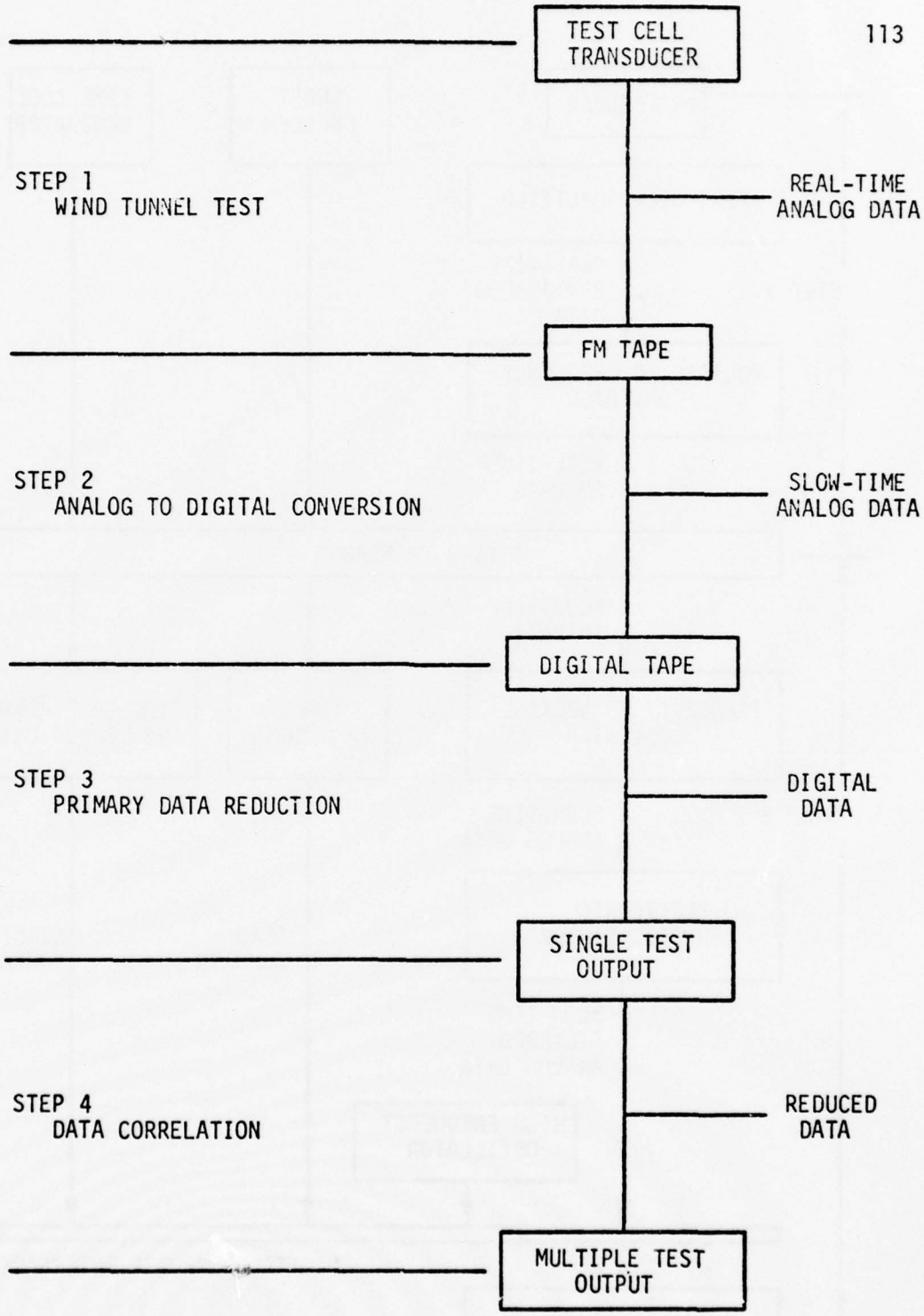

Figure 40. Data acquisition block diagram

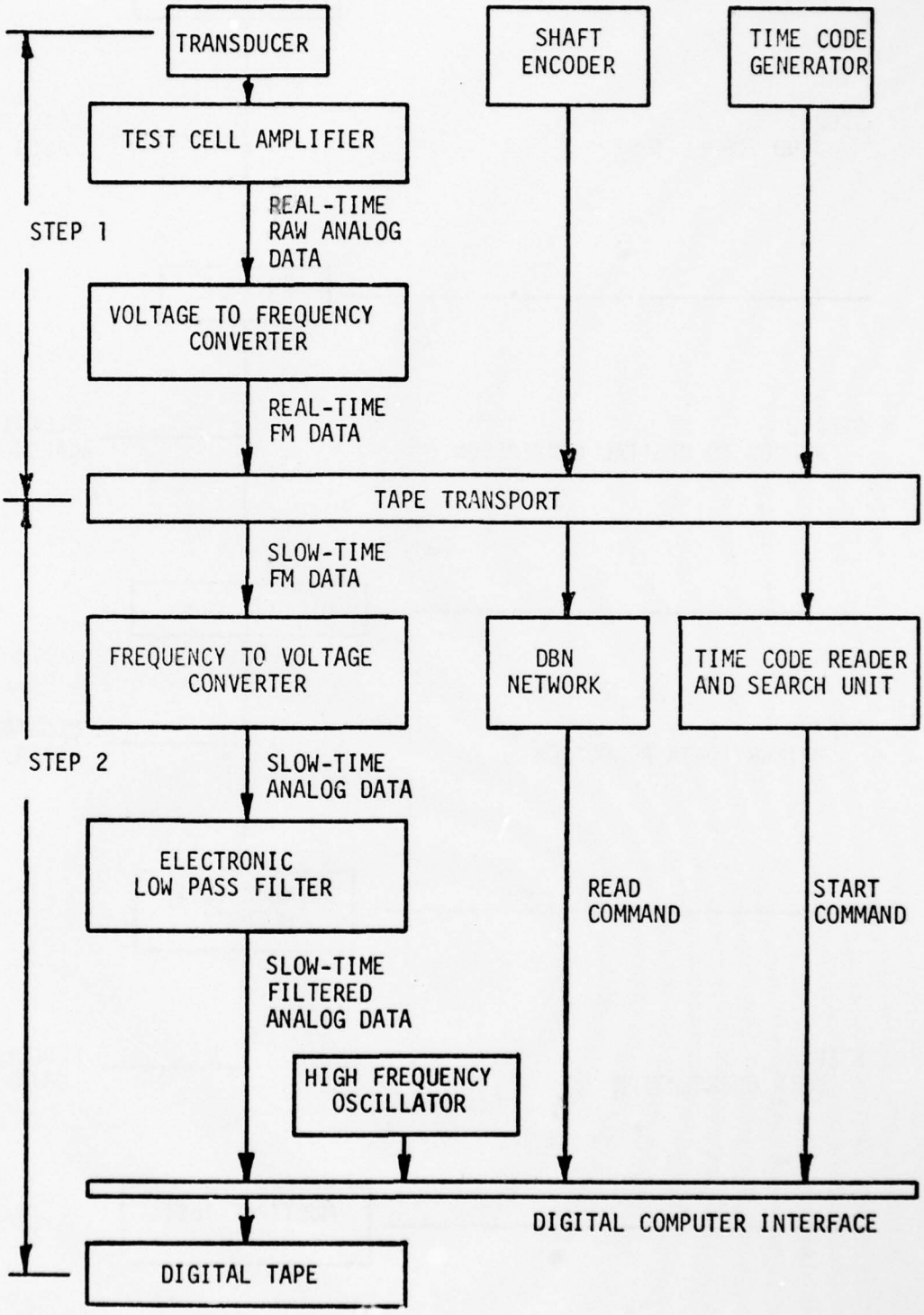

Figure 41. Data acquisition, step one and step two

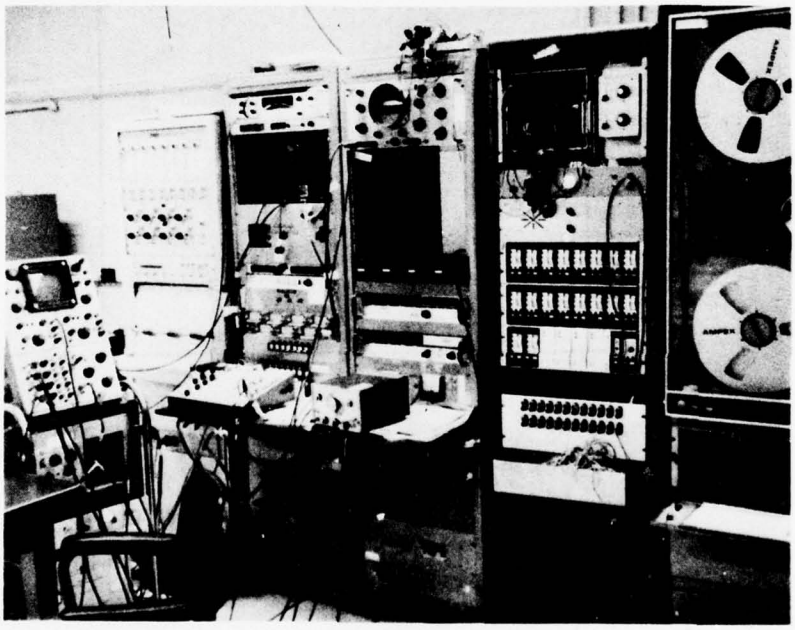

Figure 42. Tape recording room

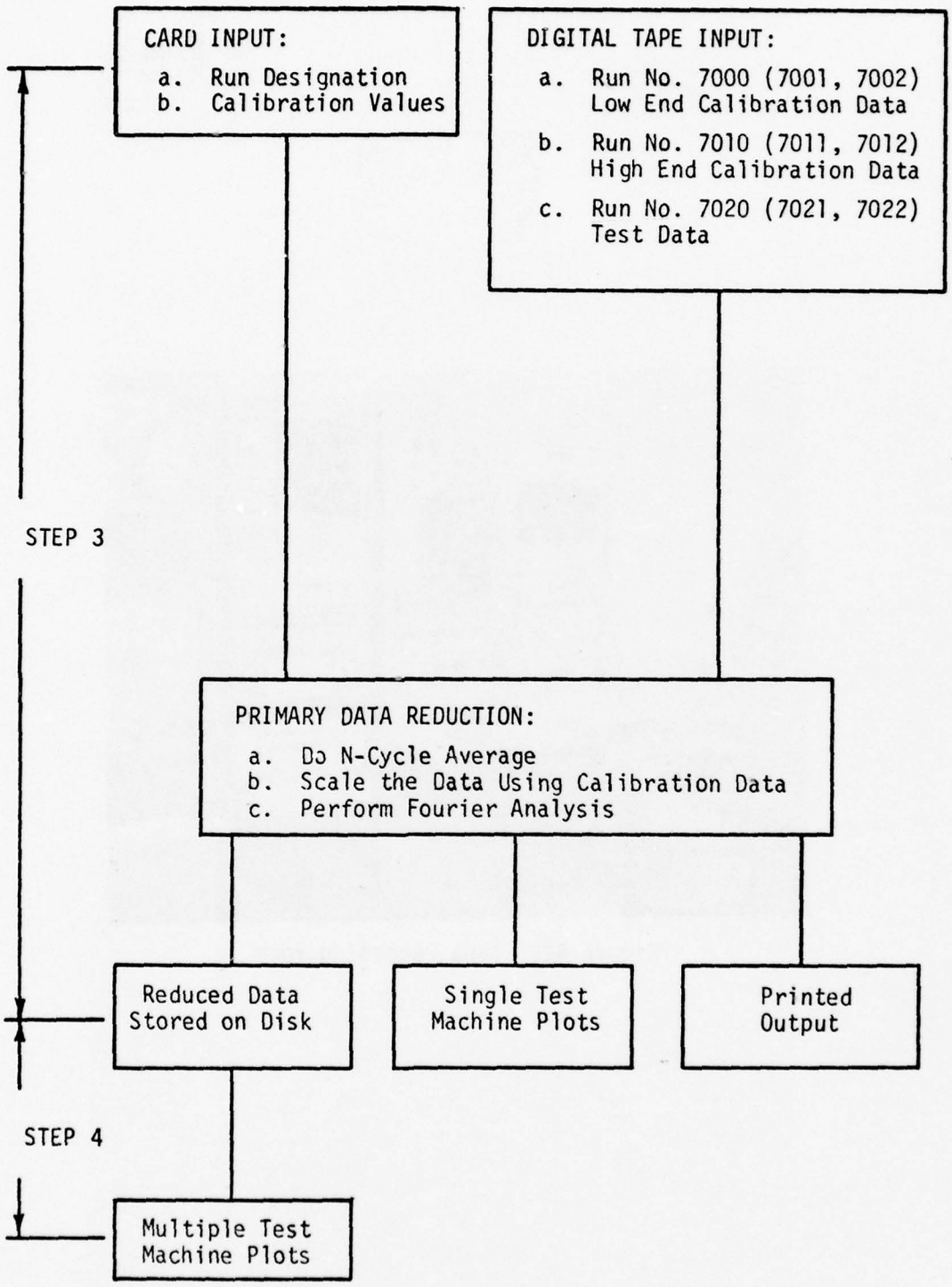

Figure 43. Data acquisition, step three and step four

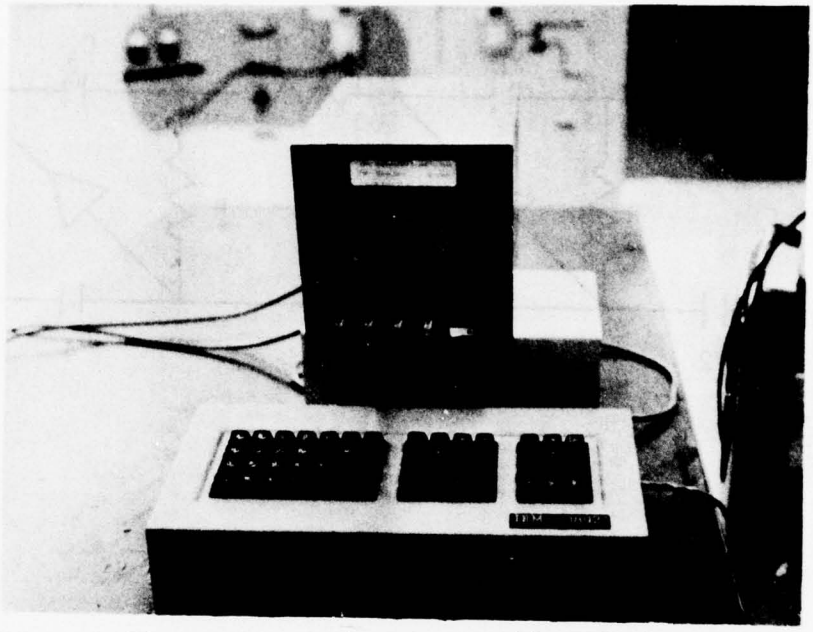

Figure 44. Keyboard and video display

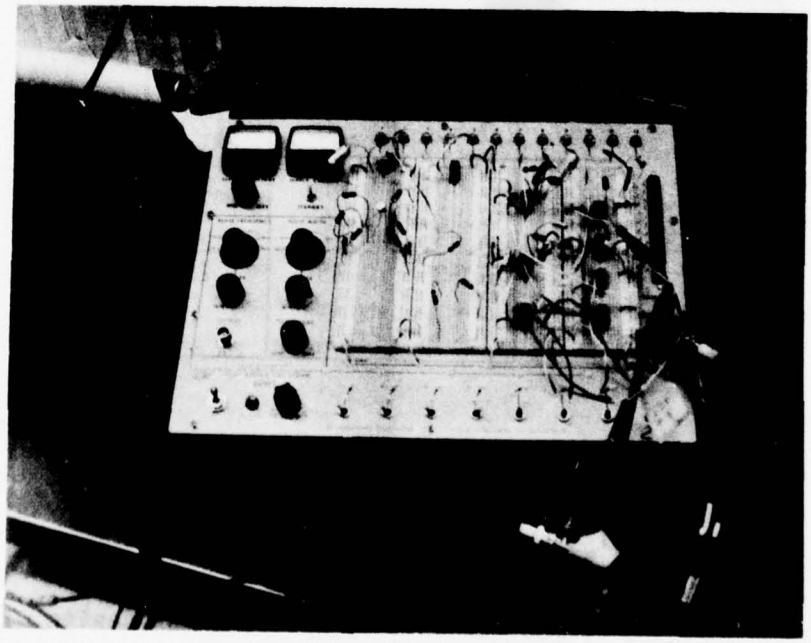

Figure 45. DBN breadboard

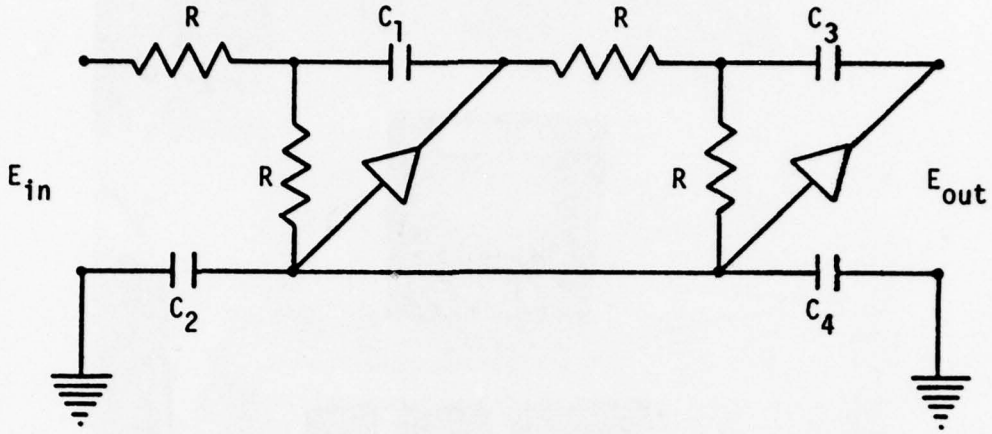

CHANNEL	R	C_1	C_2	C_3	C_4
1	5365	0.508	0.435	1.229	0.180
2	5365	0.508	0.435	1.229	0.180
3	5365	0.508	0.435	1.229	0.180
4	5365	0.508	0.435	1.229	0.180
5	5200	0.525	0.449	1.268	0.186
6	5100	0.535	0.458	1.293	0.190
7	5100	0.535	0.458	1.293	0.190

Figure 46. Electronic low-pass filter design

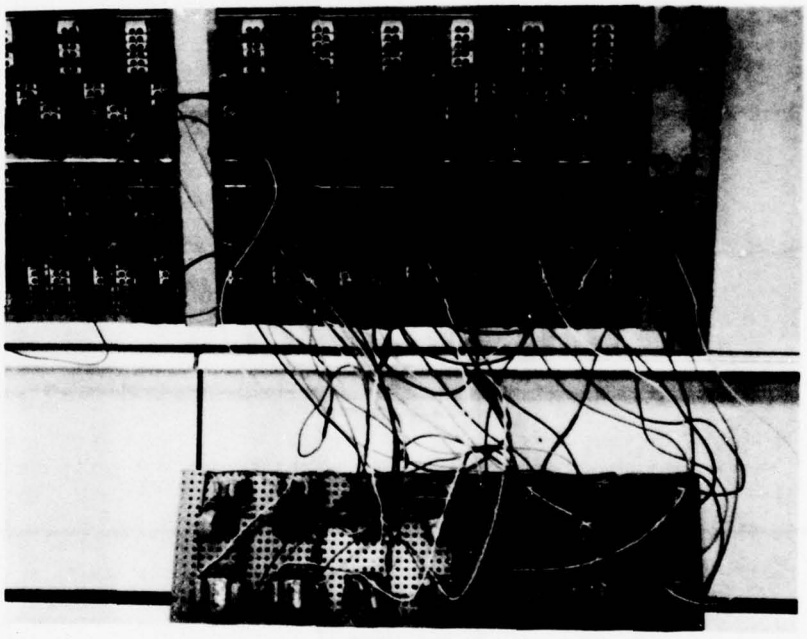

Figure 47. Electronic filter breadboard

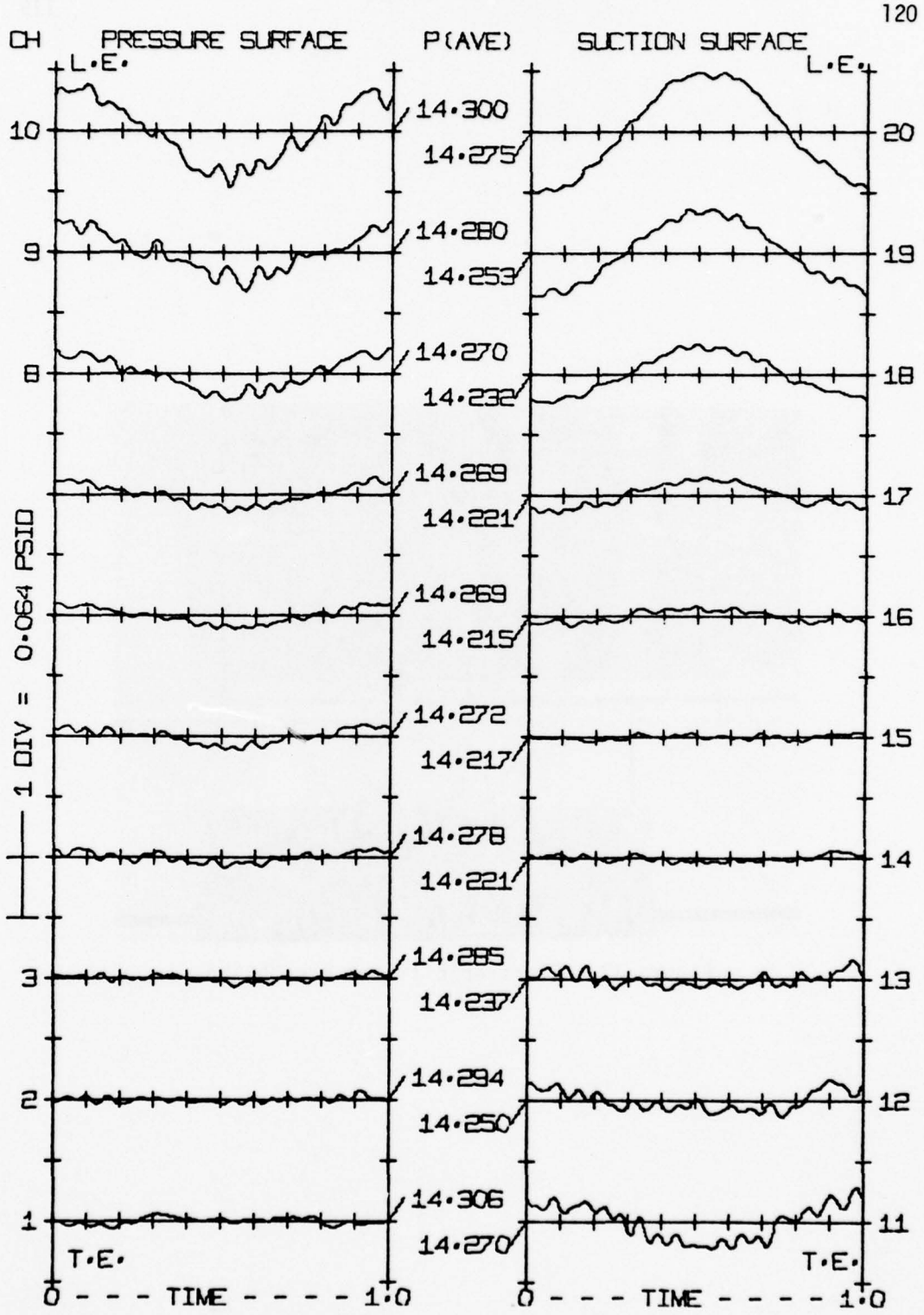

Figure 48. One cycle pressure data

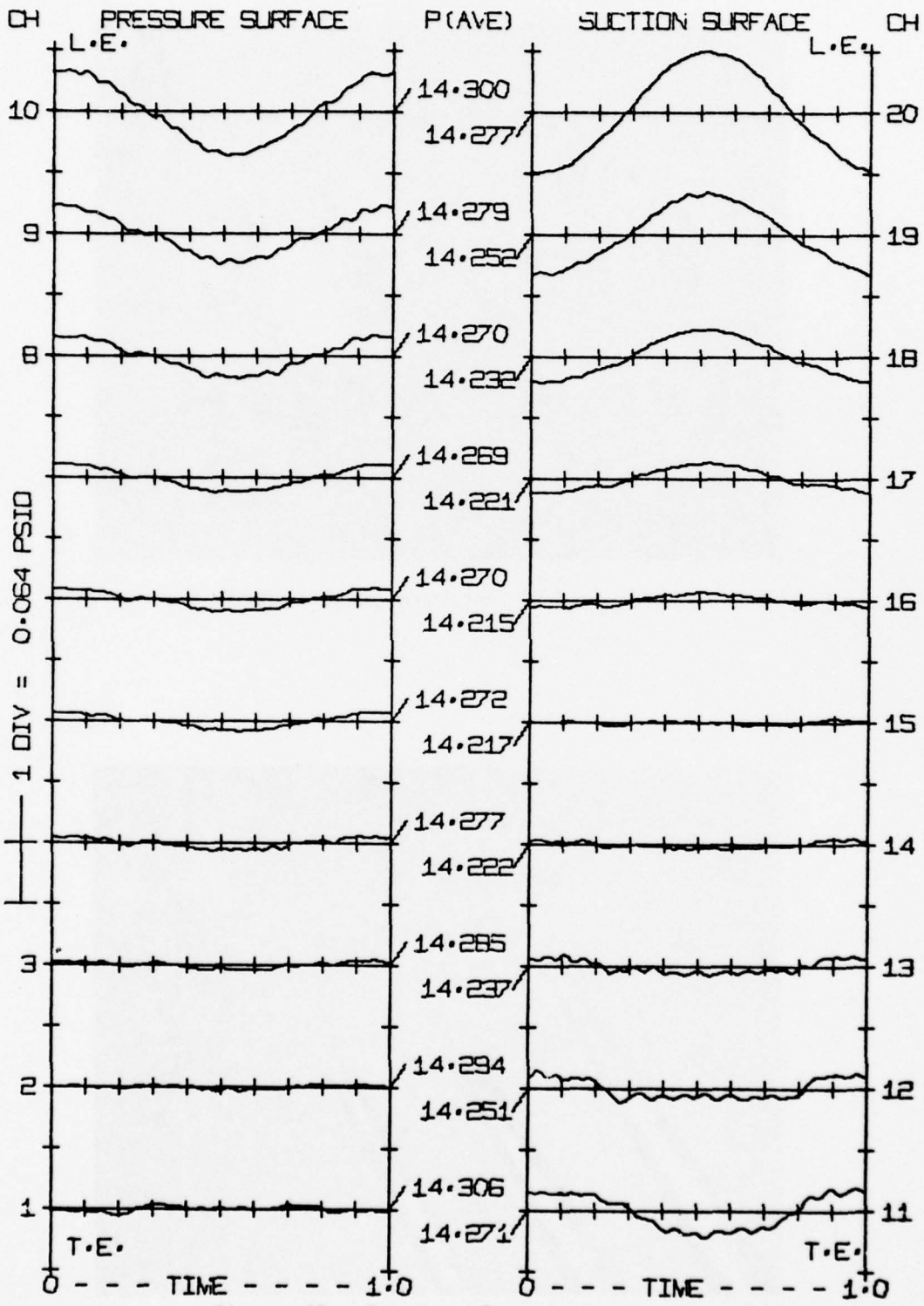

Figure 49. Eight cycle average pressure data

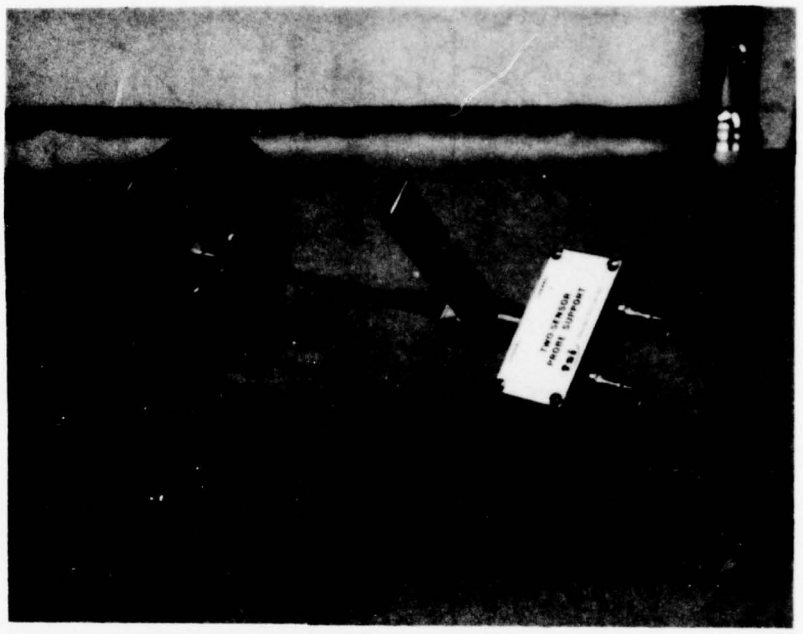

Figure 50. Hot wire probe support

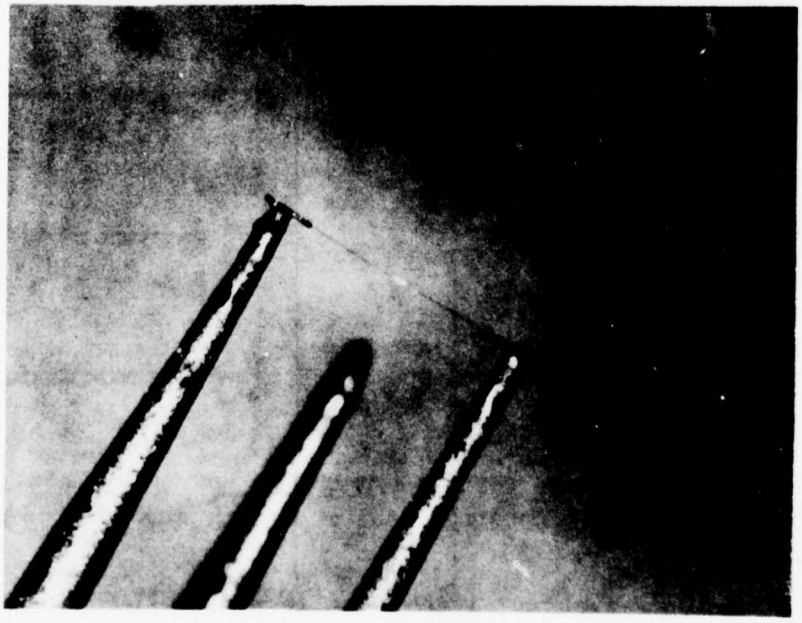

Figure 51. Clean hot wires

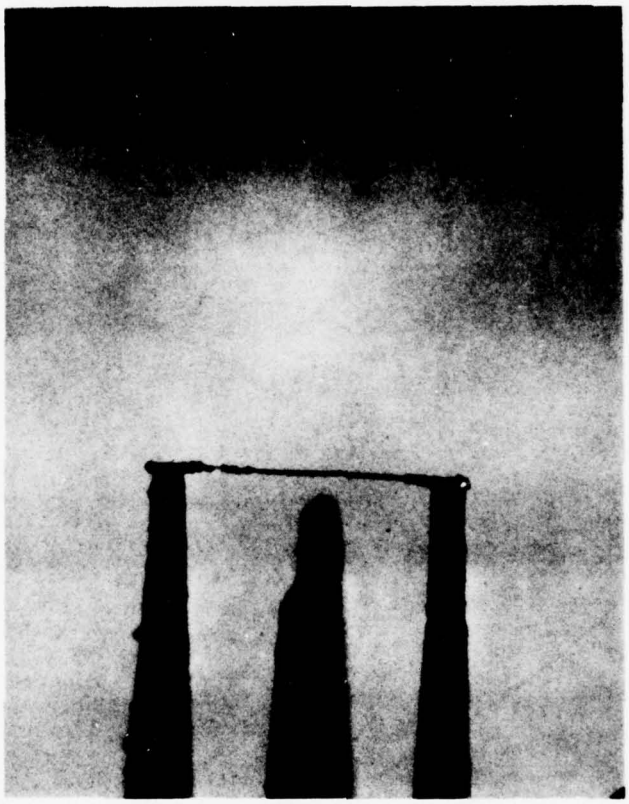

Figure 52. Dirty hot wires

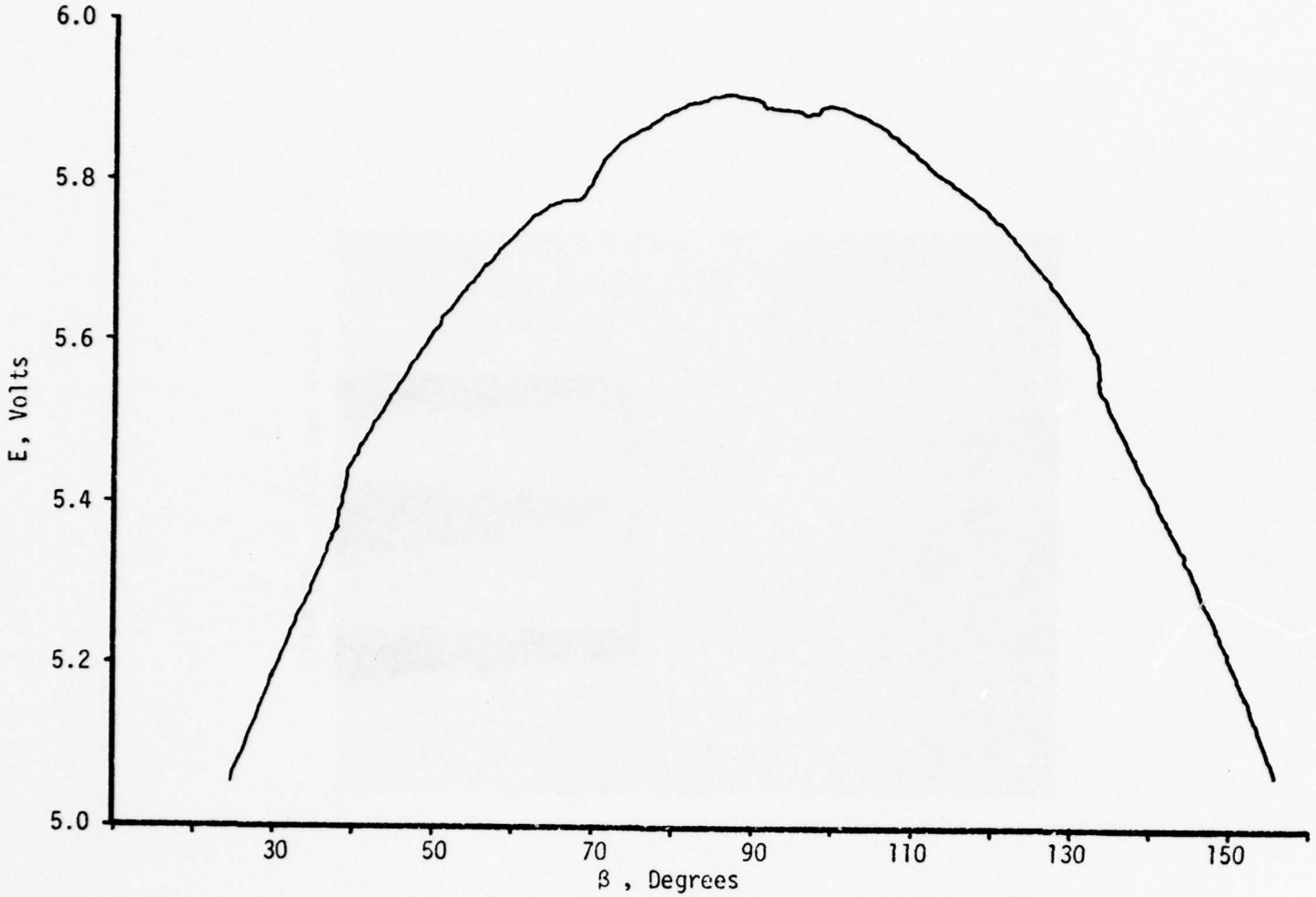

Figure 53. Hot film anemometer output versus flow angle, Channel 1

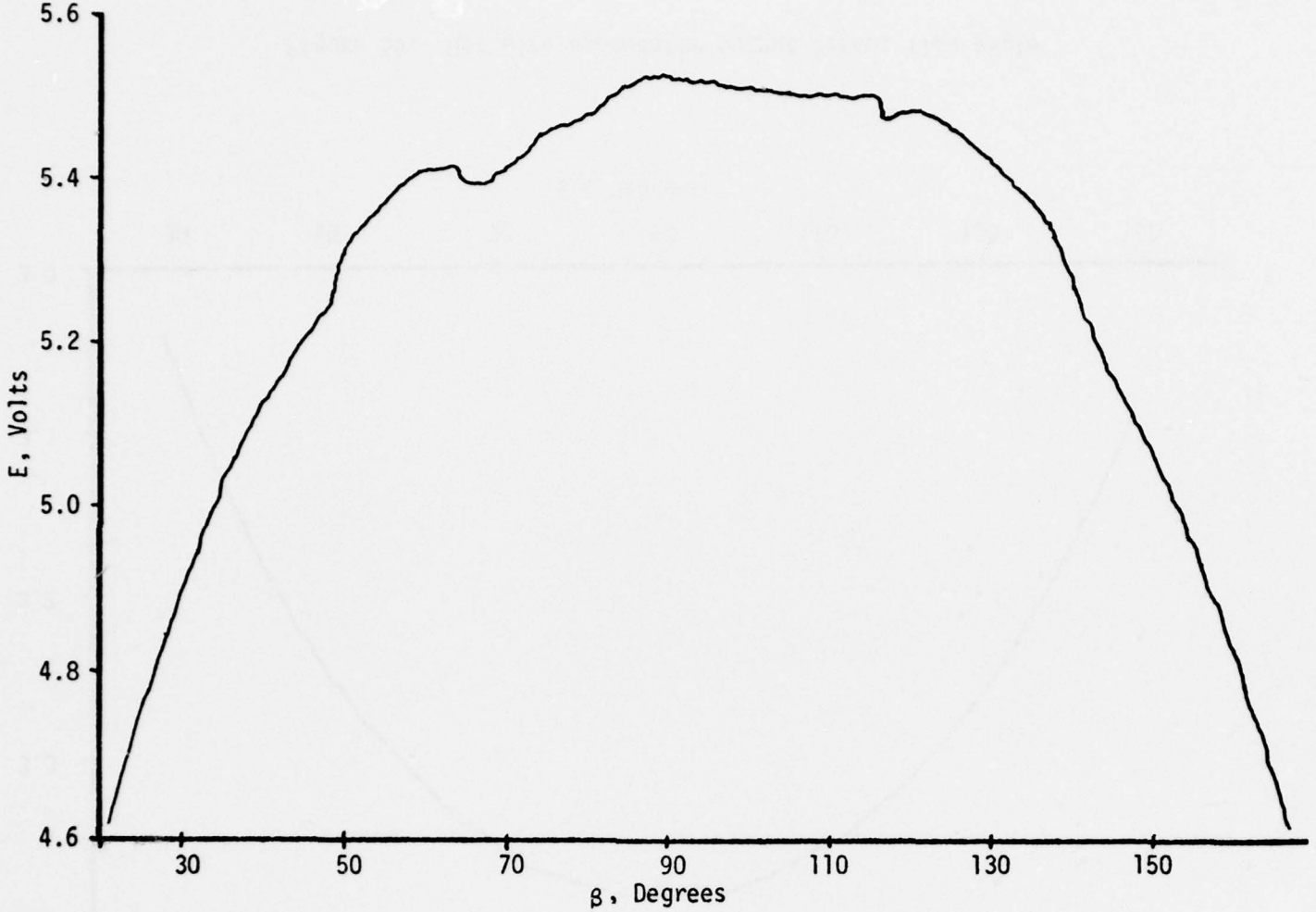

Figure 54. Hot film anemometer output versus flow angle, Channel 2

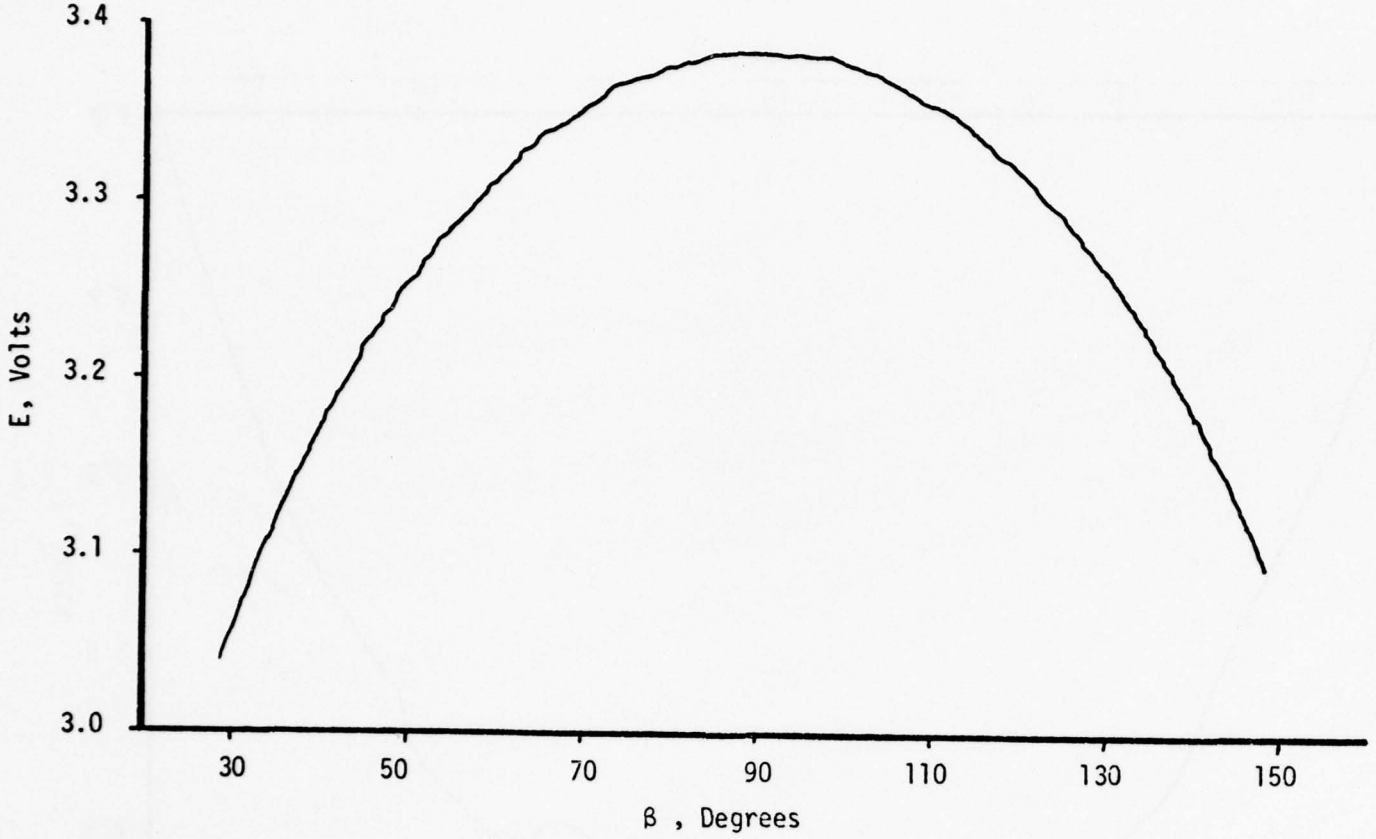

Figure 55. Hot wire anemometer output versus flow angle

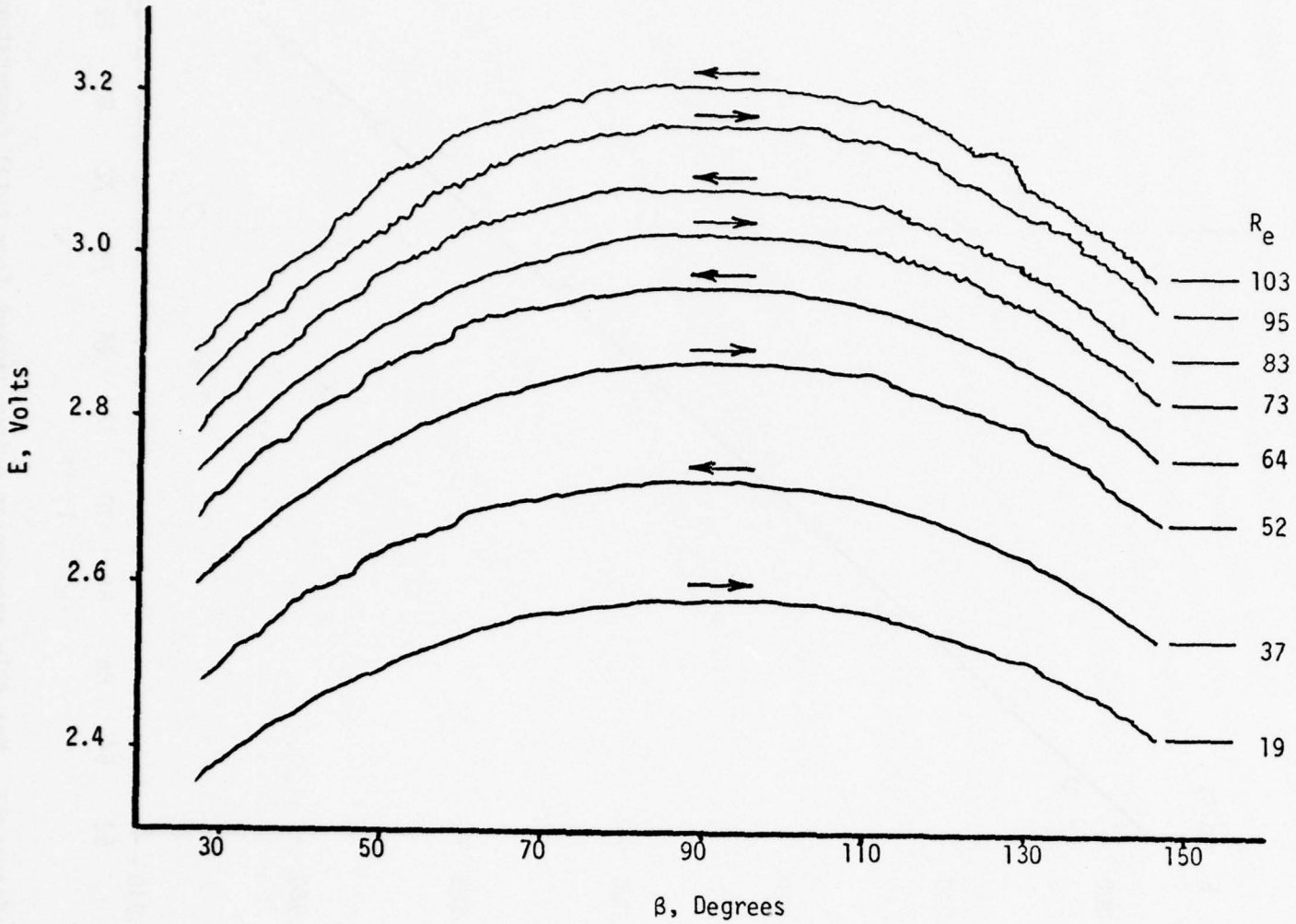

Figure 56. Hot film anemometer output versus flow angle and Reynolds Number

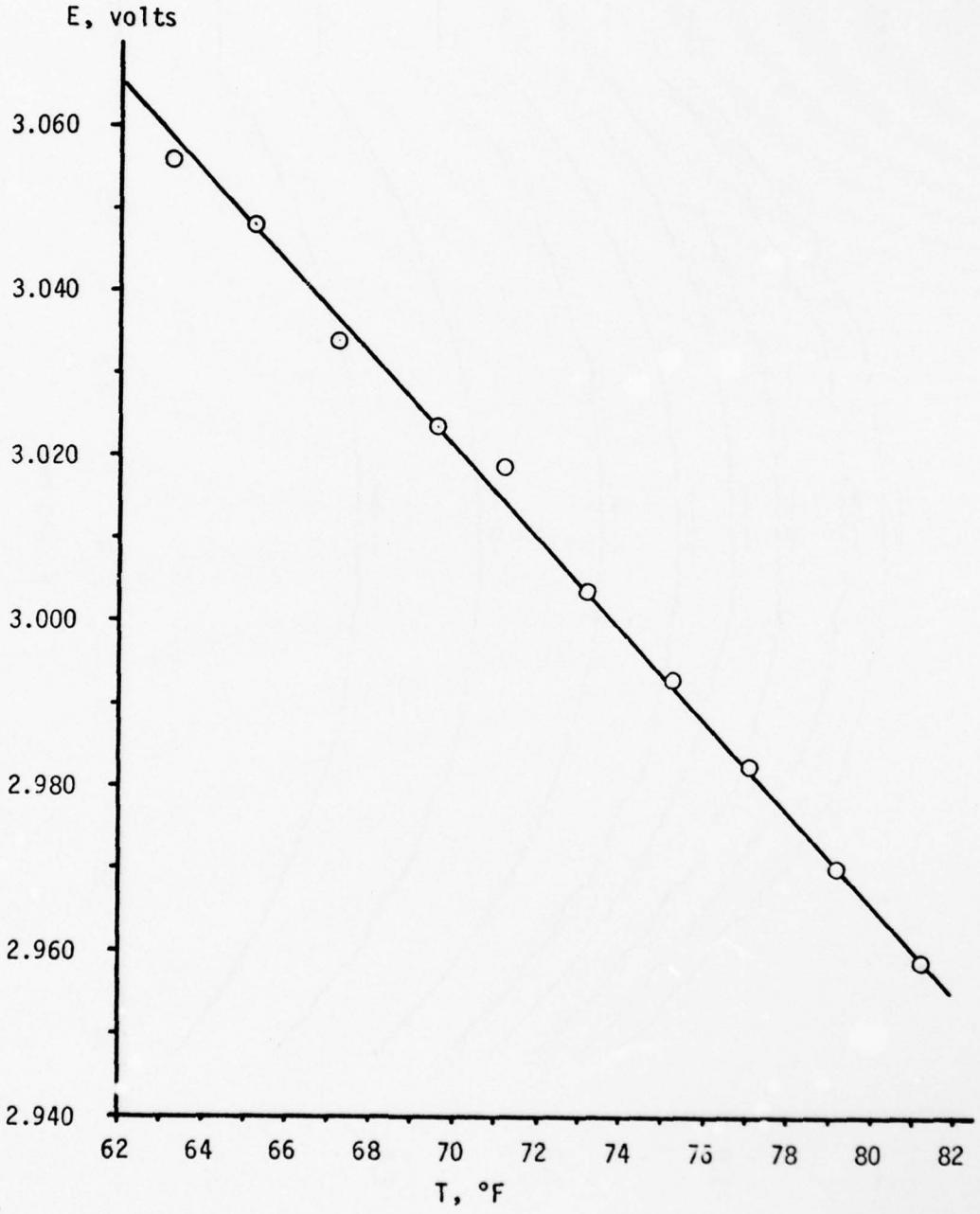

Figure 57. Hot film anemometer output versus flow total temperature

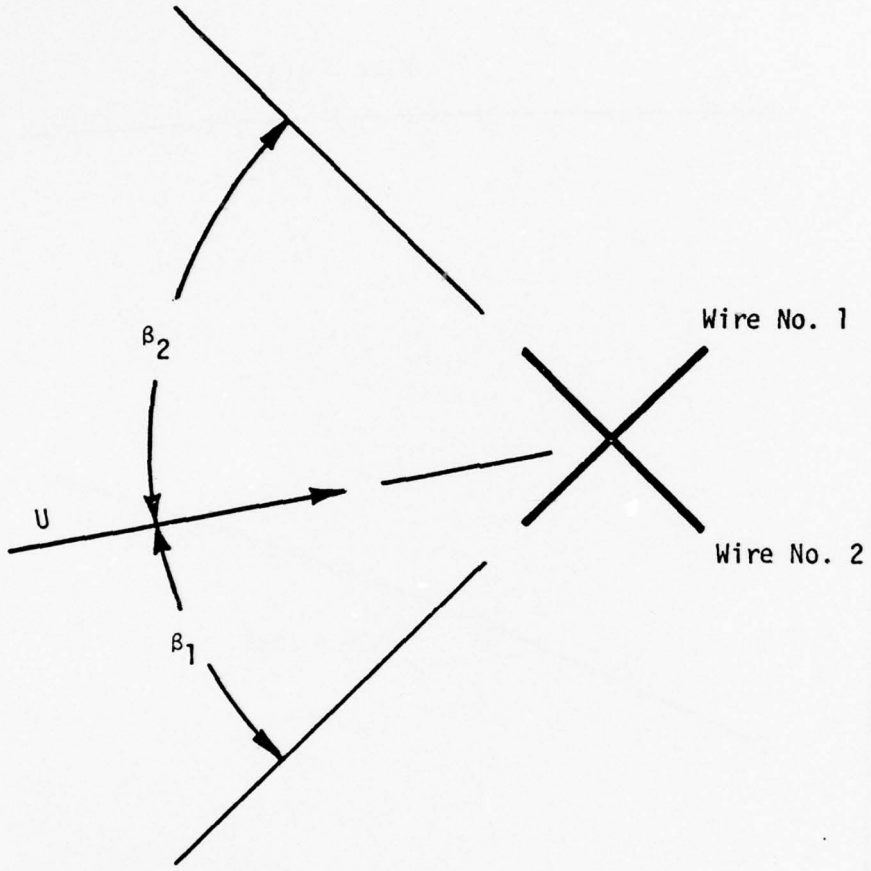

Figure 58. Hot wire angle definition

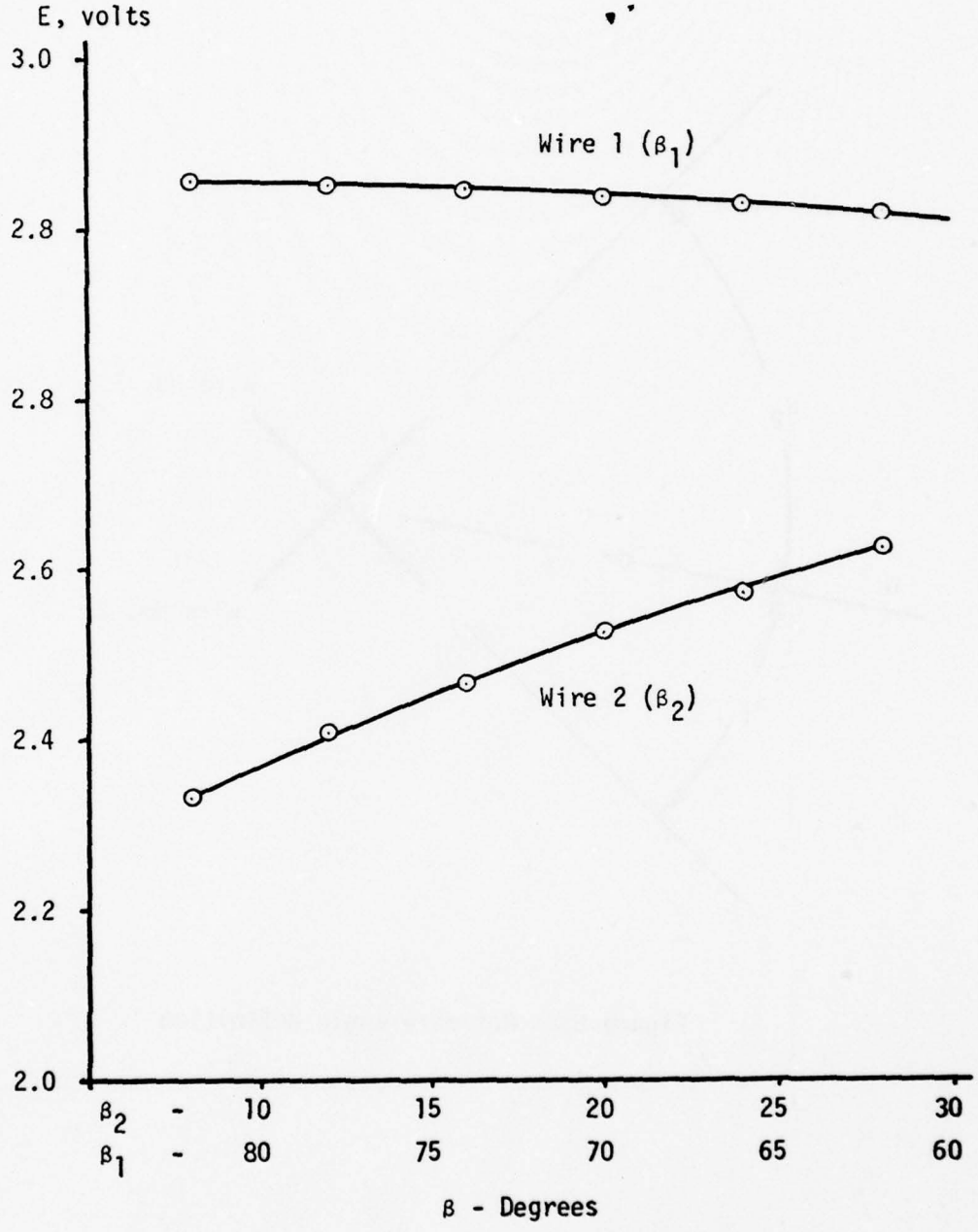

Figure 59. Hot wire anemometer output versus flow angle calibration

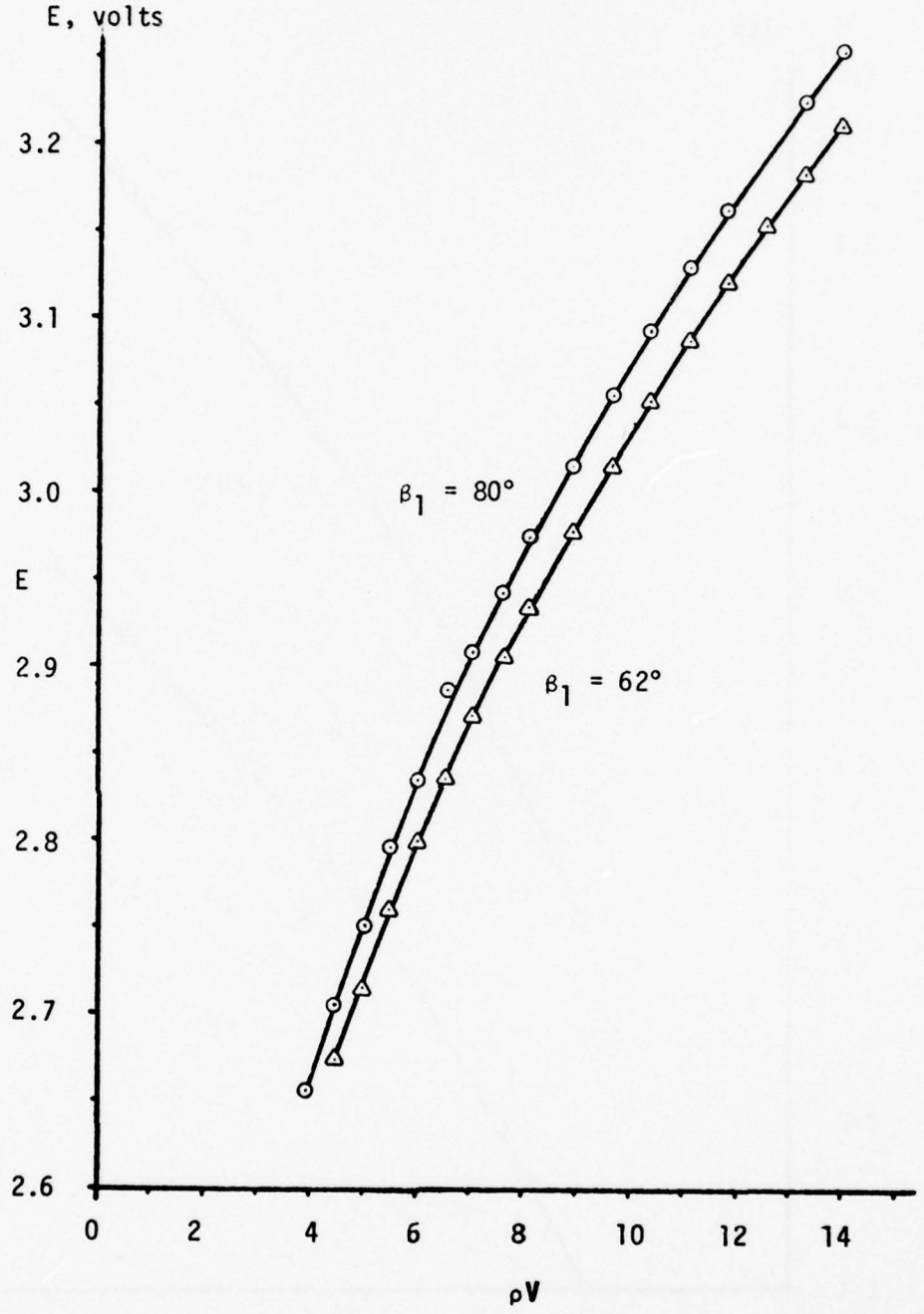

Figure 60. Hot wire anemometer output versus mass flow calibration, Channel 1

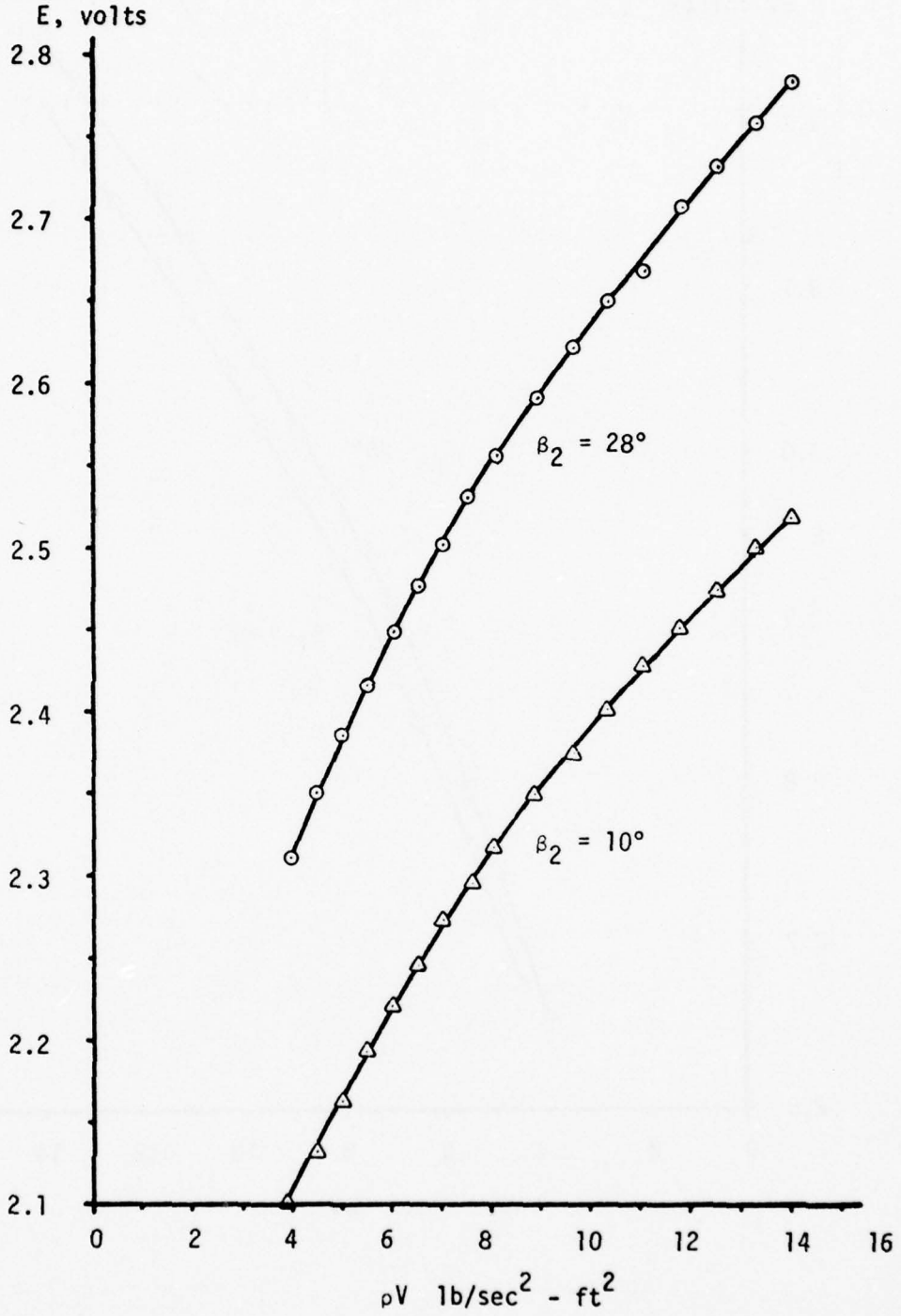

Figure 61. Hot wire anemometer output versus mass flow calibration, Channel 2

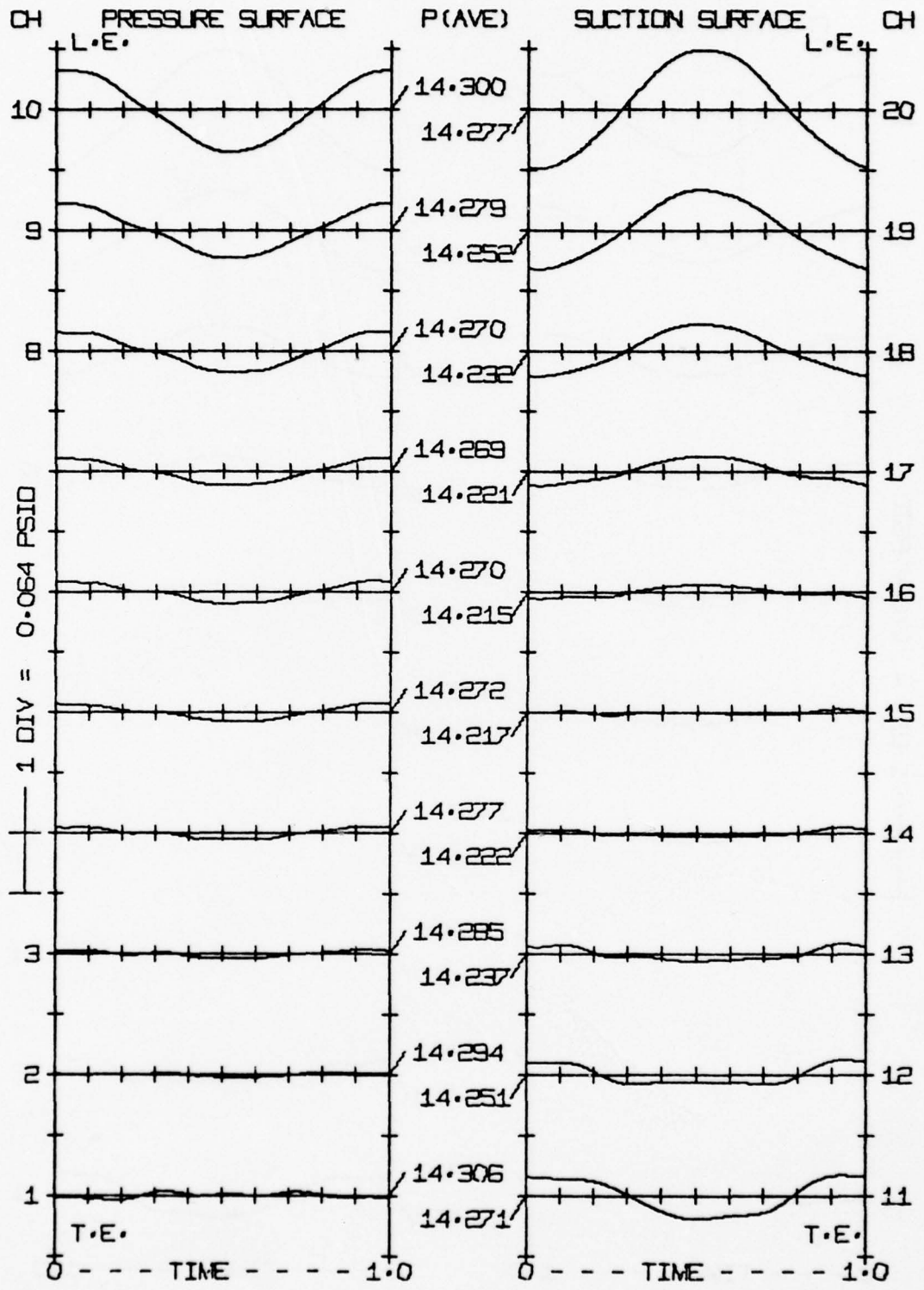

Figure 62. Pressure data using 5-terms of Fourier series

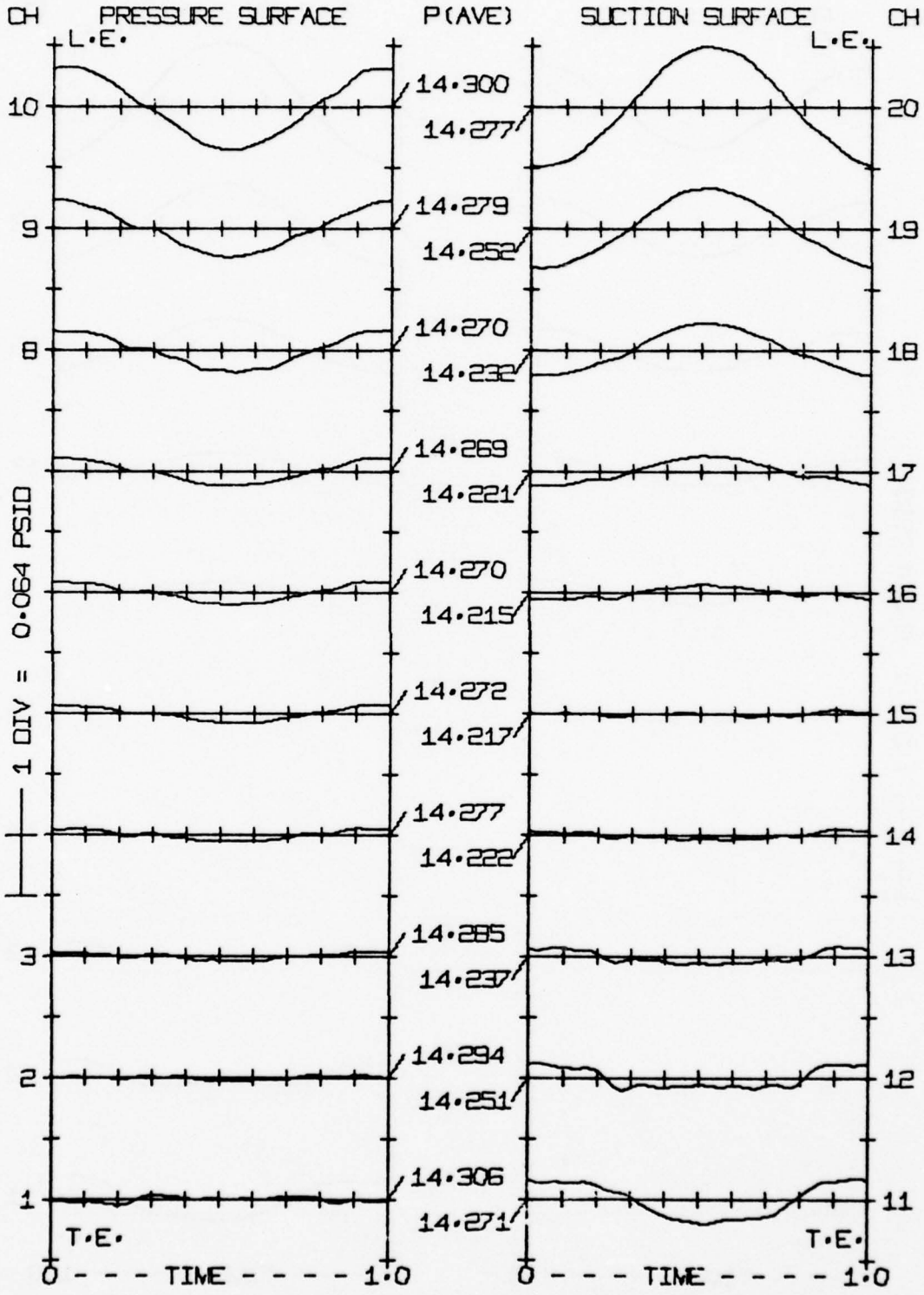

Figure 63. Pressure data using 10-terms of Fourier series

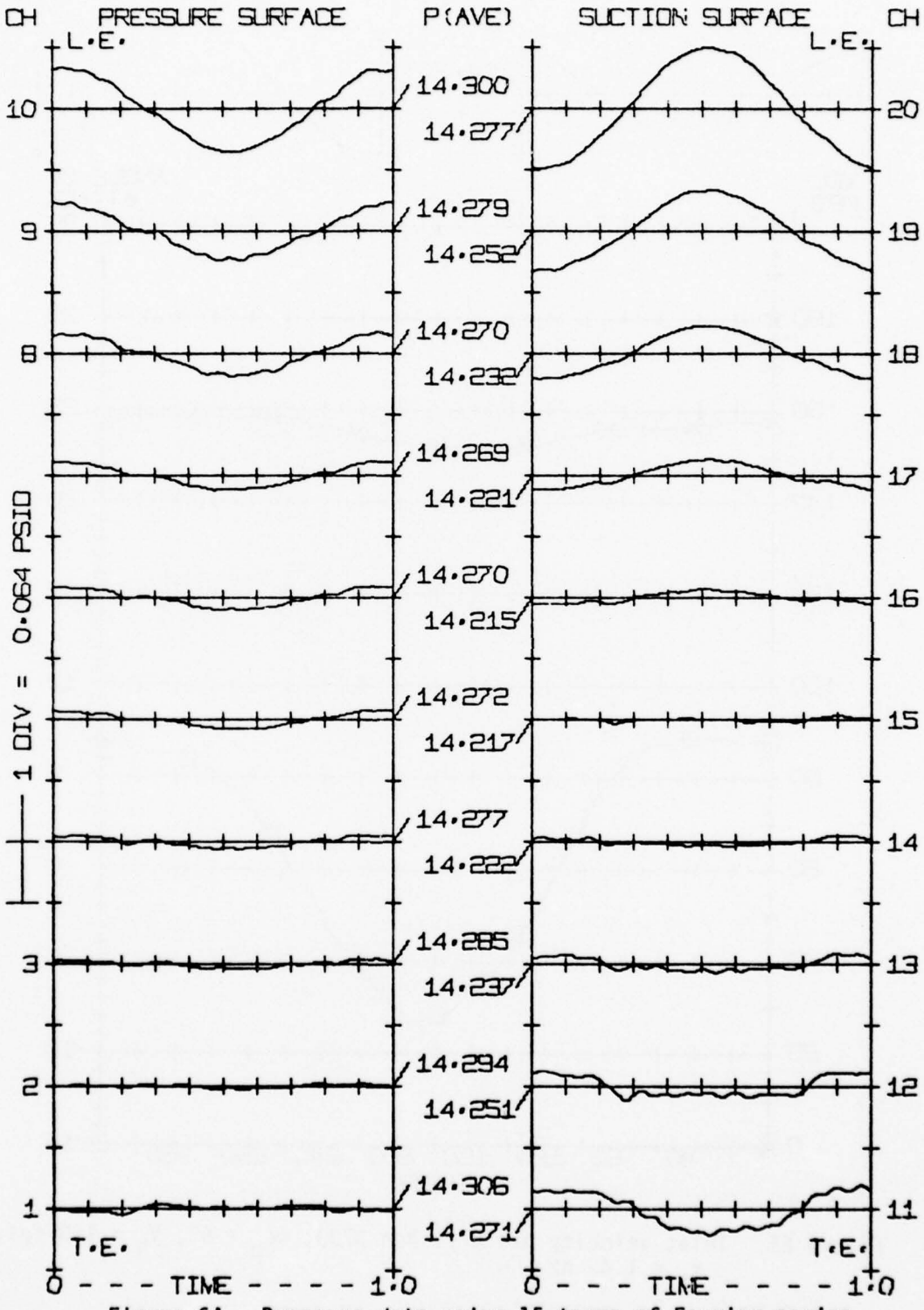

Figure 64. Pressure data using 15-terms of Fourier series

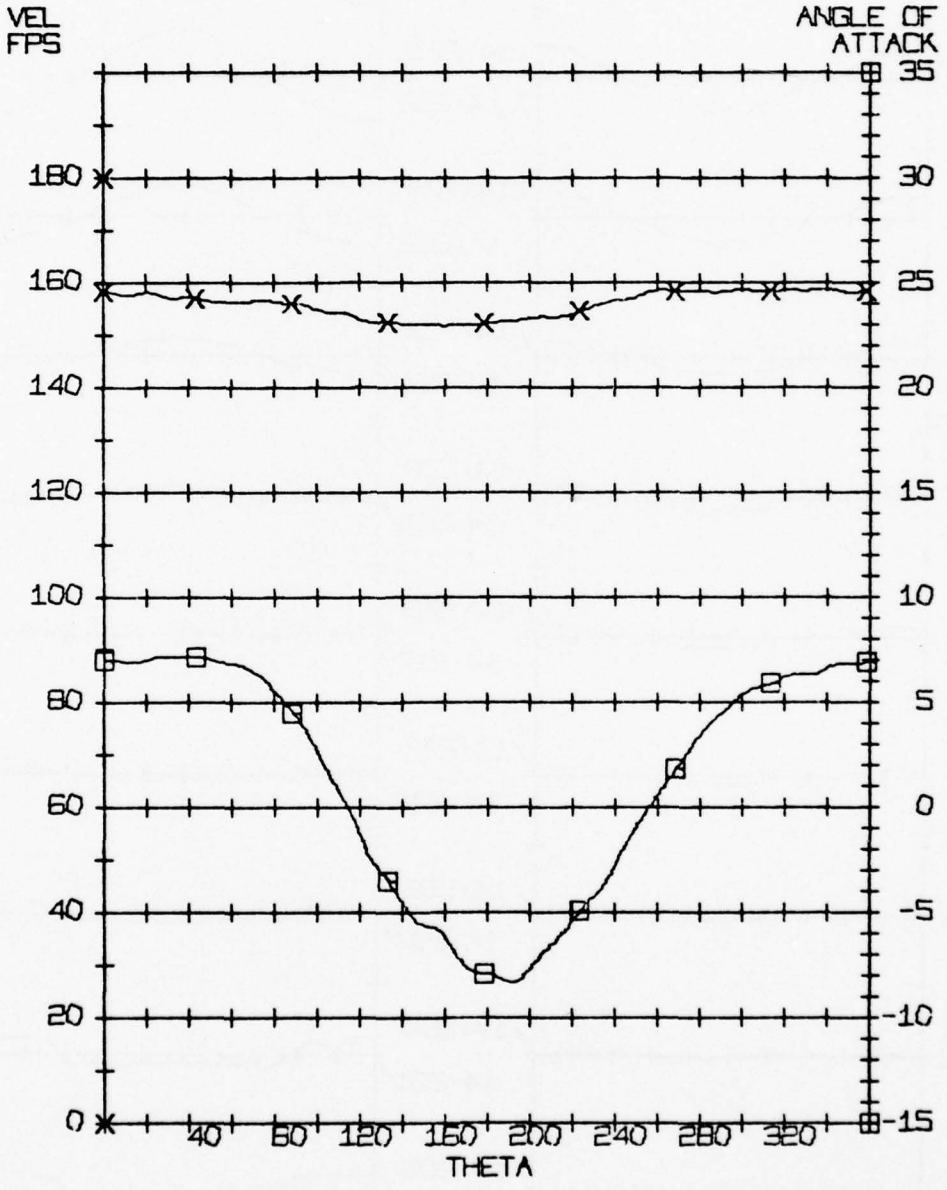

Figure 65. Inlet velocity history, Run 3730, α_m = 6°, V_N = 150 fps, f_t = 1.43 hz

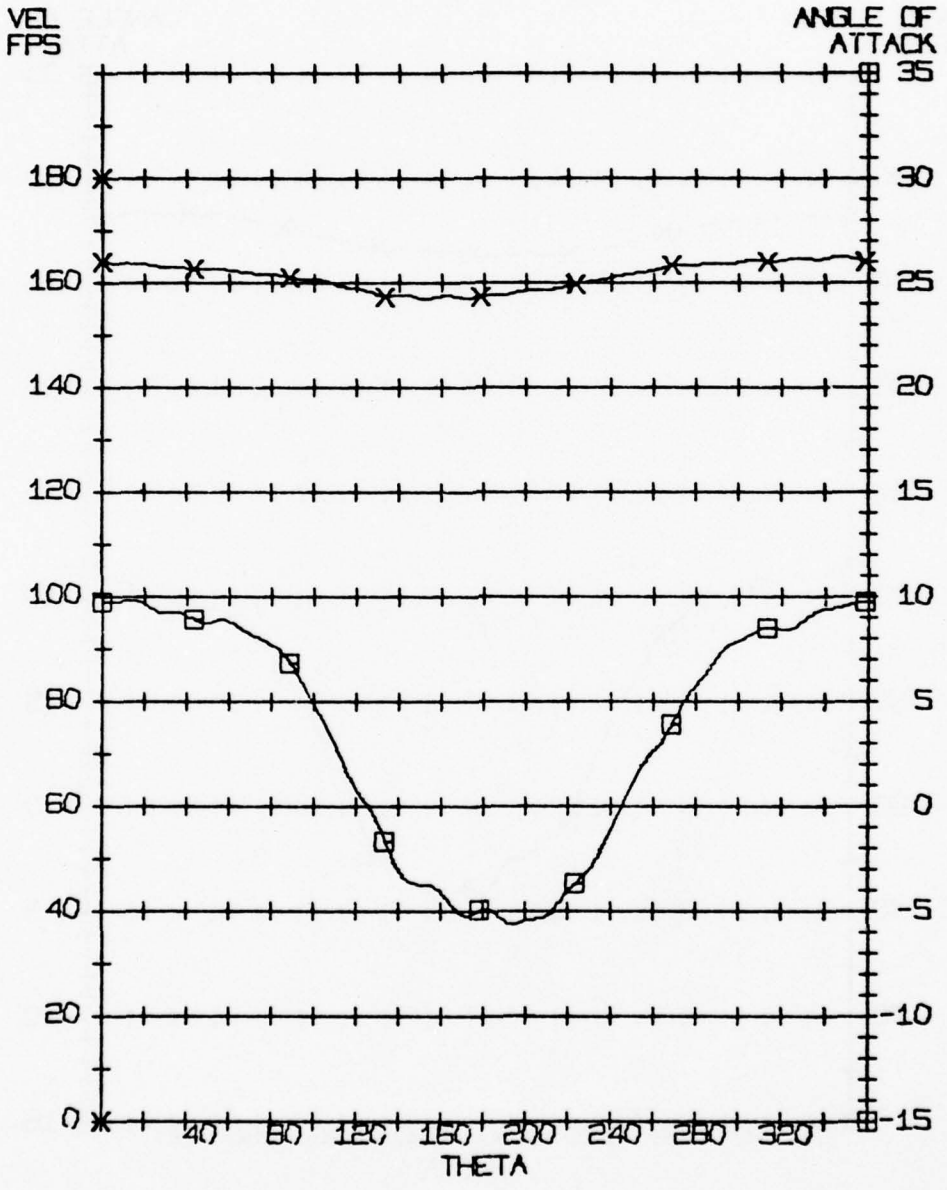

Figure 66. Inlet velocity history, Run 3850, α_m = 8°, V_N = 150 fps, f_t = 1.43 hz

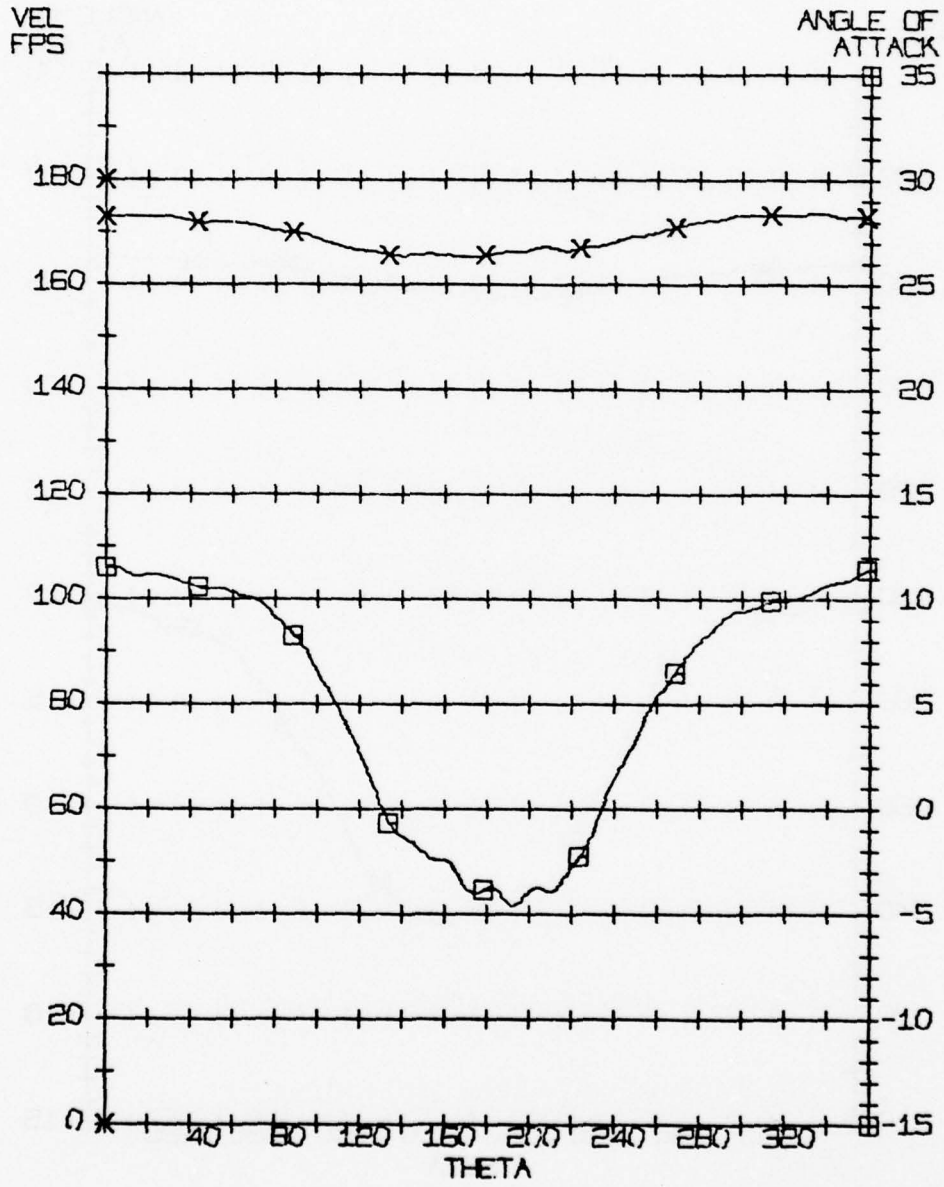

Figure 67. Inlet velocity history, Run 3970, α_m = 10°, V_N = 150 fps, f_t = 1.43 hz

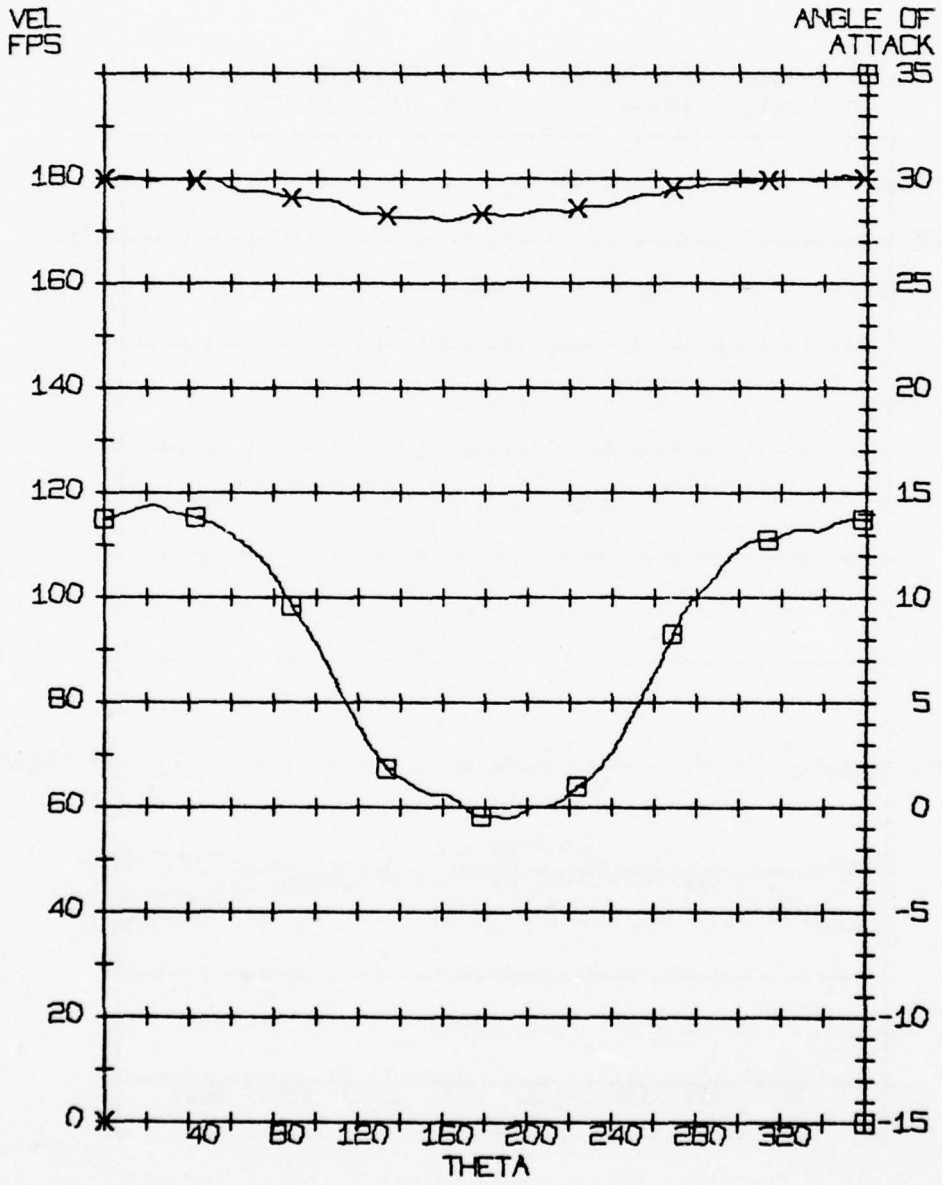

Figure 68. Inlet velocity history, Run 4060, α_m = 12°, V_N = 150 fps, f_t = 1.43 hz

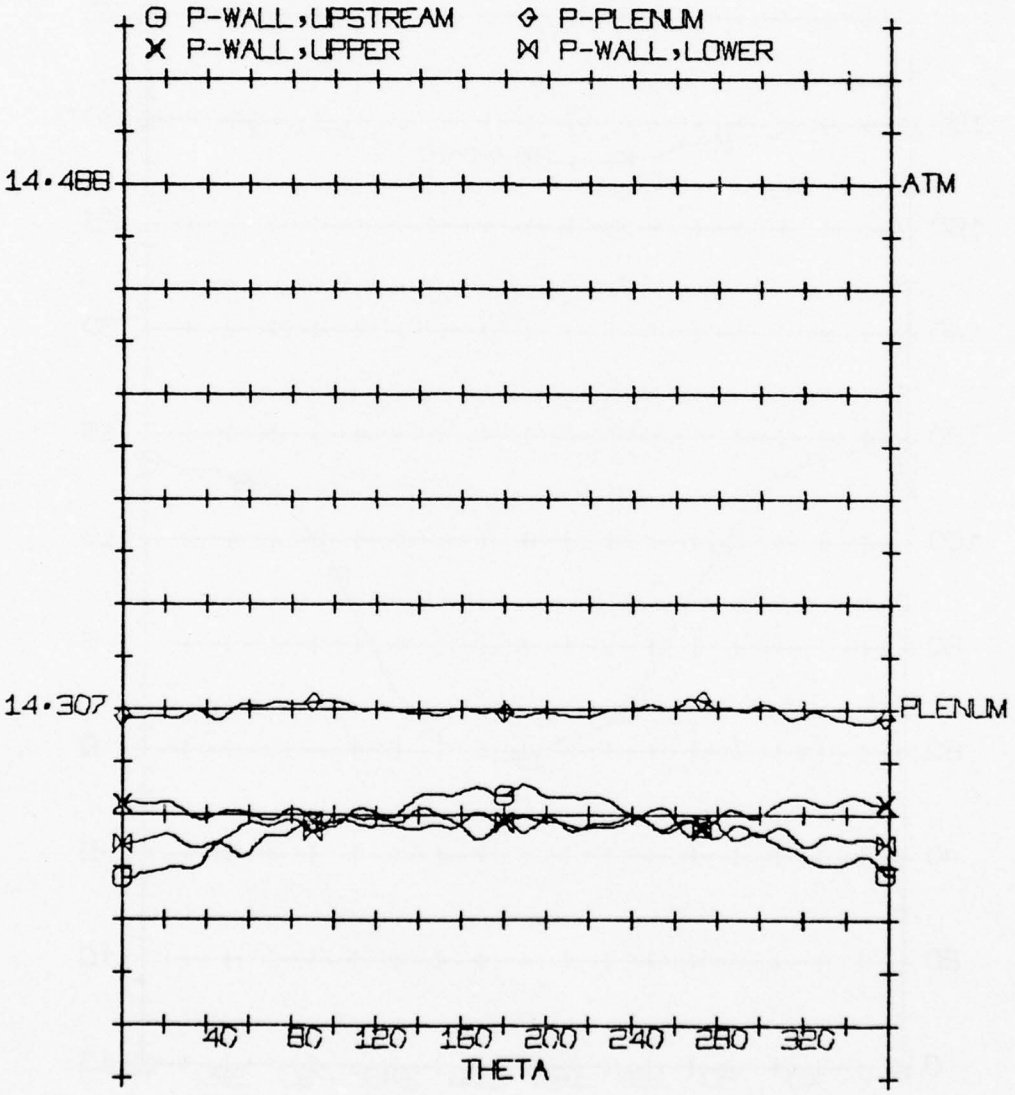

Figure 69. Inlet pressure history, Run 7490, α_m = 10°, V_N = 150 fps, f_t = 0.2 hz

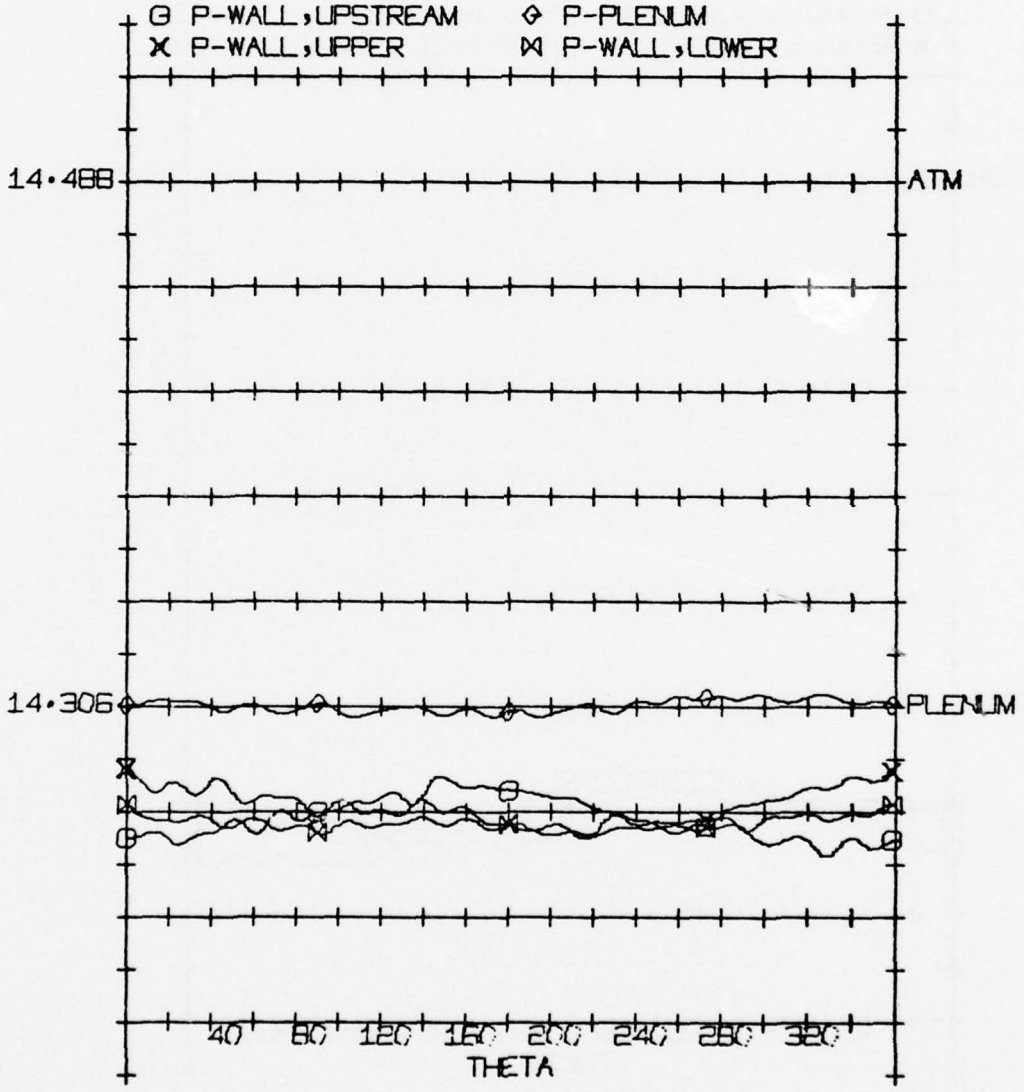

Figure 70. Inlet pressure history, Run 7520, α_m = 10°, V_N = 150 fps, f_t = 6.14 hz

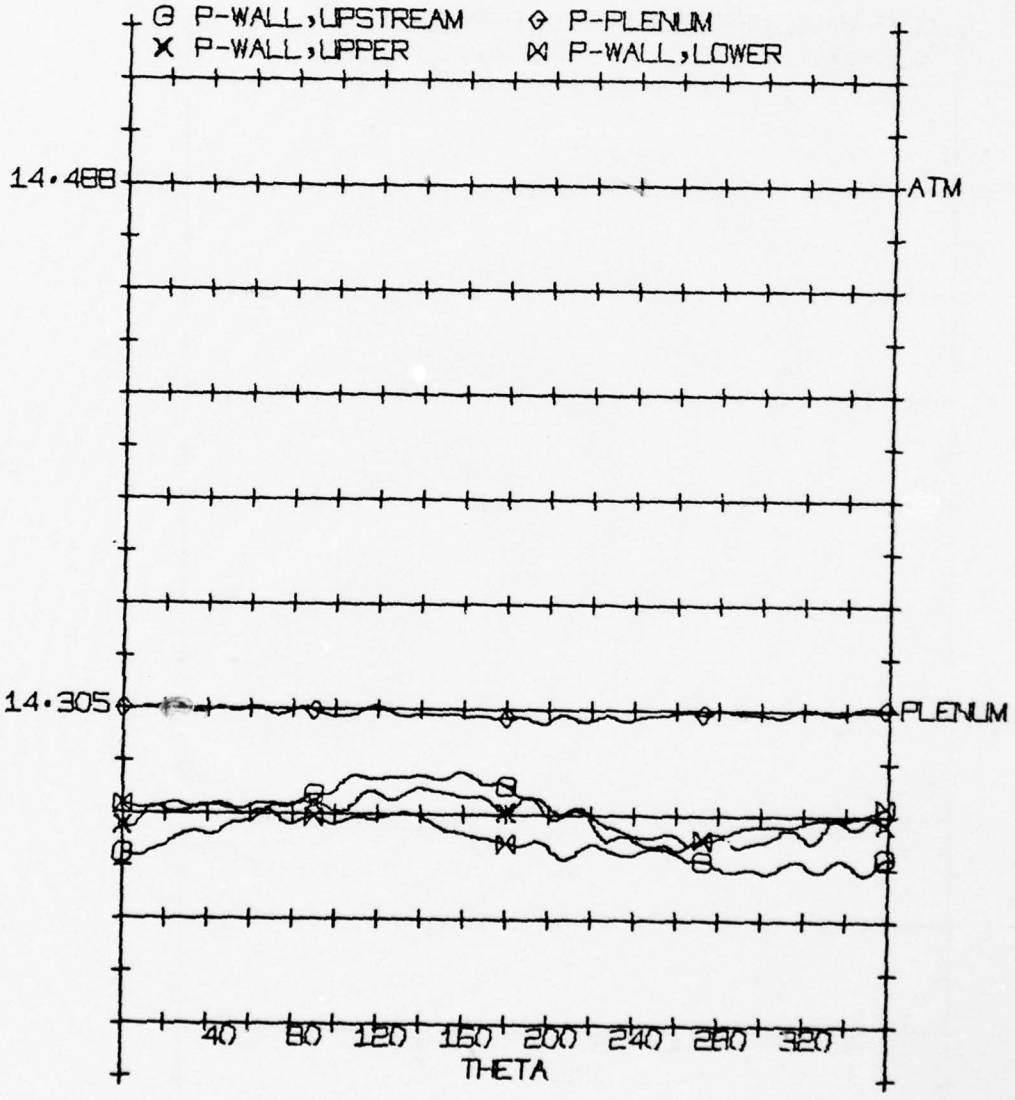

Figure 71. Inlet pressure history, Run 7570, α_m = 10°, V_N = 150 fps, f_t = 16.21 hz

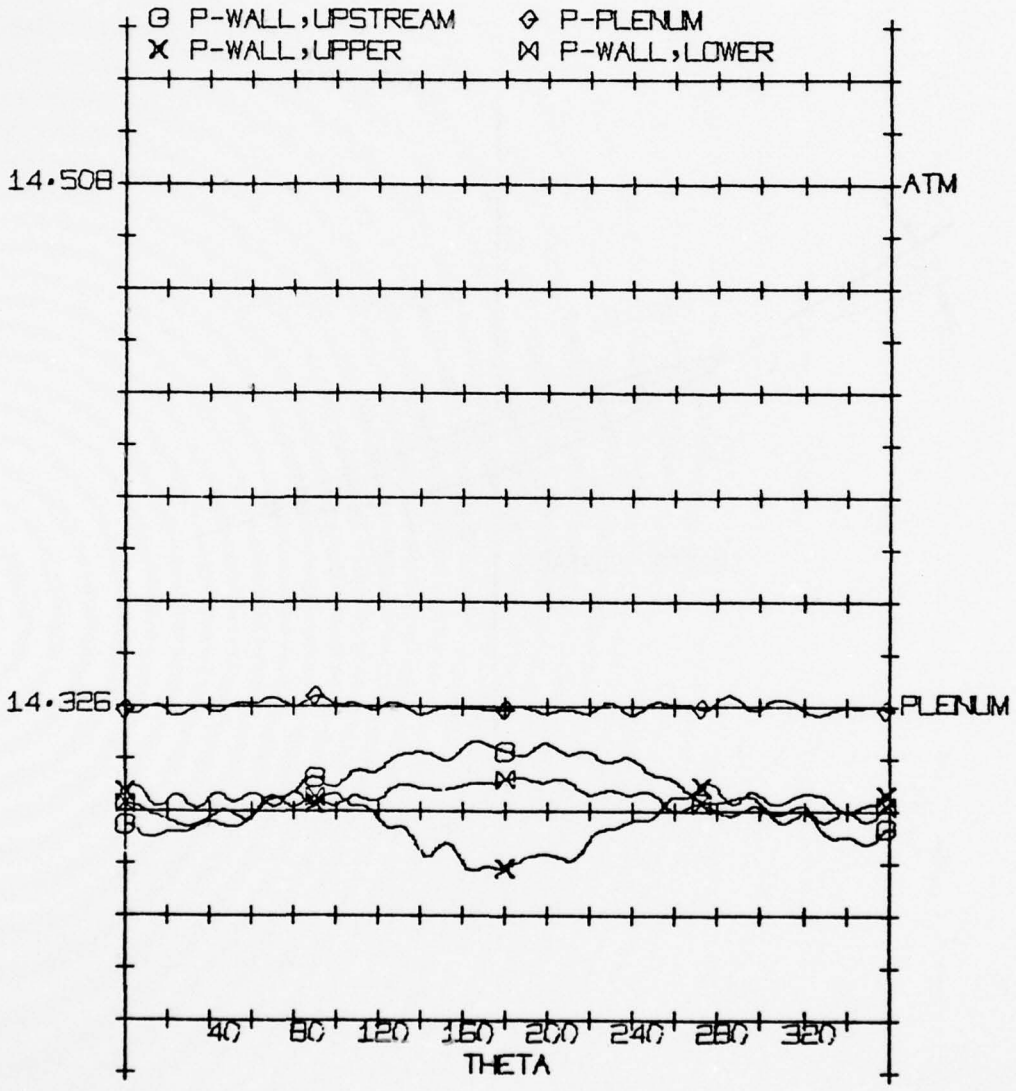

Figure 72. Inlet pressure history, Run 7020, α_m = 6°, V_N = 150 fps, f_t = 0.2 hz

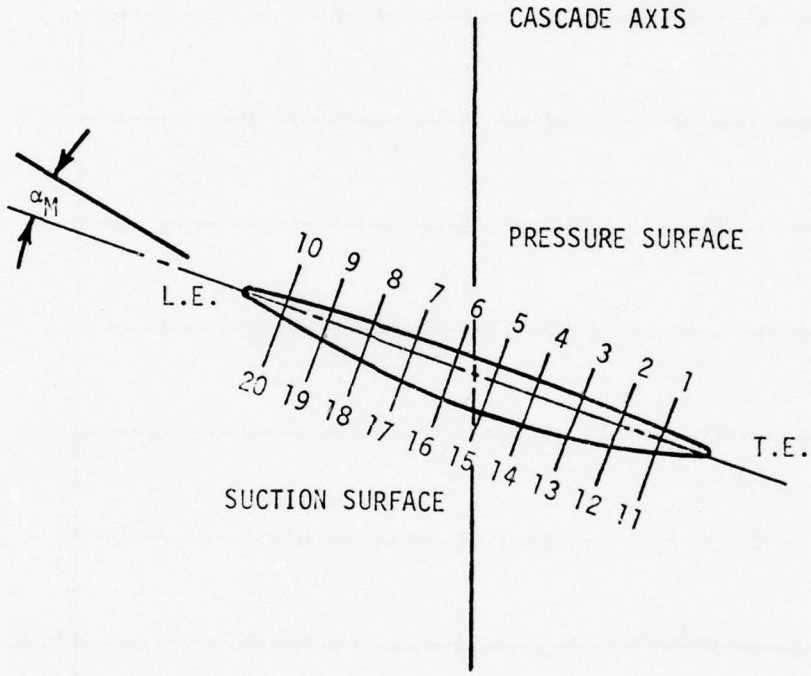

Figure 73. Airfoil pressure port designation

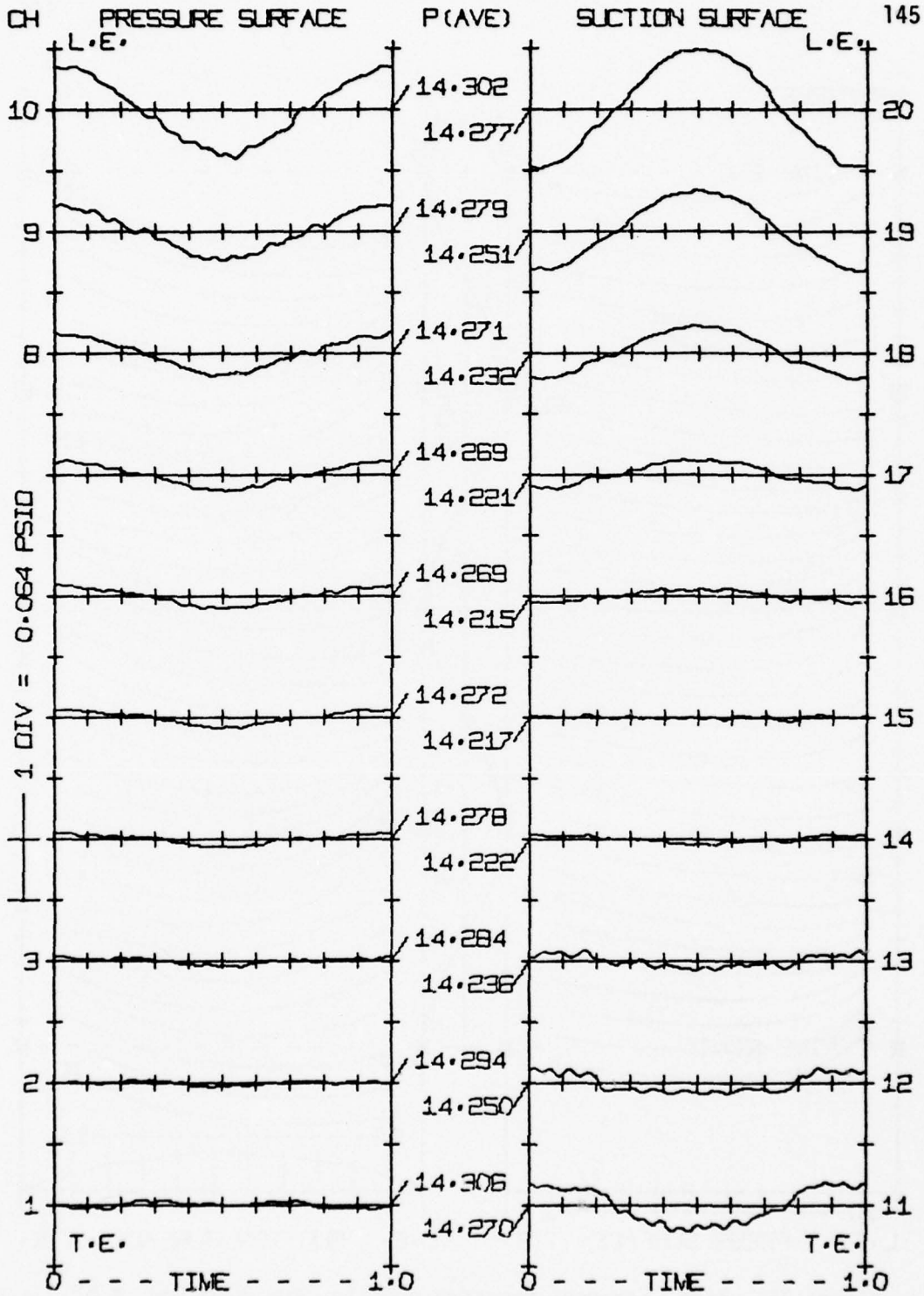

Figure 74. Airfoil pressure history, Run 7020, α_m = 6°, V_N = 150 fps, f_t = 0.2 hz

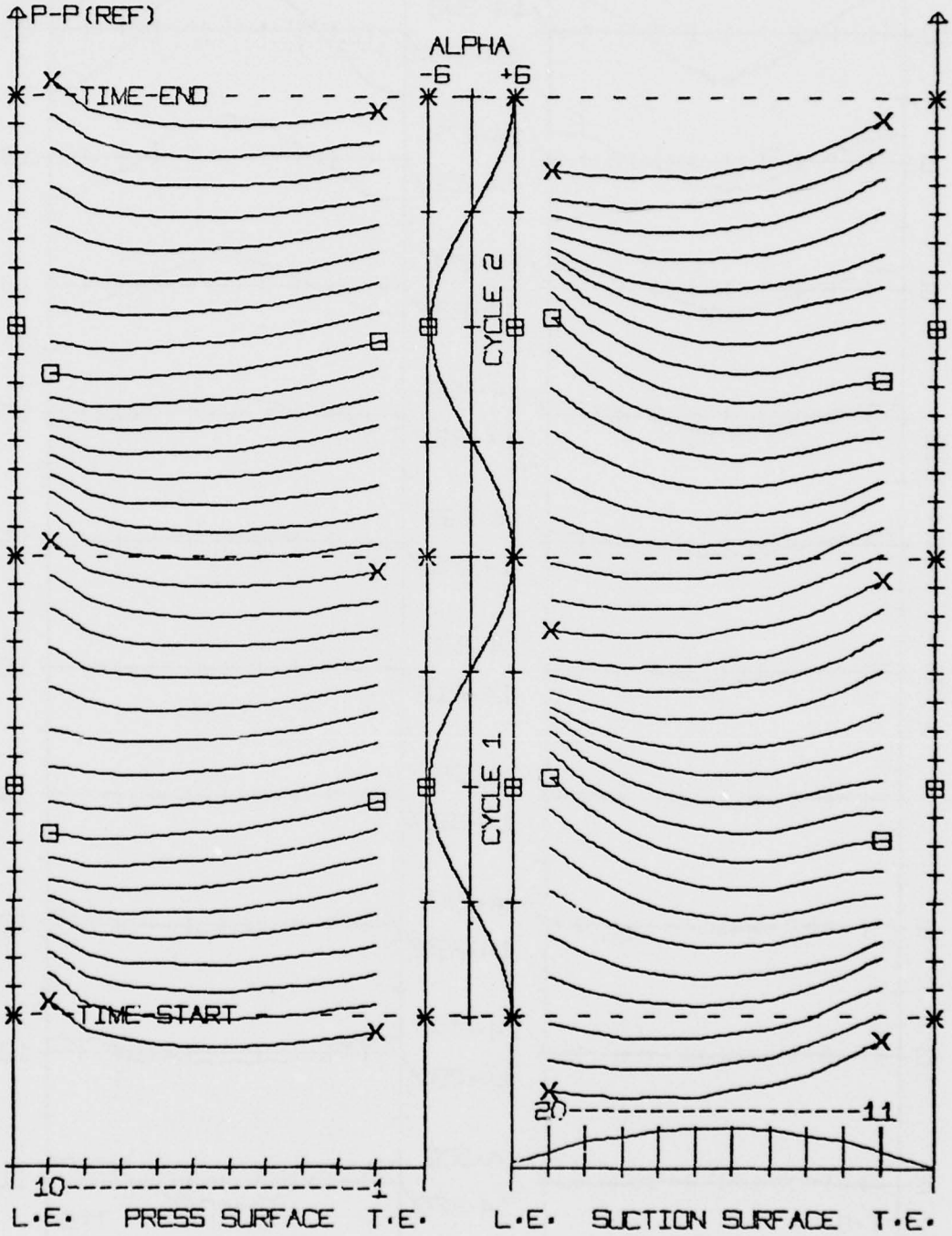

Figure 75. Time increment pressure profile, Run 7020, α_m = 6°, V_N = 150 fps, f_t = 0.2 hz

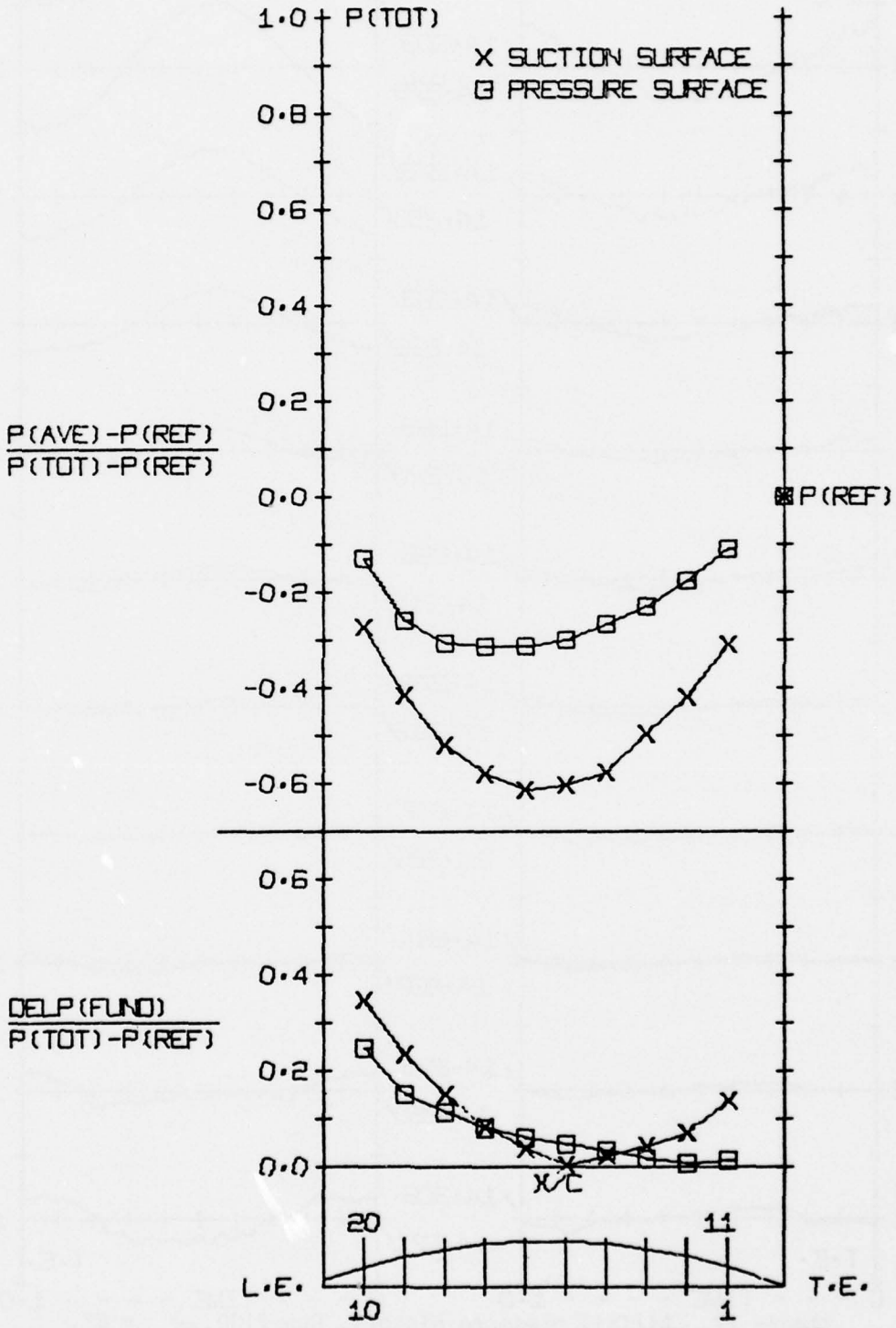

Figure 76. Normalized Pressure Profile, Run 7020, α_m = 6°, V_N = 150 fps, f_t = 0.2 hz

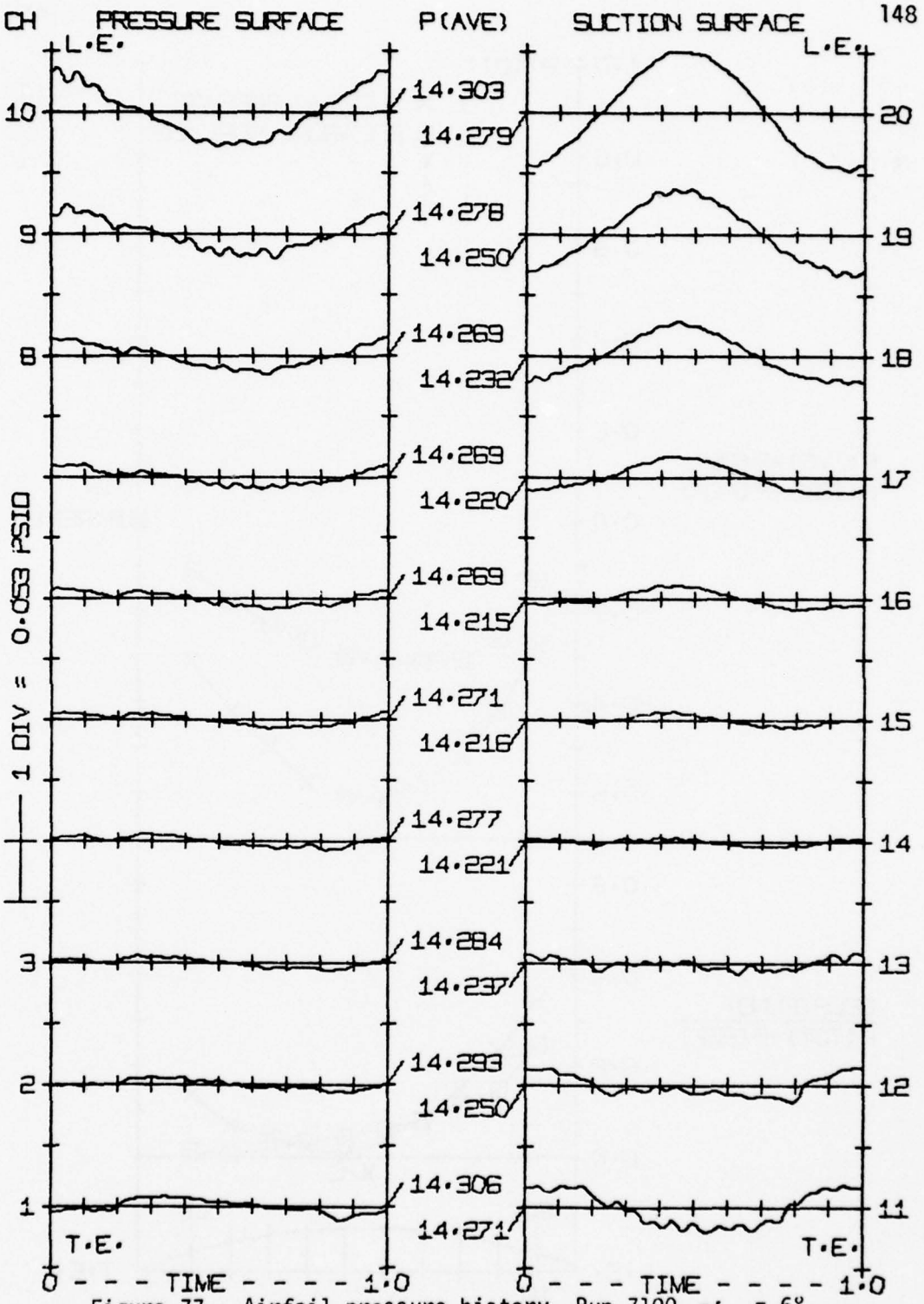

Figure 77. Airfoil pressure history, Run 7100, α_m = 6°, V_N = 150 fps, f_t = 16.2 hz

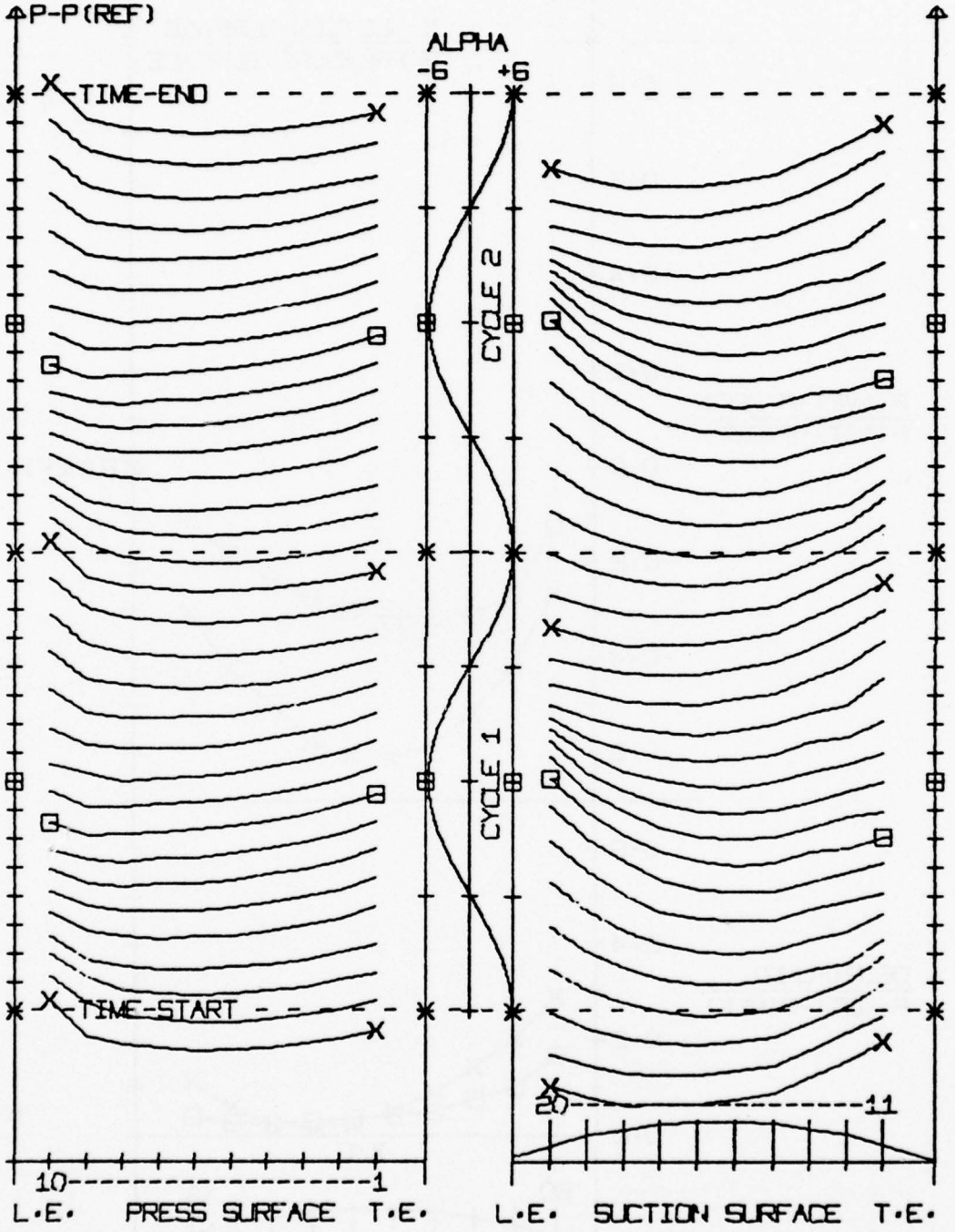

Figure 78. Time increment pressure profiles, Run 7100, α_m = 6°, V_N = 150 fps, f_t = 16.2 hz

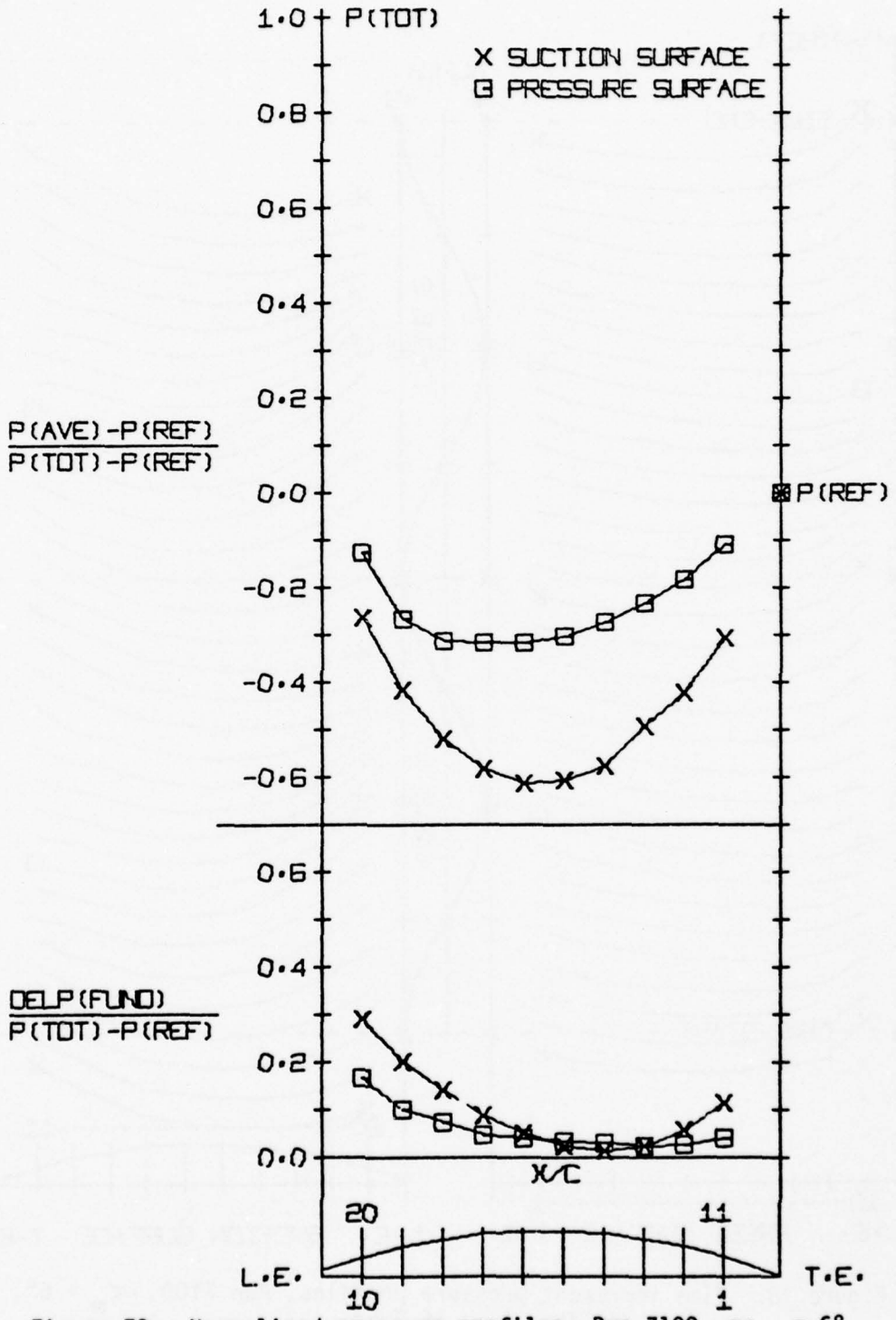

Figure 79. Normalized pressure profiles, Run 7100, α_m = 6°, V_N = 150 fps, f_t = 16.2 hz

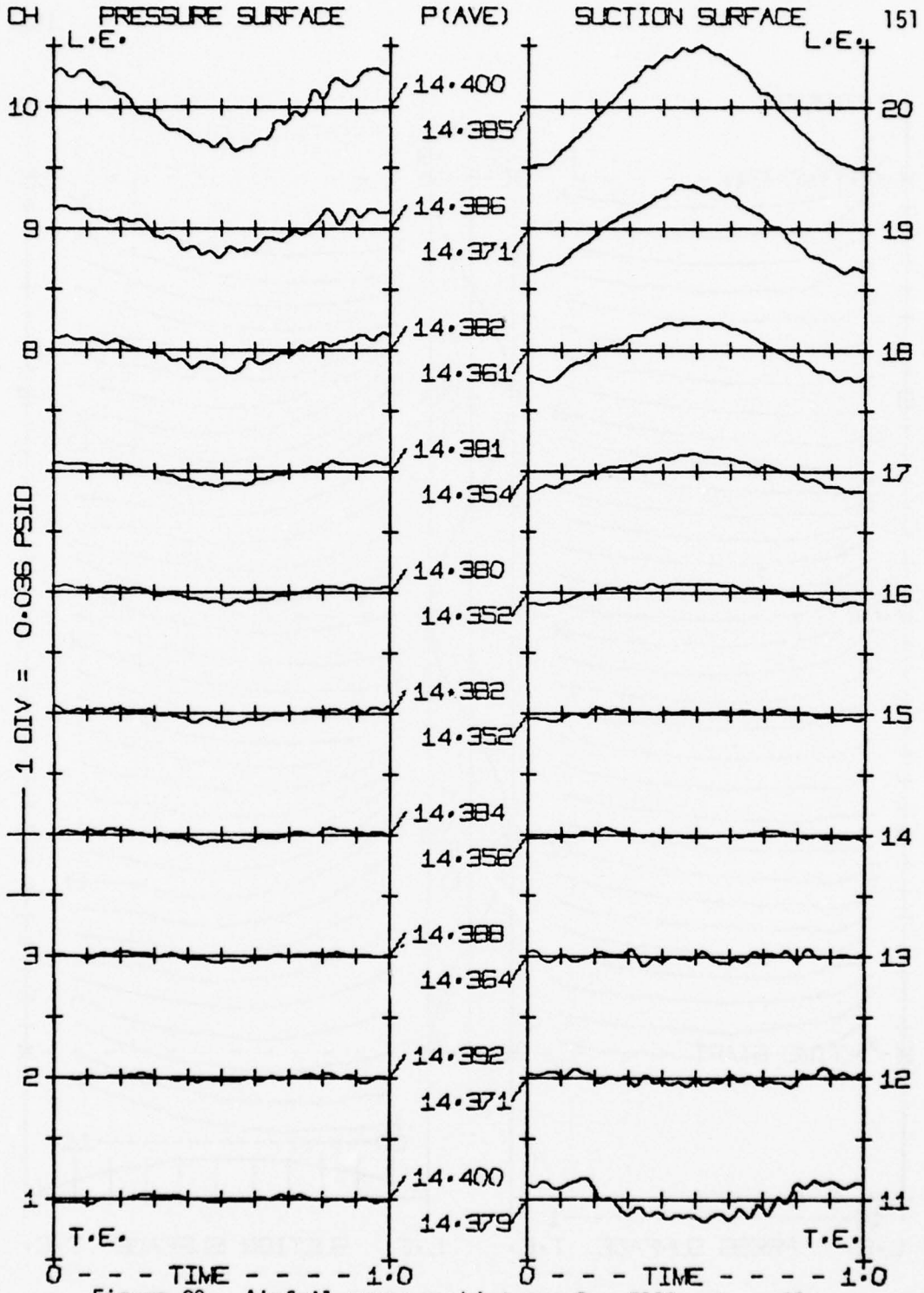

Figure 80. Airfoil pressure history, Run 7110, α_m = 6°, V_N = 110 fps, f_t = 0.2 hz

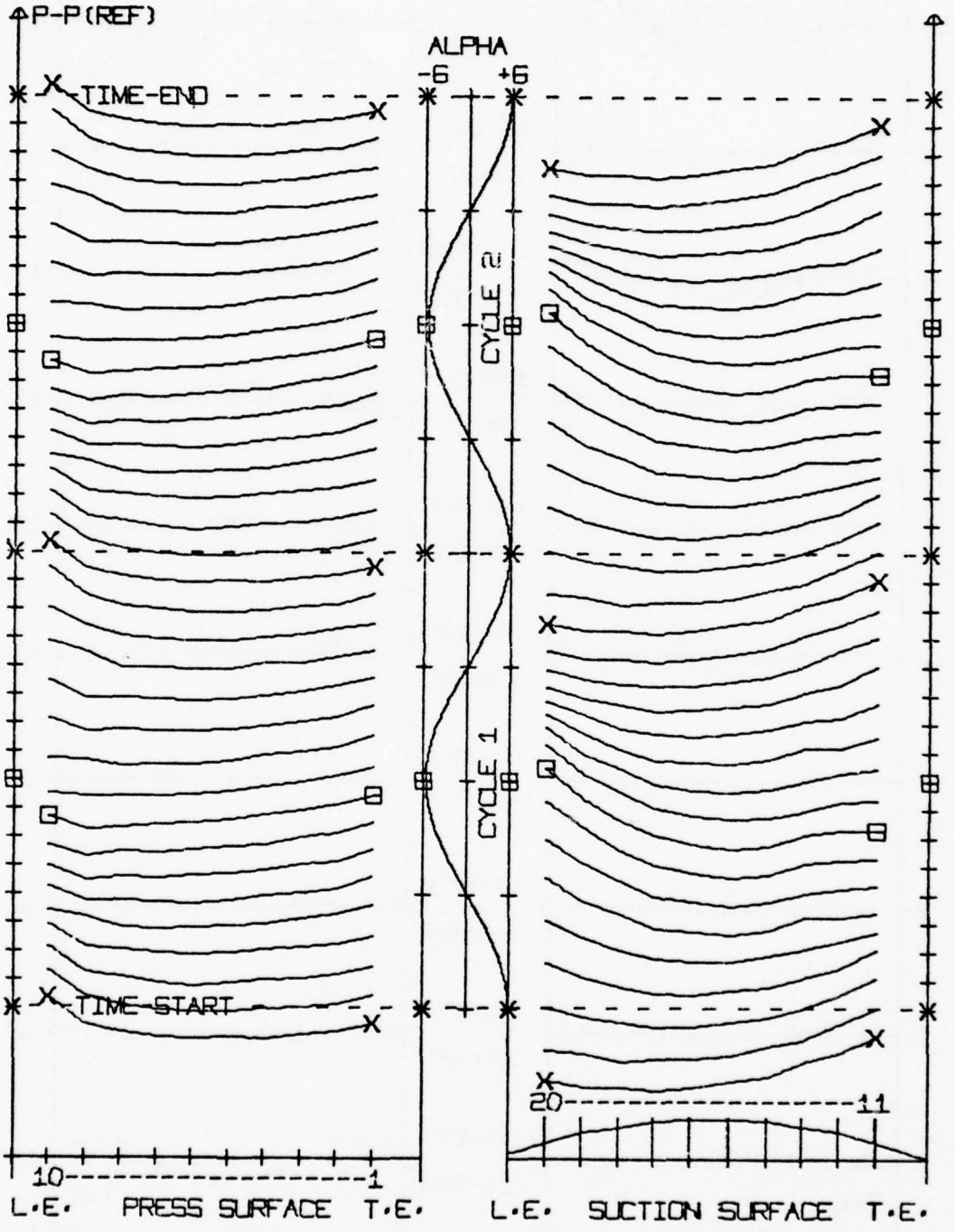

Figure 81. Time increment pressure profiles, Run 7110, α_m = 6°, V_N = 110 fps, f_t = 0.2 hz

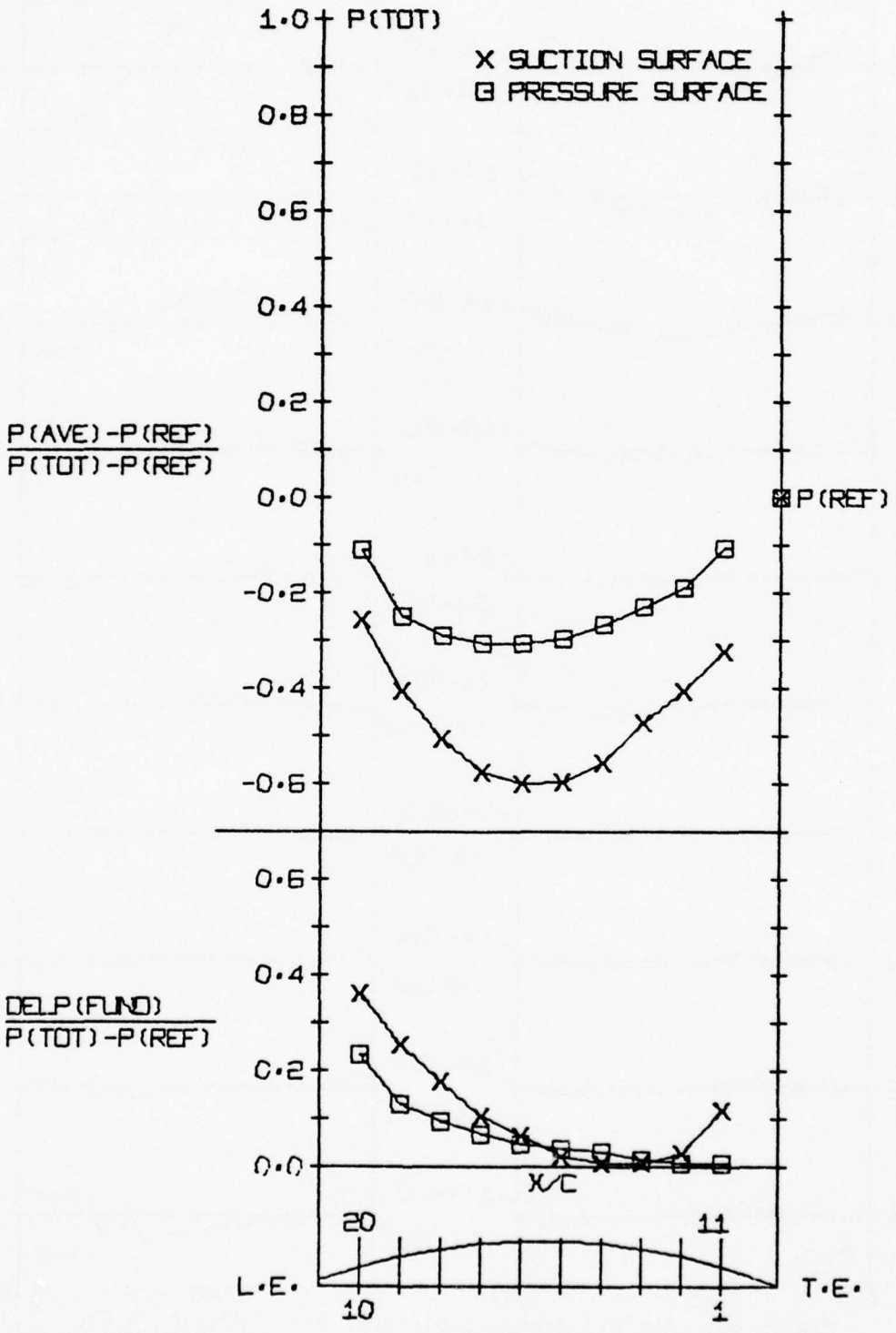

Figure 82. Normalized pressure profiles, Run 7110, α_m = 6°, V_N = 110 fps, f_t = 0.2 hz

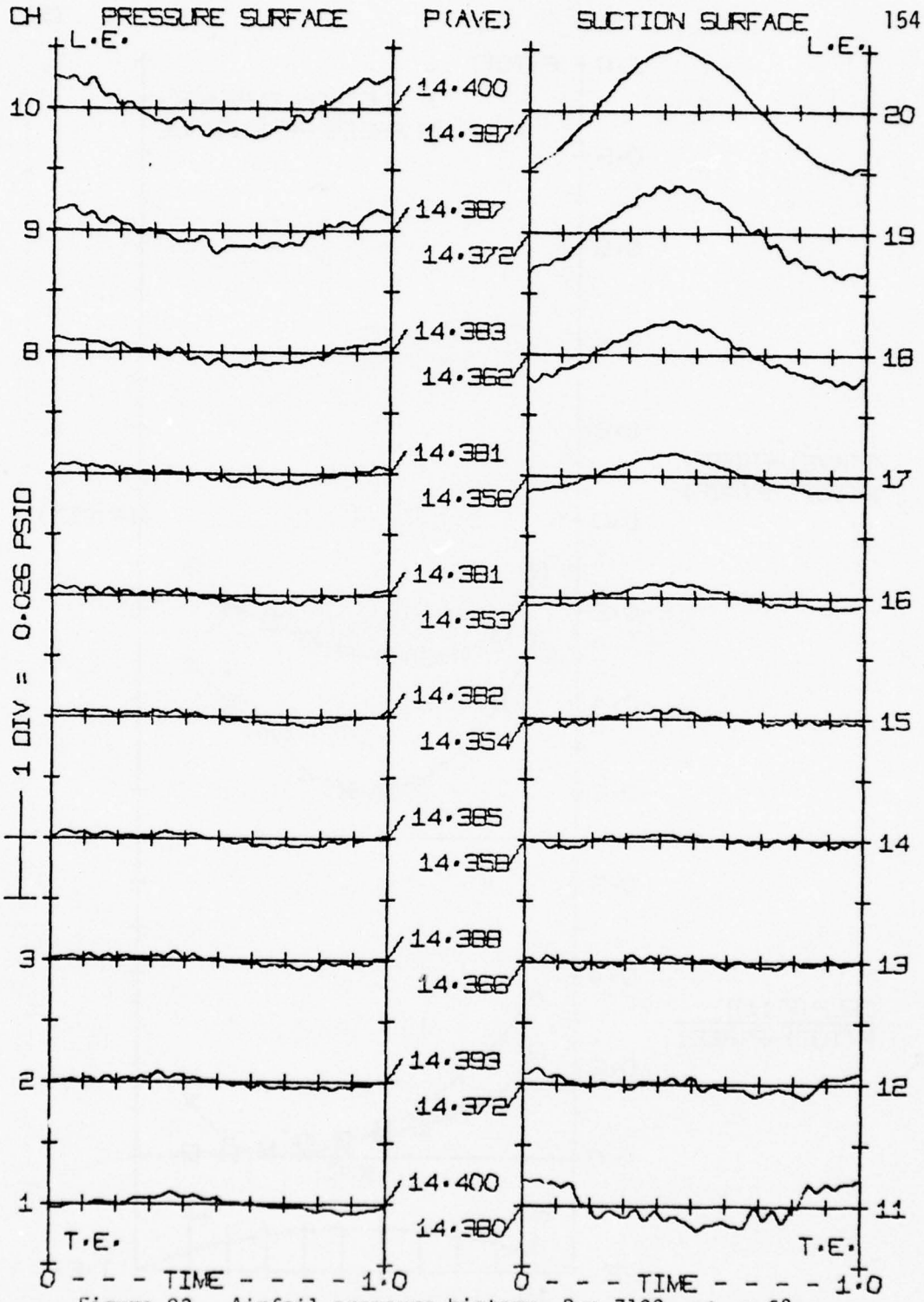

Figure 83. Airfoil pressure history, Run 7190, α_m = 6°, V_N = 110 fps, f_t = 16.2 hz

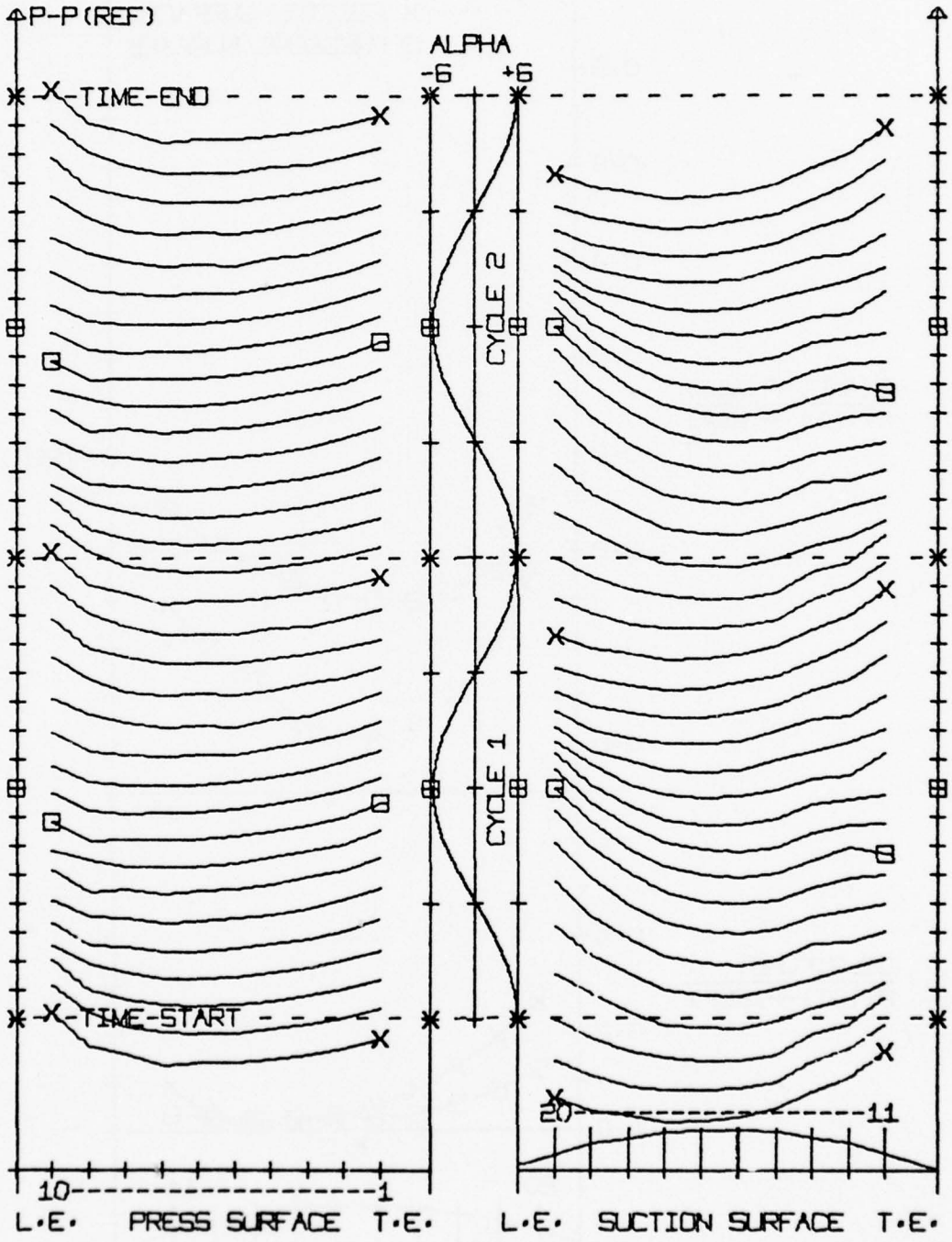

Figure 84. Time increment pressure profiles, Run 7190, α_m = 6°, V_N = 110 fps, f_t = 16.2 hz

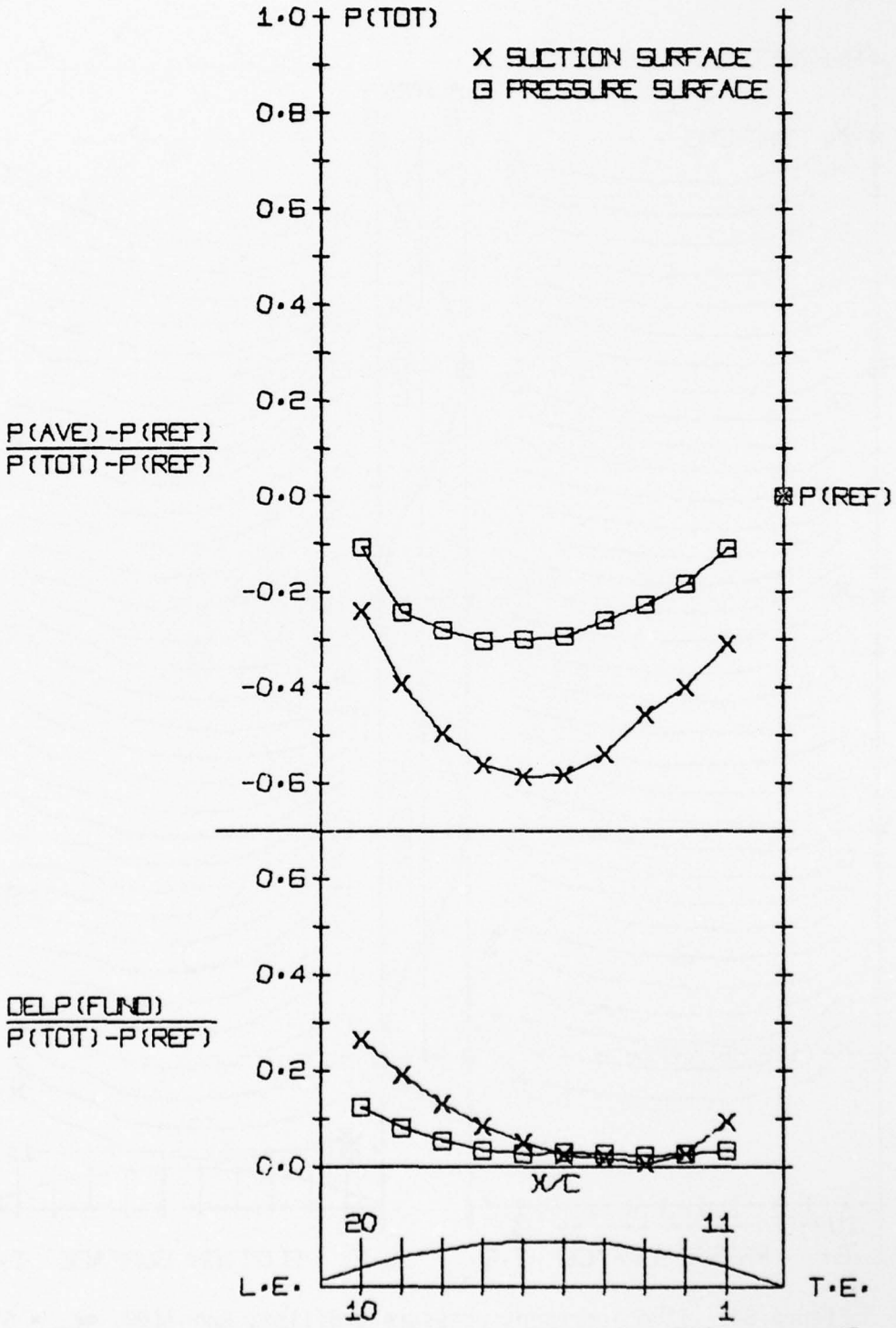

Figure 85. Normalized pressure profiles, Run 7190, α_m = 6°, V_N = 110 fps, f_t = 16.2 hz

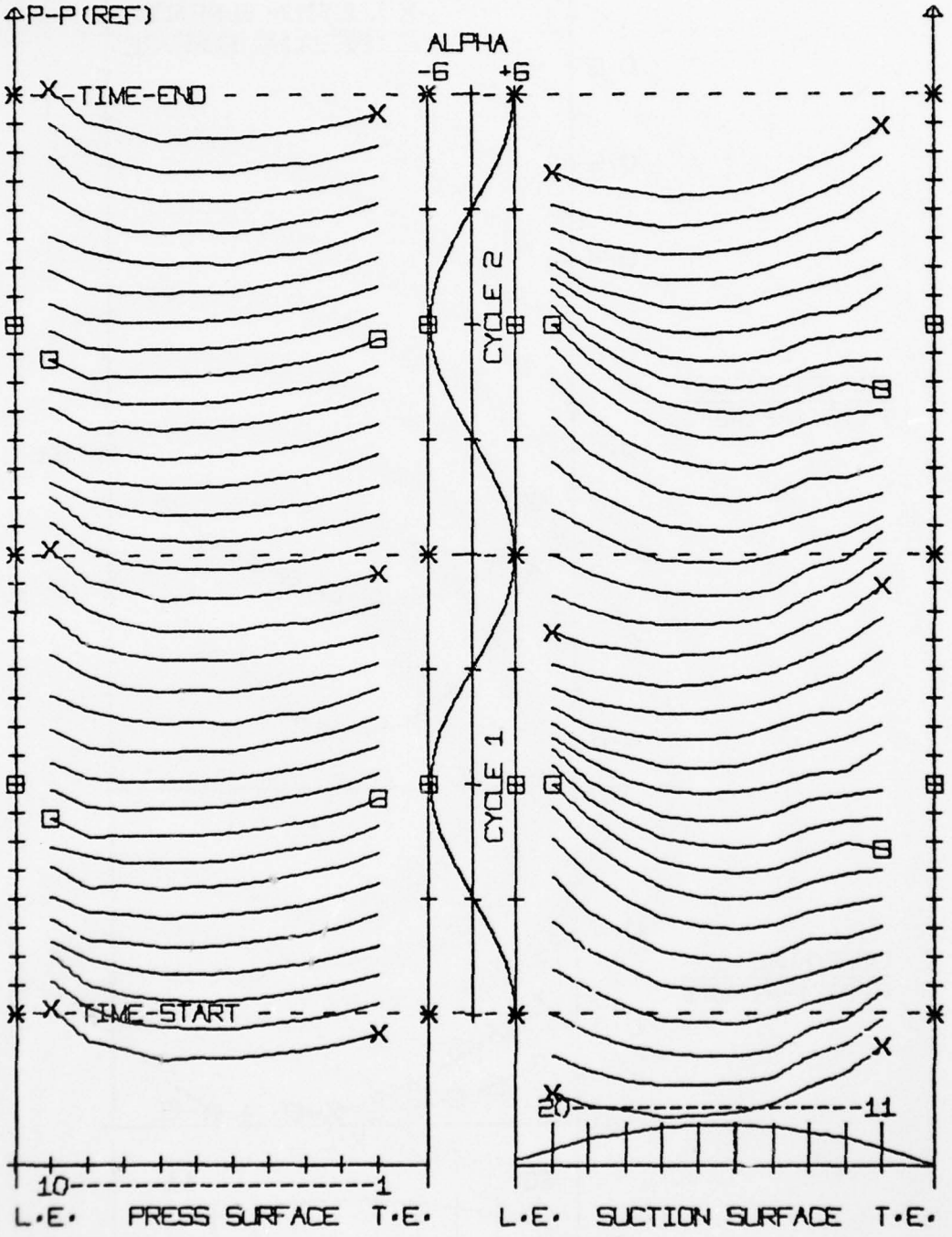

Figure 84. Time increment pressure profiles, Run 7190, α_m = 6°, V_N = 110 fps, f_t = 16.2 hz

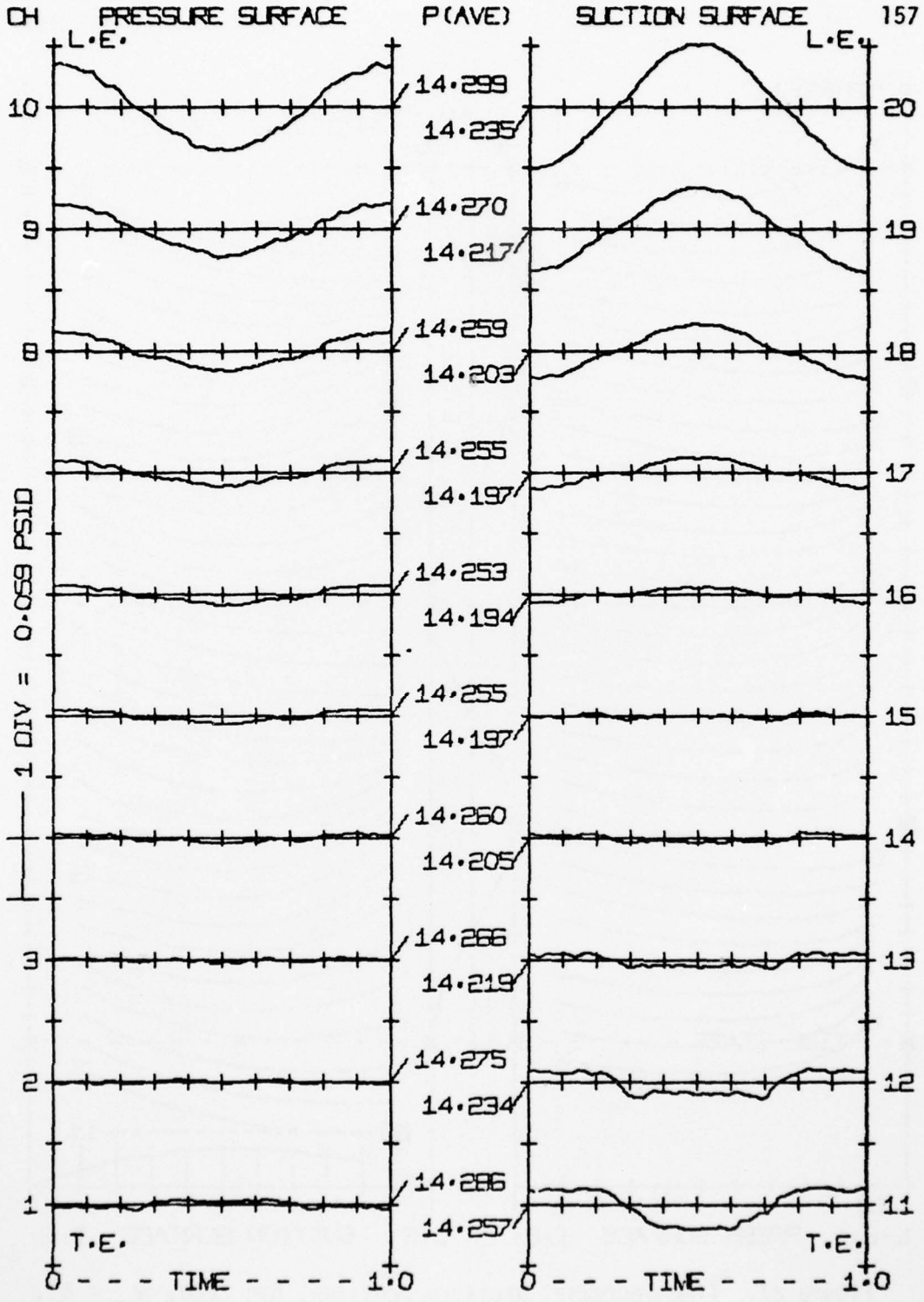

Figure 86. Airfoil pressure history, Run 7220, α_m = 8°, V_N = 150 fps, f_t = 0.2 hz

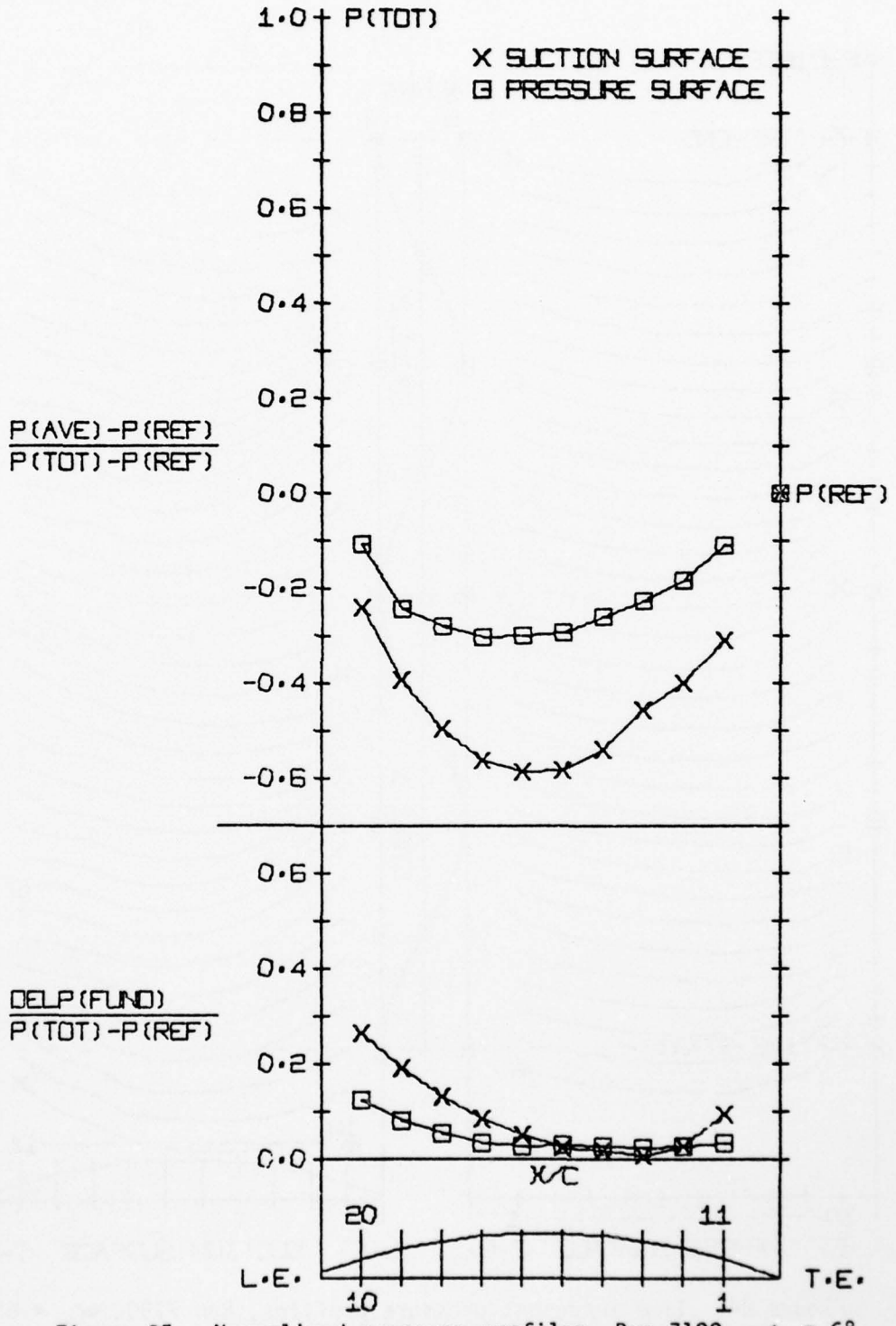

Figure 85. Normalized pressure profiles, Run 7190, α_m = 6°, V_N = 110 fps, f_t = 16.2 hz

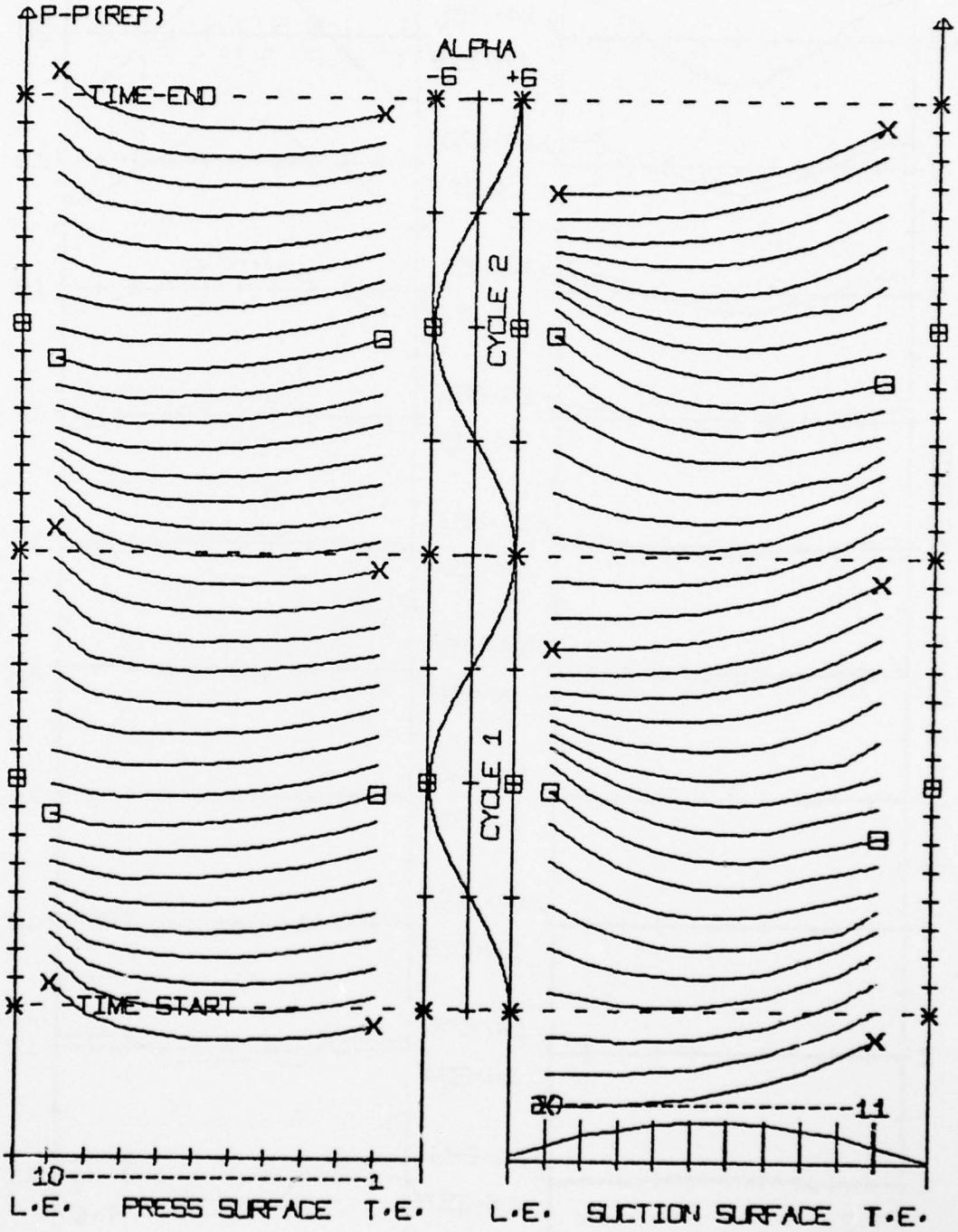

Figure 87. Time increment pressure profiles, Run 7220, α_m = 8°, V_N = 150 fps, f_t = 0.2 hz

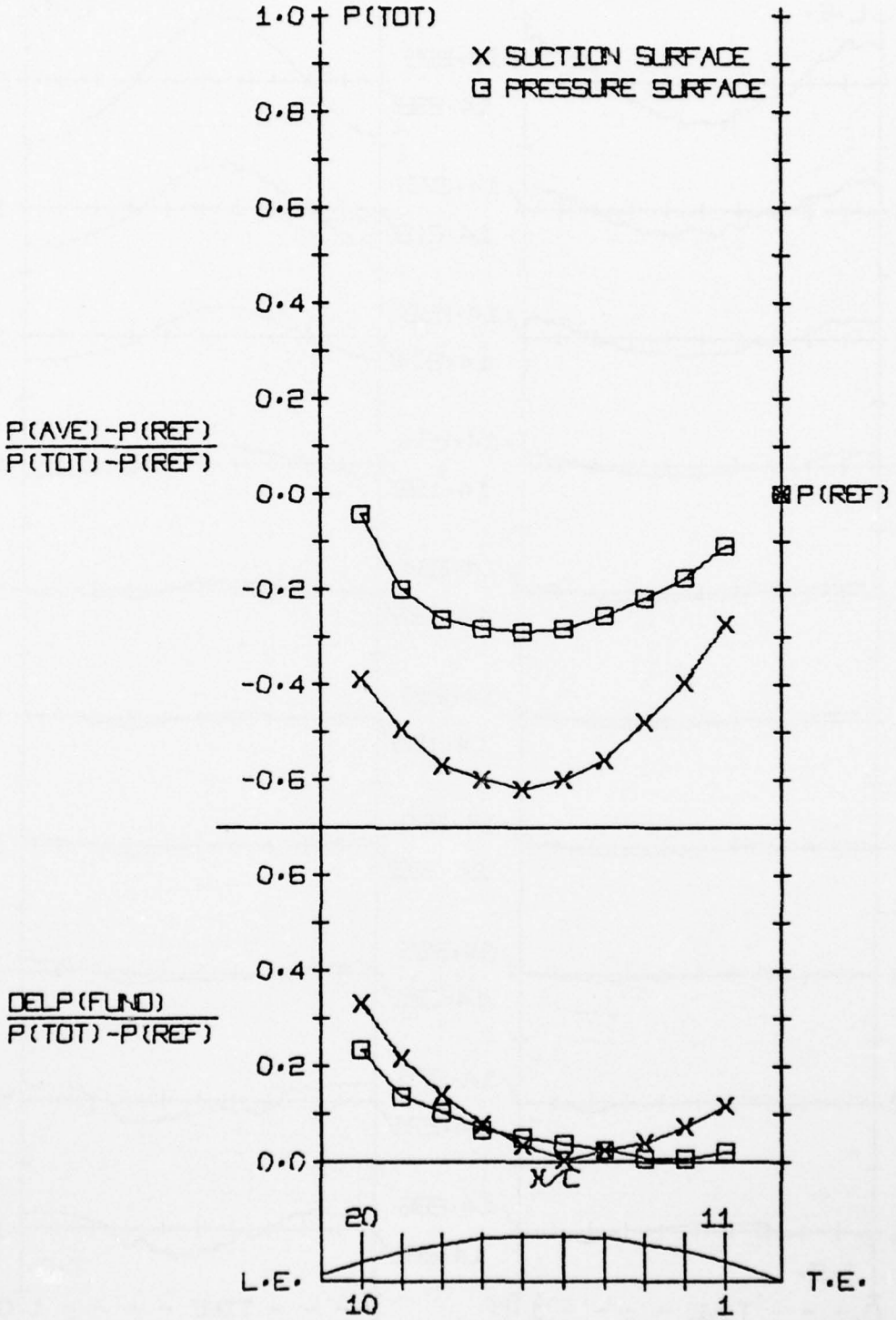

Figure 88. Normalized pressure profiles, Run 7220, α_m = 8°, V_N = 150 fps, f_t = 0.2 hz

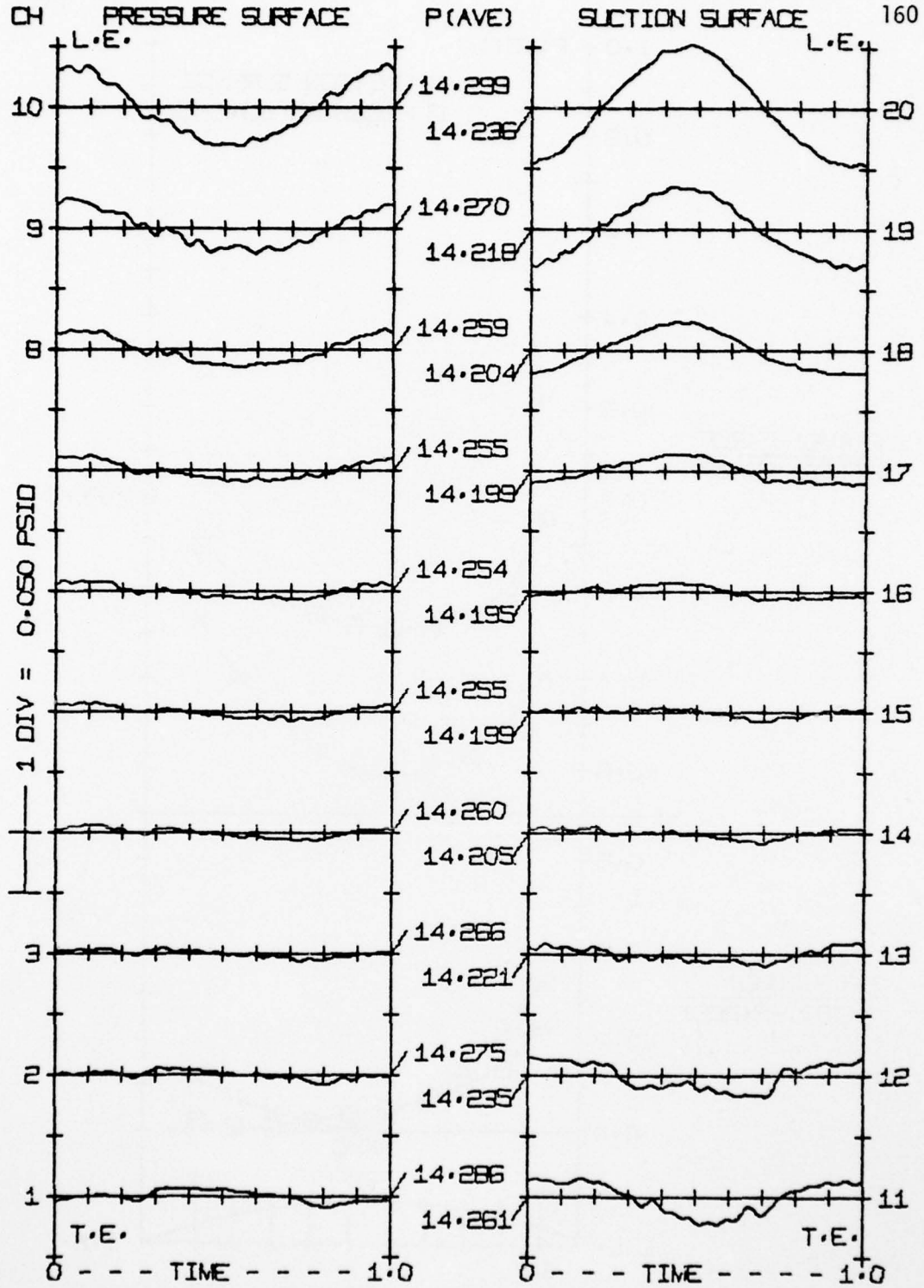

Figure 89. Airfoil pressure history, Run 7360, α_m = 8°, V_N = 150 fps, f_t = 16.2 hz

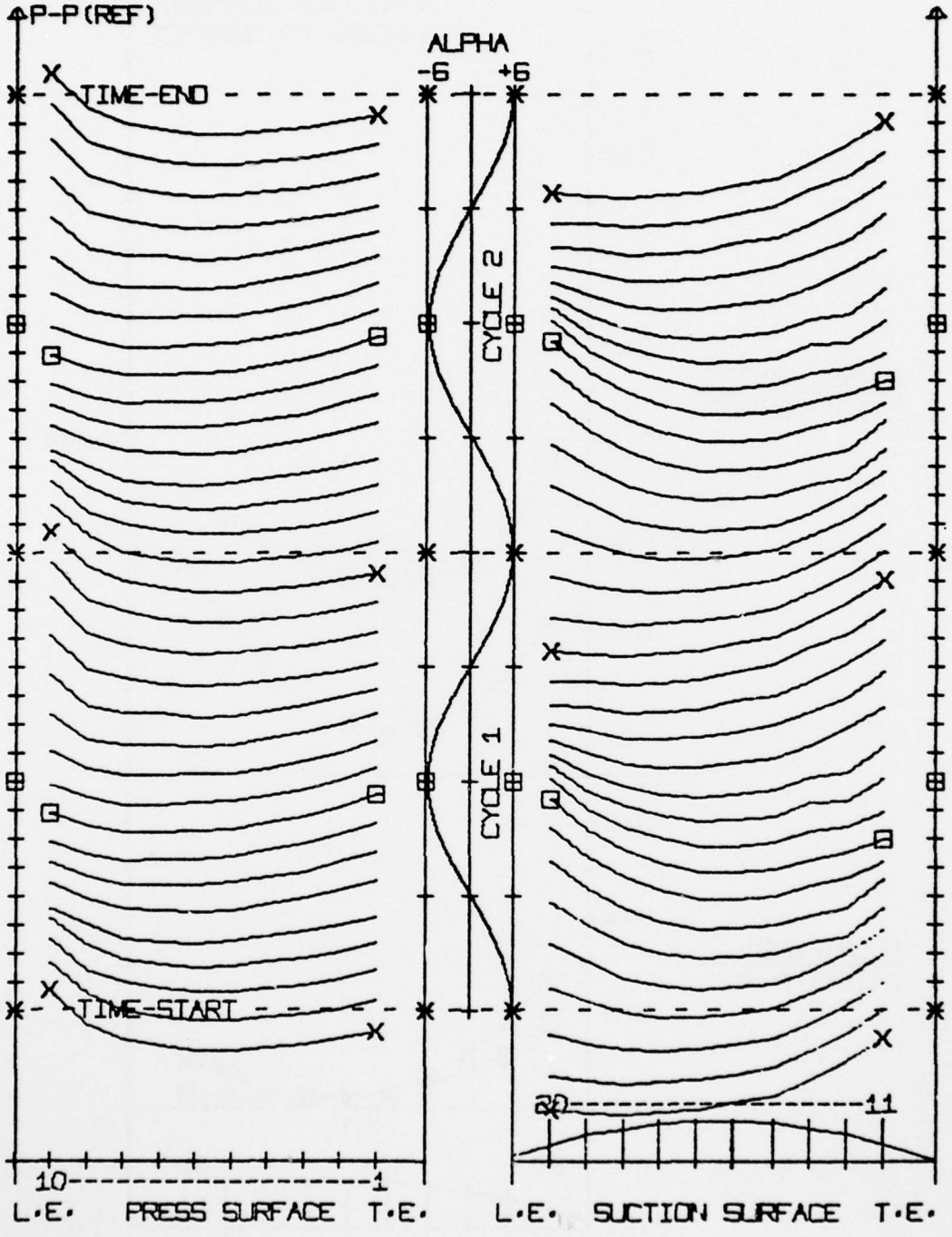

Figure 90. Time increment pressure profiles, Run 7360, α_m = 8°, V_N = 150 fps, f_t = 16.2 hz

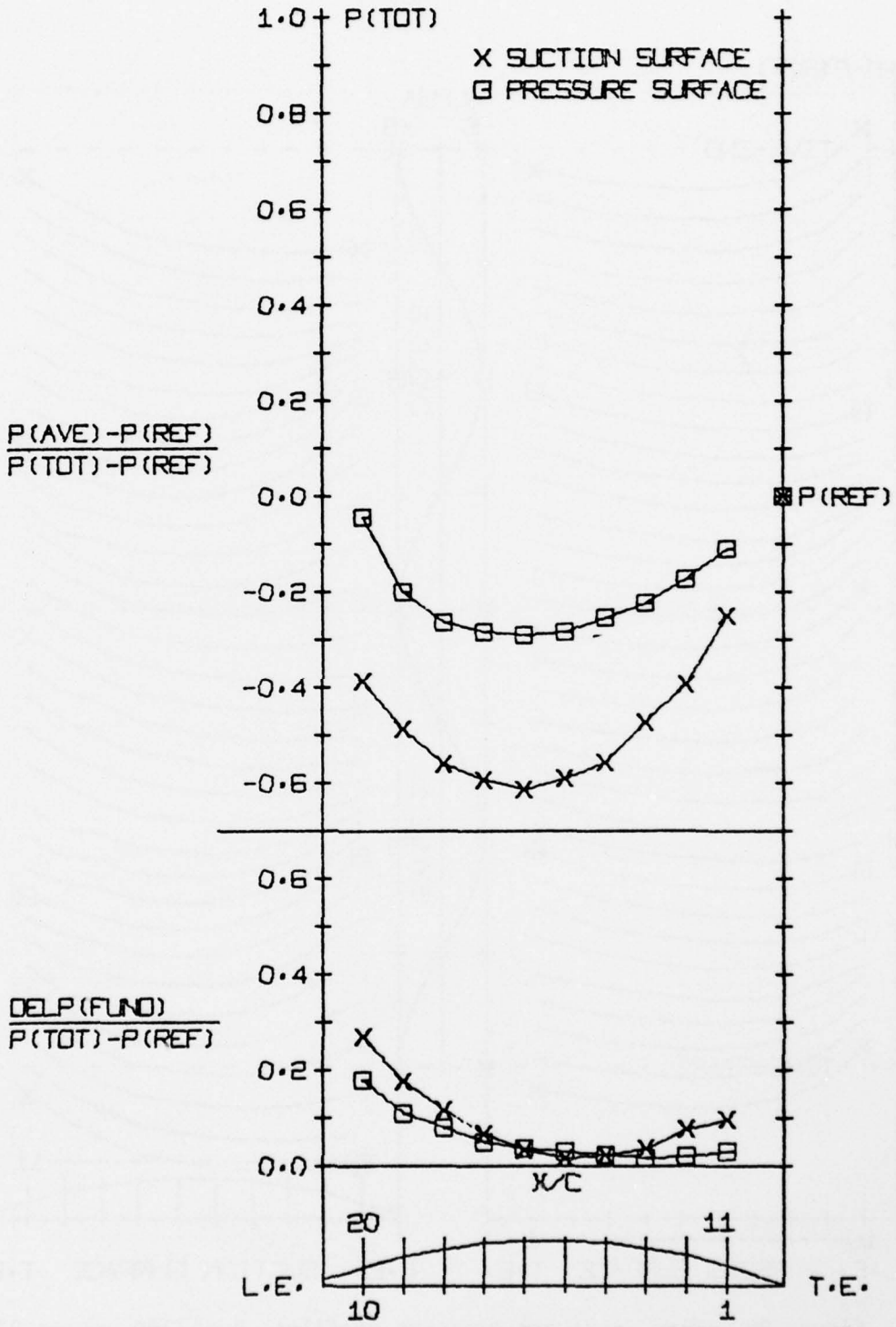

Figure 91. Normalized pressure profiles, Run 7360, α_m = 8°, V_N = 150 fps, f_t = 16.2 hz

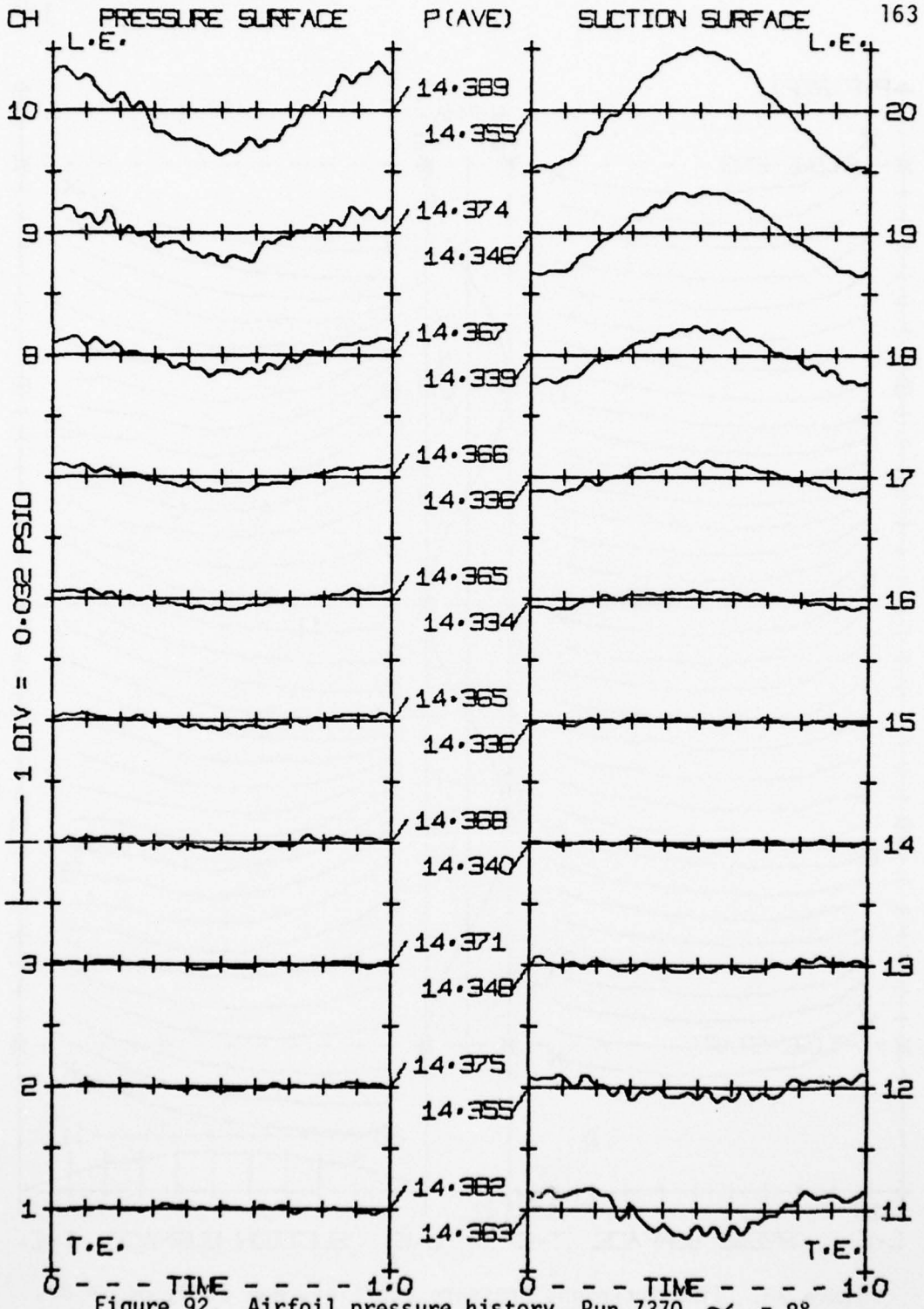

Figure 92. Airfoil pressure history, Run 7370, α_m = 8°, V_N = 110 fps, f_t = 0.2 hz

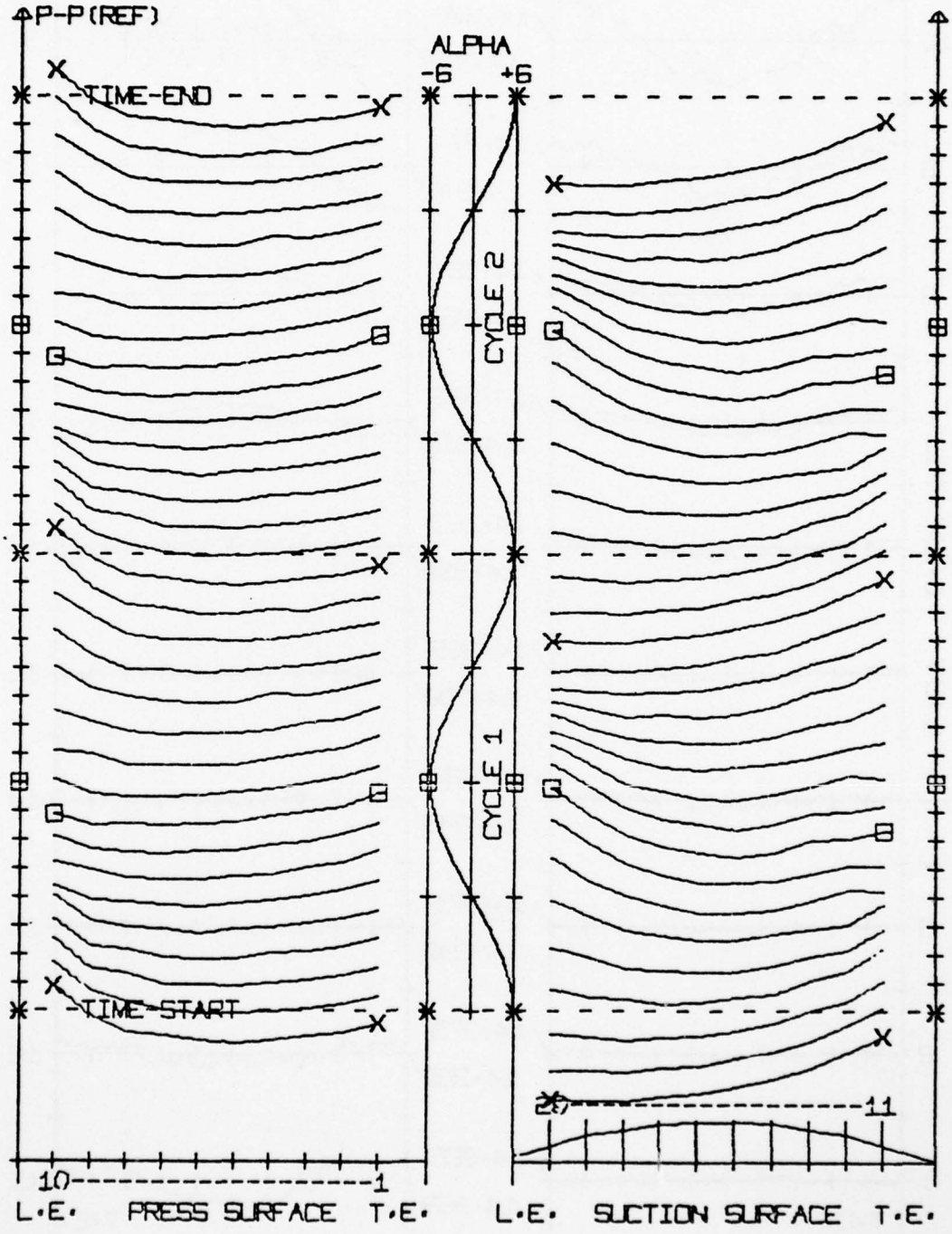

Figure 93. Time increment pressure profiles, Run 7370, α_m = 8°, V_N = 110 fps, f_t = 0.2 hz

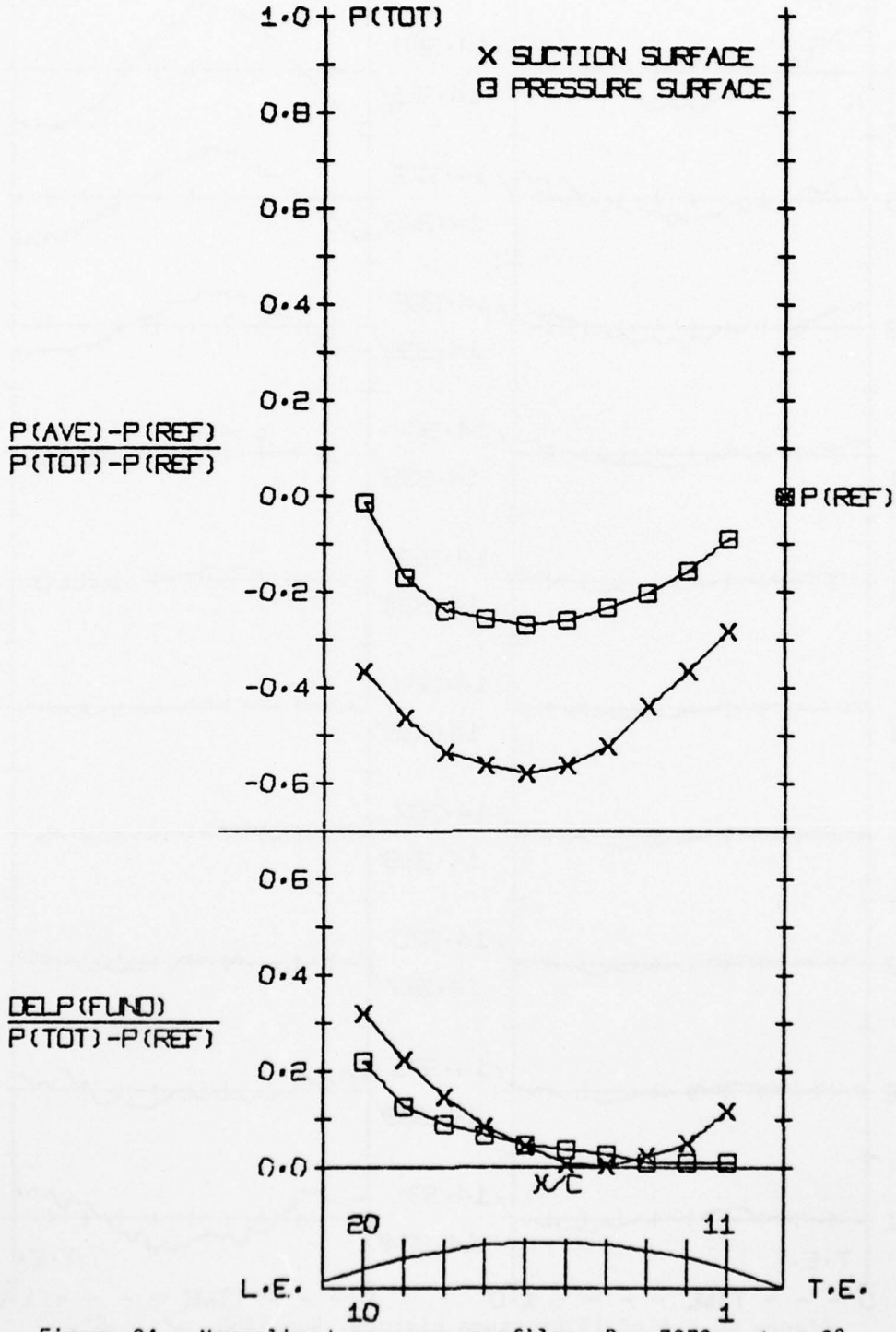

Figure 94. Normalized pressure profiles, Run 7370, α_m = 8°, V_N = 110 fps, f_t = 0.2 hz

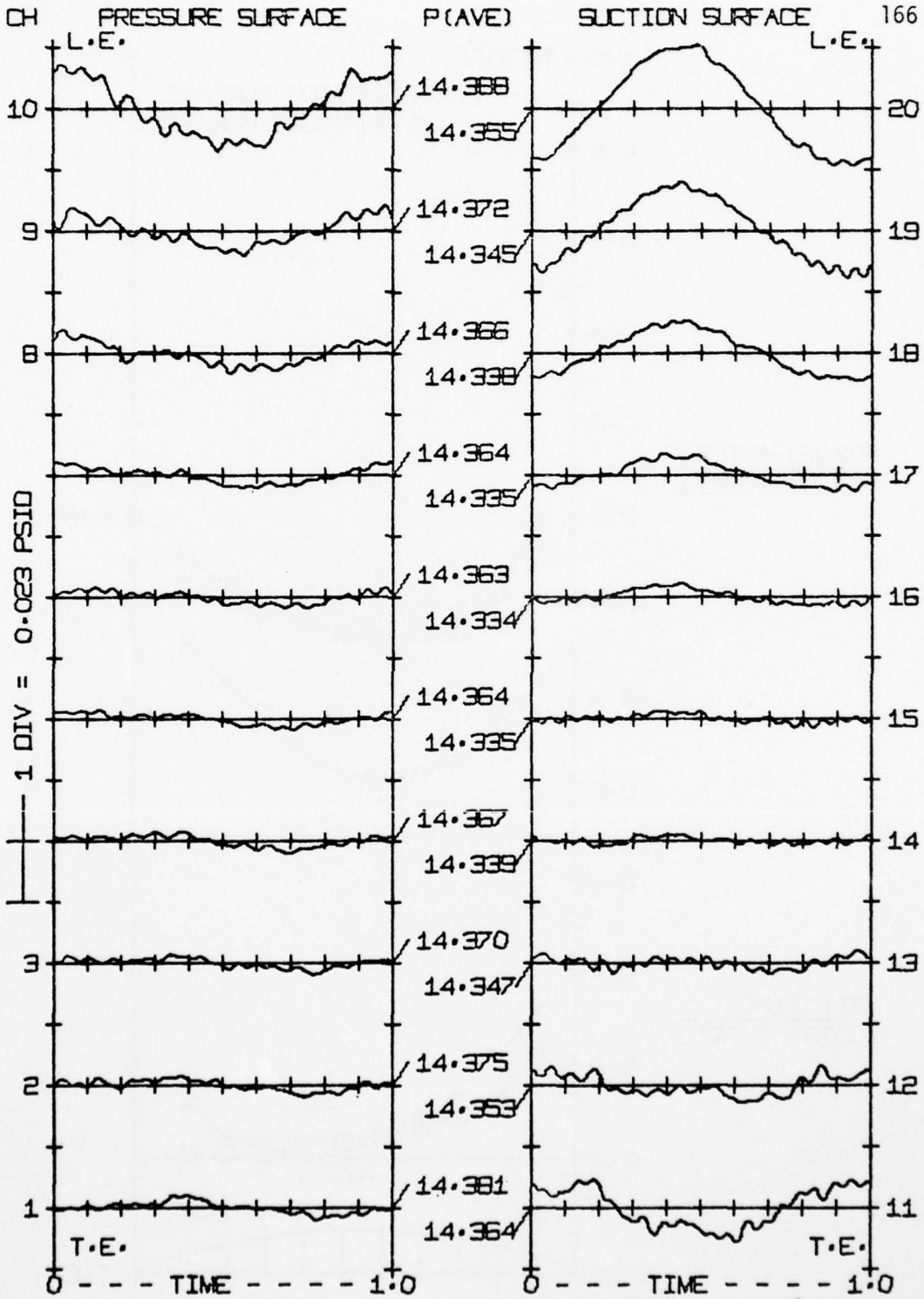

Figure 95. Airfoil pressure history, Run 7450, α_m = 8°, V_N = 110 fps, f_t = 16.2 hz

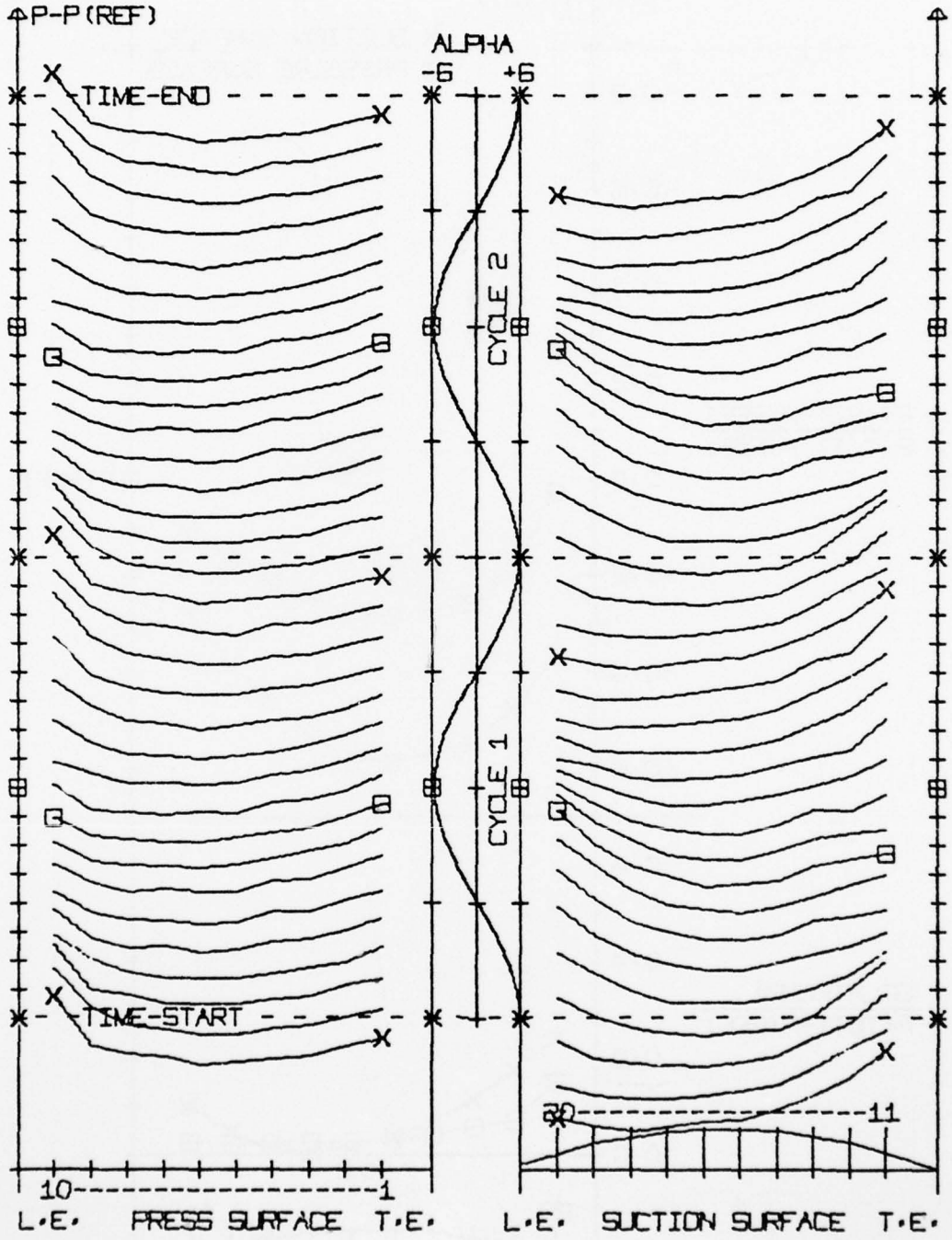

Figure 96. Time increment pressure profiles, Run 7450, α_m = 8°, V_N = 110 fps, f_t = 16.2 hz

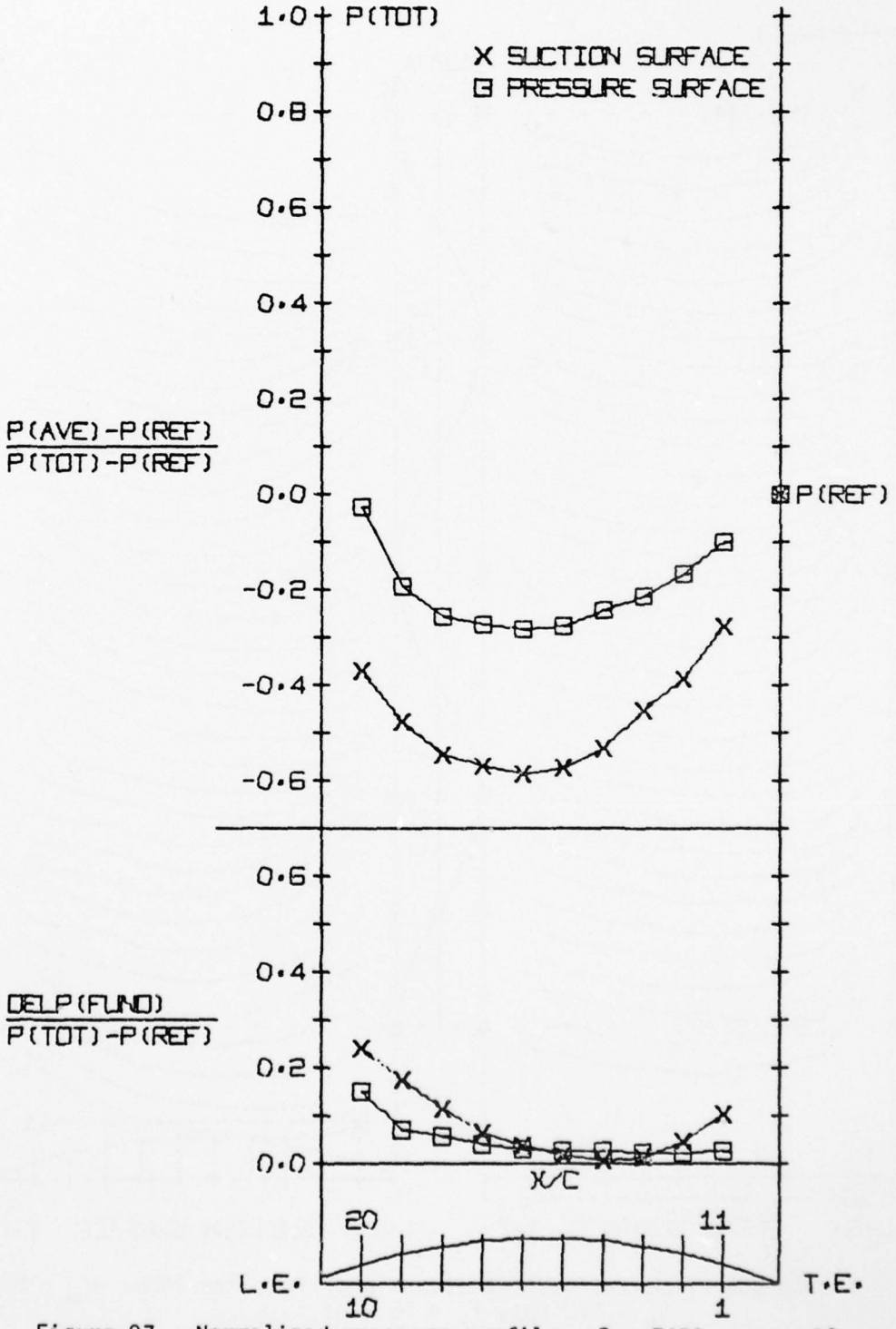

Figure 97. Normalized pressure profiles, Run 7450, α_m = 8°, V_N = 110 fps, f_t = 16.2 hz

AD-A045 319 AIR FORCE AERO PROPULSION LAB WRIGHT-PATTERSON AFB OHIO F/G 20/4
A CASCADE IN UNSTEADY FLOW.(U)
DEC 76 F R OSTDIEK
UNCLASSIFIED AFAPL-TR-76-115 NL

3 OF 3
ADA
045319

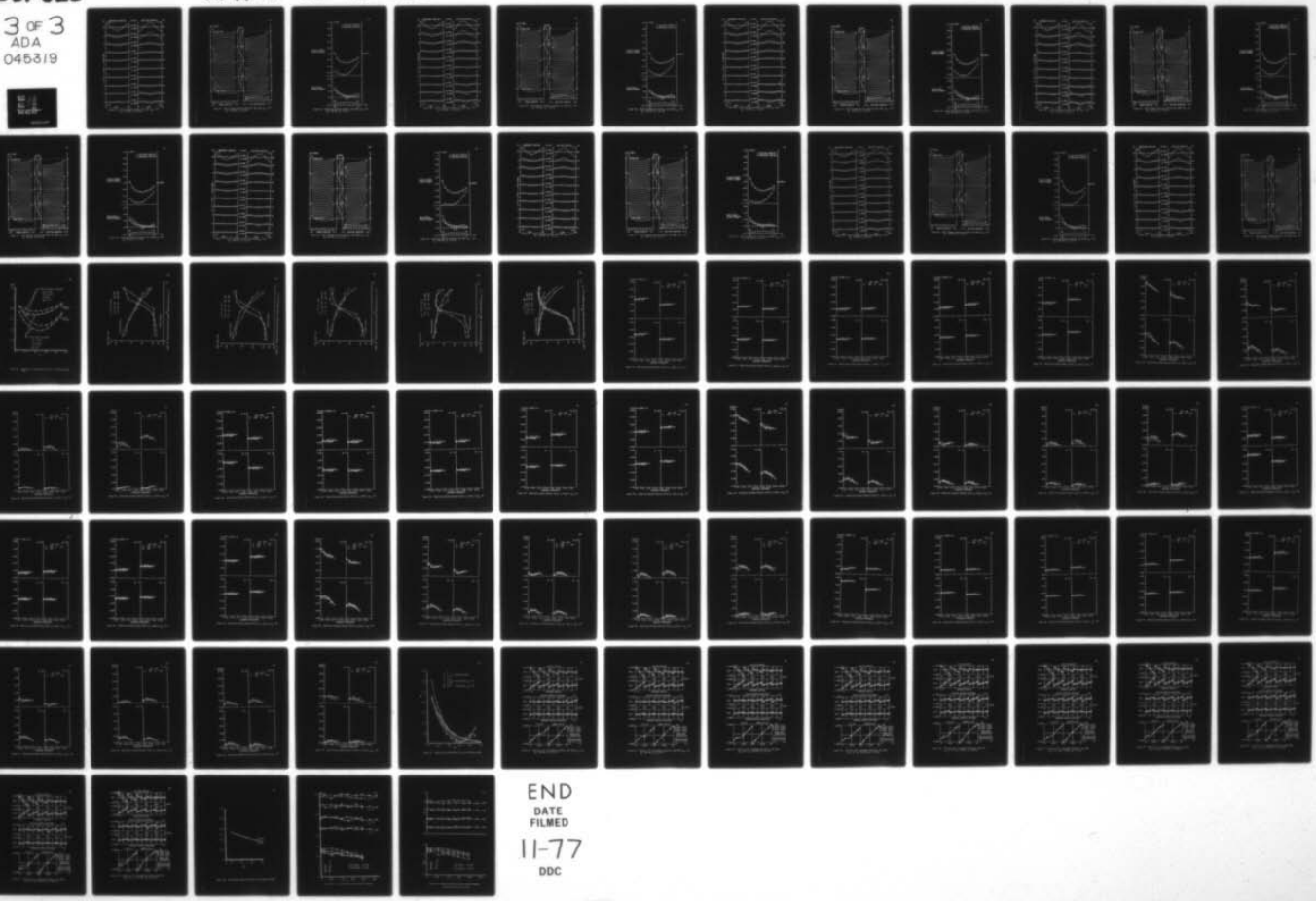

END
DATE
FILMED
11-77
DDC

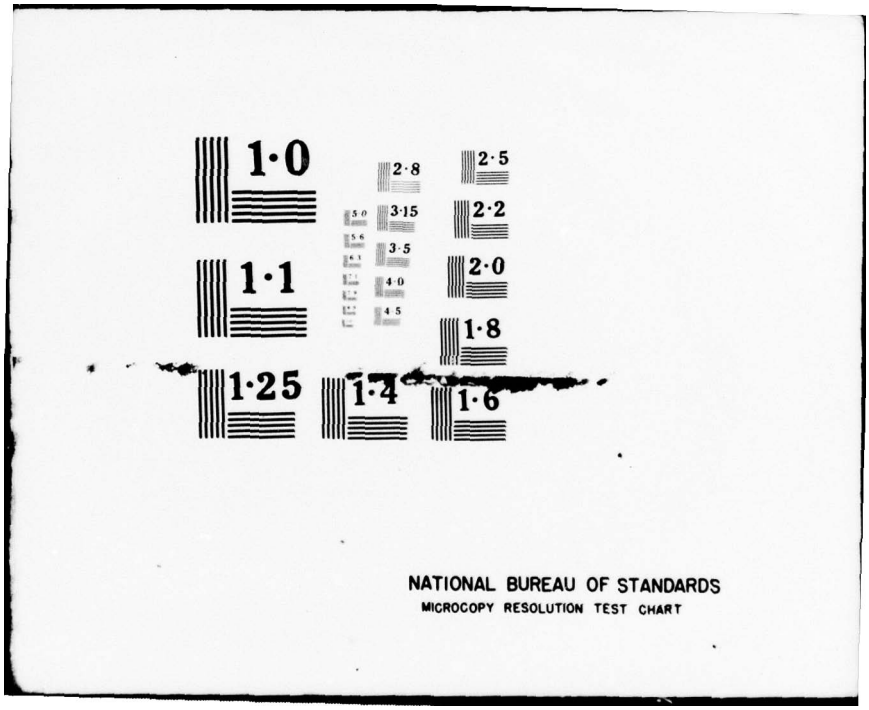
1·0
1·1
1·25
1·4
1·6
1·8
2·0
2·2
2·5
2·8
3·15
3·5
4·0
4·5
5·0
5·6
NATIONAL BUREAU OF STANDARDS
MICROCOPY RESOLUTION TEST CHART

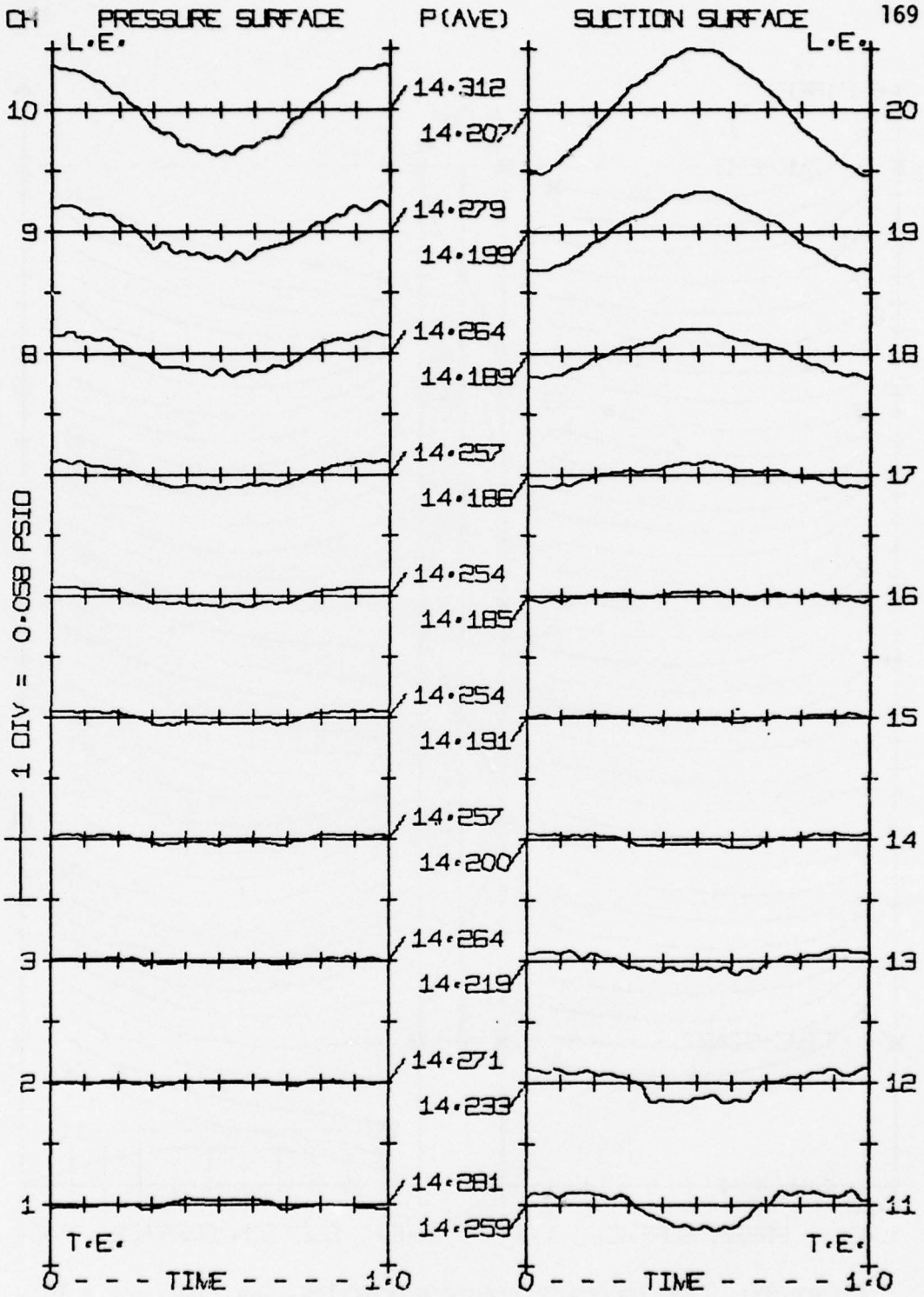

Figure 98. Airfoil pressure history, Run 7490, α_m = 10°, V_N = 150 fps, f_t = 0.2 hz

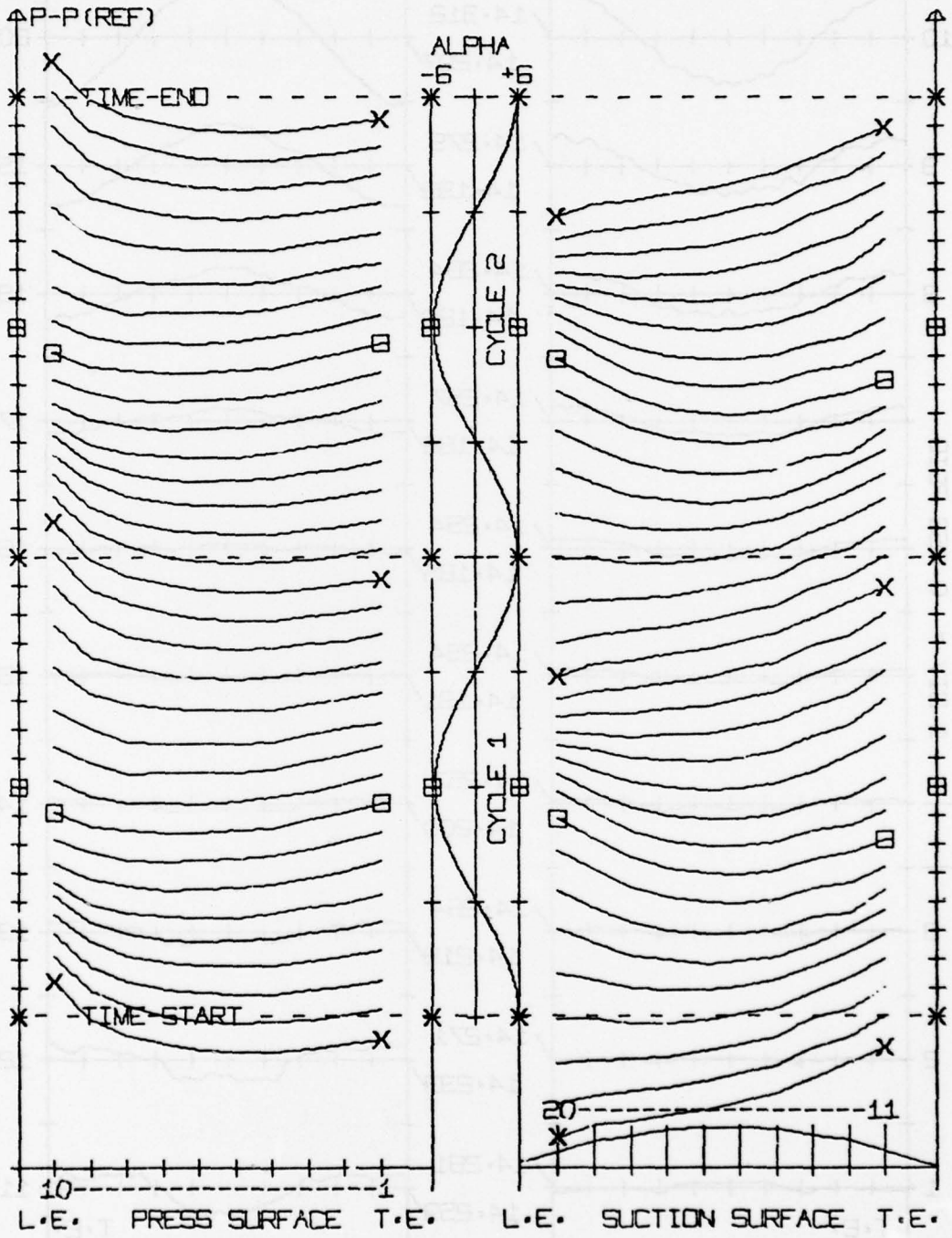

Figure 99. Time increment pressure profiles, Run 7490, α_m = 10°, V_N = 150 fps, f_t = 0.2 hz

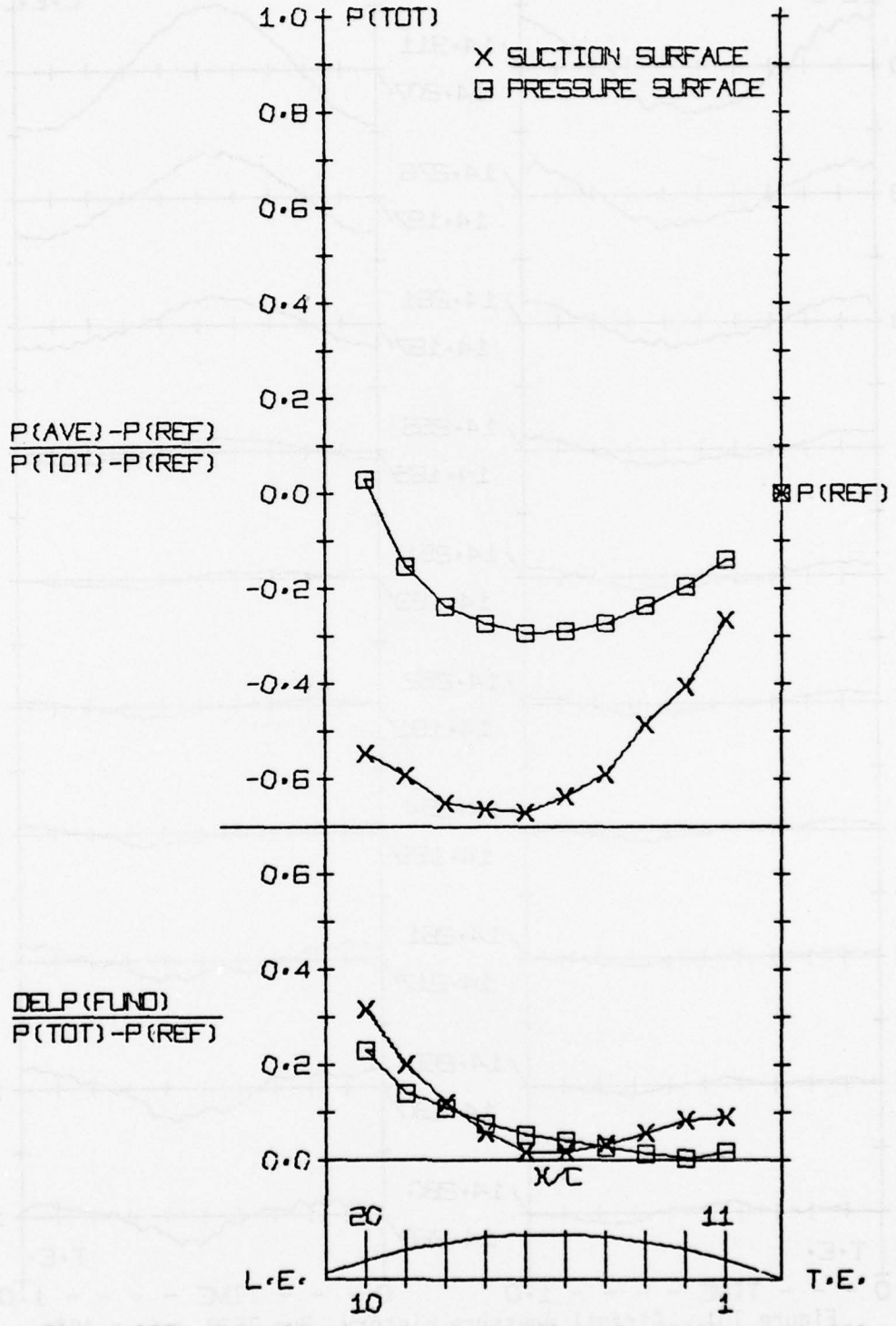

Figure 100. Normalized pressure profiles, Run 7490, α_m = 10°, V_N = 150 fps, f_t = 0.2 hz

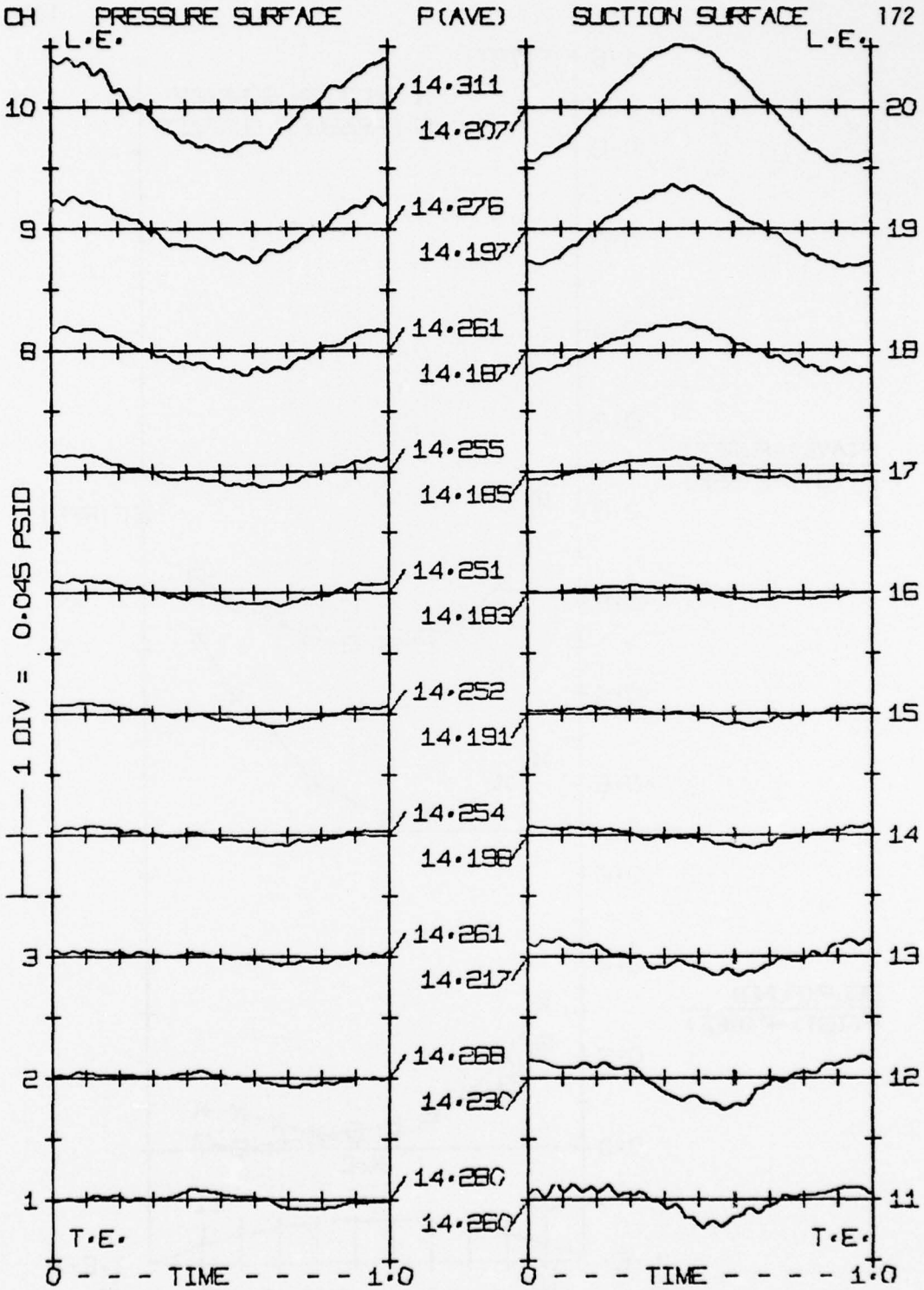

Figure 101. Airfoil pressure history, Run 7570, α_m = 10°, V_N = 150 fps, f_t = 16.2 hz

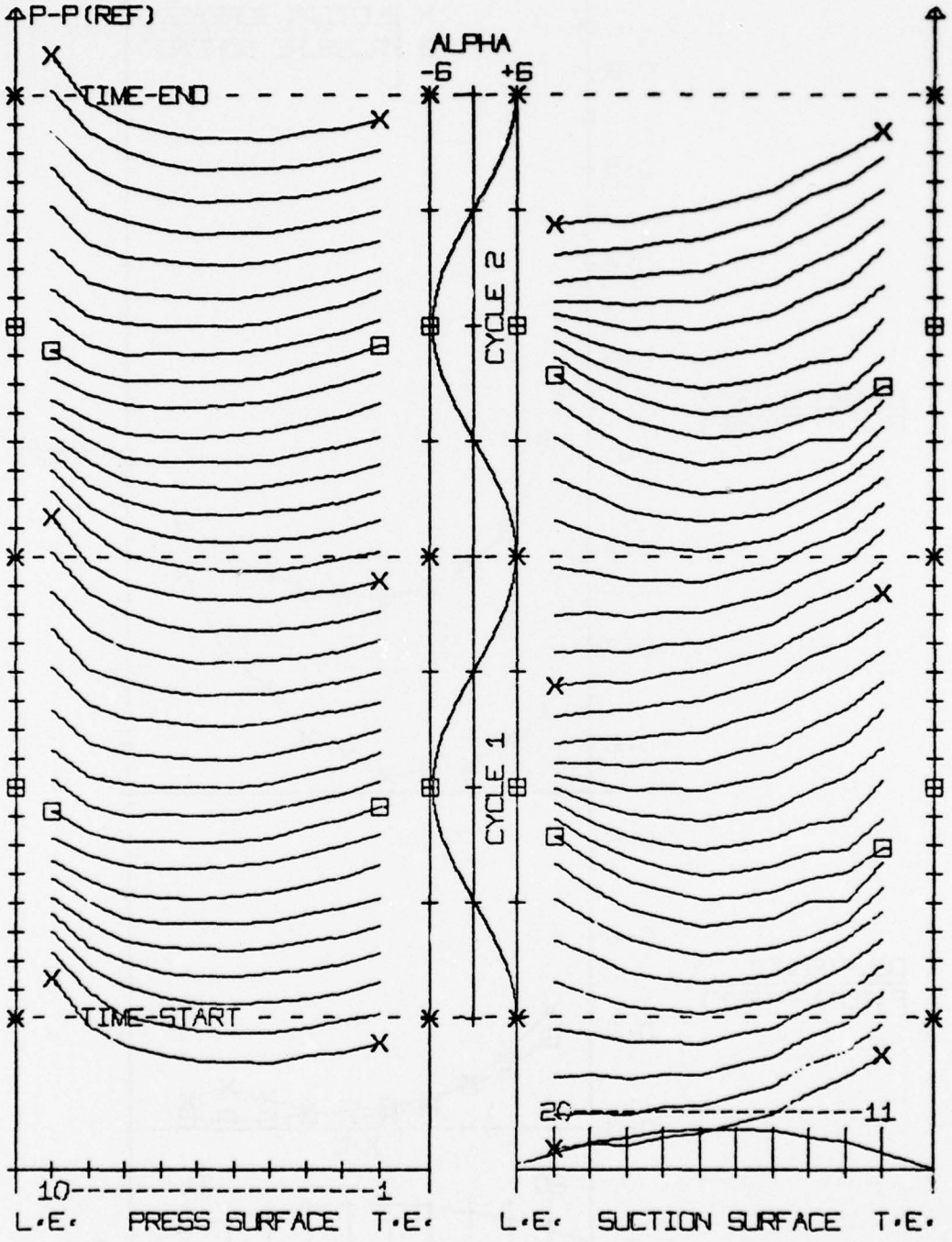

Figure 102. Time increment pressure profiles, Run 7570, α_m = 10°, V_N = 150 fps, f_t = 16.2 hz

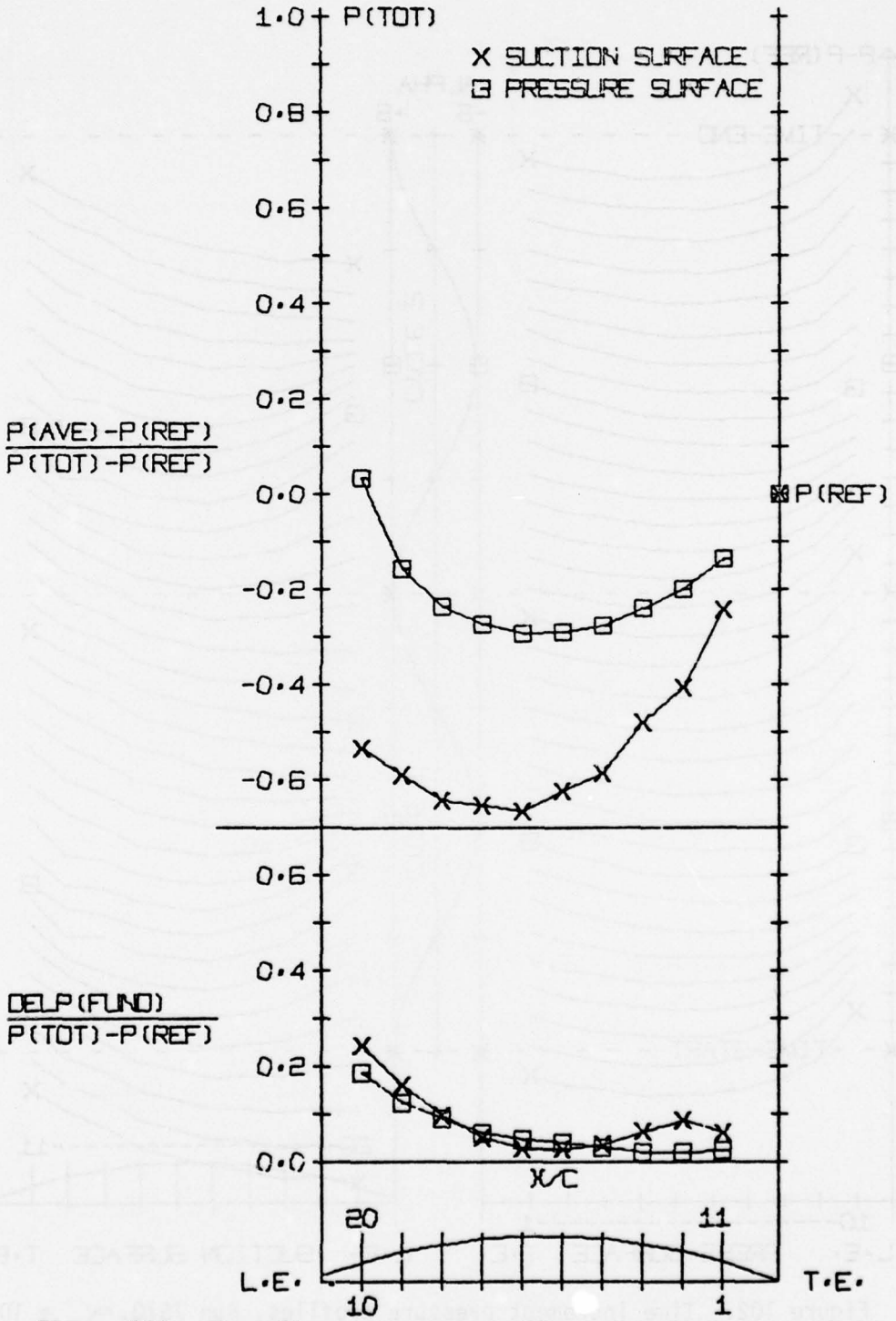

Figure 103. Normalized pressure profiles, Run 7570, α_m = 10°, V_N = 150 fps, f_t = 16.2 hz

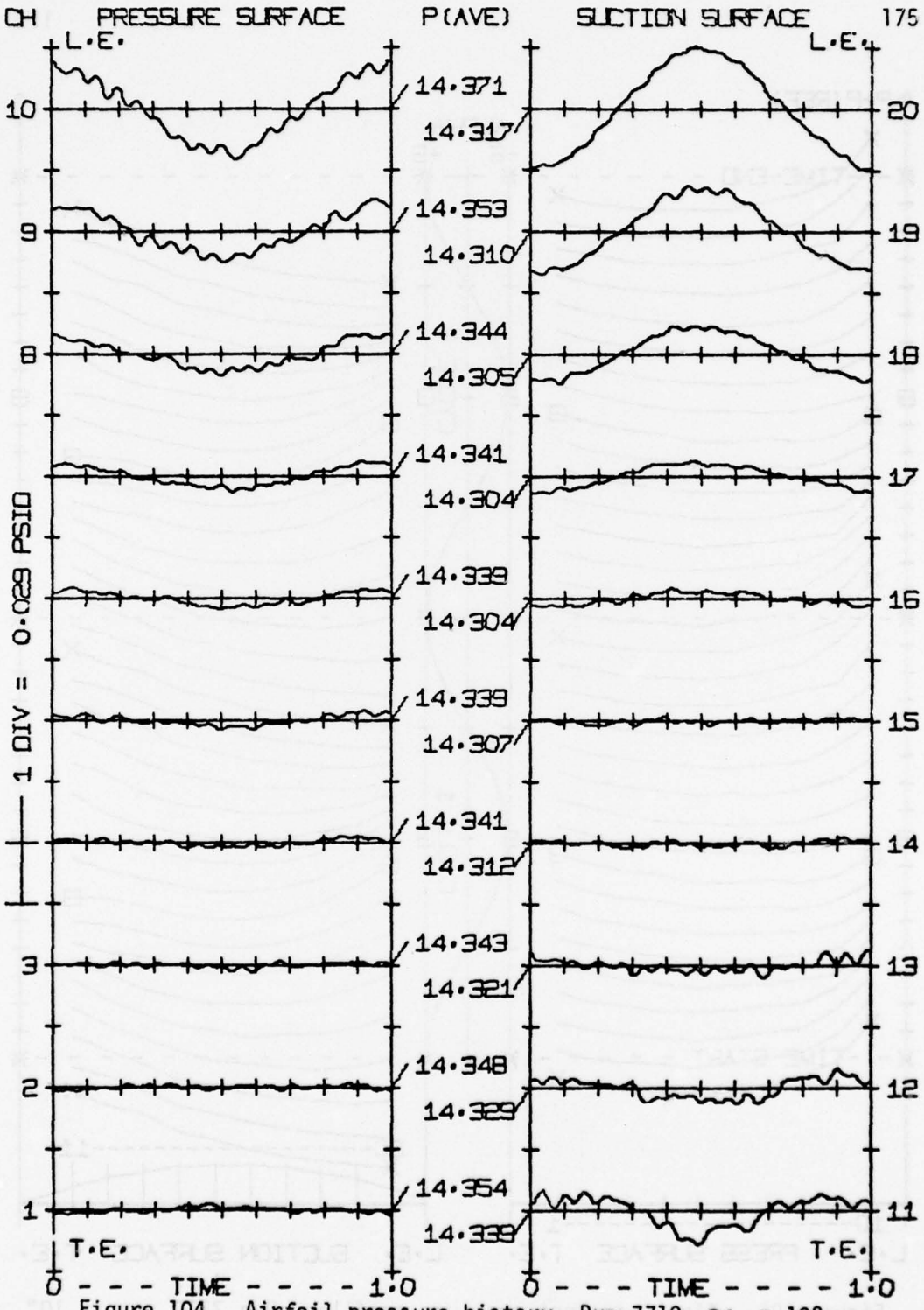

Figure 104. Airfoil pressure history, Run 7710, α_m = 10°, V_N = 110 fps, f_t = 1.43 hz

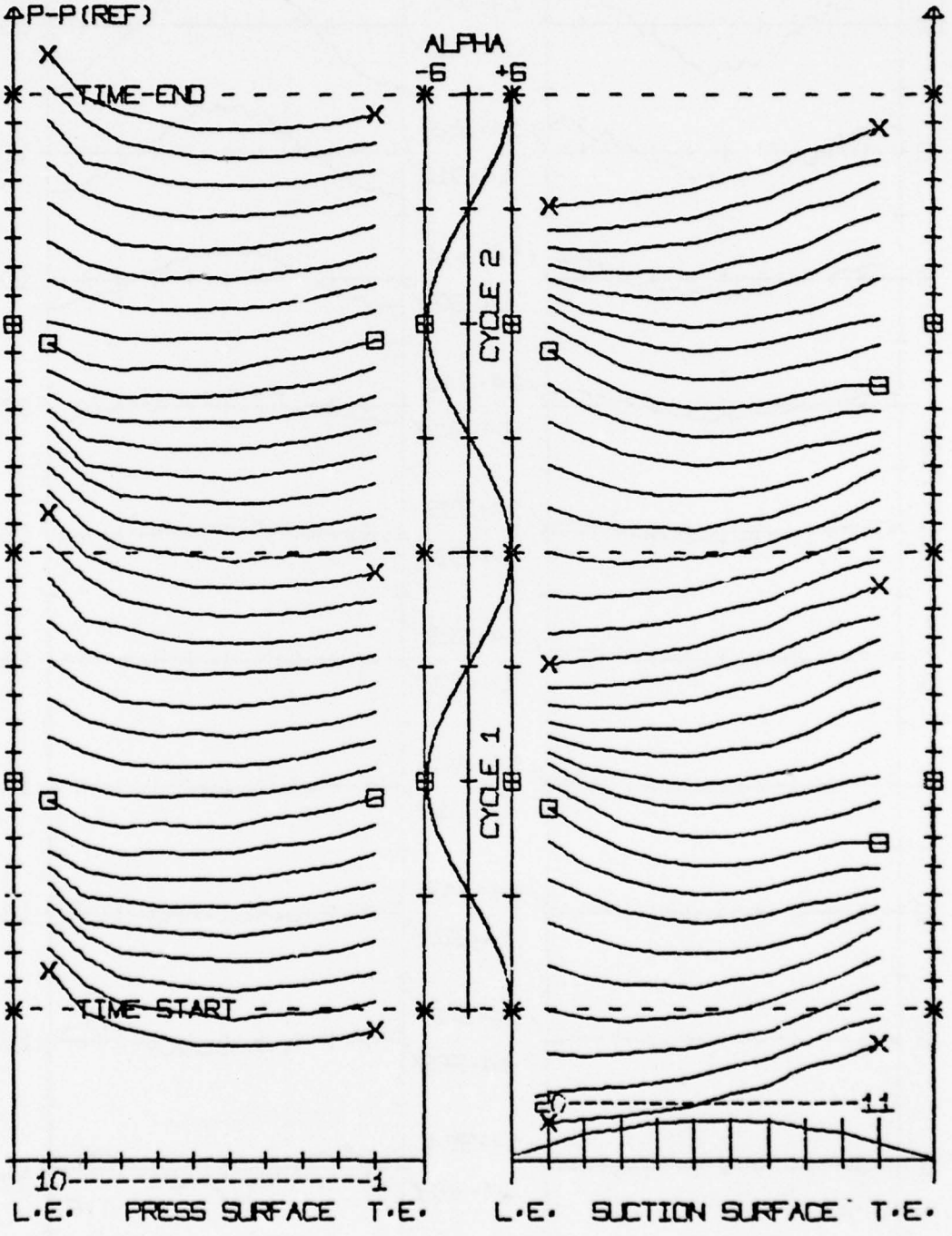

Figure 105. Time increment pressure profiles, Run 7710, α_m = 10°, V_N = 110 fps, f_t = 1.43 hz

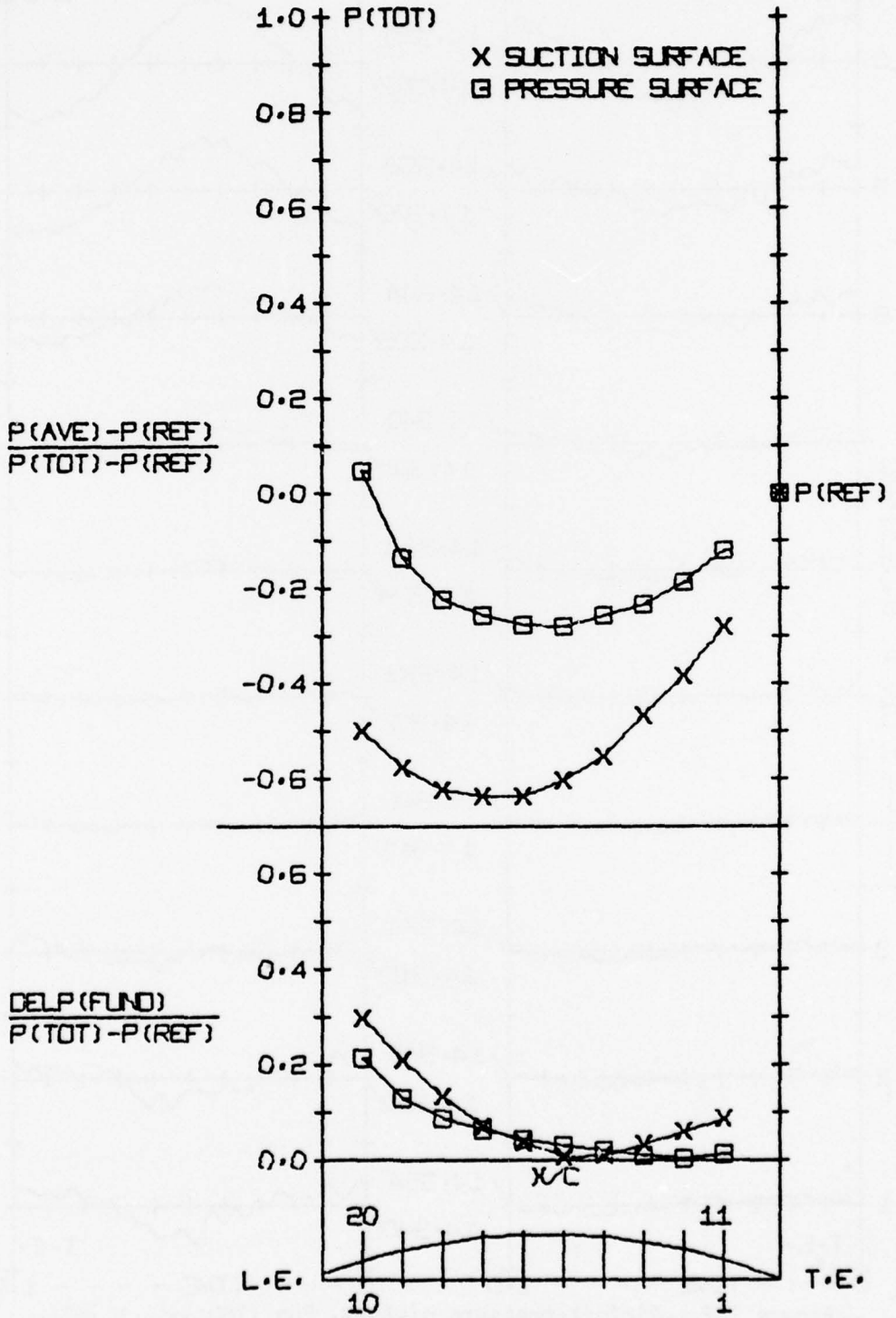

Figure 106. Normalized Pressure Profiles, Run 7710, α_m = 10°, V_N = 110 fps, f_t = 1.43 hz

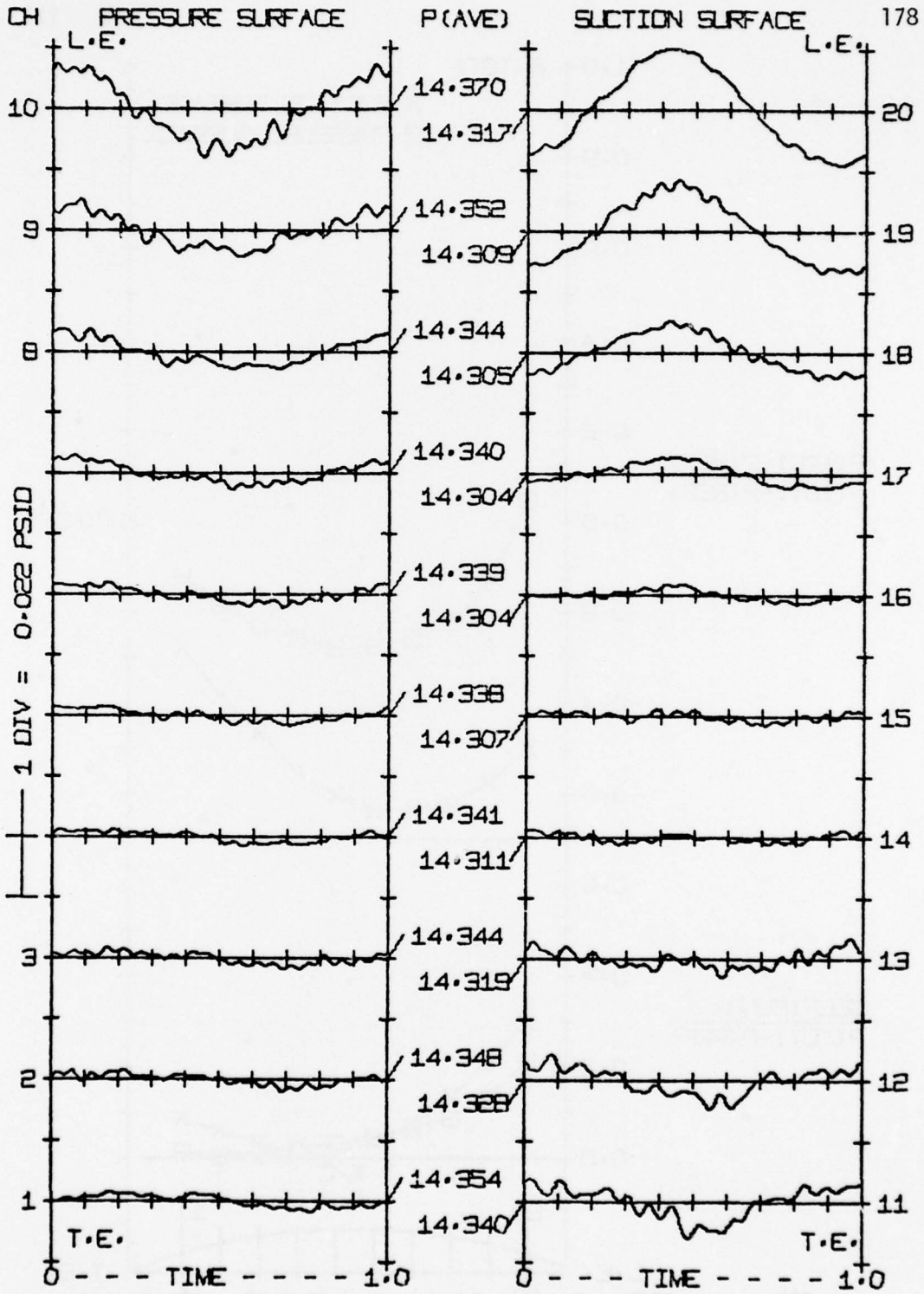

Figure 107. Airfoil pressure history, Run 7780, α_m = 10°, V_N = 110 fps, f_t = 16.2 hz

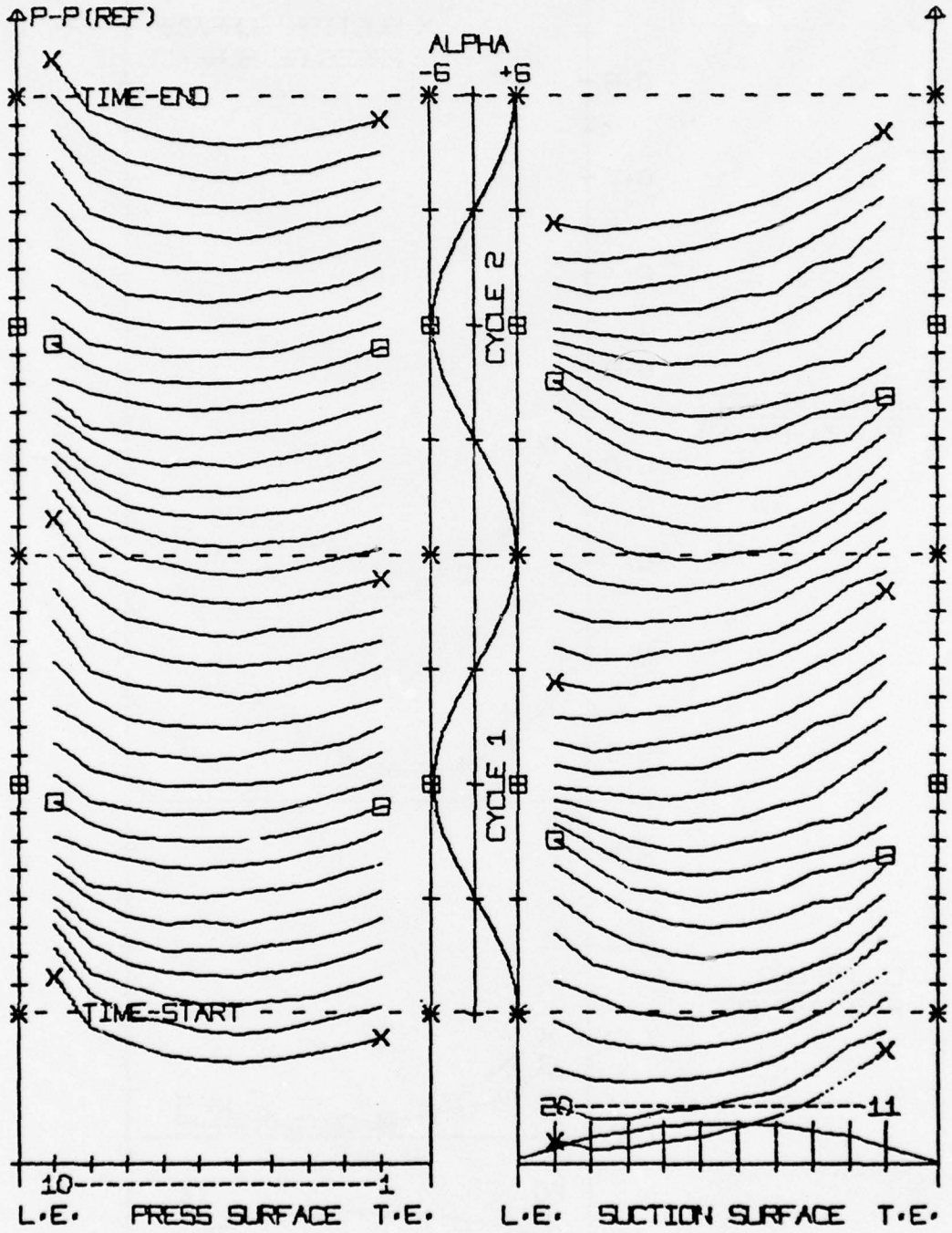

Figure 108. Time increment pressure profiles, Run 7780, α_m = 10°, V_N = 110 fps, f_t = 16.2 hz

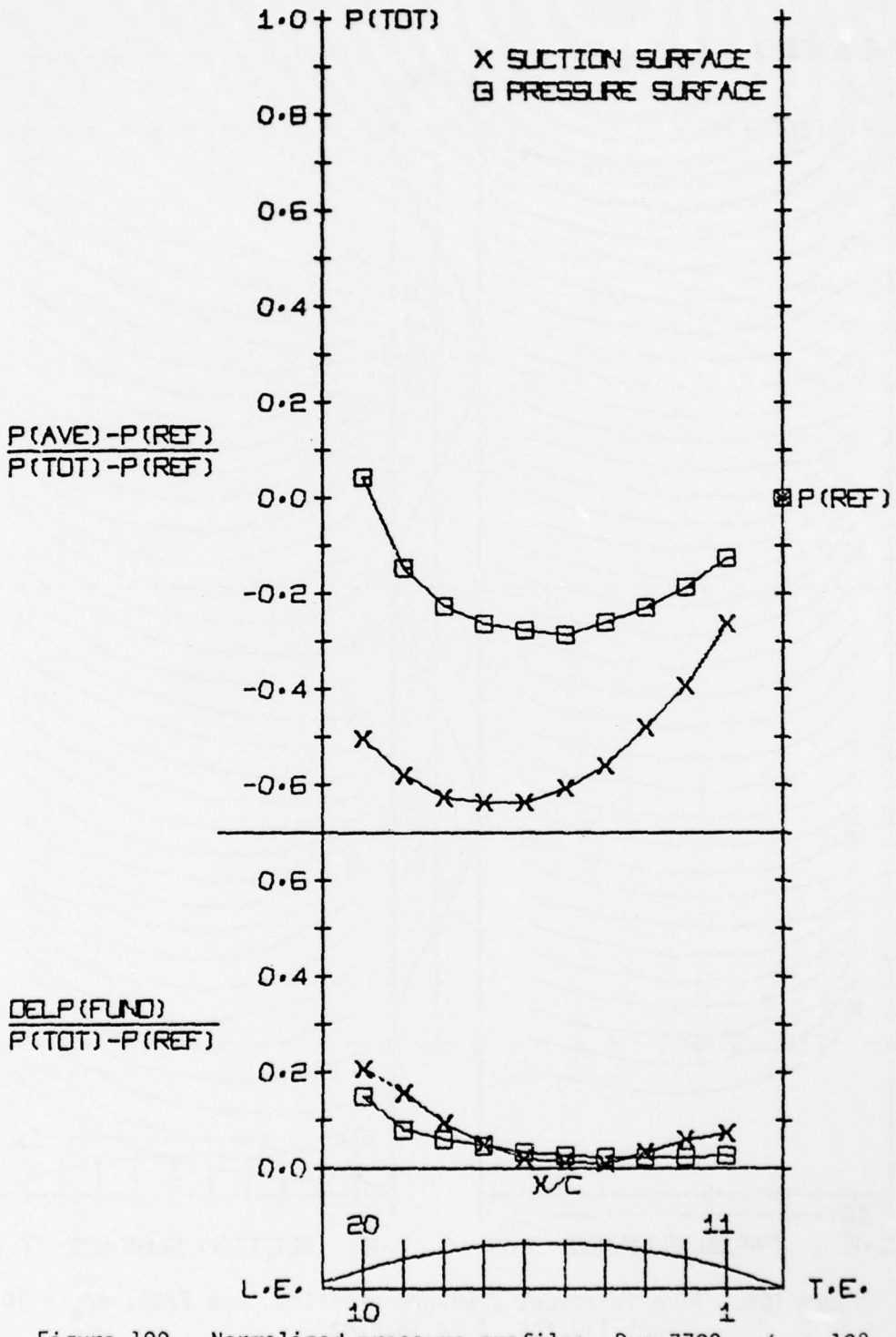

Figure 109. Normalized pressure profiles, Run 7780, α_m = 10°, V_N = 110 fps, f_t = 16.2 hz

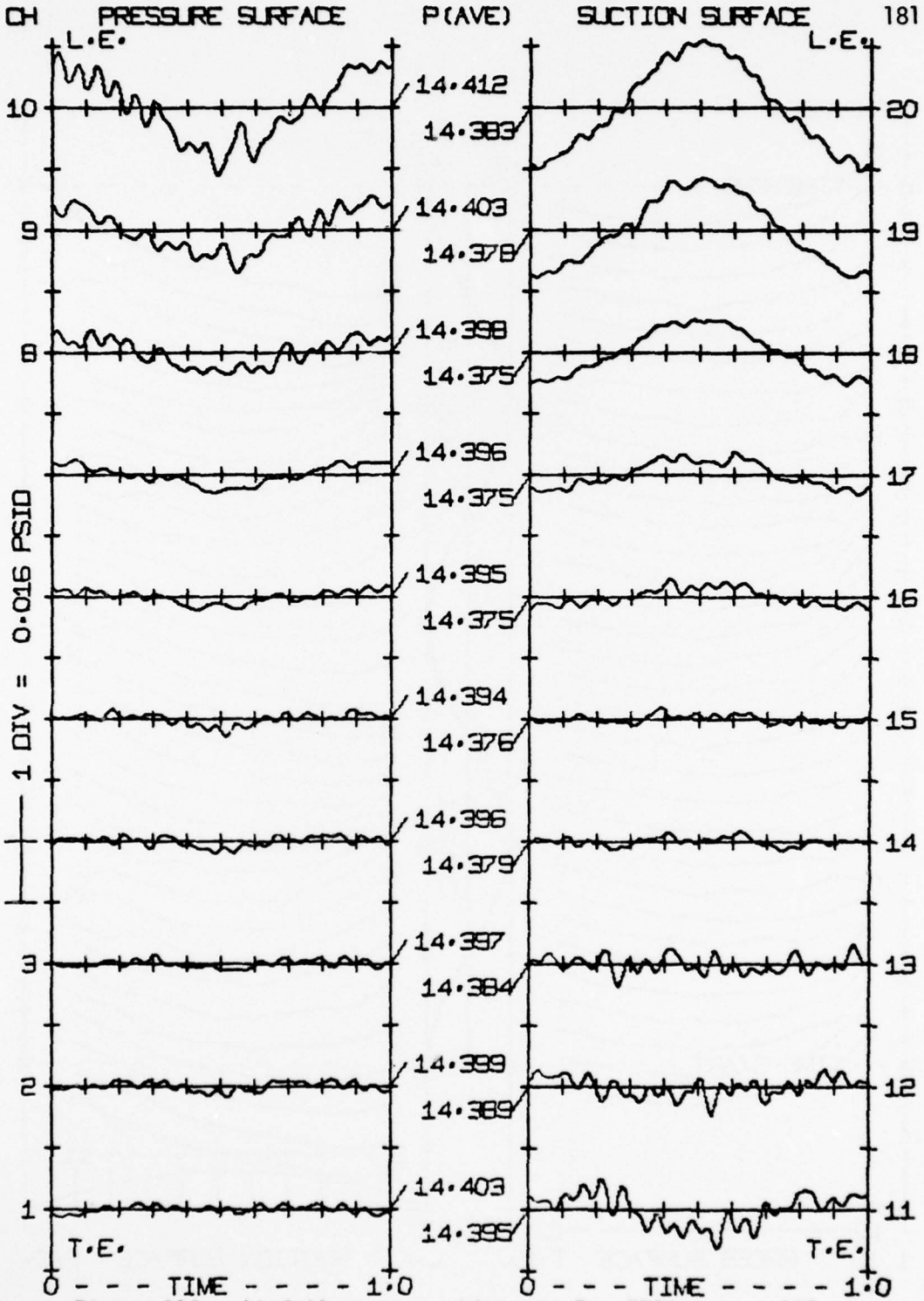

Figure 110. Airfoil pressure history, Run 7790, α_m = 10°, V_N = 82 fps, f_t = 0.2 hz

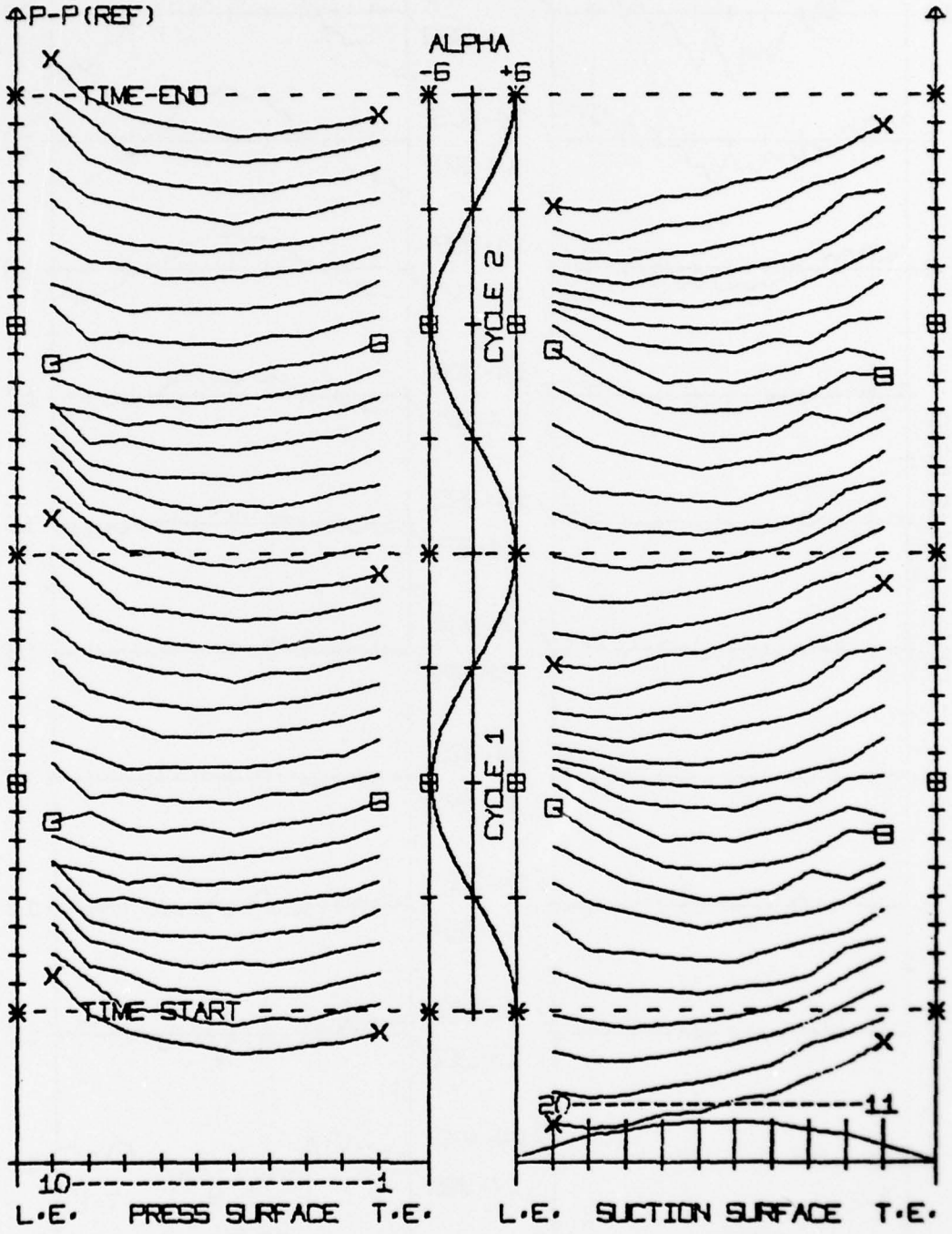

Figure 111. Time increment pressure profiles, Run 7790, α_m = 10°, V_N = 82 fps, f_t = 0.2 hz

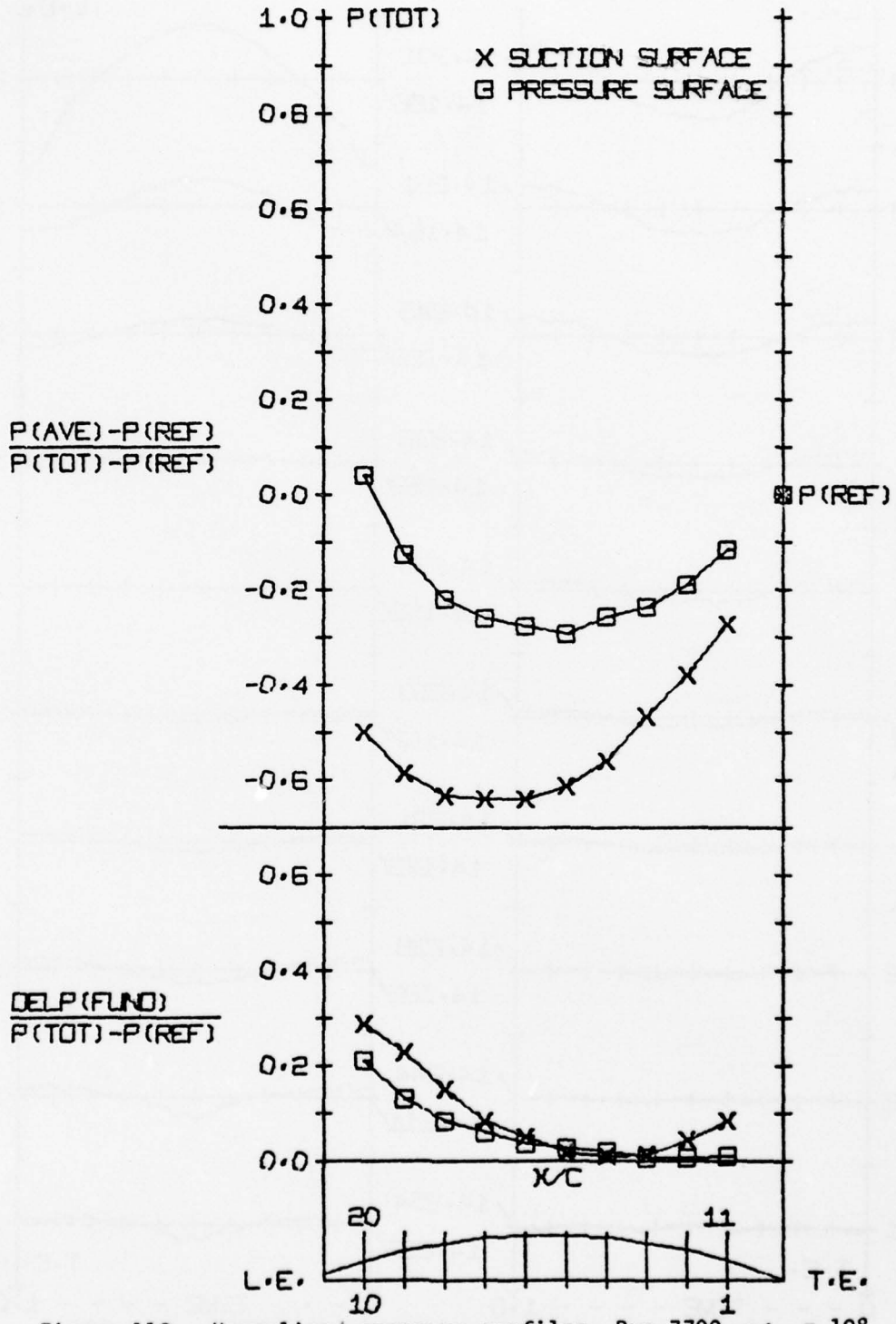

Figure 112. Normalized pressure profiles, Run 7790, α_m = 10°, V_N = 82 fps, f_t = 0.2 hz

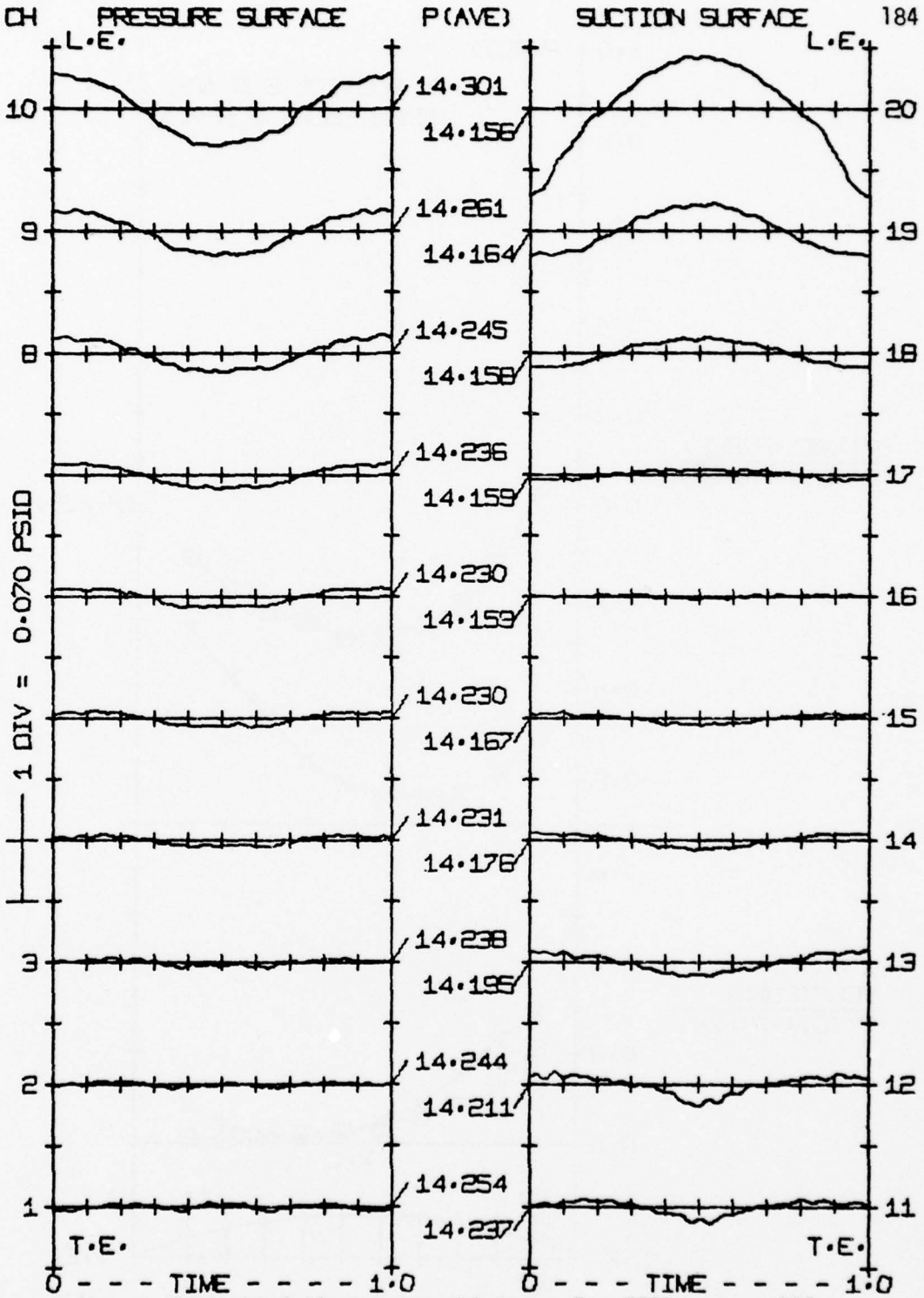

Figure 113. Airfoil pressure history. Run 7920, α_m = 12°, V_N = 150 fps, f_t = 0.2 hz

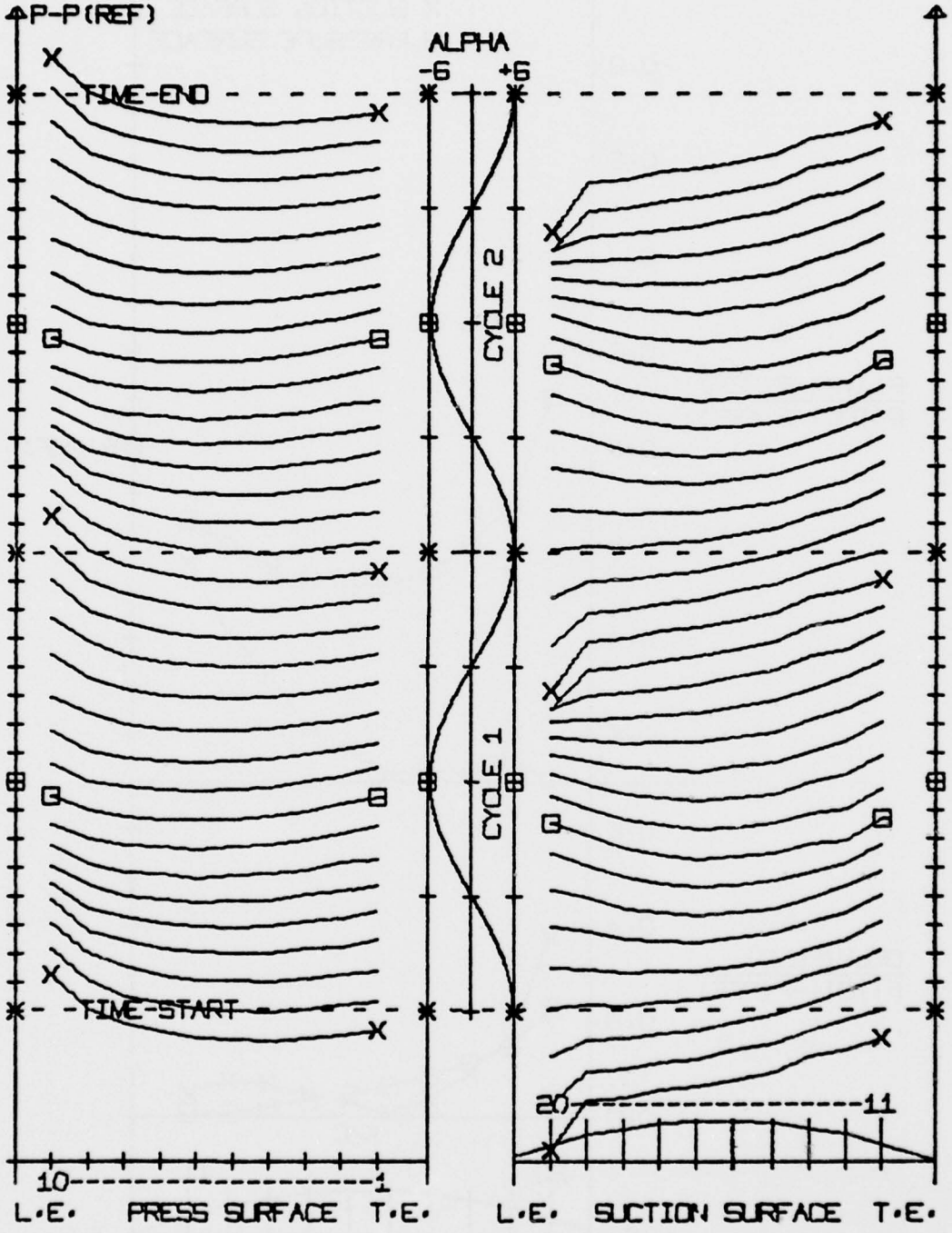

Figure 114. Time increment pressure profiles, Run 7920, α_m = 12°, V_N = 150 fps, f_t = 0.2 hz

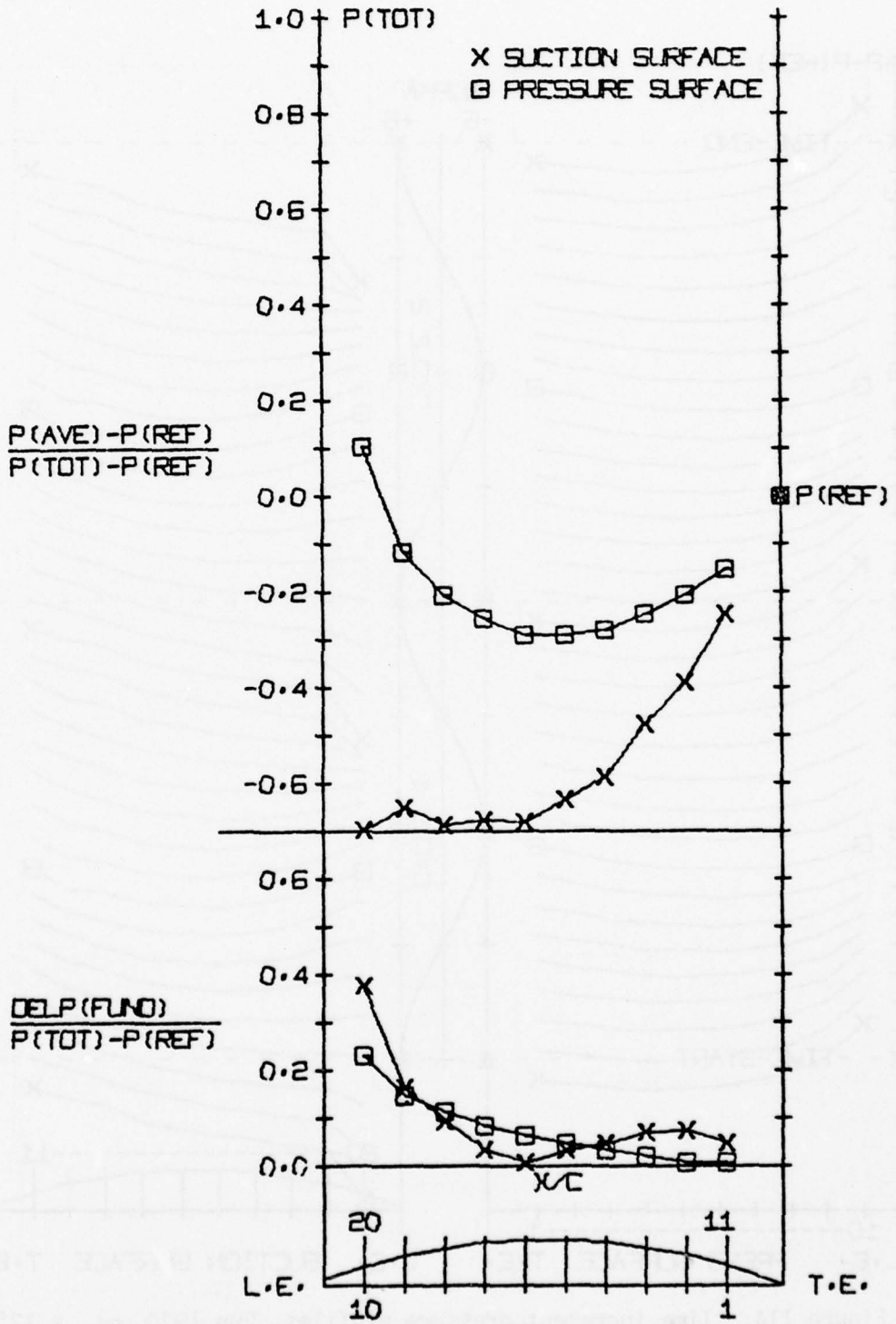

Figure 115. Normalized pressure profiles, Run 7920, α_m = 12°, V_N = 150 fps, f_t = 0.2 hz

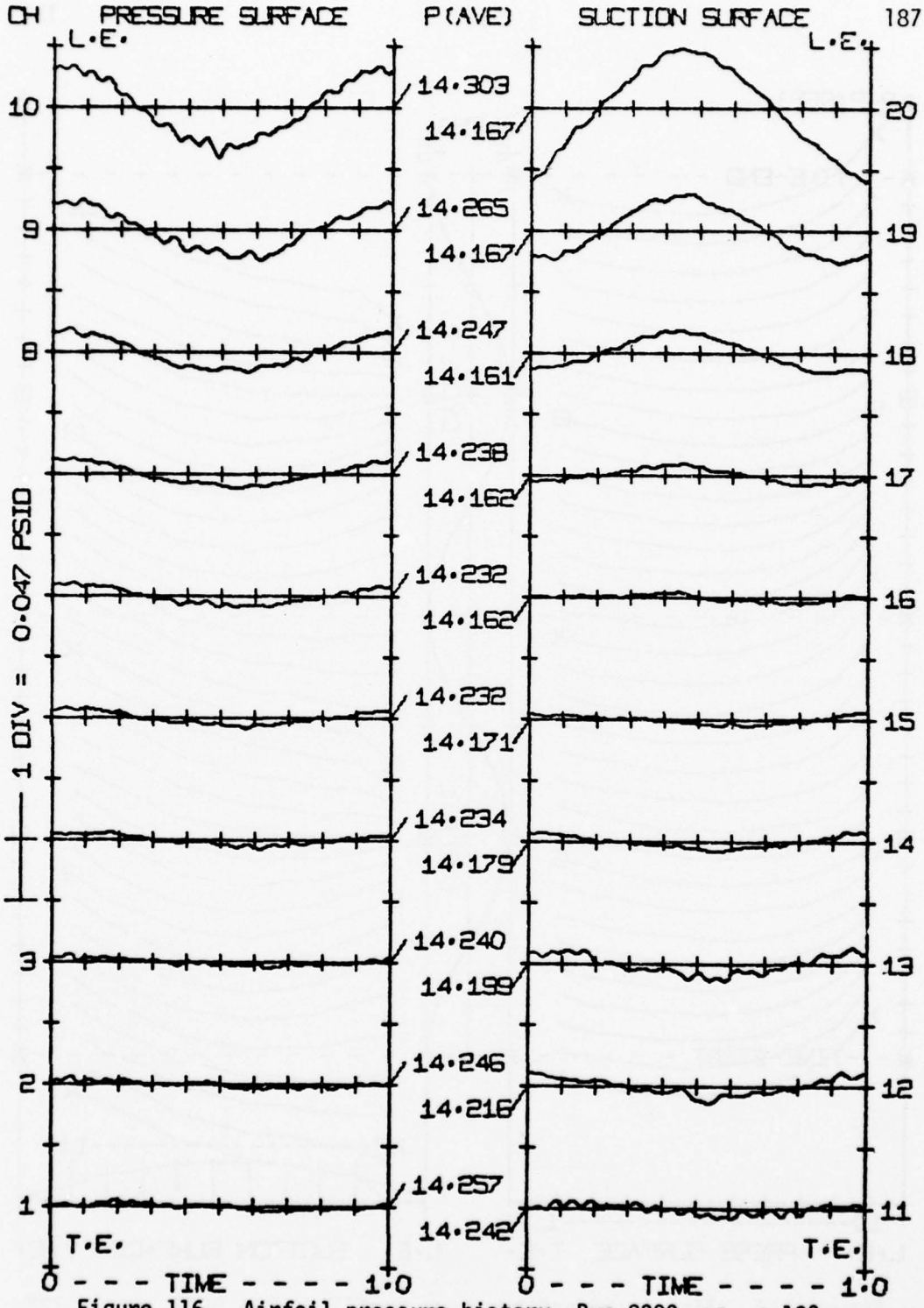

Figure 116. Airfoil pressure history, Run 8000, α_m = 12°, V_N = 150 fps, f_t = 16.1 hz

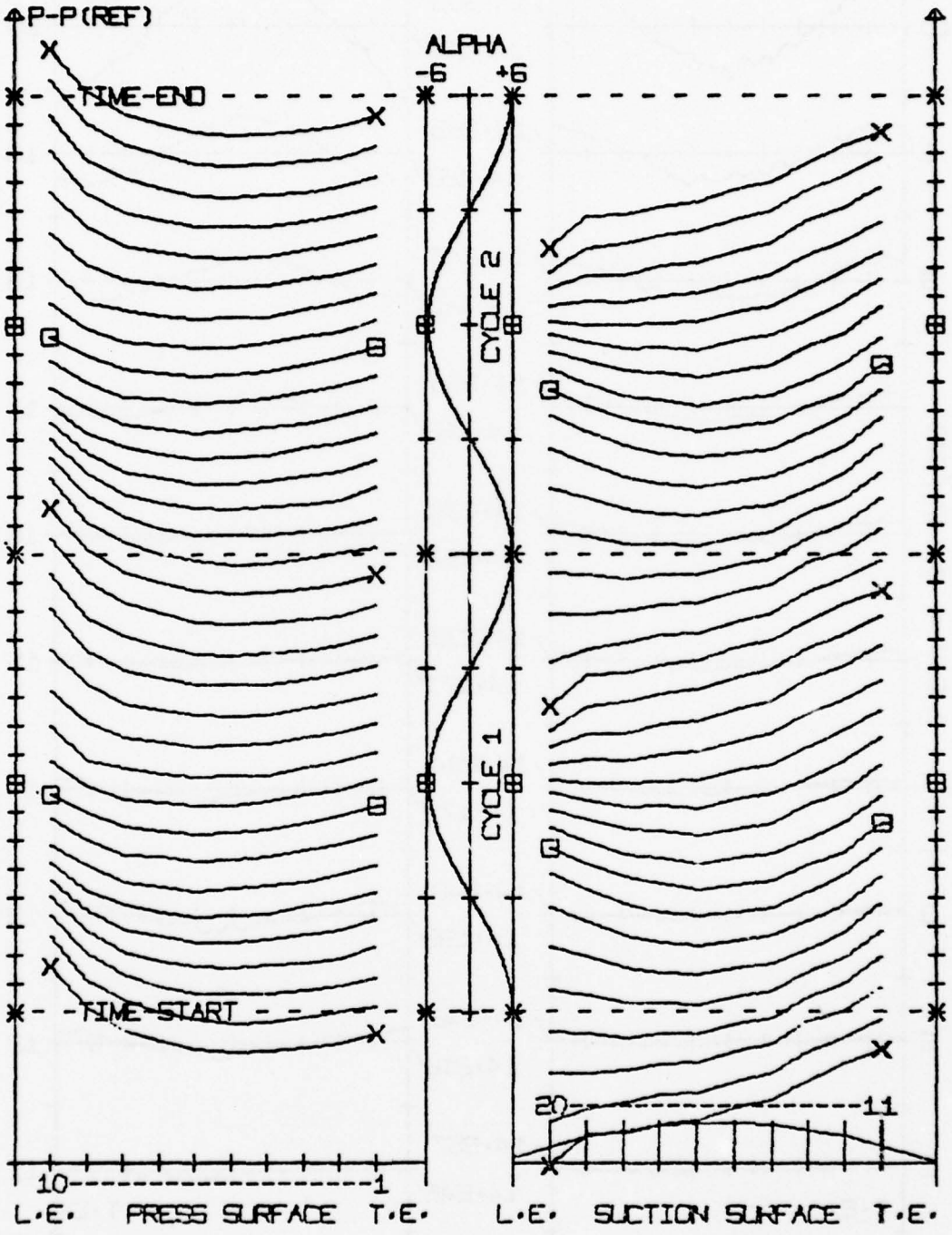

Figure 117. Time increment pressure profiles, Run 8000, α_m = 12°, V_N = 150 fps, f_t = 16.1 hz

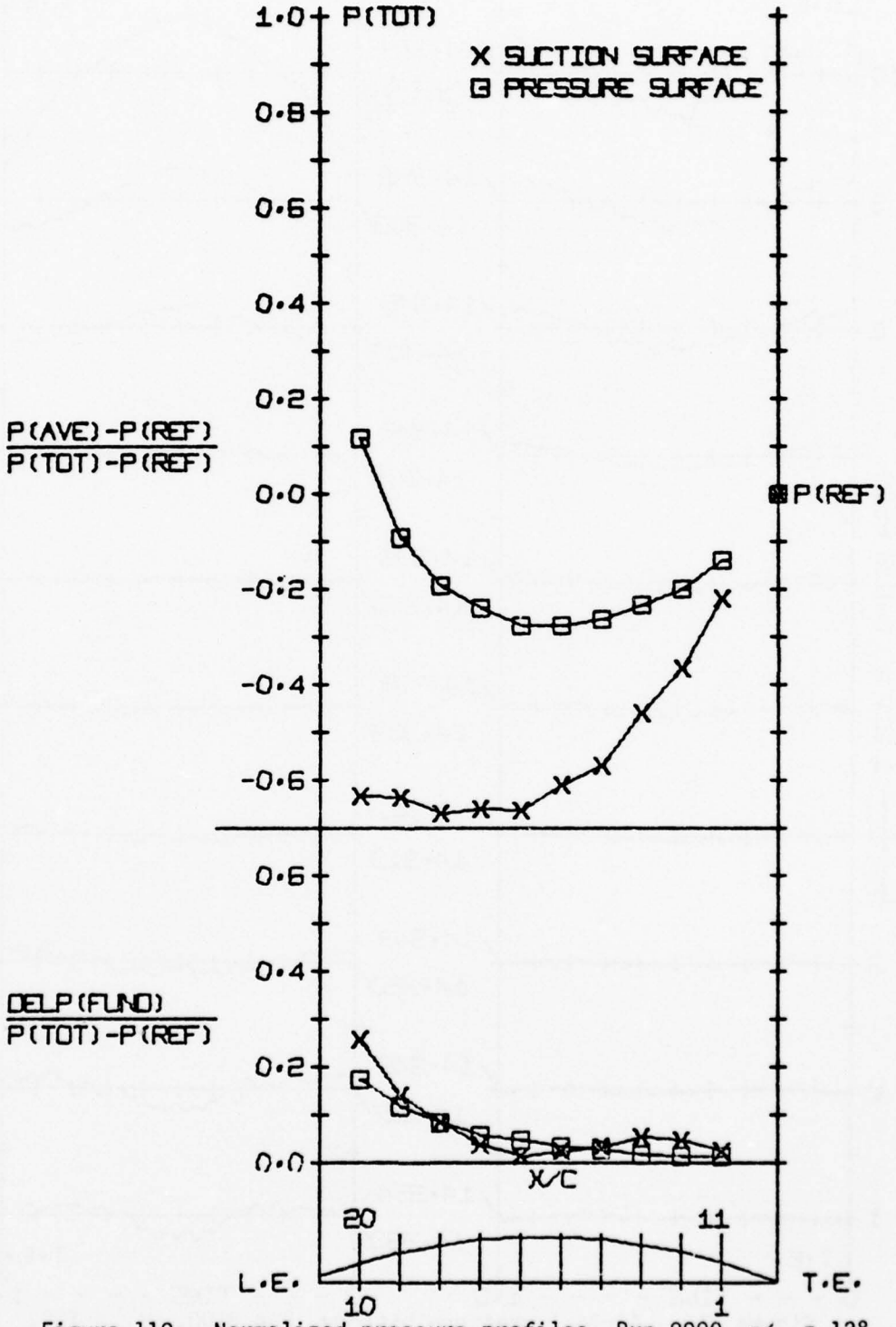

Figure 118. Normalized pressure profiles, Run 8000, α_m = 12°, V_N = 150 fps, f_t = 16.1 hz

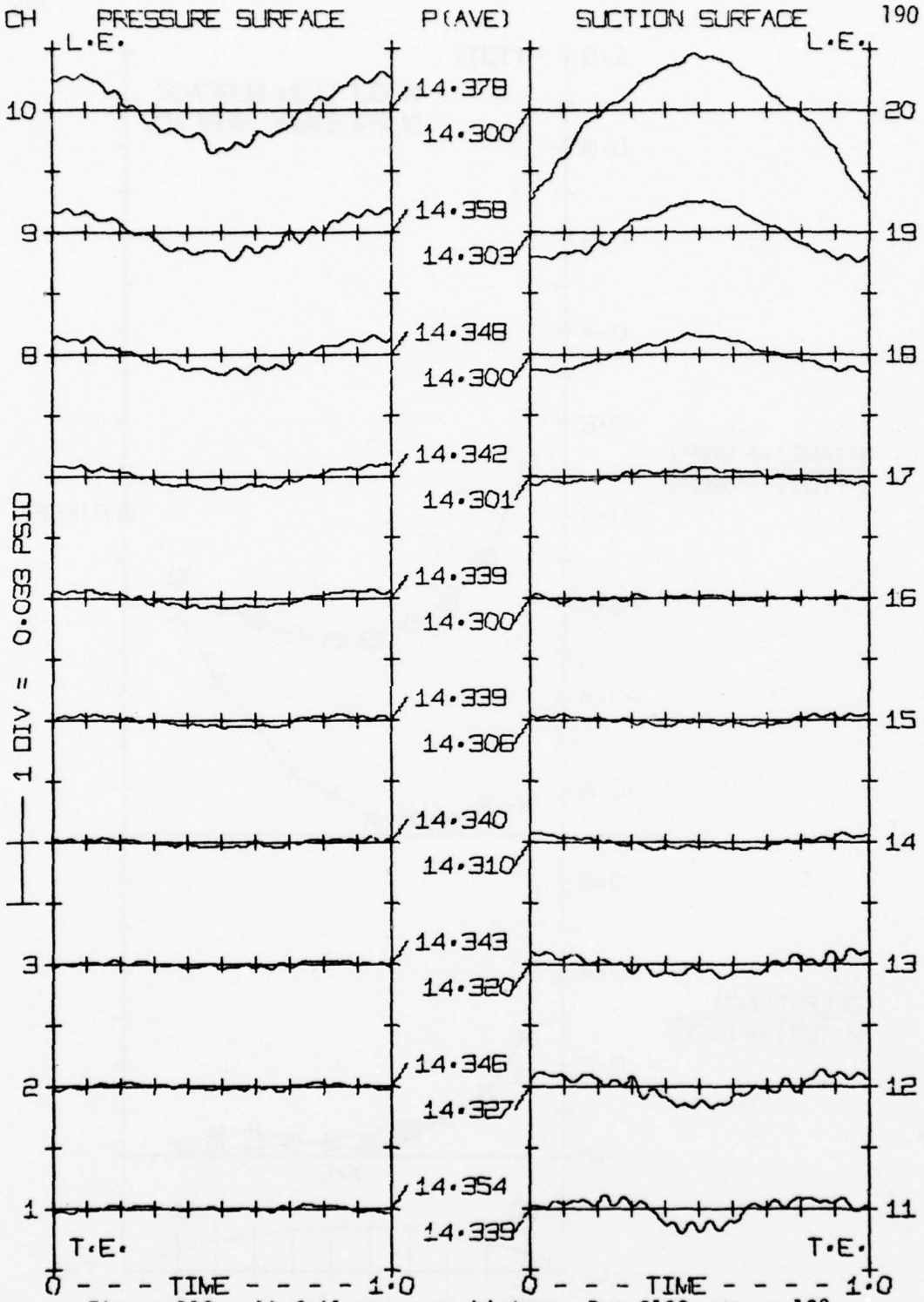

Figure 119. Airfoil pressure history, Run 8100, α_m = 12°, V_N = 110 fps, f_t = 0.2 hz

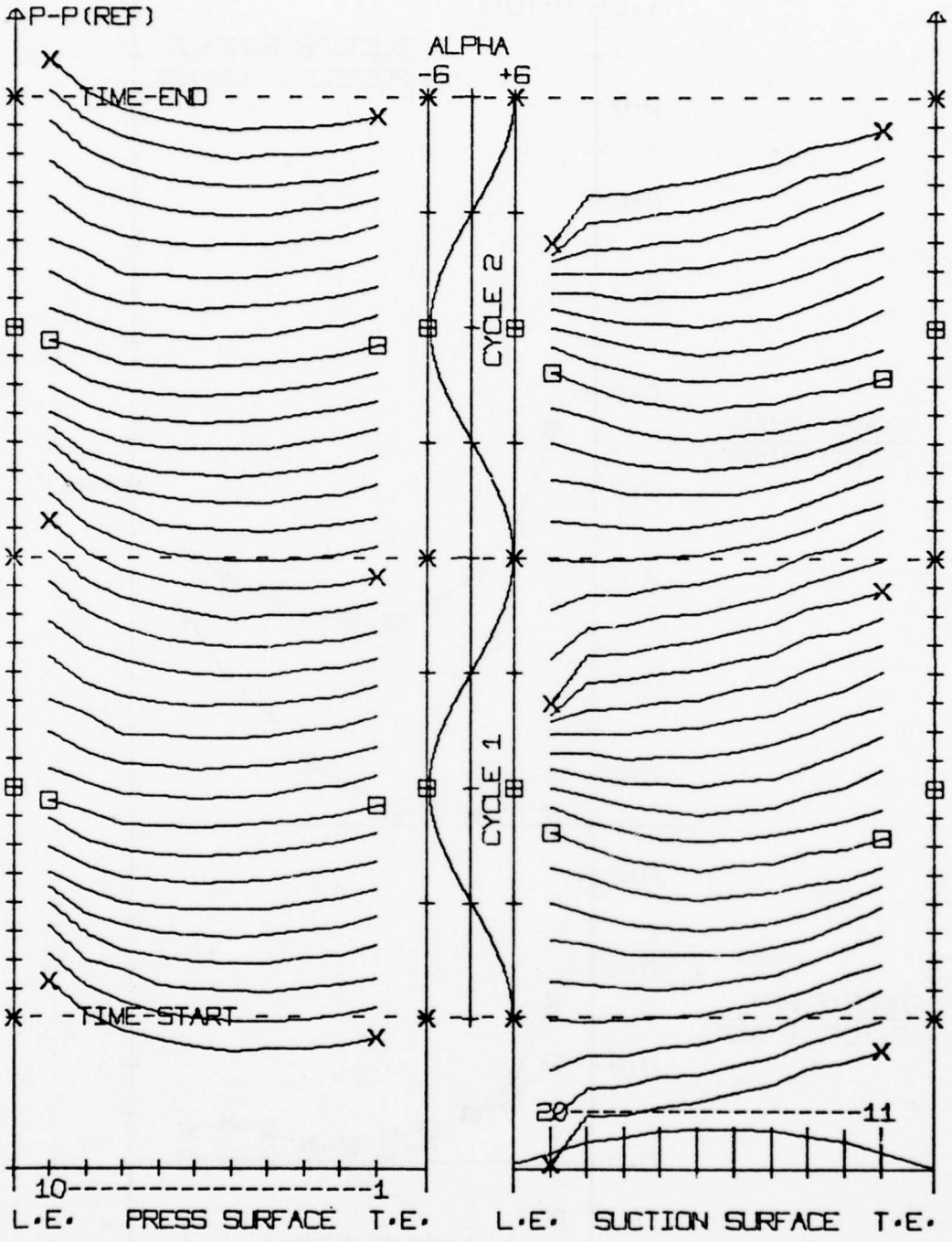

Figure 120. Time increment pressure profiles, Run 8100, α_m = 12°, V_N = 110 fps, f_t = 0.2 hz

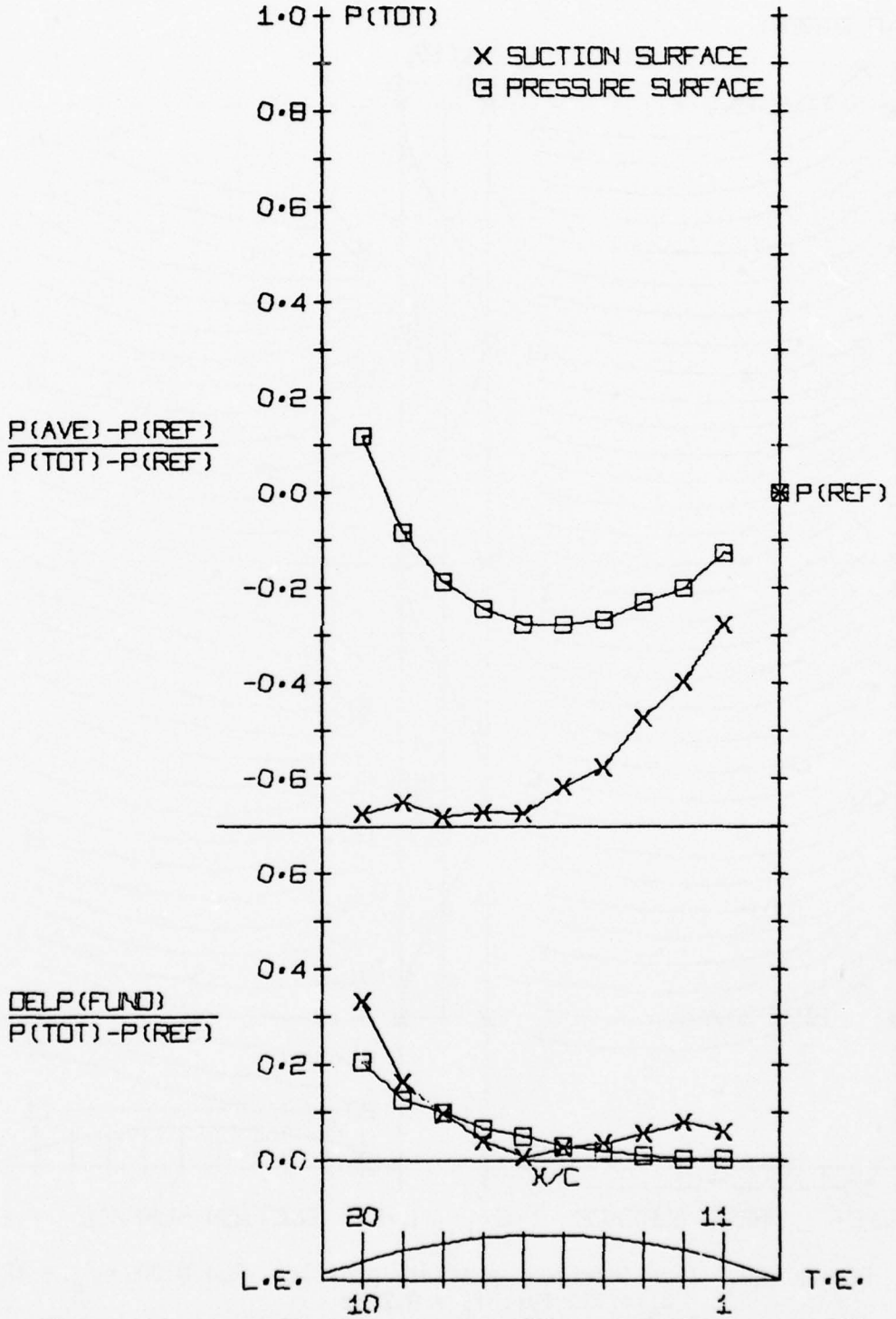

Figure 121. Normalized pressure profiles, Run 8100, α_m = 12°, V_N = 110 fps, f_t = 0.2 hz

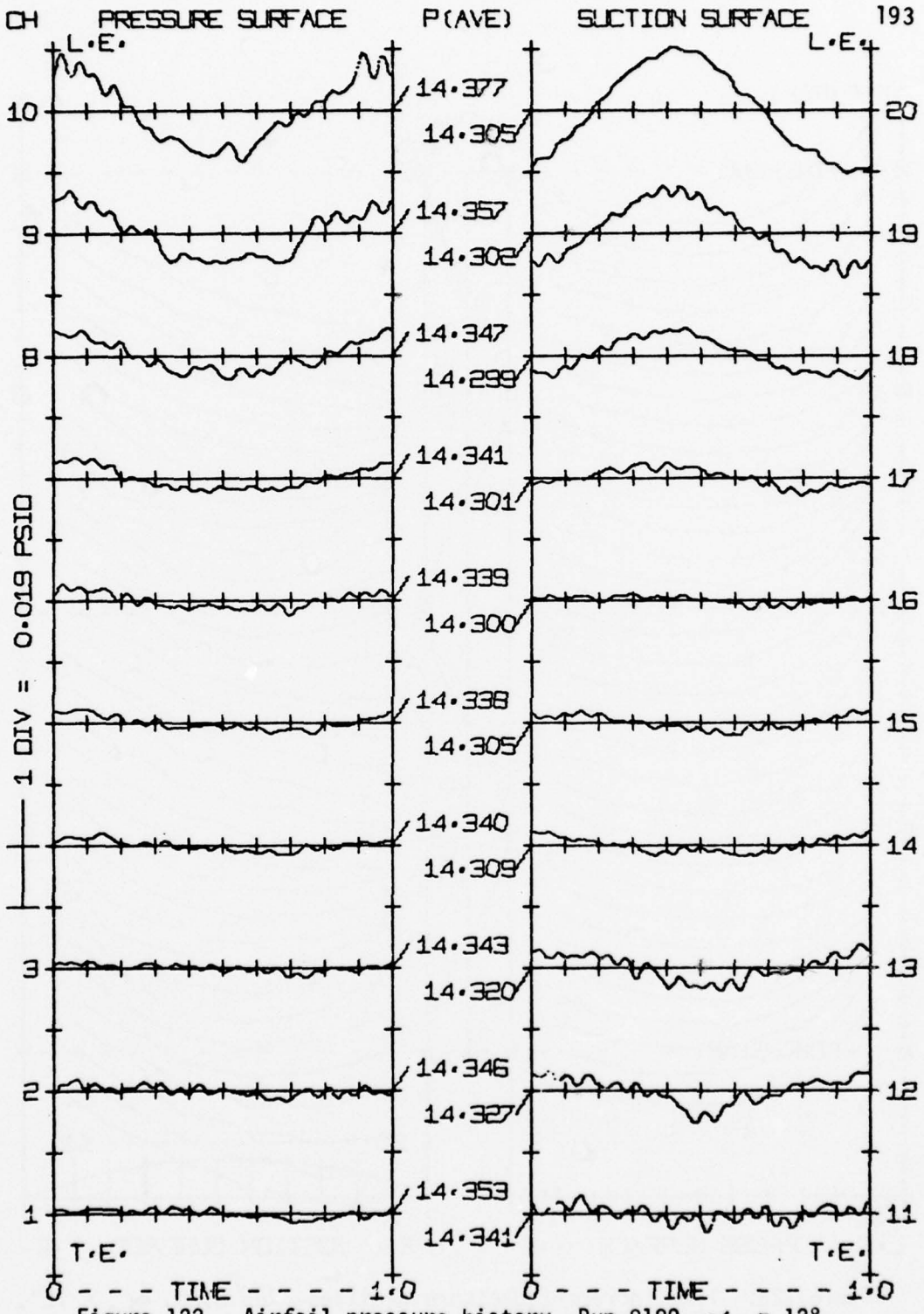

Figure 122. Airfoil pressure history, Run 8180, α_m = 12°, V_N = 110 fps, f_t = 16.2 hz

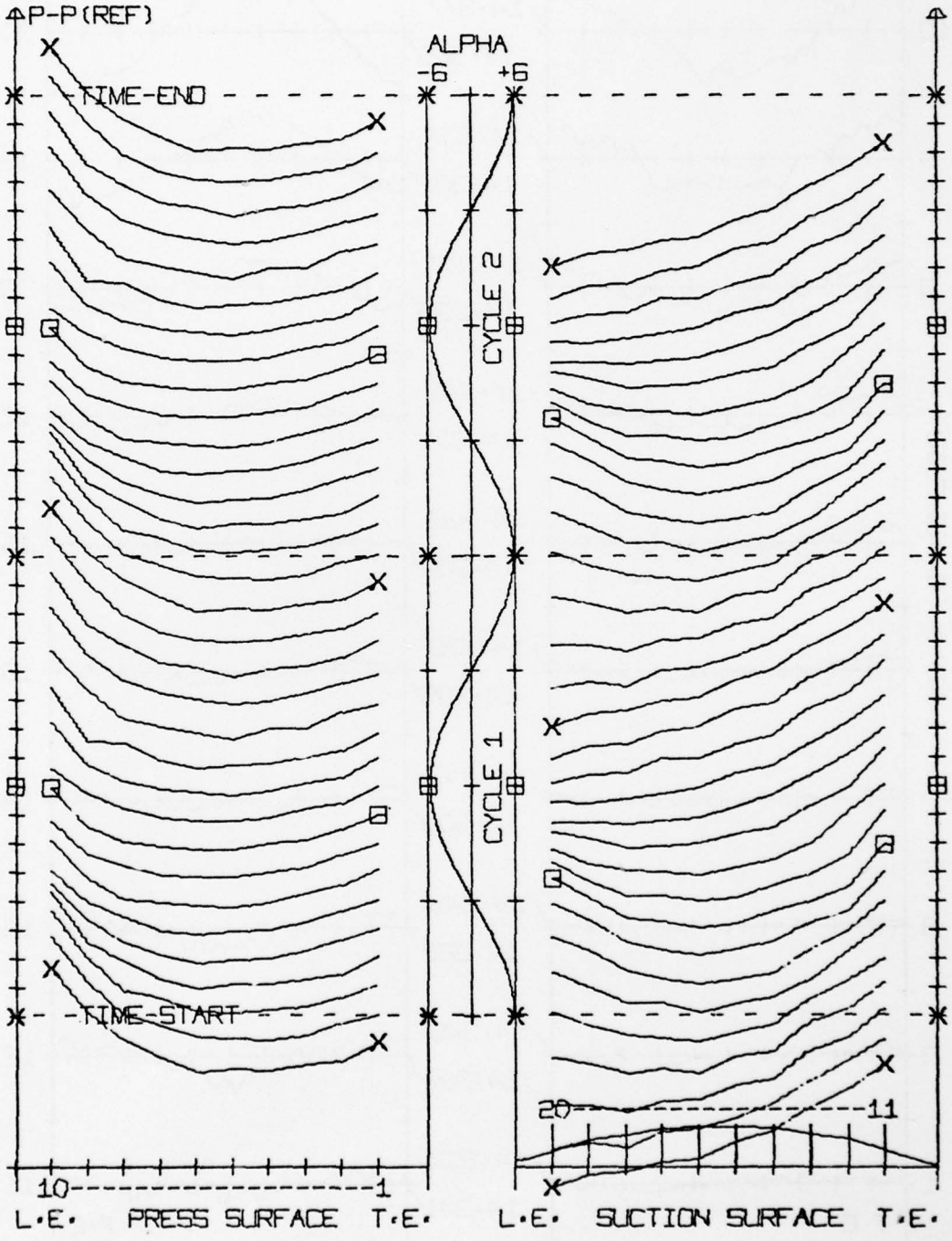

Figure 123. Time increment pressure profiles, Run 8180, α_m = 12°, V_N = 110 fps, f_t = 16.2 hz

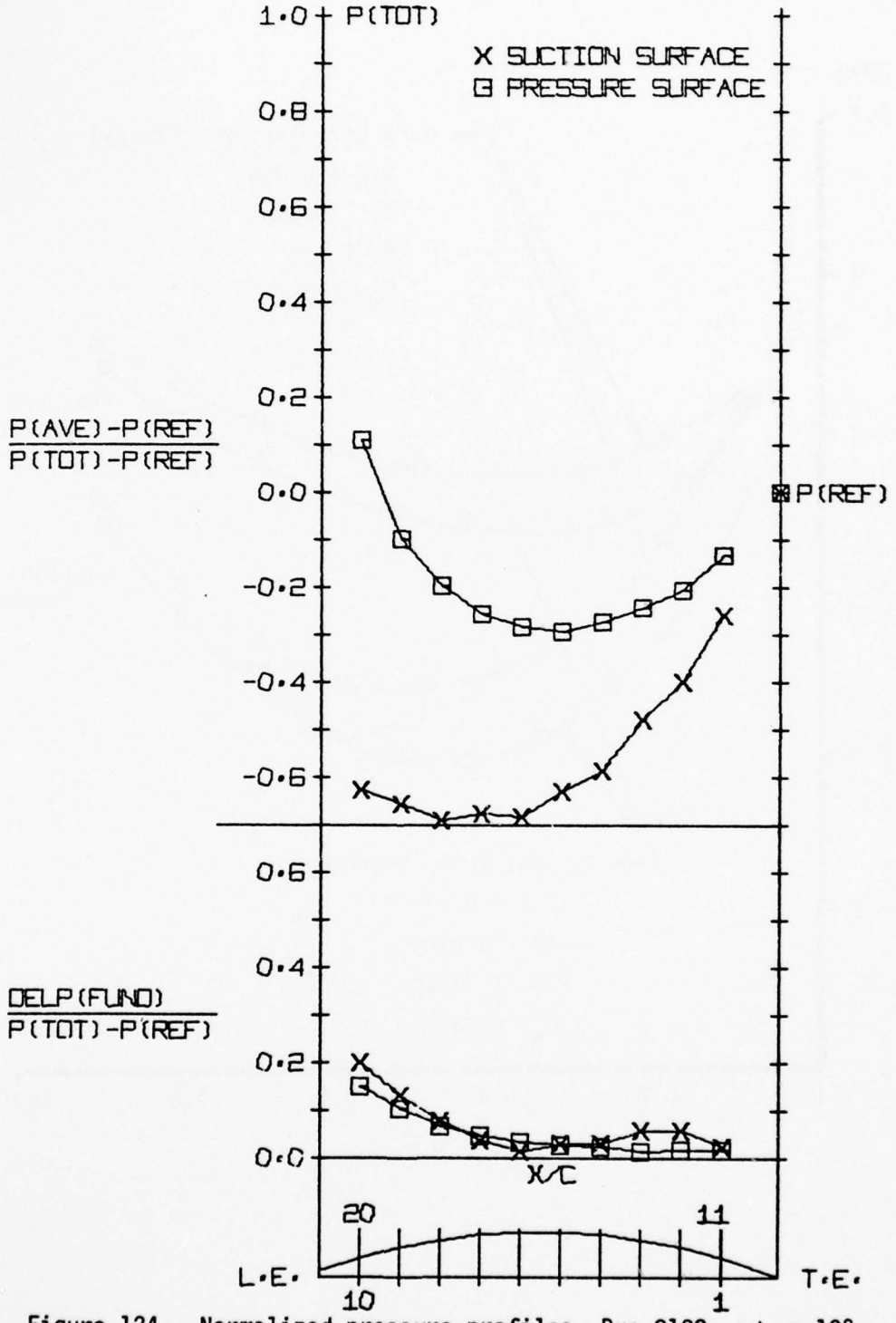

Figure 124. Normalized pressure profiles, Run 8180, α_m = 12°, V_N = 110 fps, f_t = 16.2 hz

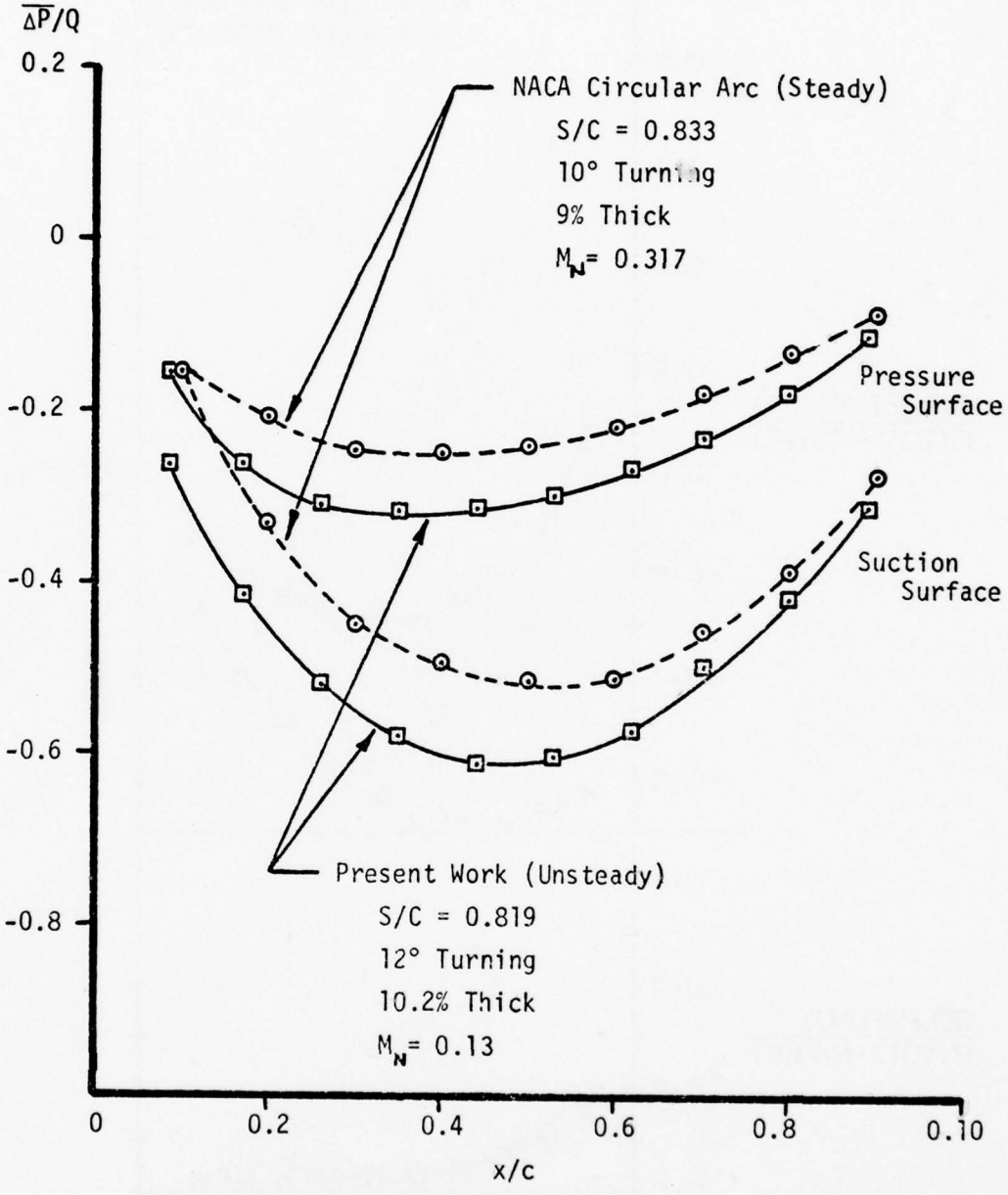

Figure 125. Comparison of steady pressure profile to steady cascade data

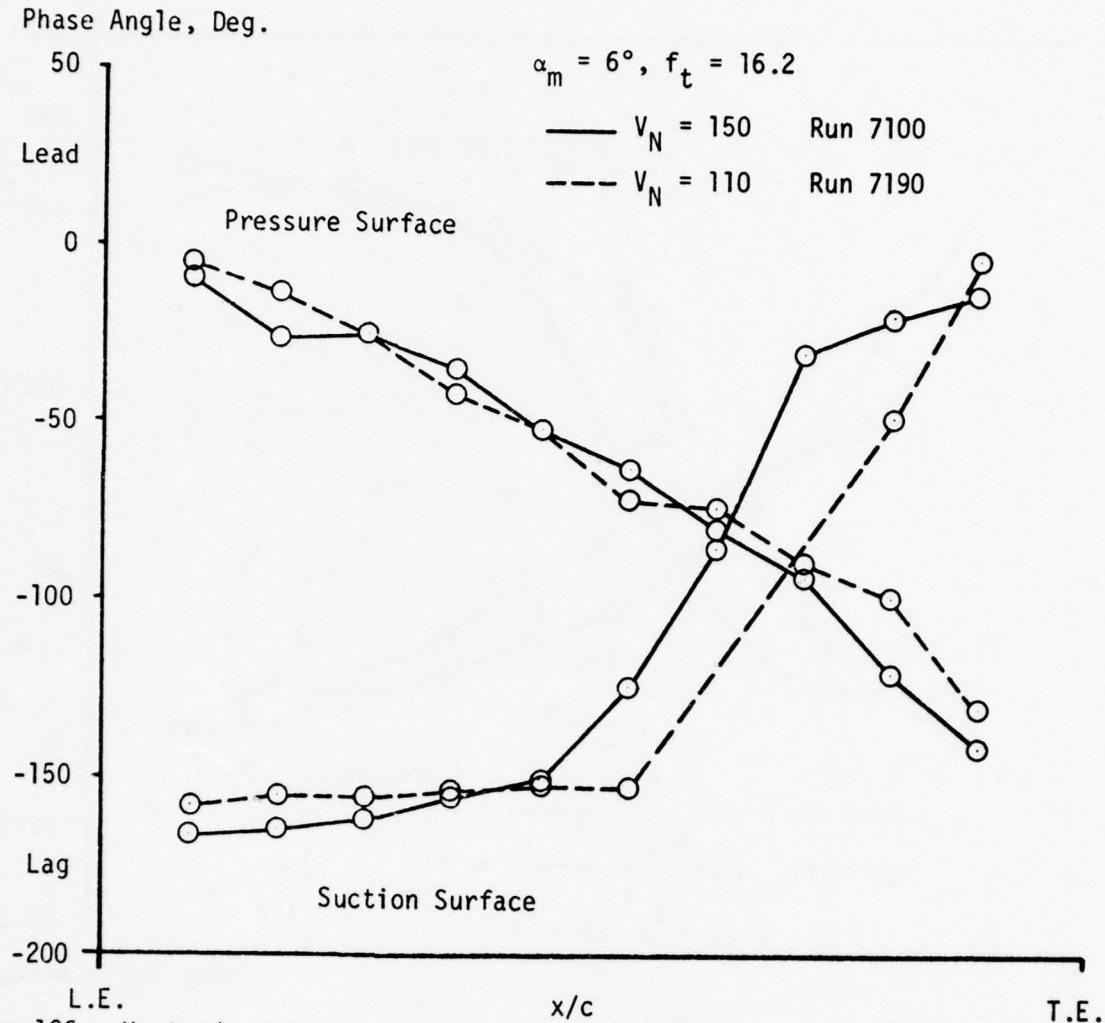

Figure 126. Unsteady pressure phase angle, variable velocity, α_m = 6°

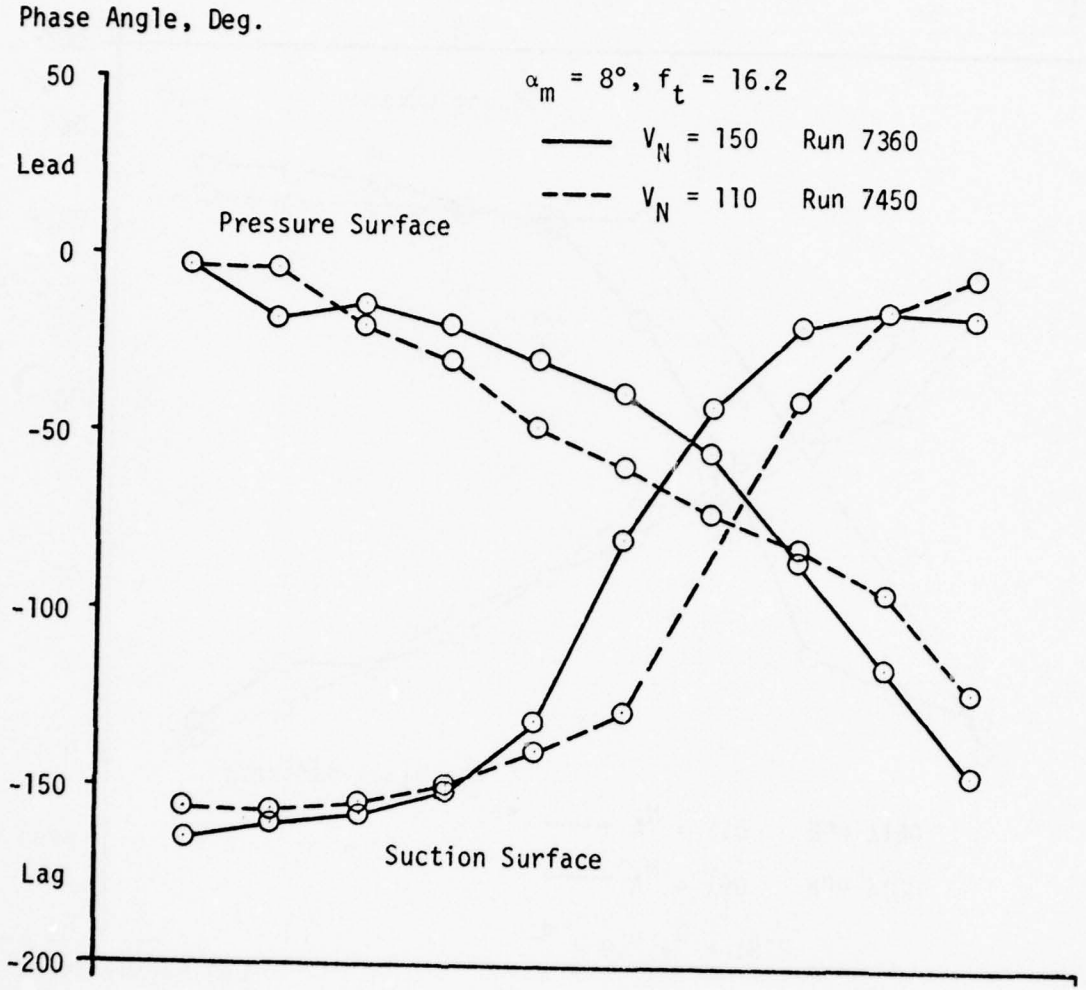

Figure 127. Unsteady pressure phase angle, variable velocity, α_m = 8°

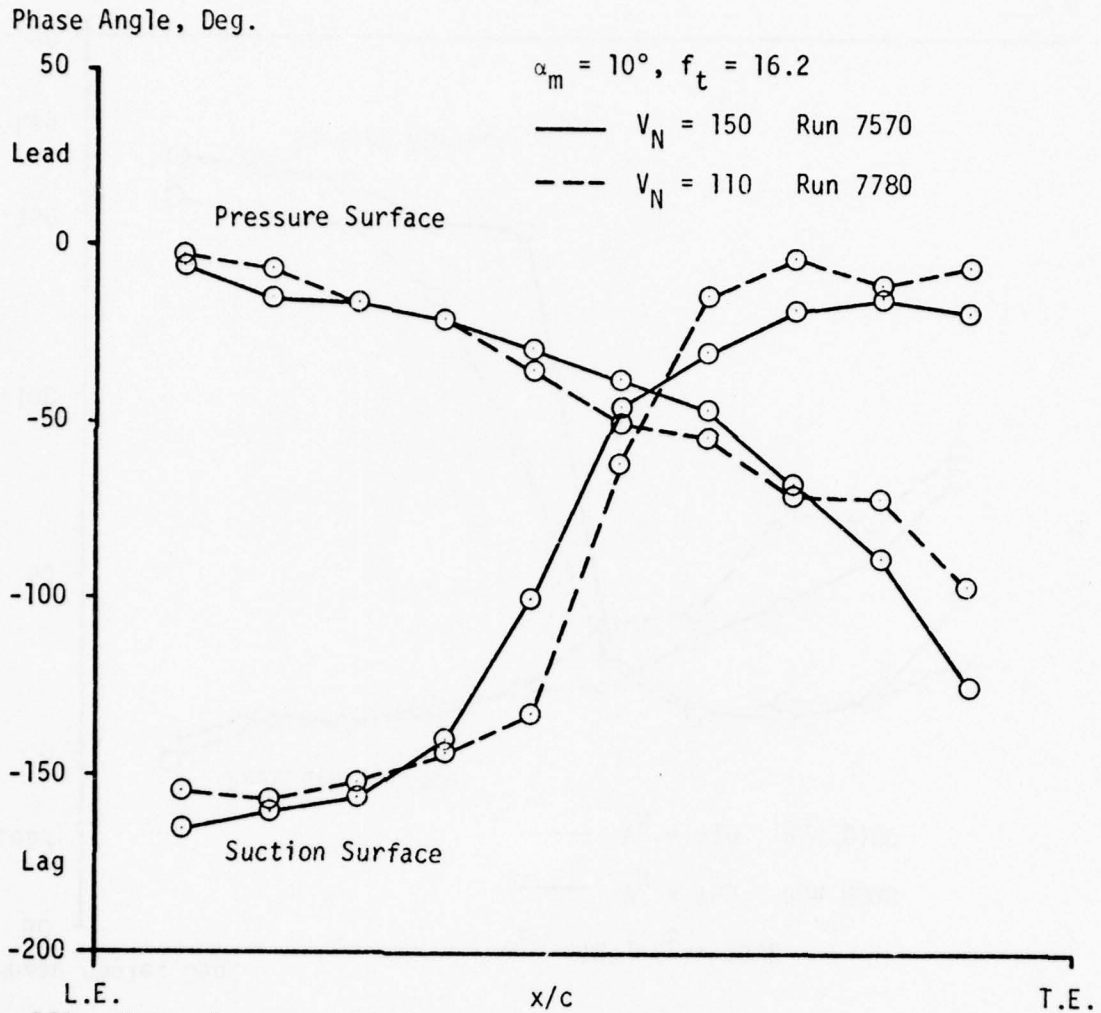

Figure 128. Unsteady pressure phase angle, variable velocity, α_m = 10°

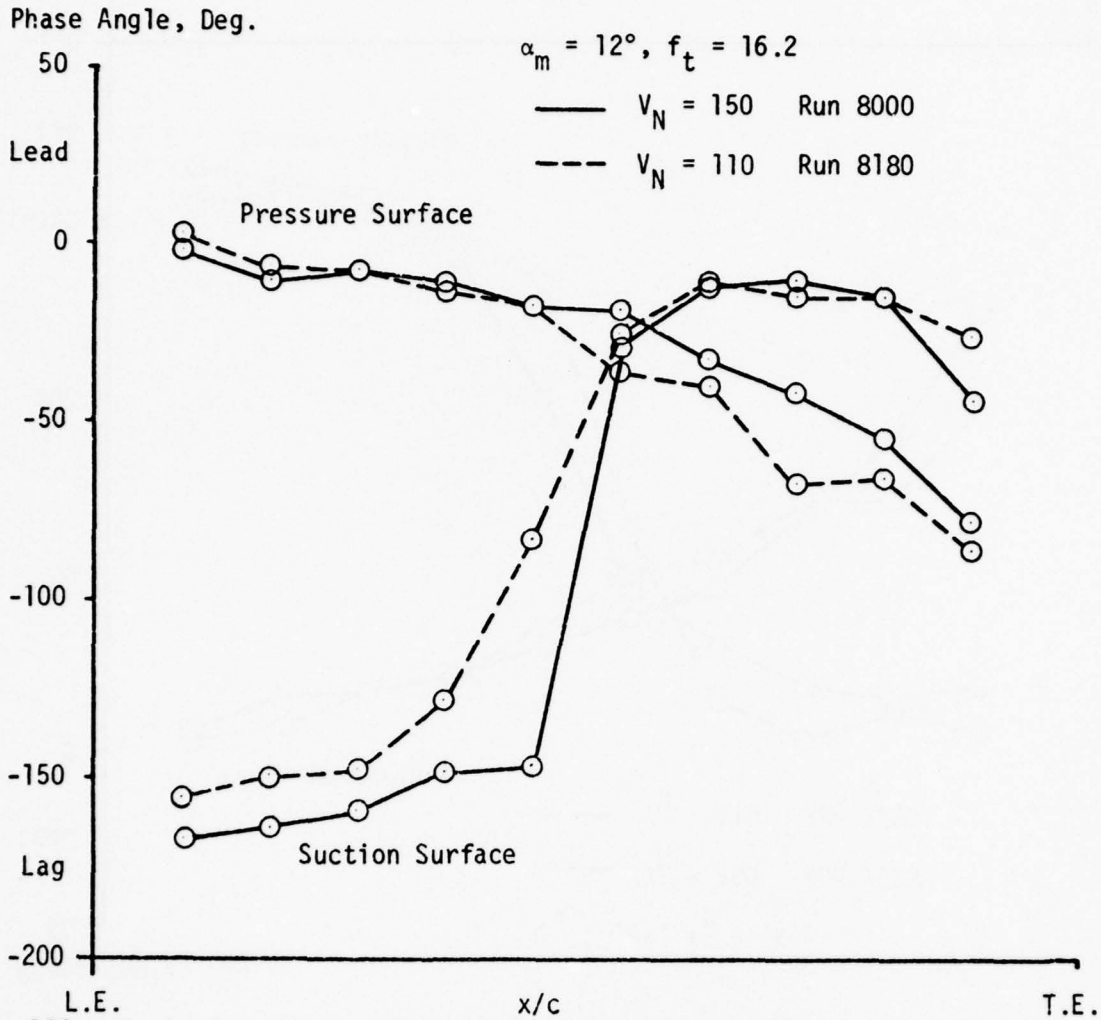

Figure 129. Unsteady pressure phase angle, variable velocity, α_m = 12°

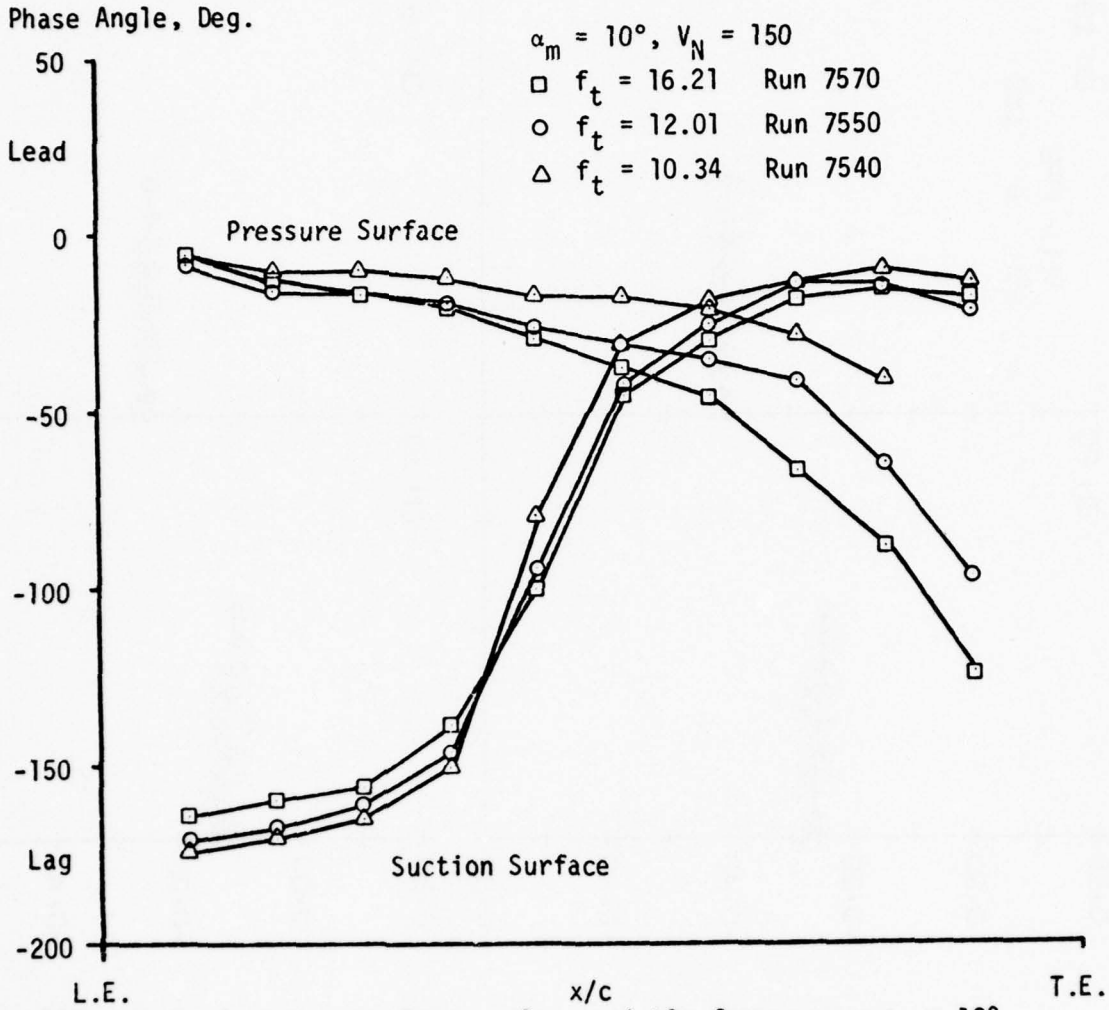

Figure 130. Unsteady pressure phase angle, variable frequency, α_m = 12°

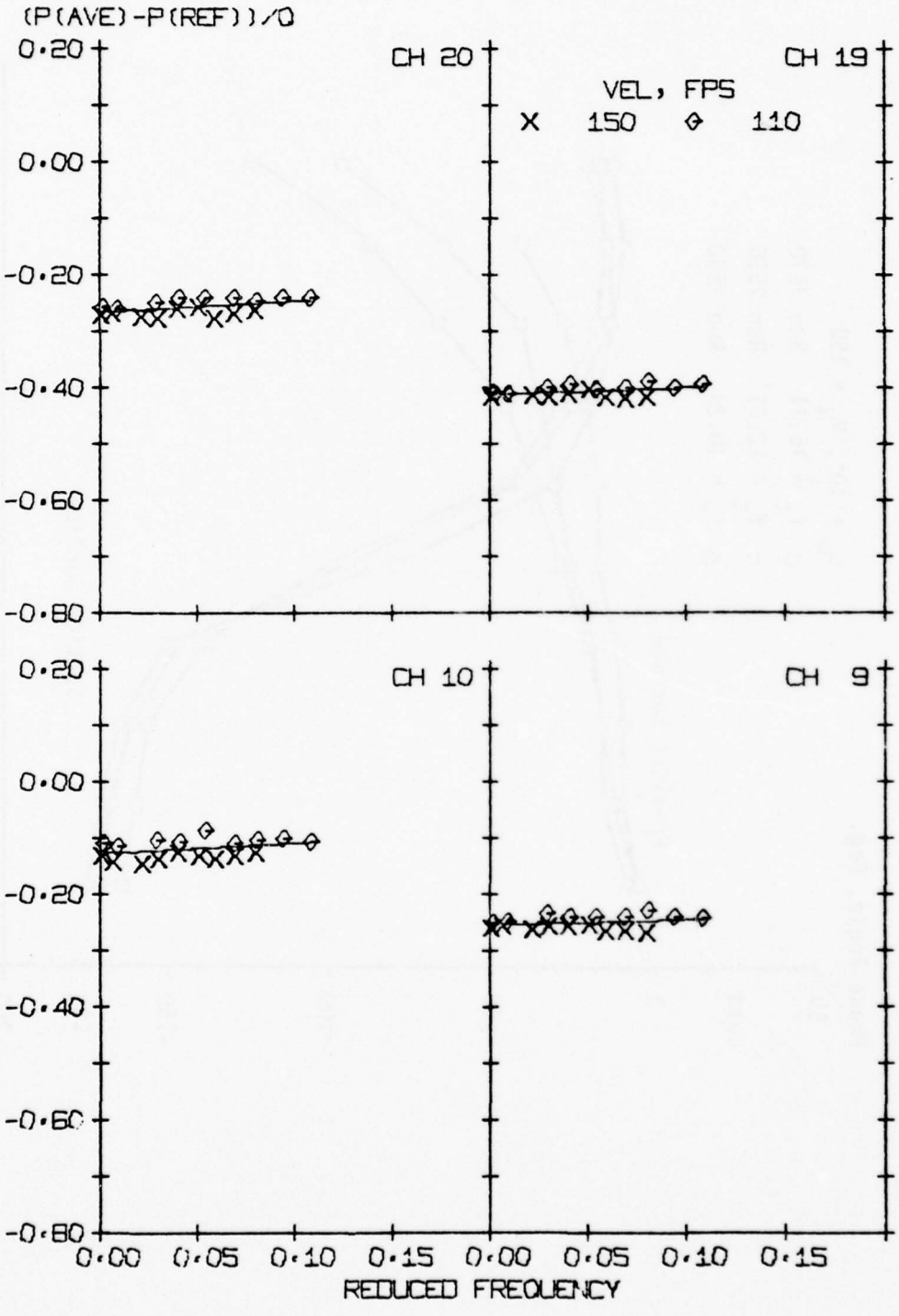

Figure 131. Normalized average pressure versus f_t, Group 1, $\alpha_m = 6°$

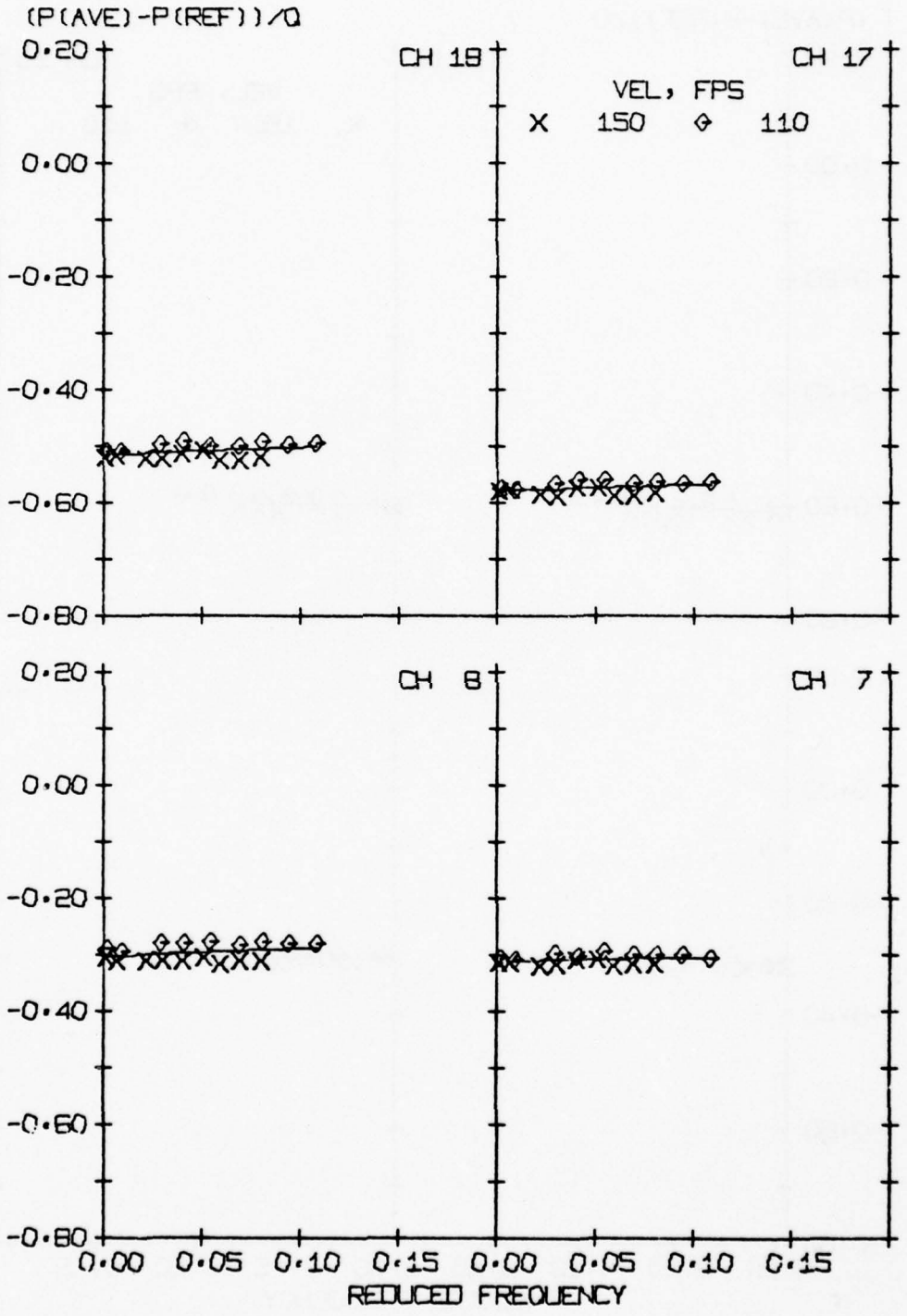

Figure 132. Normalized average pressure versus f_t, Group 2, $\alpha_m = 6°$

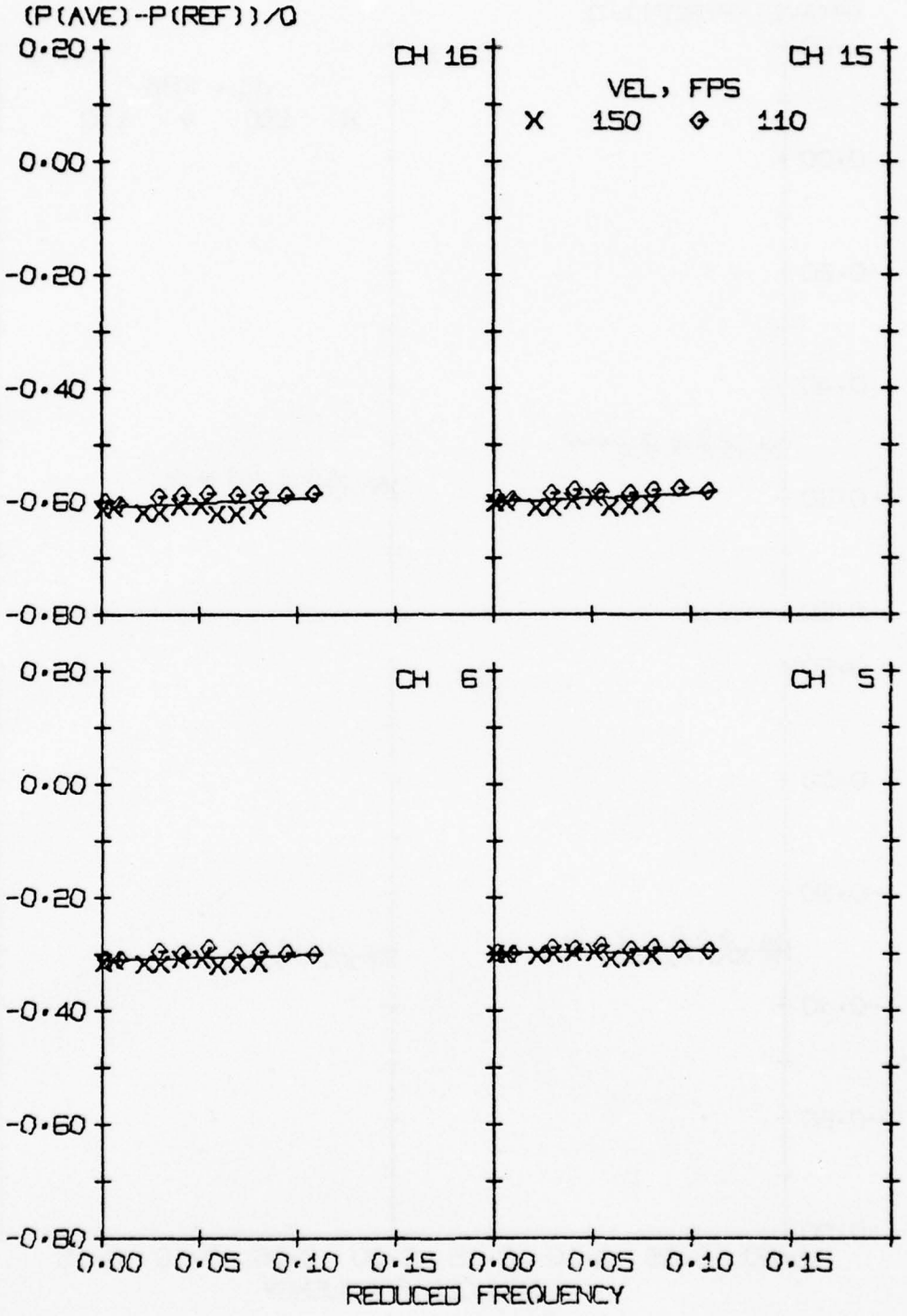

Figure 133. Normalized average pressure versus f_t, Group 3, $\alpha_m = 6°$

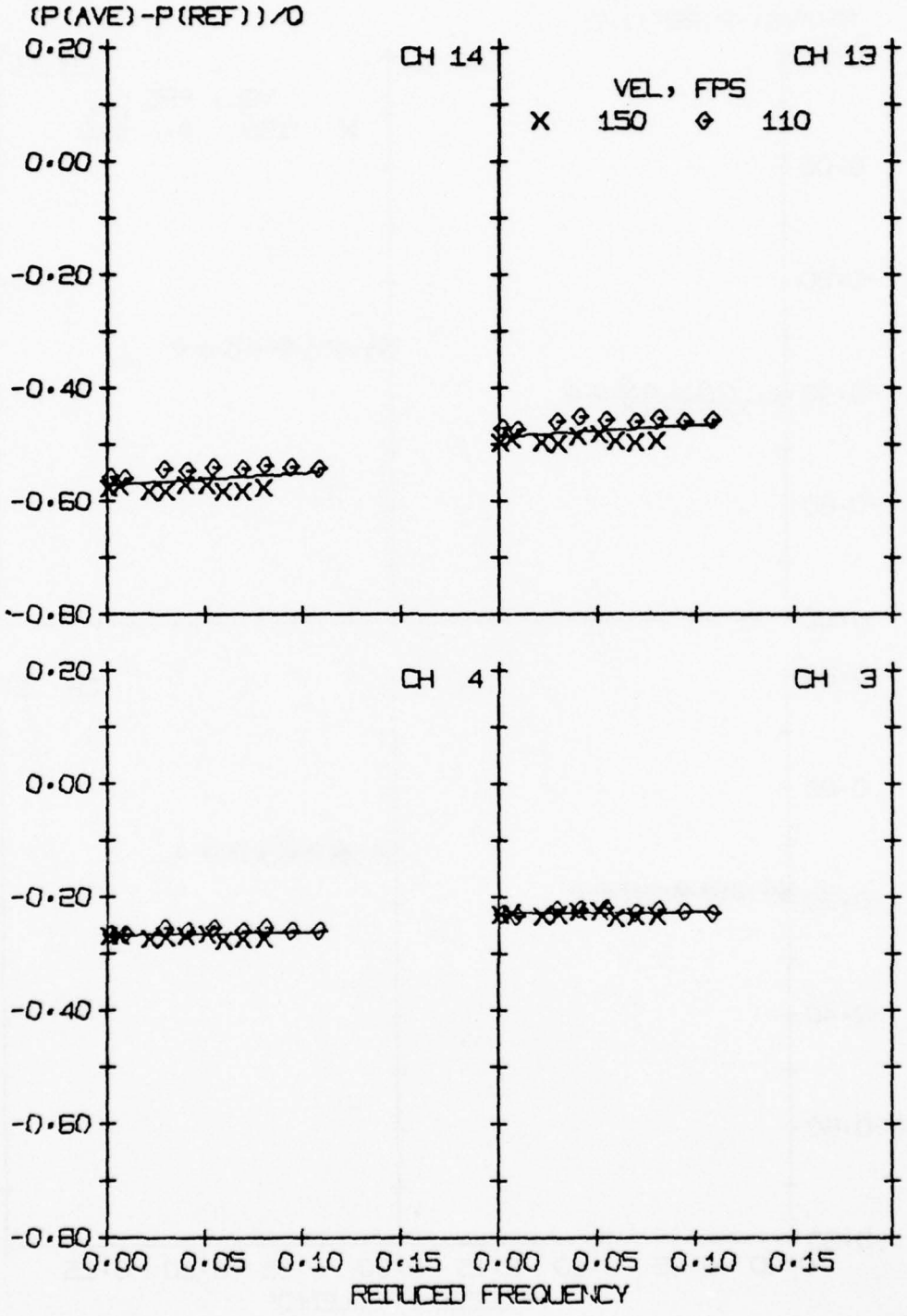

Figure 134. Normalized average pressure versus f_t, Group 4, $\alpha_m = 6°$

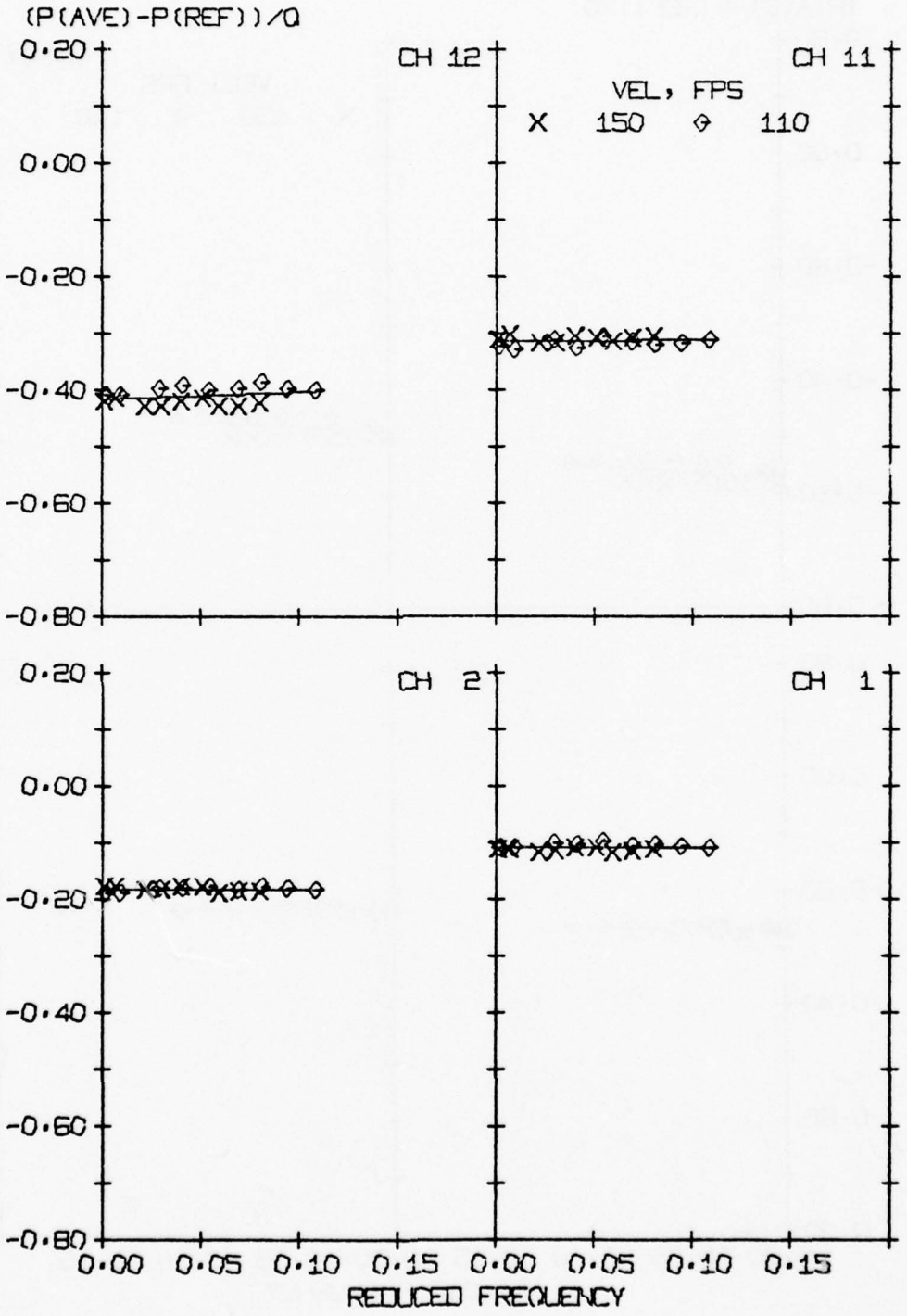

Figure 135. Normalized average pressure versus f_t, Group 5, $\alpha_m = 6°$

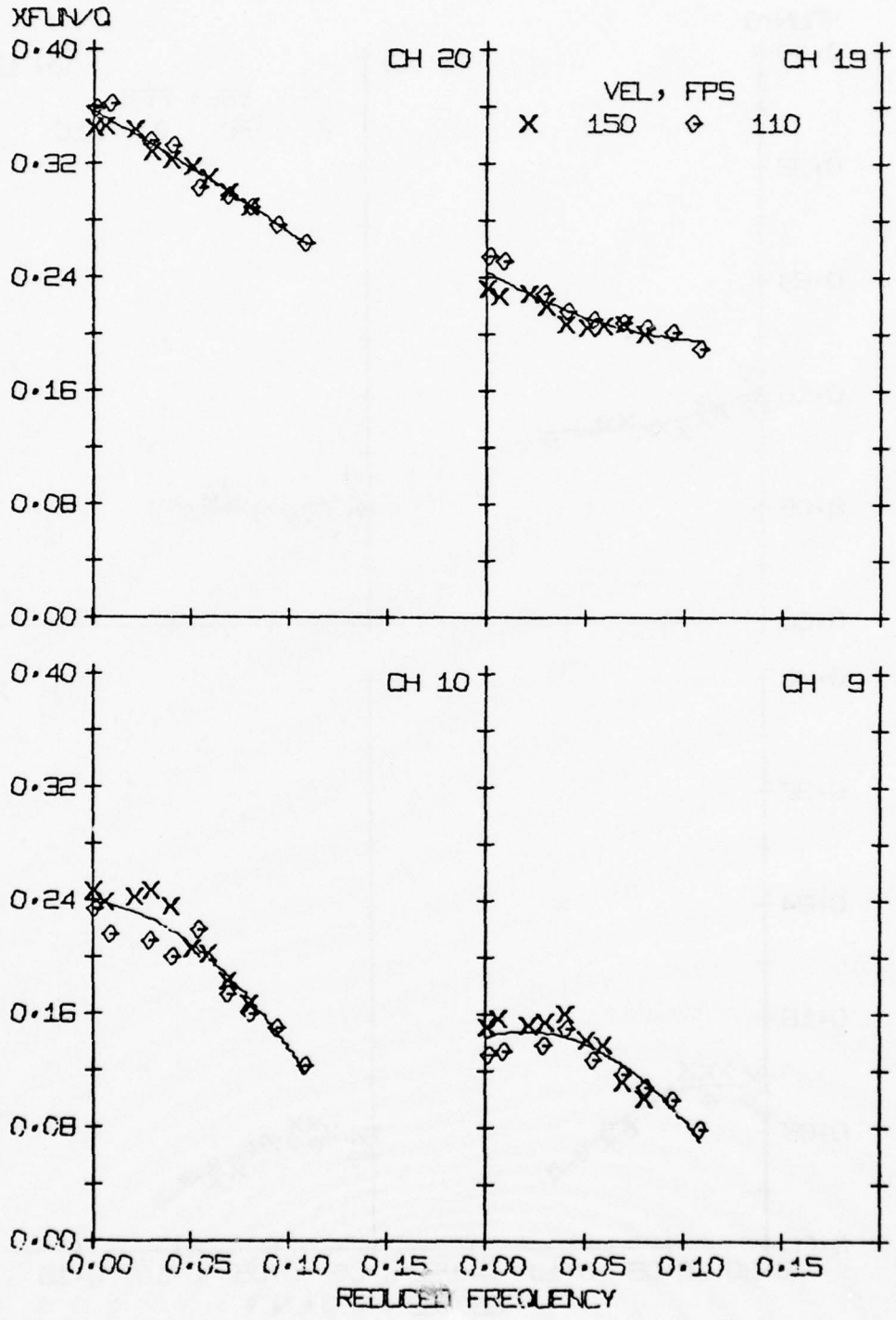

Figure 136. Normalized unsteady pressure versus f_t, Group 1, $\alpha_m = 6°$

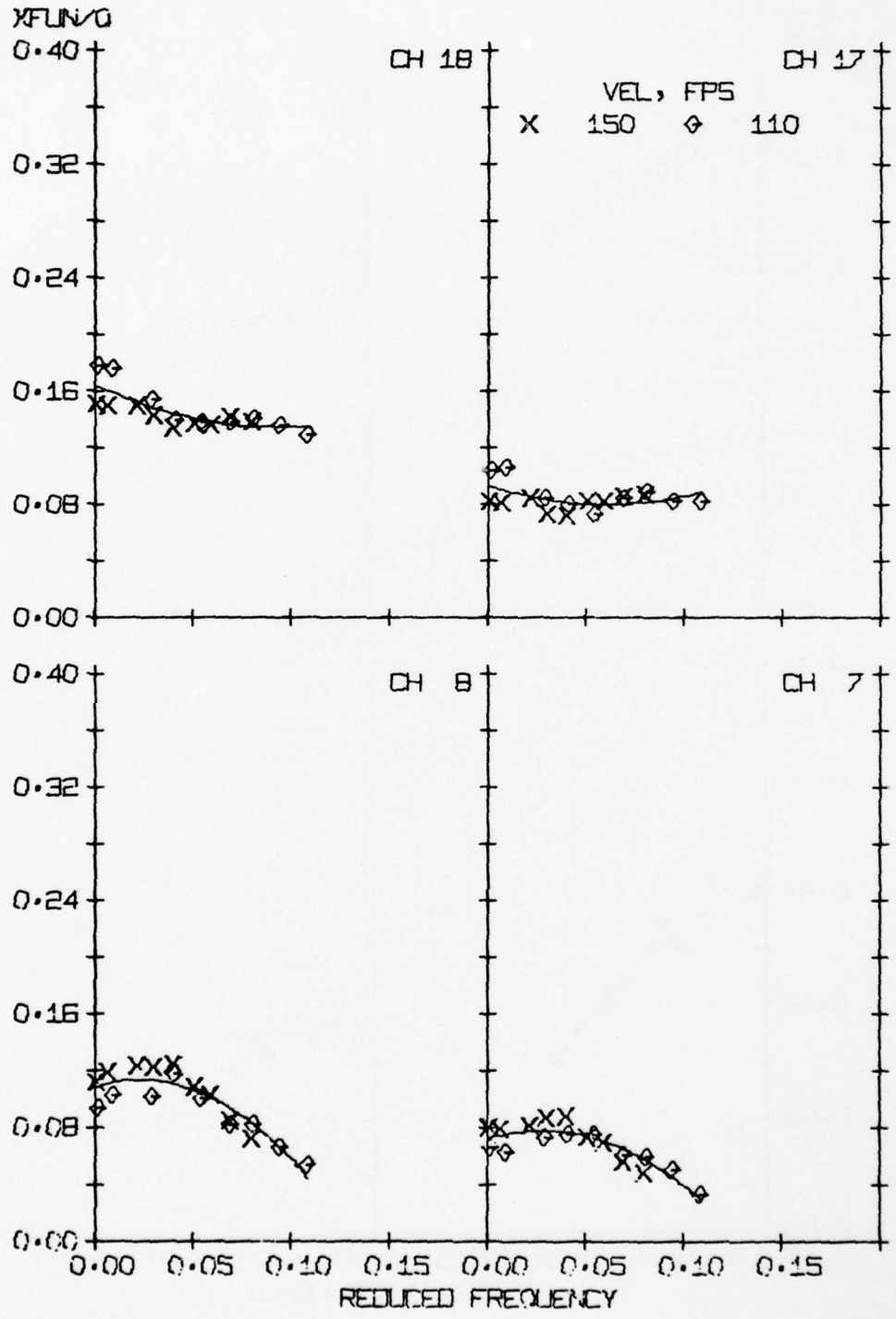

Figure 137. Normalized unsteady pressure versus f_t, Group 2, $\alpha_m = 6°$

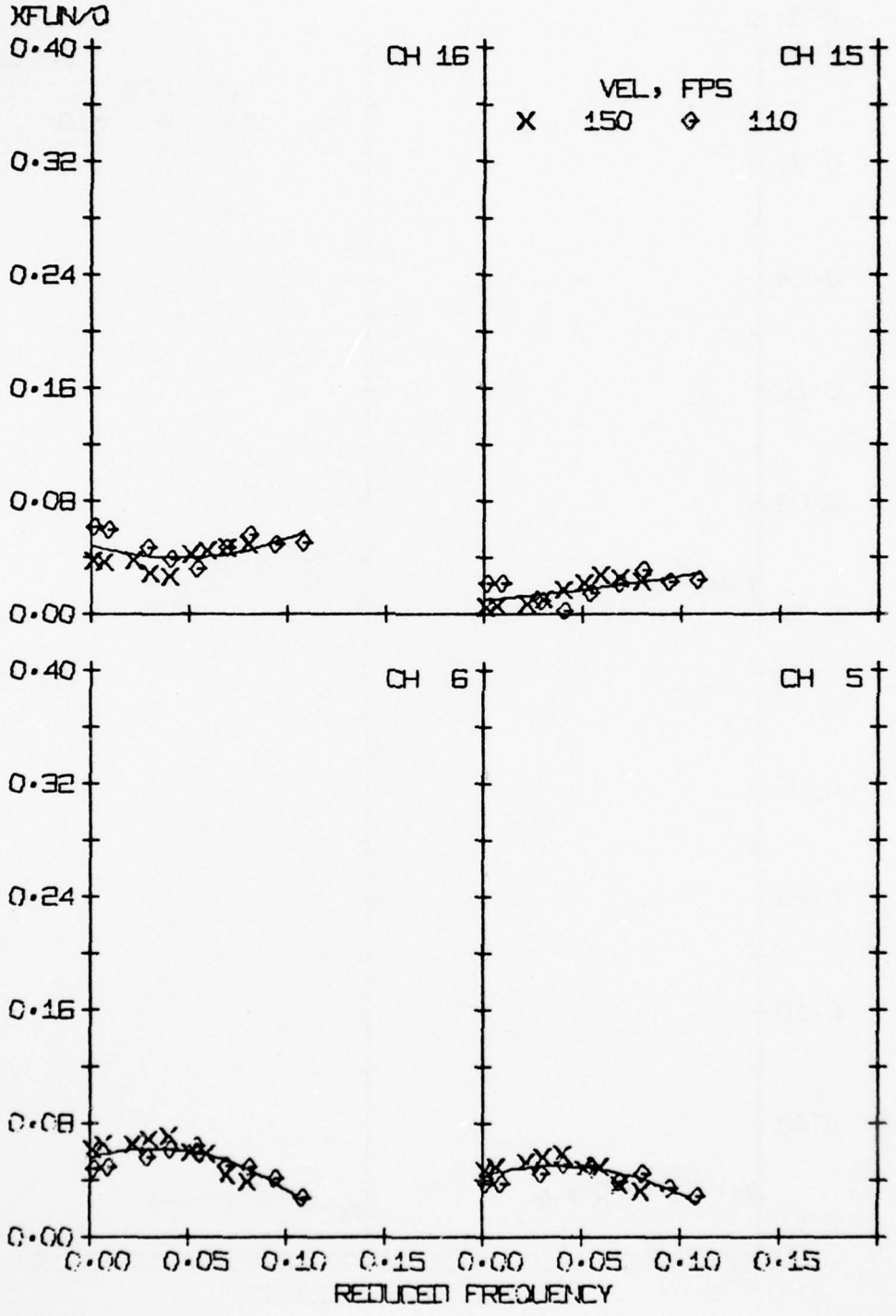

Figure 138. Normalized unsteady pressure versus f_t, Group 3, $\alpha_m = 6°$

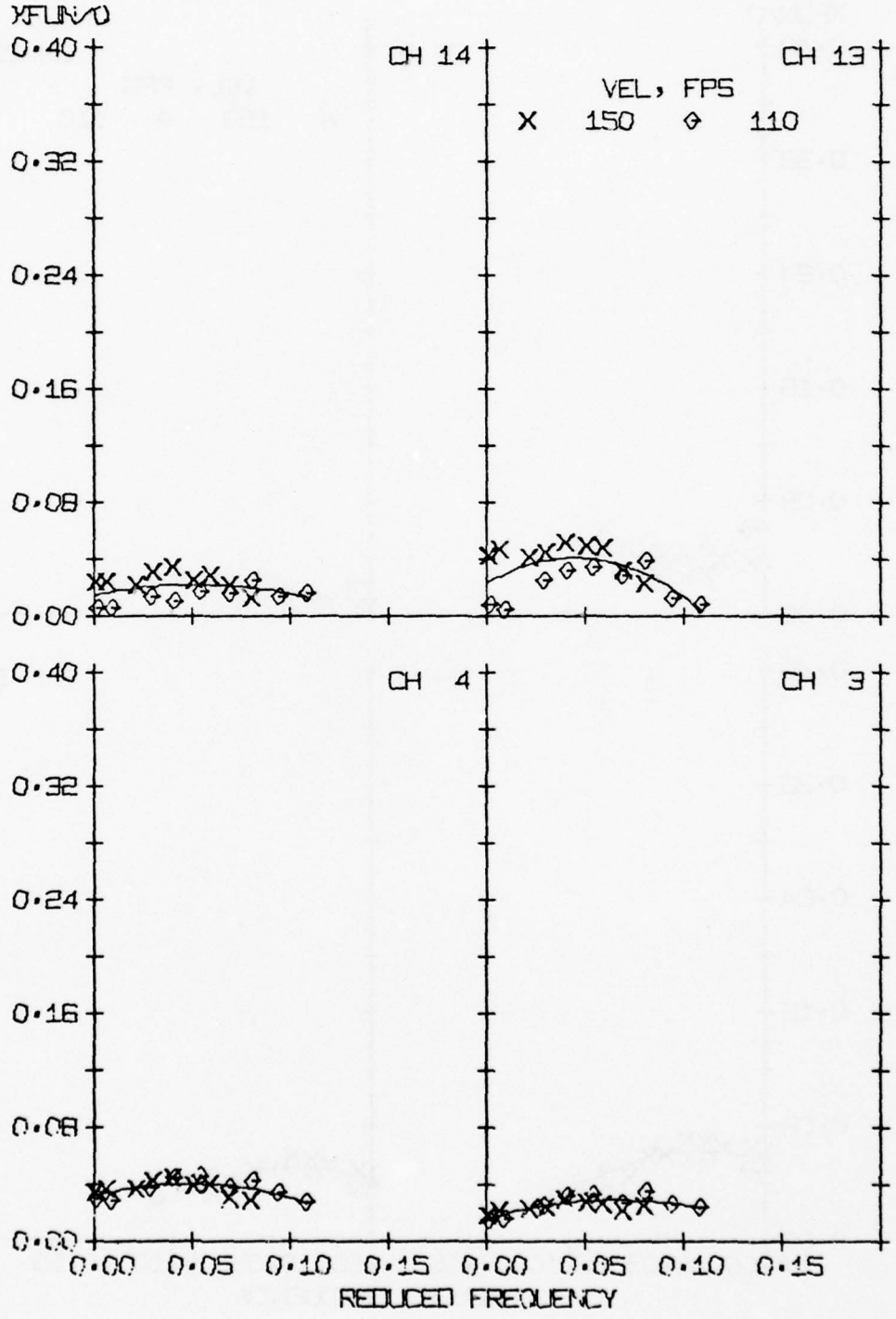

Figure 139. Normalized unsteady pressure versus f_t, Group 4, $\alpha_m = 6°$

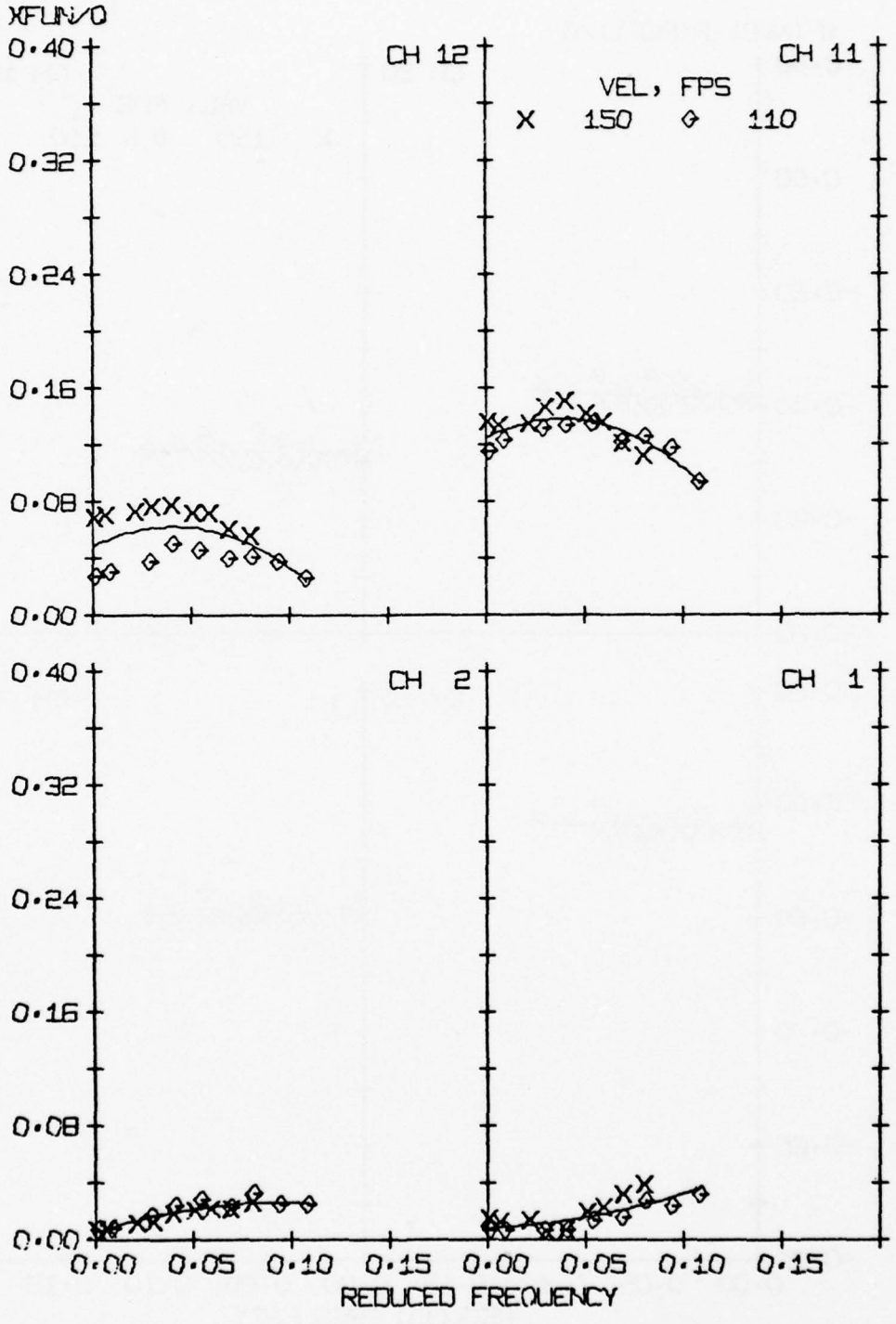

Figure 140. Normalized unsteady pressure versus f_t, Group 5, $\alpha_m = 6°$

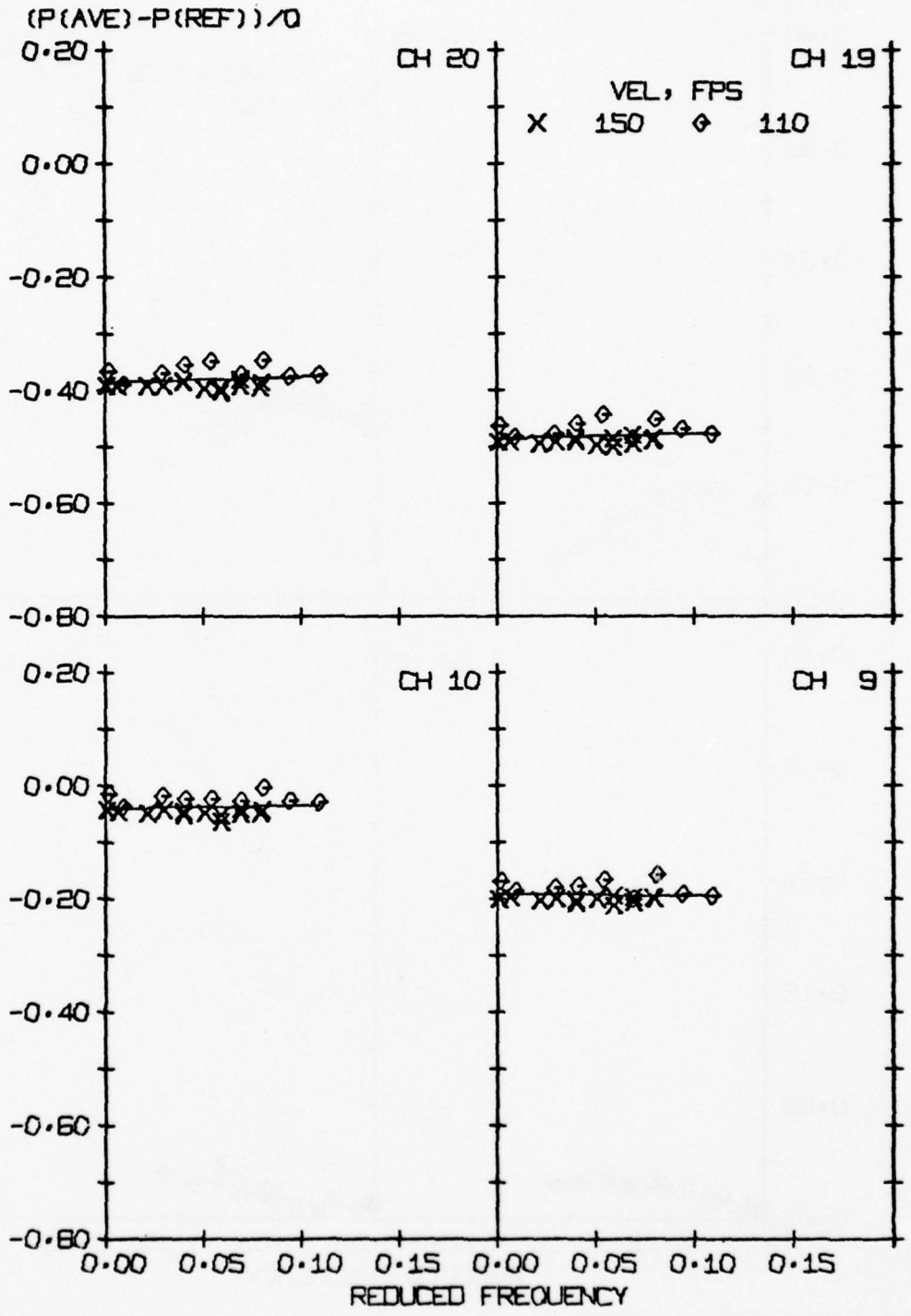

Figure 141. Normalized average pressure versus f_t, Group 1, $\alpha_m = 8°$

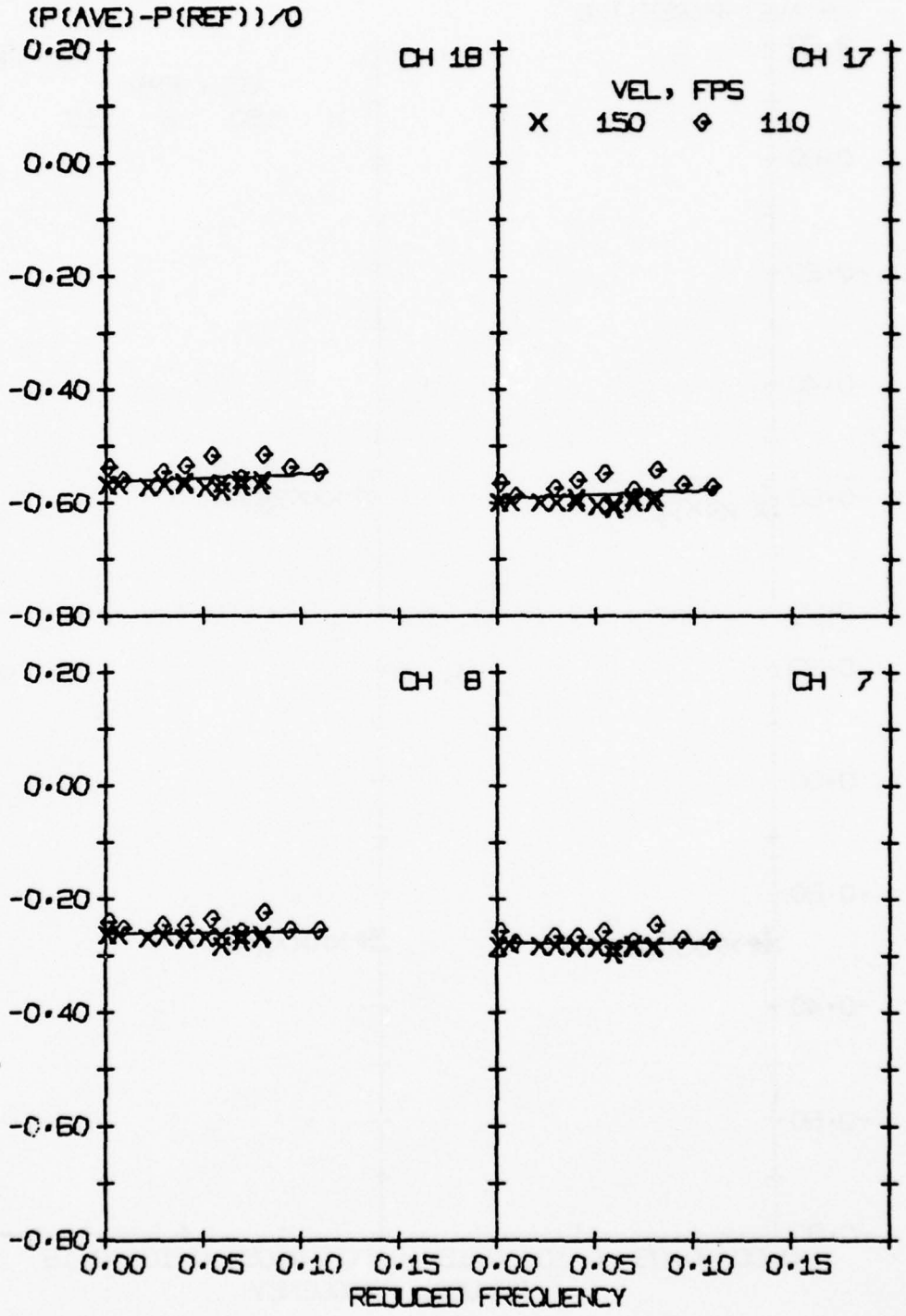

Figure 142. Normalized average pressure versus f_t, Group 2, $\alpha_m = 8°$

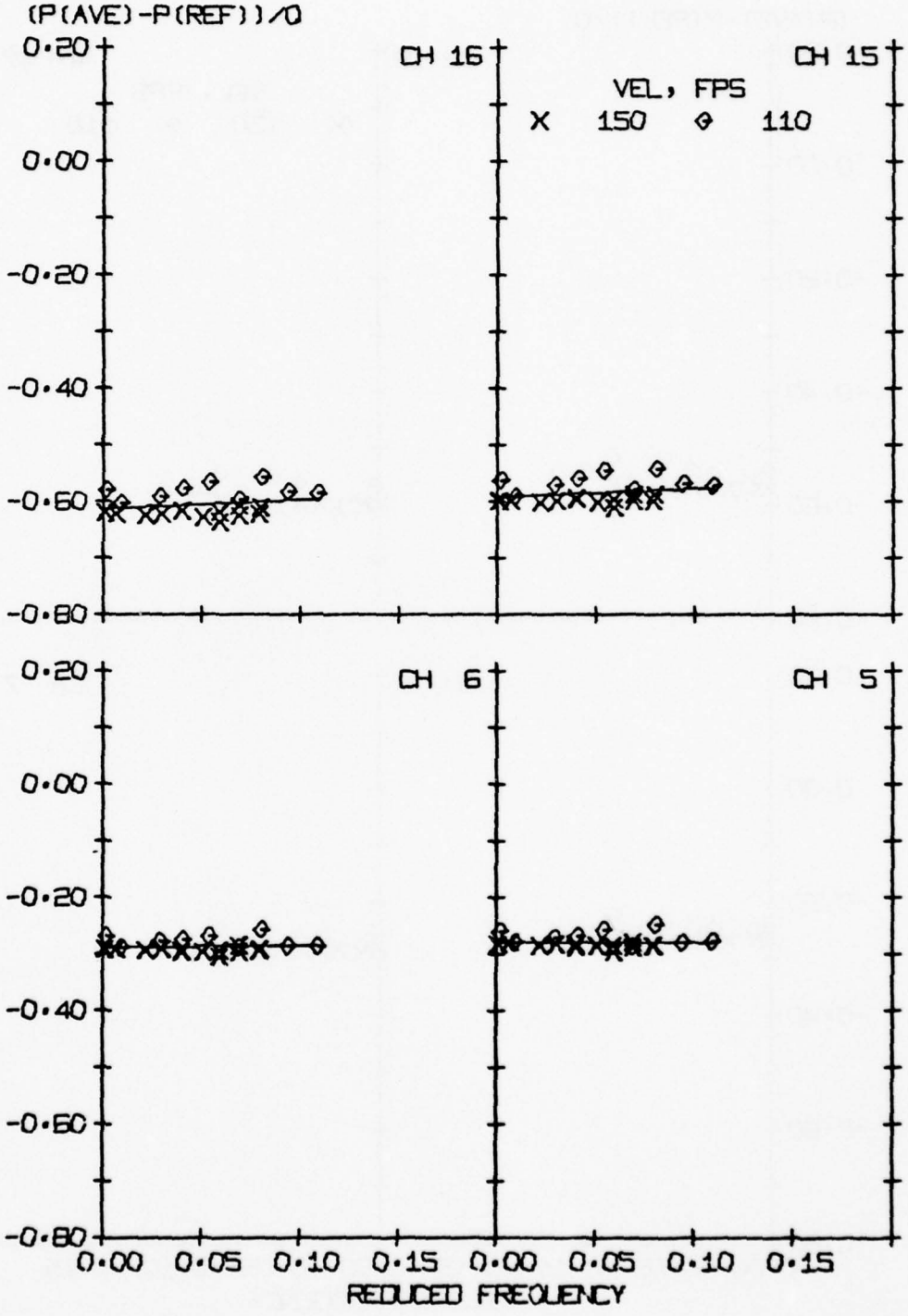

Figure 143. Normalized average pressure versus f_t, Group 3, α_m = 8°

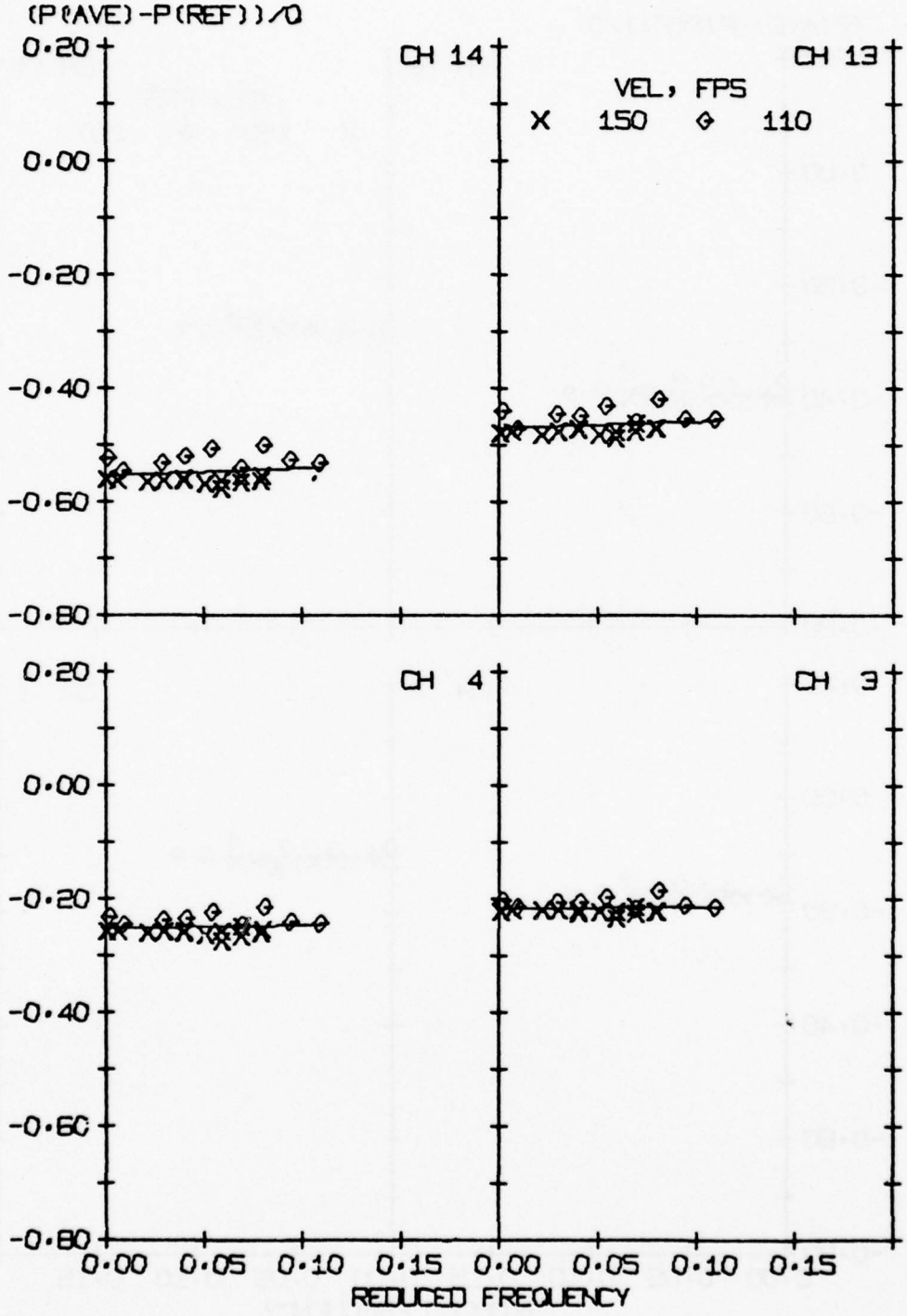

Figure 144. Normalized average pressure versus f_t, Group 4, $\alpha_m = 8°$

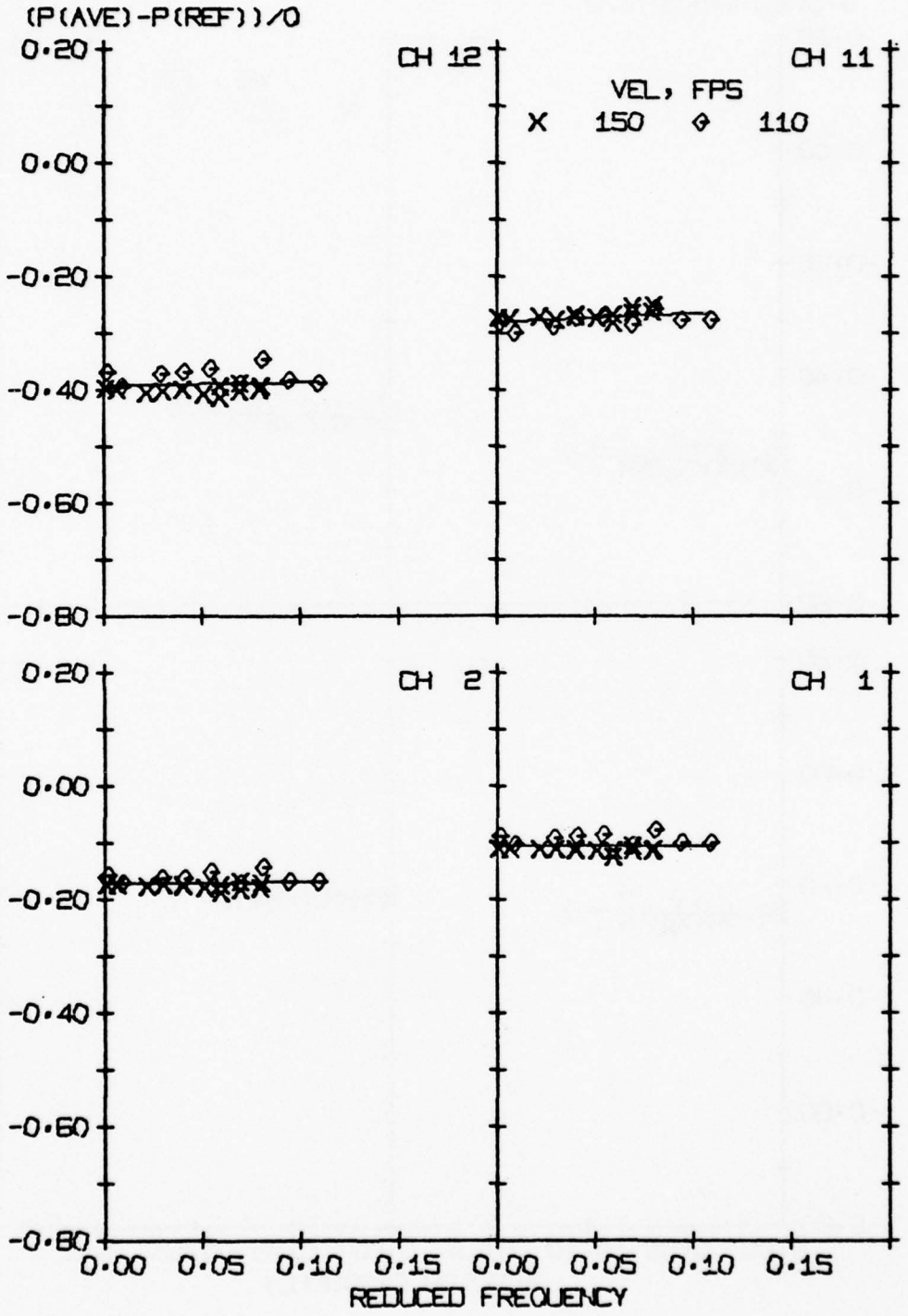

Figure 145. Normalized average pressure versus f_t, Group 5, α_m = 8°

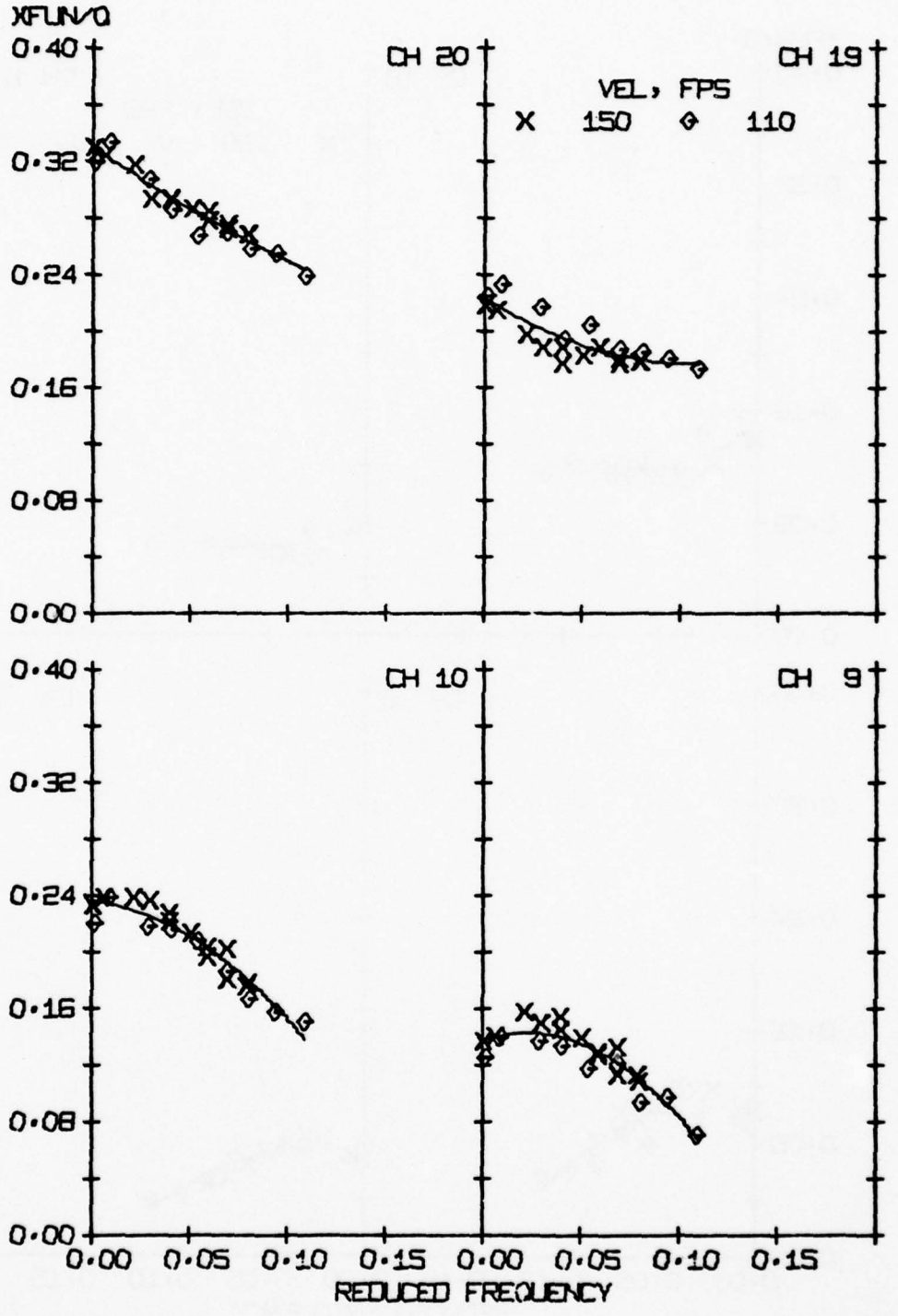

Figure 146. Normalized unsteady pressure versus f_t, Group 1, α_m = 8°

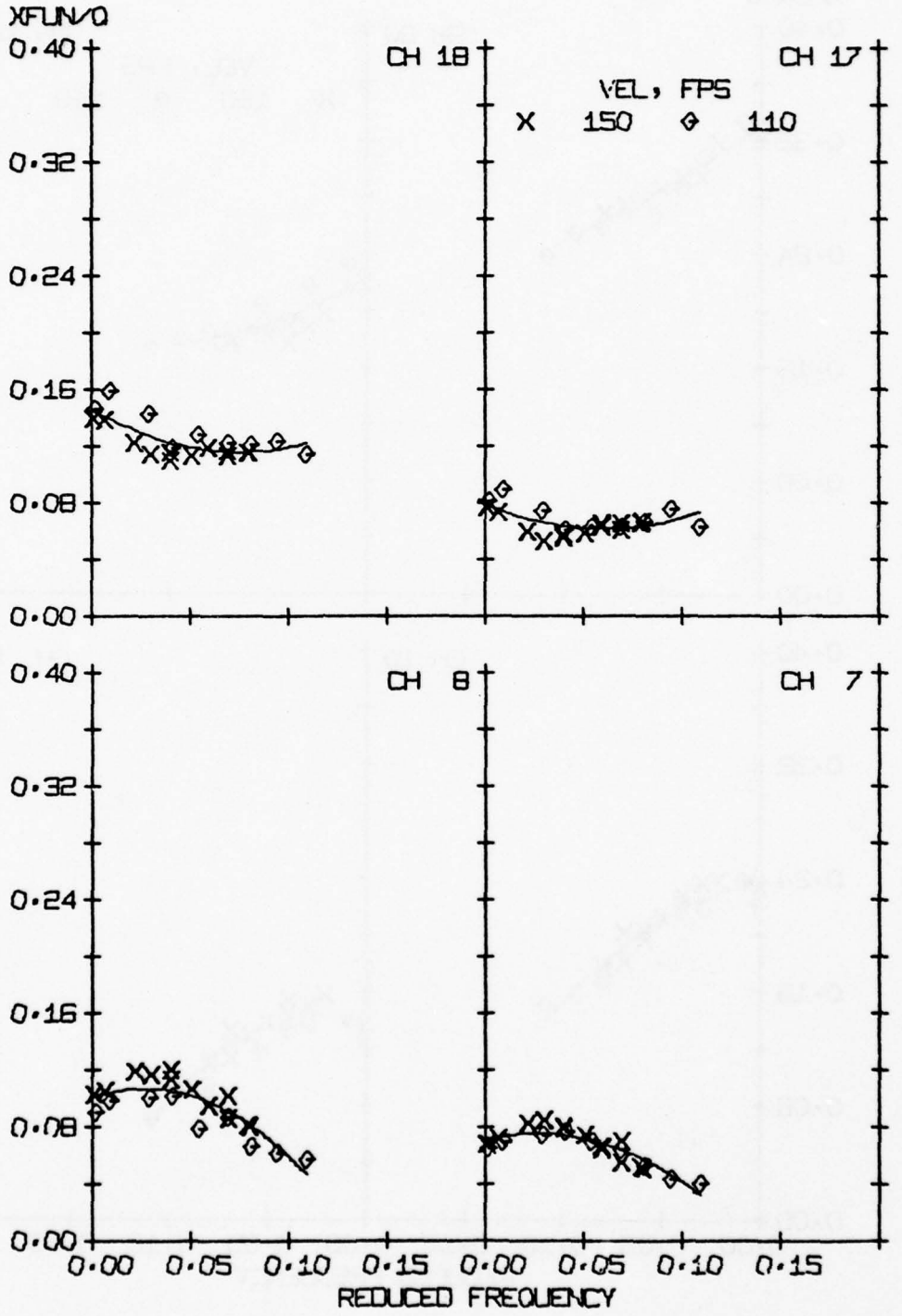

Figure 147. Normalized unsteady pressure versus f_t, Group 2, $\alpha_m = 8°$

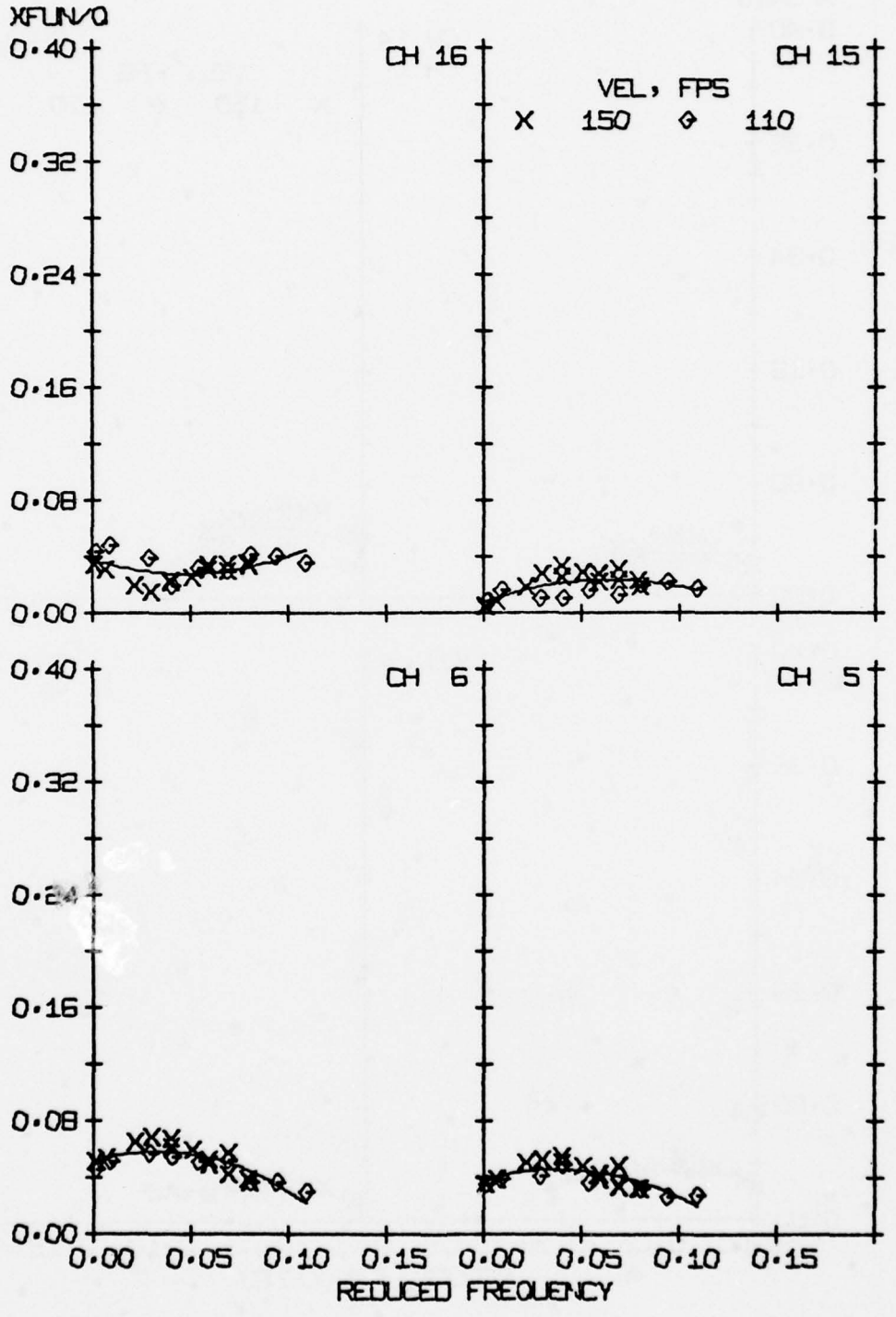

Figure 148. Normalized unsteady pressure versus f_t, Group 3, $\alpha_m = 8°$

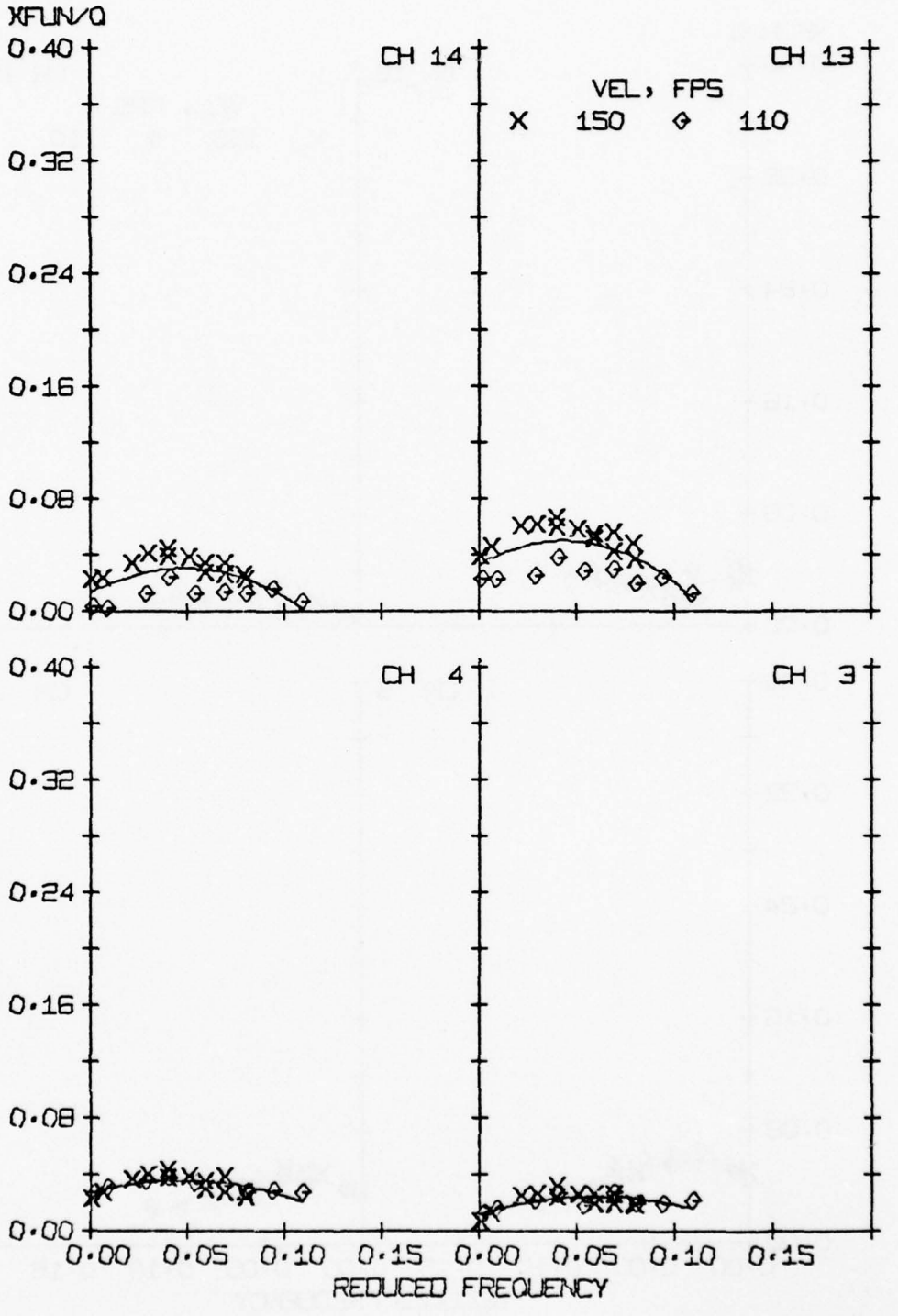

Figure 149. Normalized unsteady pressure versus f_t, Group 4, $\alpha_m = 8°$

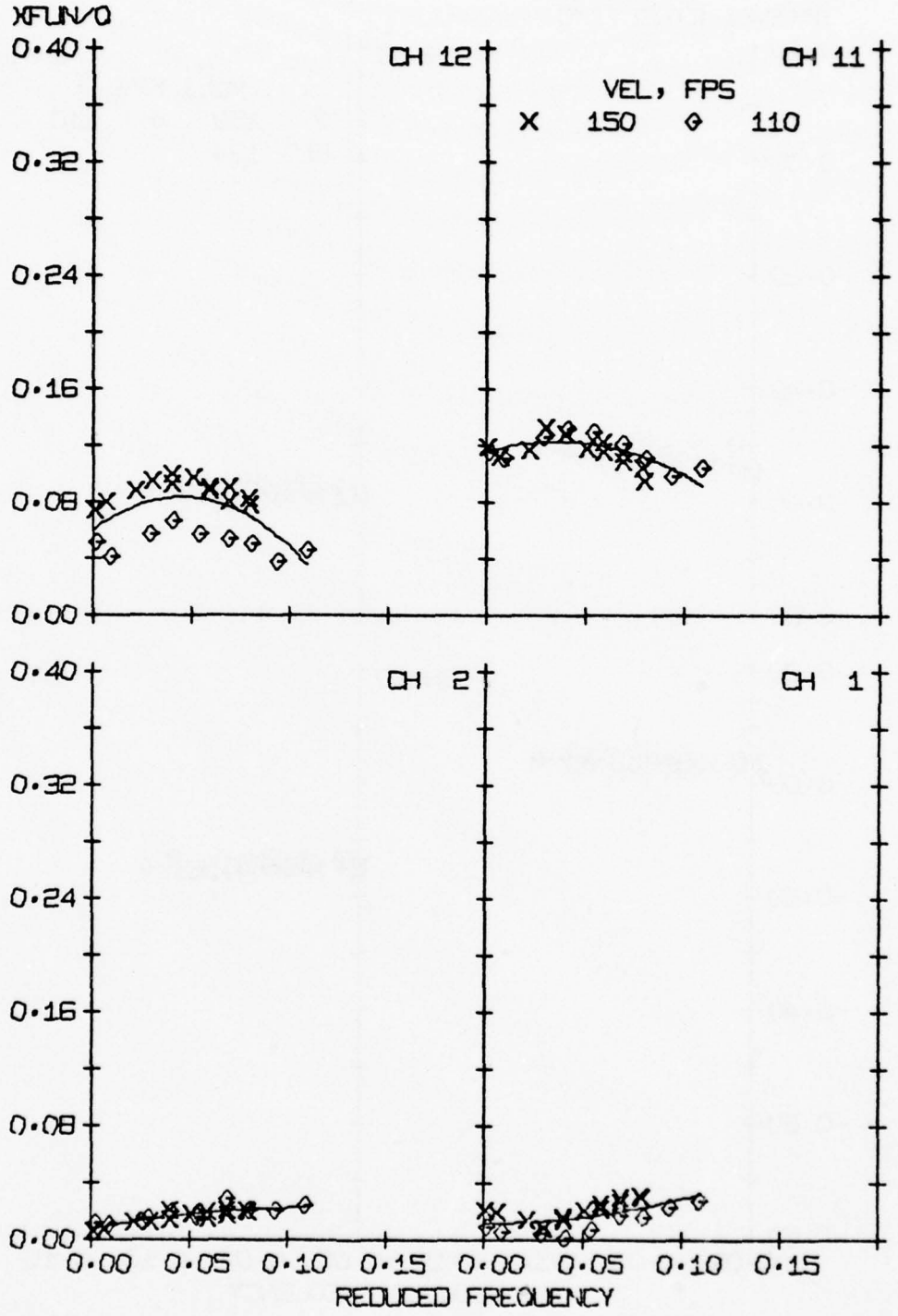

Figure 150. Normalized unsteady pressure versus f_t, Group 5, $\alpha_m = 8°$

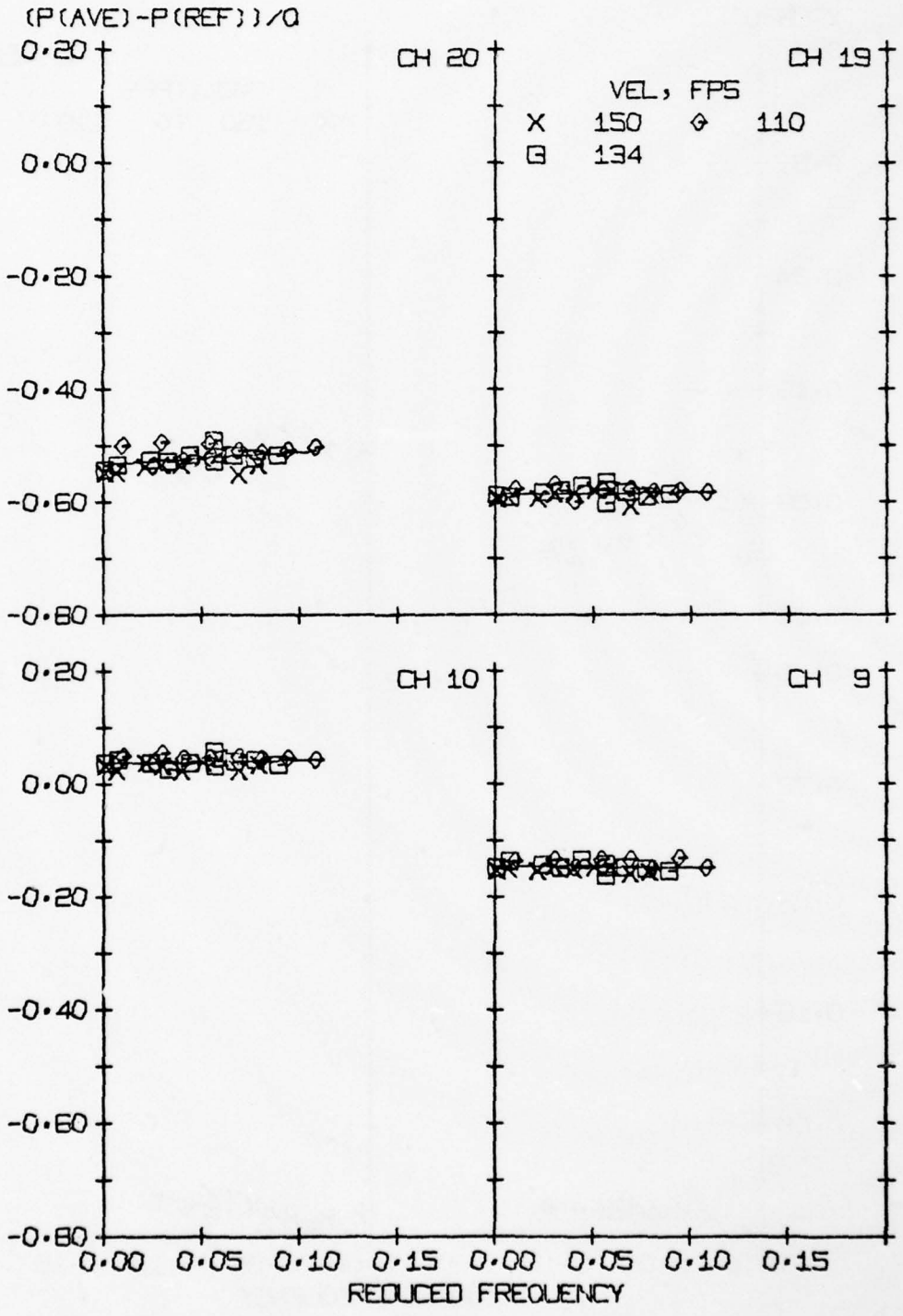

Figure 151. Normalized average pressure versus f_t, Group 1, $\alpha_m = 10°$

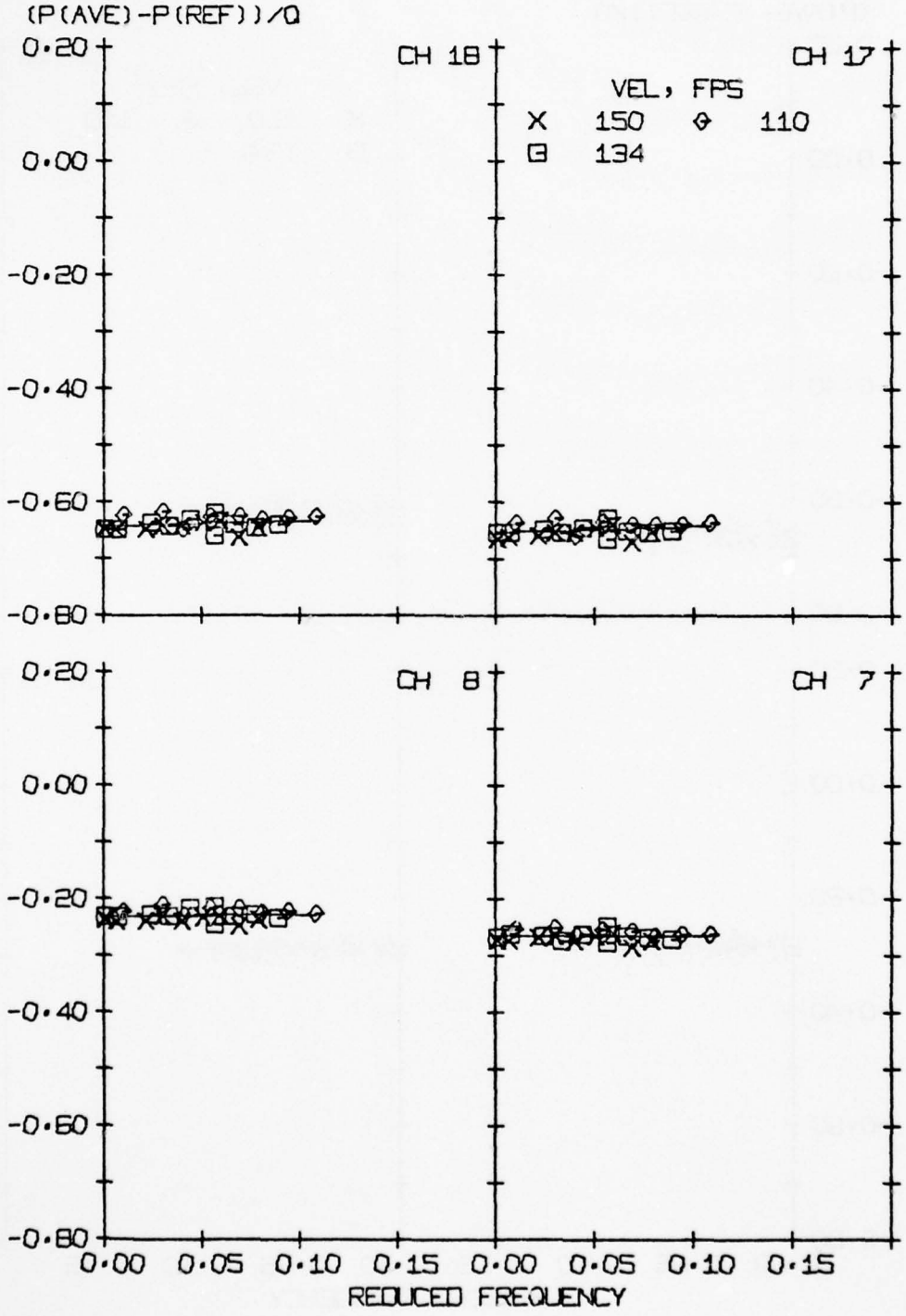

Figure 152. Normalized average pressure versus f_t, Group 2, α_m = 10°

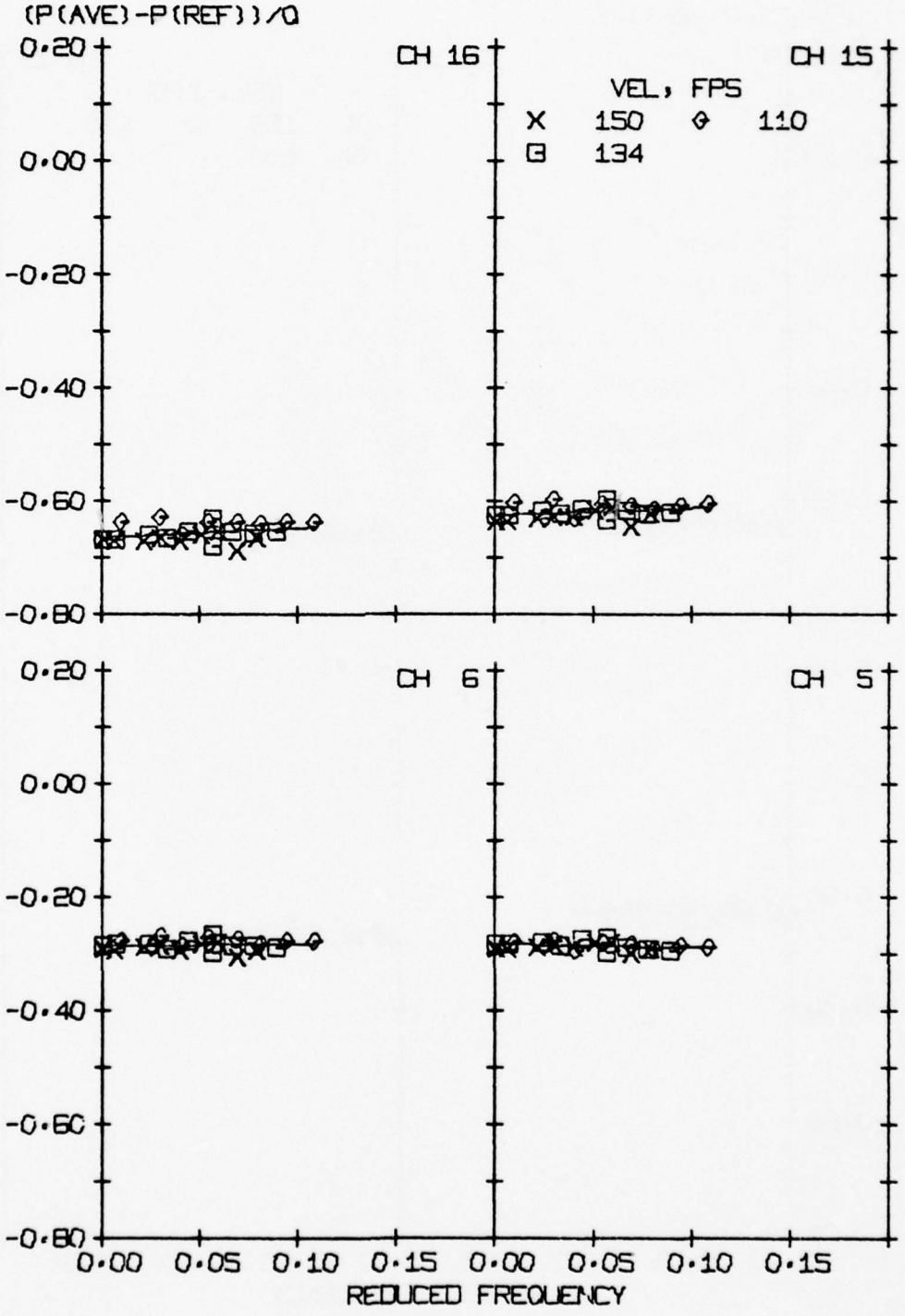

Figure 153. Normalized average pressure versus f_t, Group 3, $\alpha_m = 10°$

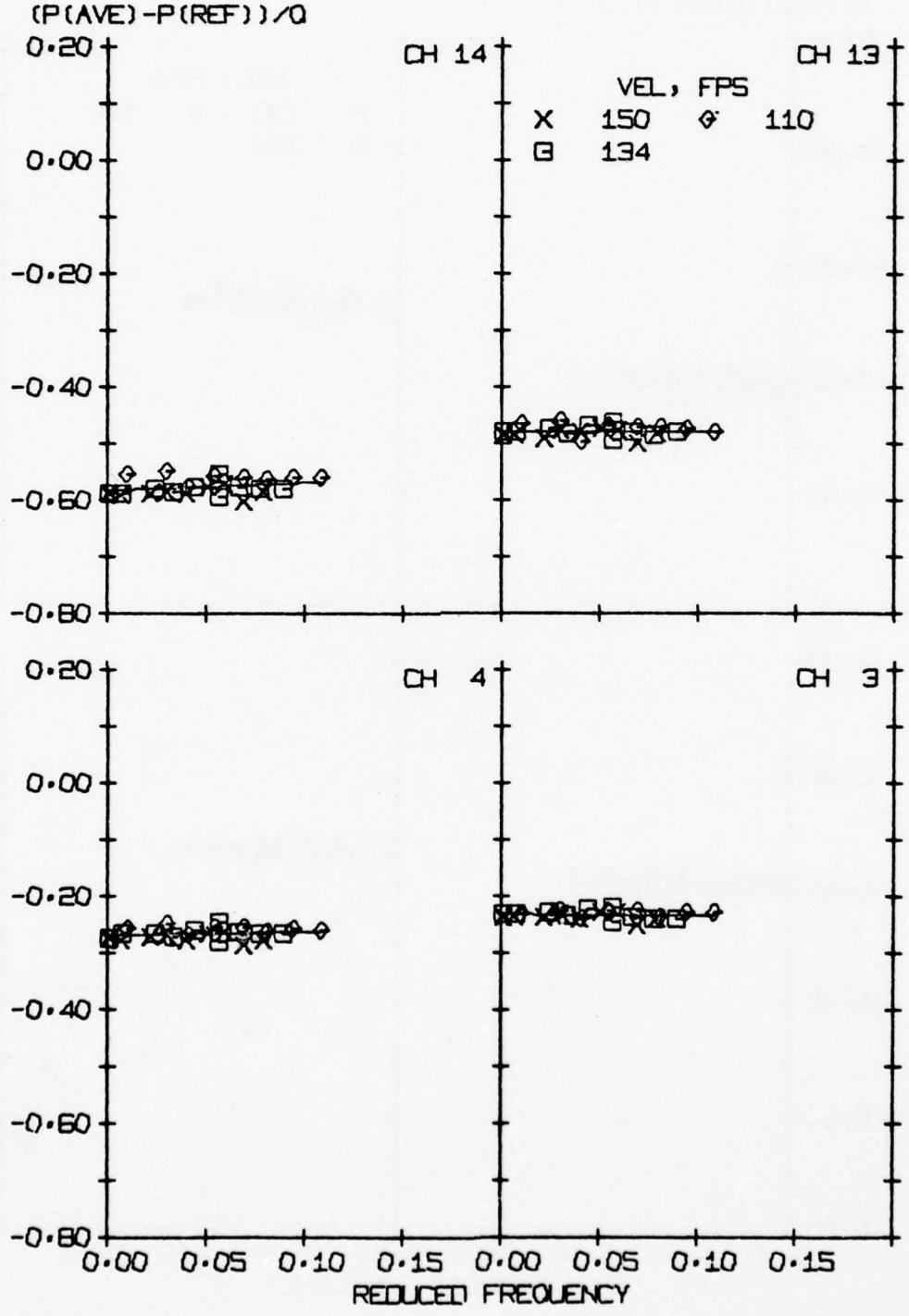

Figure 154. Normalized average pressure versus f_t, Group 4, α_m = 10°

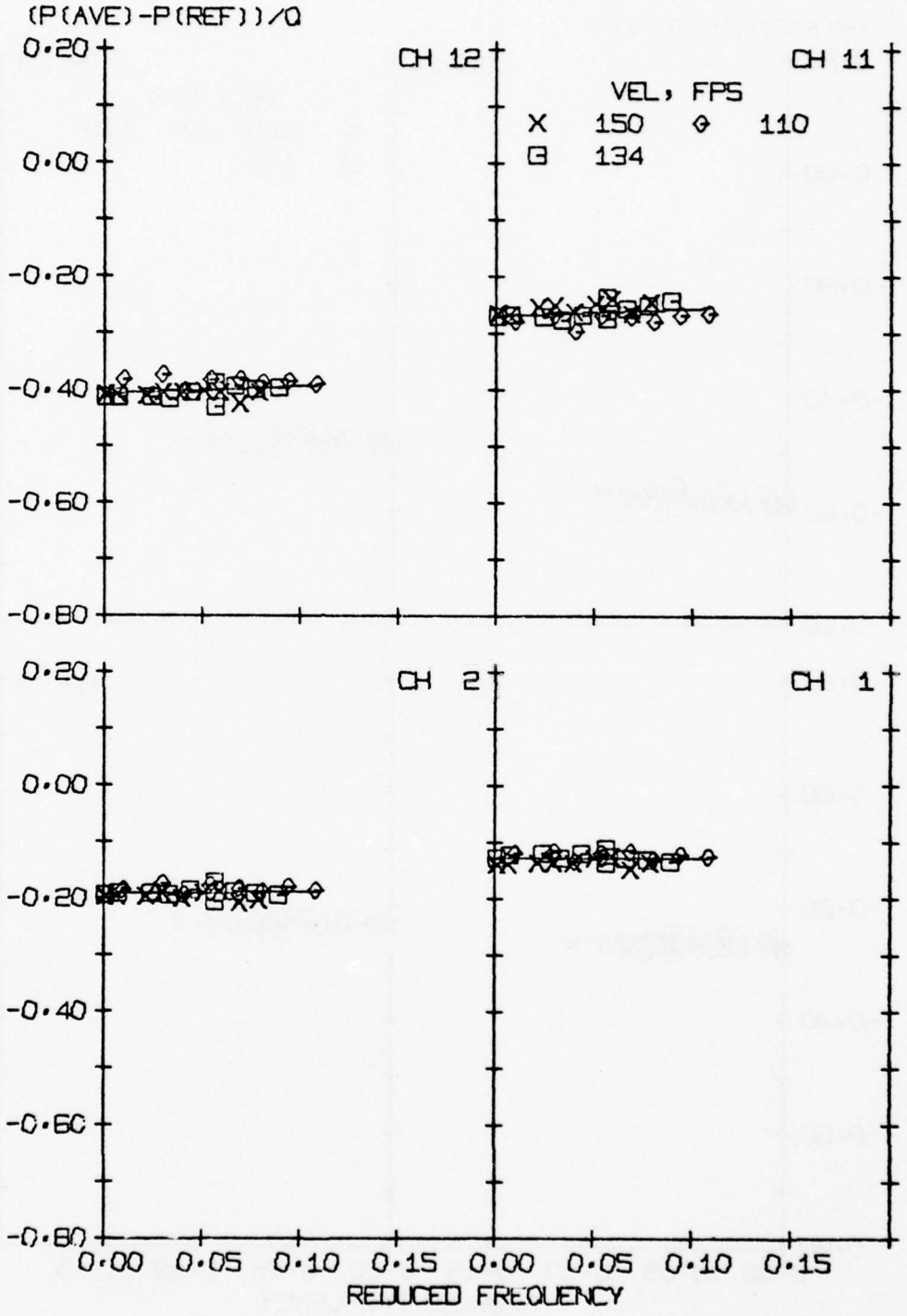

Figure 155. Normalized average pressure versus f_t, Group 5, α_m = 10°

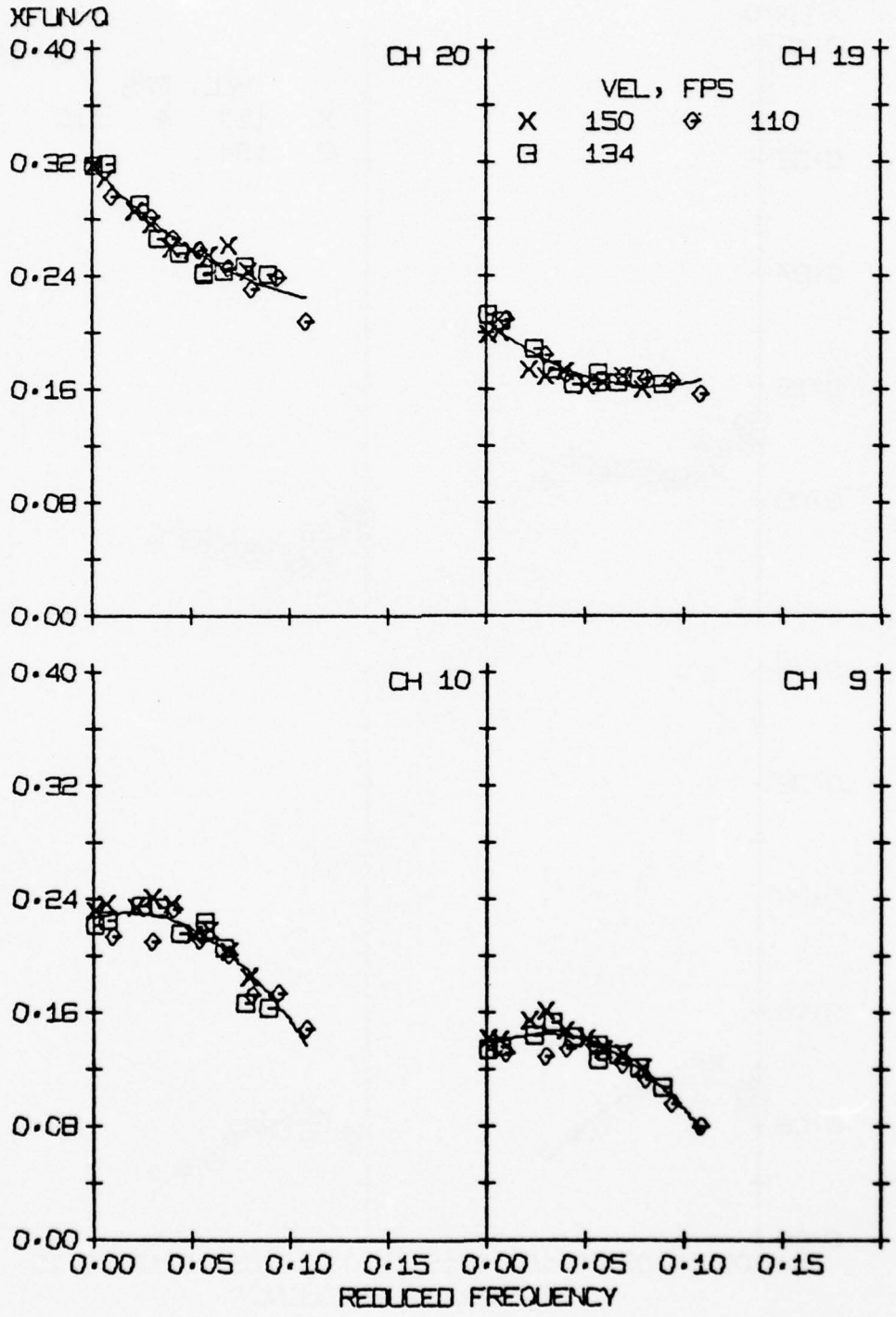

Figure 156. Normalized unsteady pressure versus f_t, Group 1, α_m = 10°

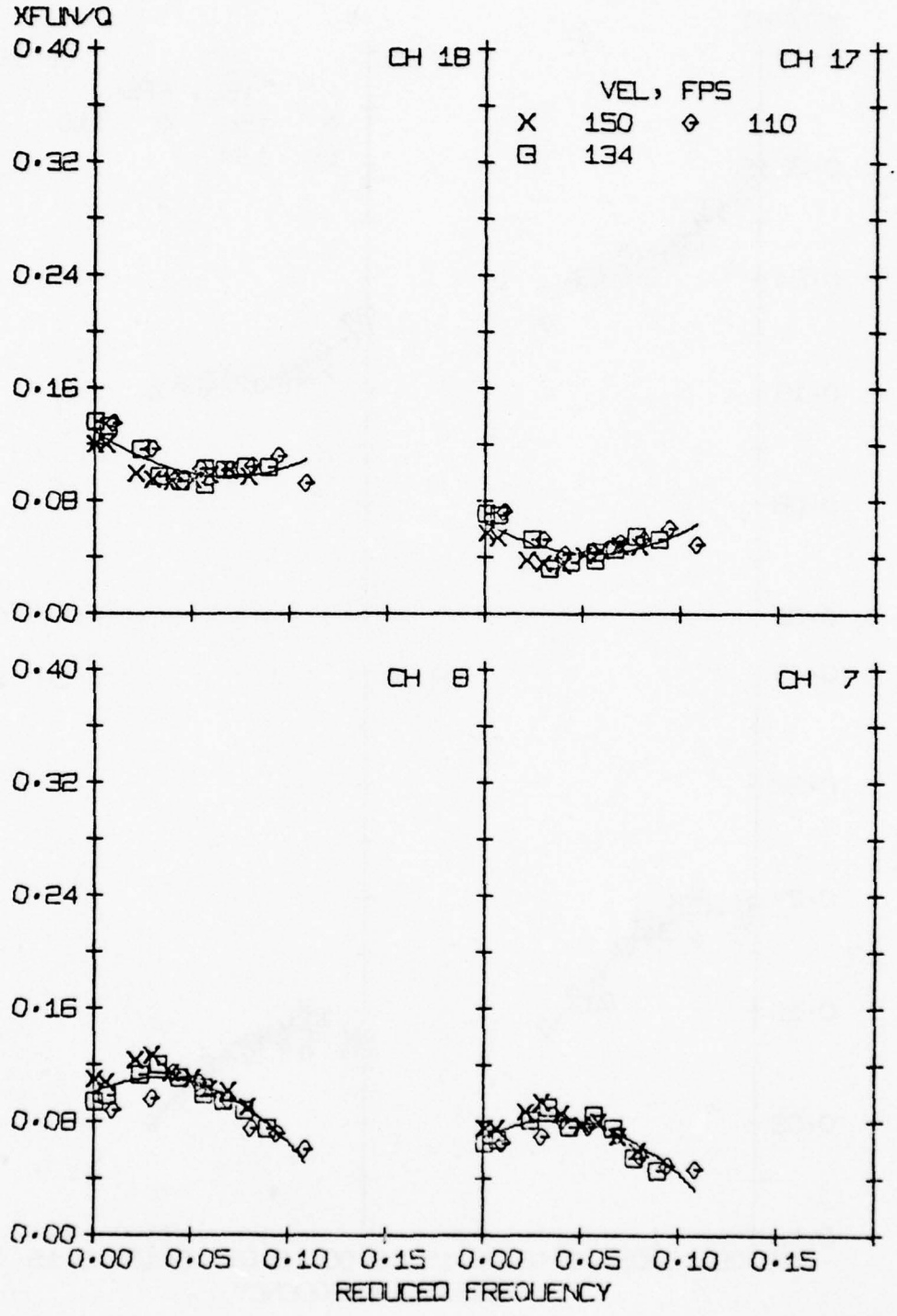

Figure 157. Normalized unsteady pressure versus f_t, Group 2, α_m = 10°

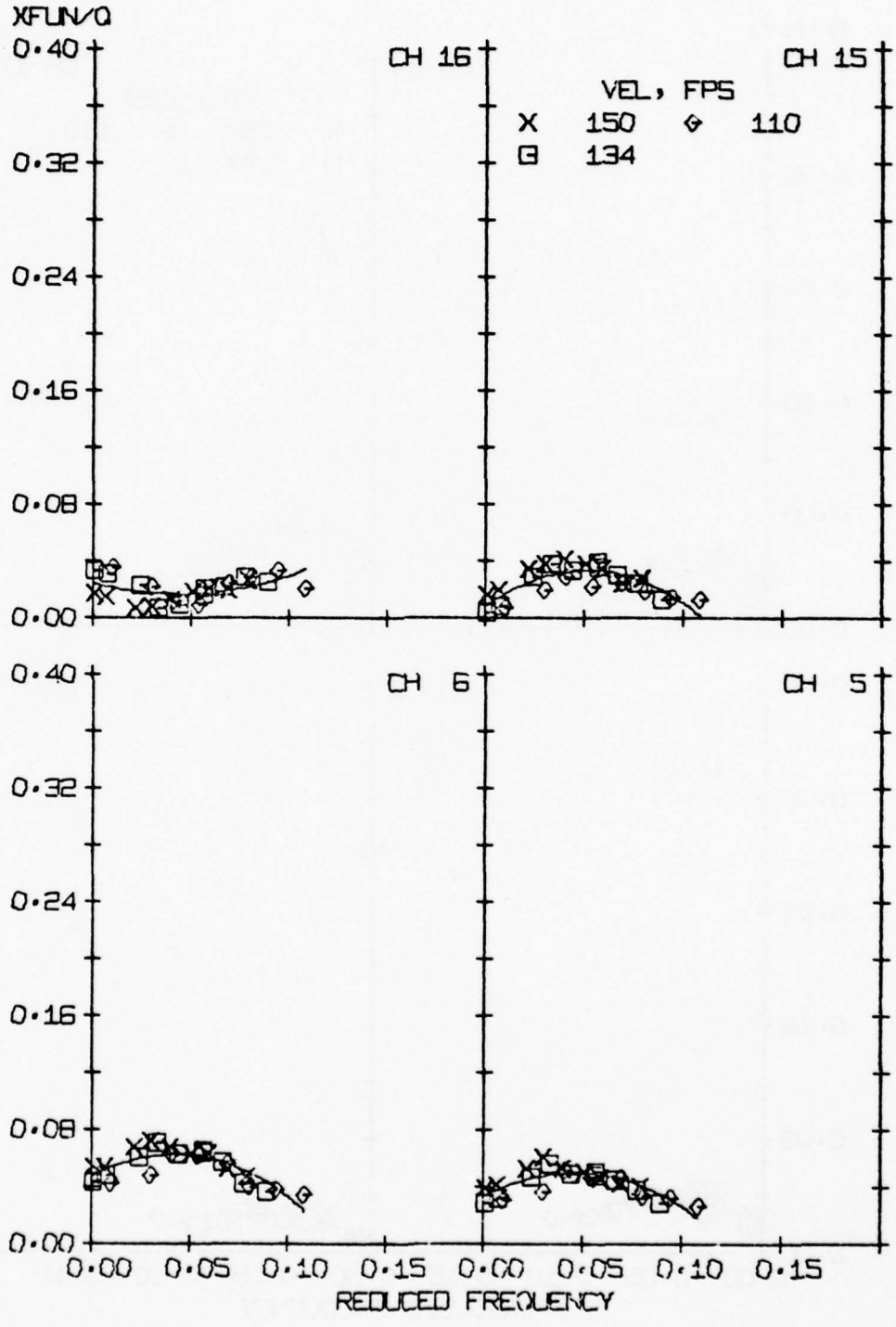

Figure 158. Normalized unsteady pressure versus f_t, Group 3, $\alpha_m = 10°$

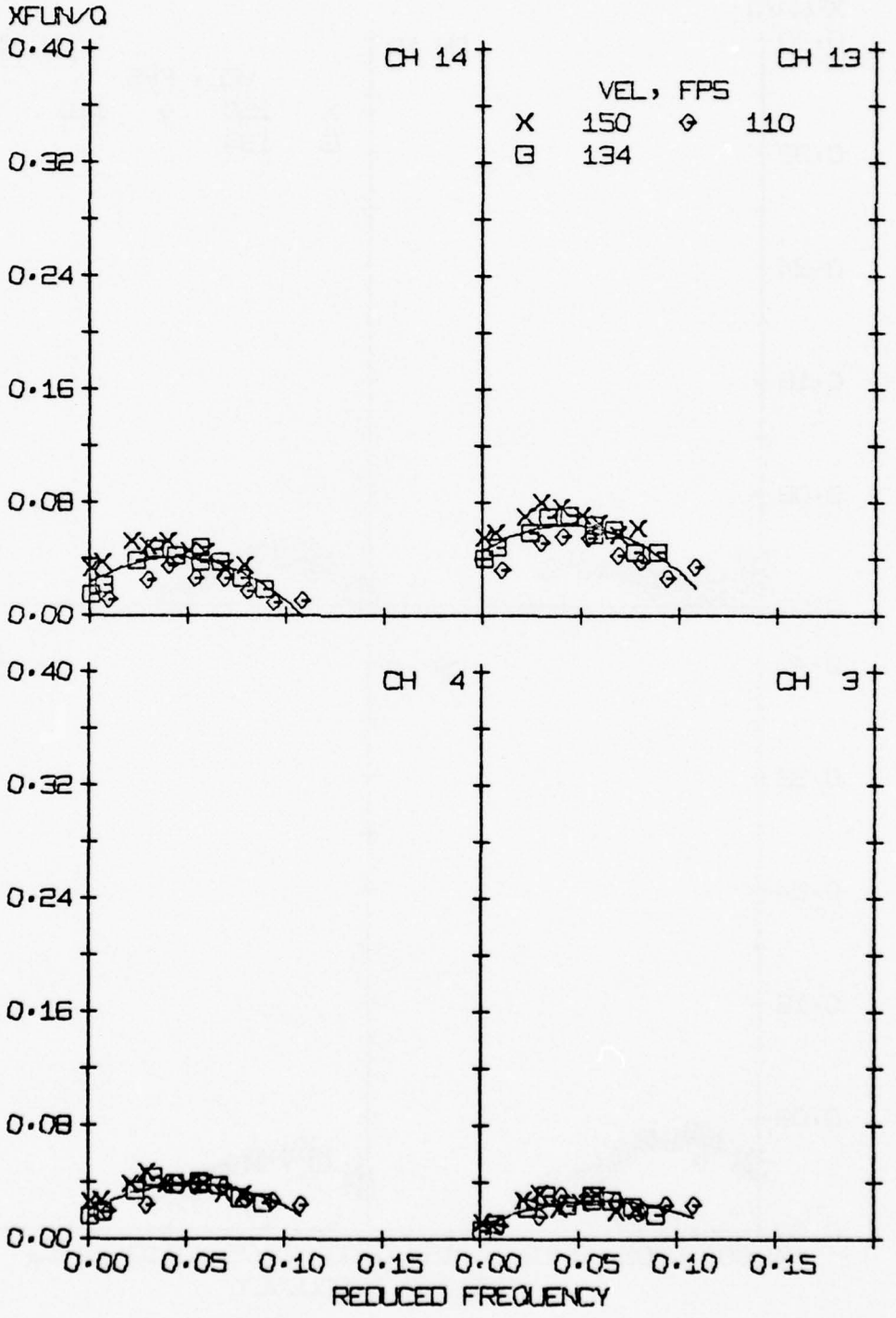

Figure 159. Normalized unsteady pressure versus f_t, Group 4, α_m = 10°

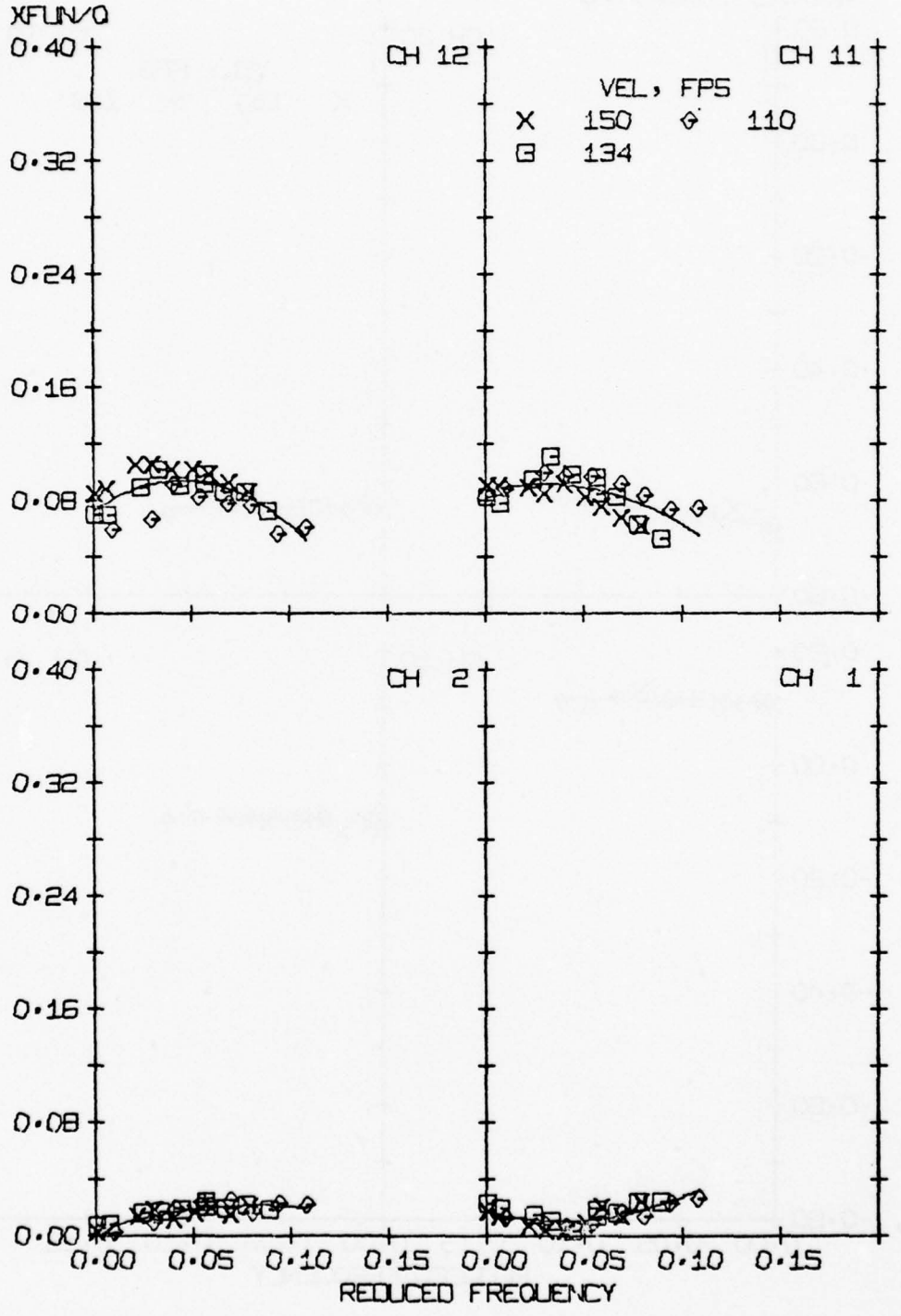

Figure 160. Normalized unsteady pressure versus f_t, Group 5, $\alpha_m = 10°$

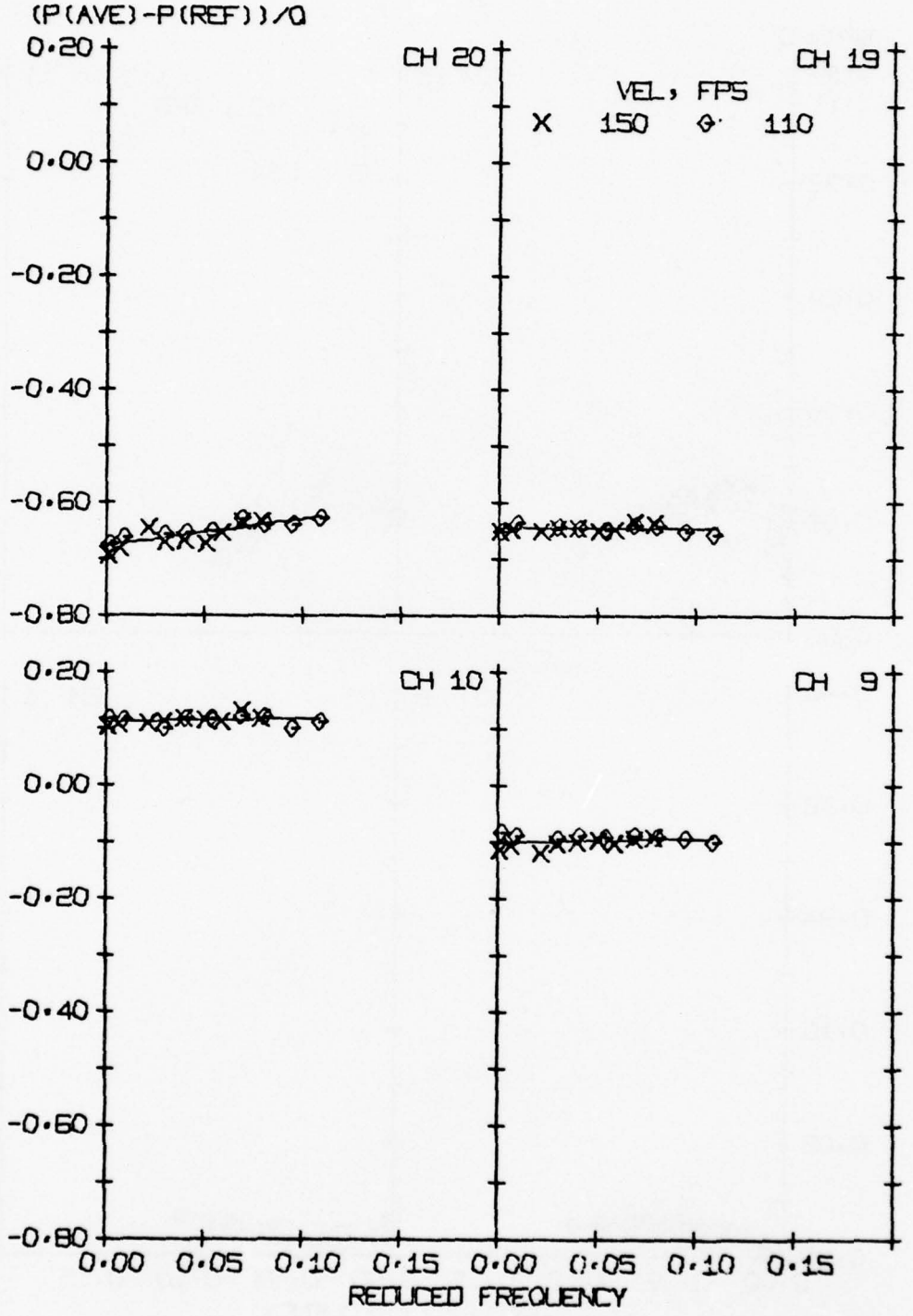

Figure 161. Normalized average pressure versus f_t, Group 1, α_m = 12°

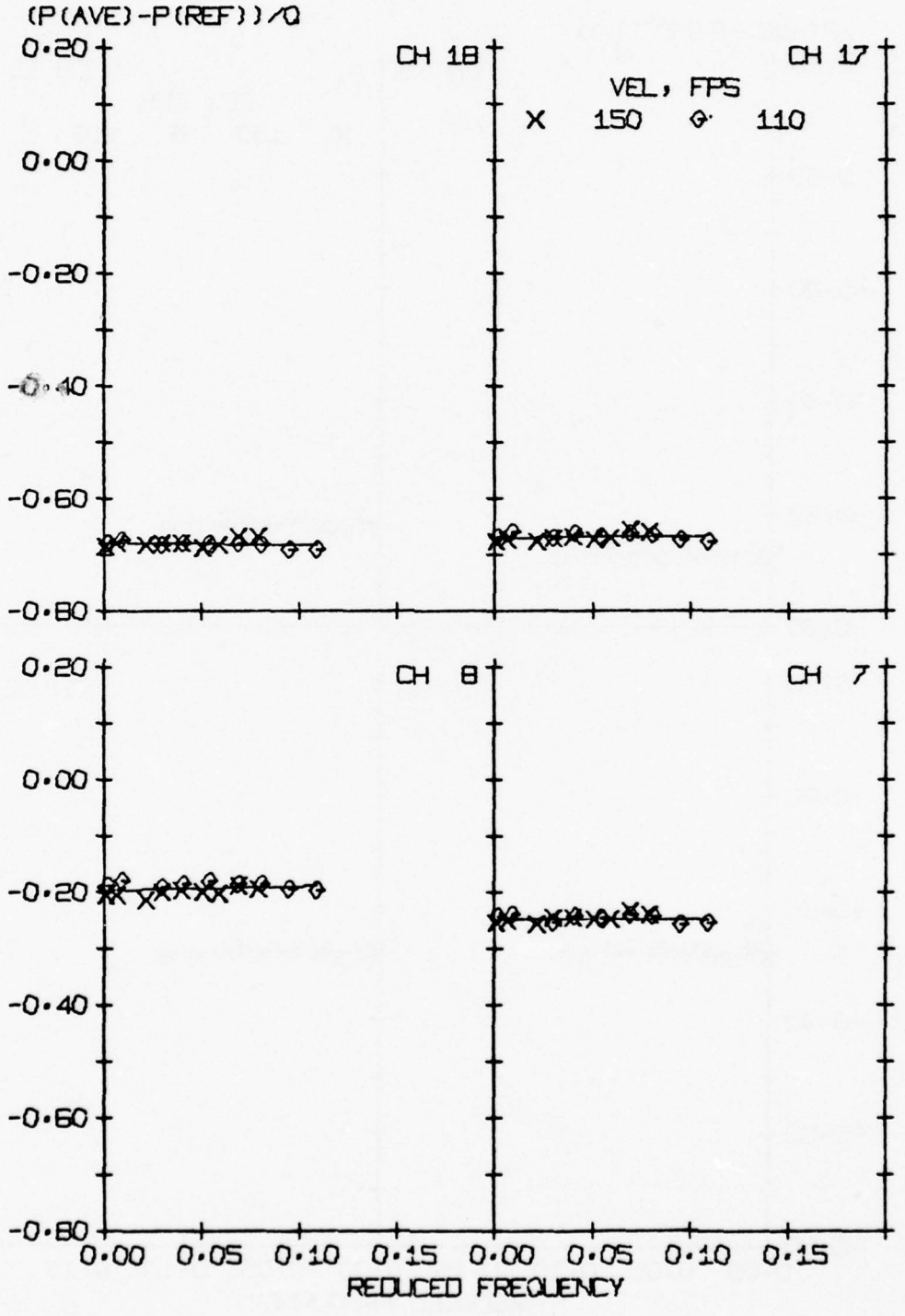

Figure 162. Normalized average pressure versus f_t, Group 2, α_m = 12°

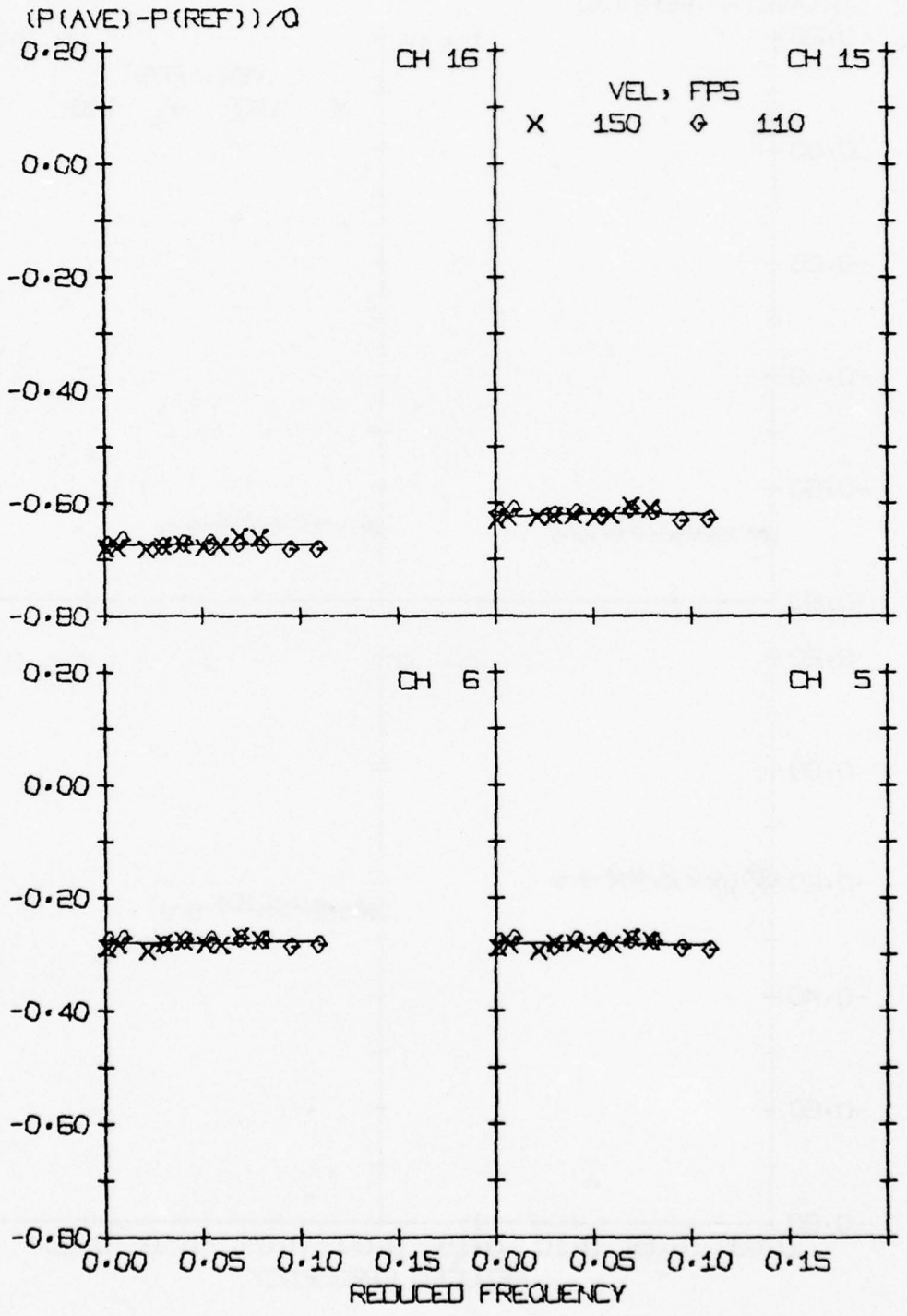

Figure 163. Normalized average pressure versus f_t, Group 3, α_m = 12°

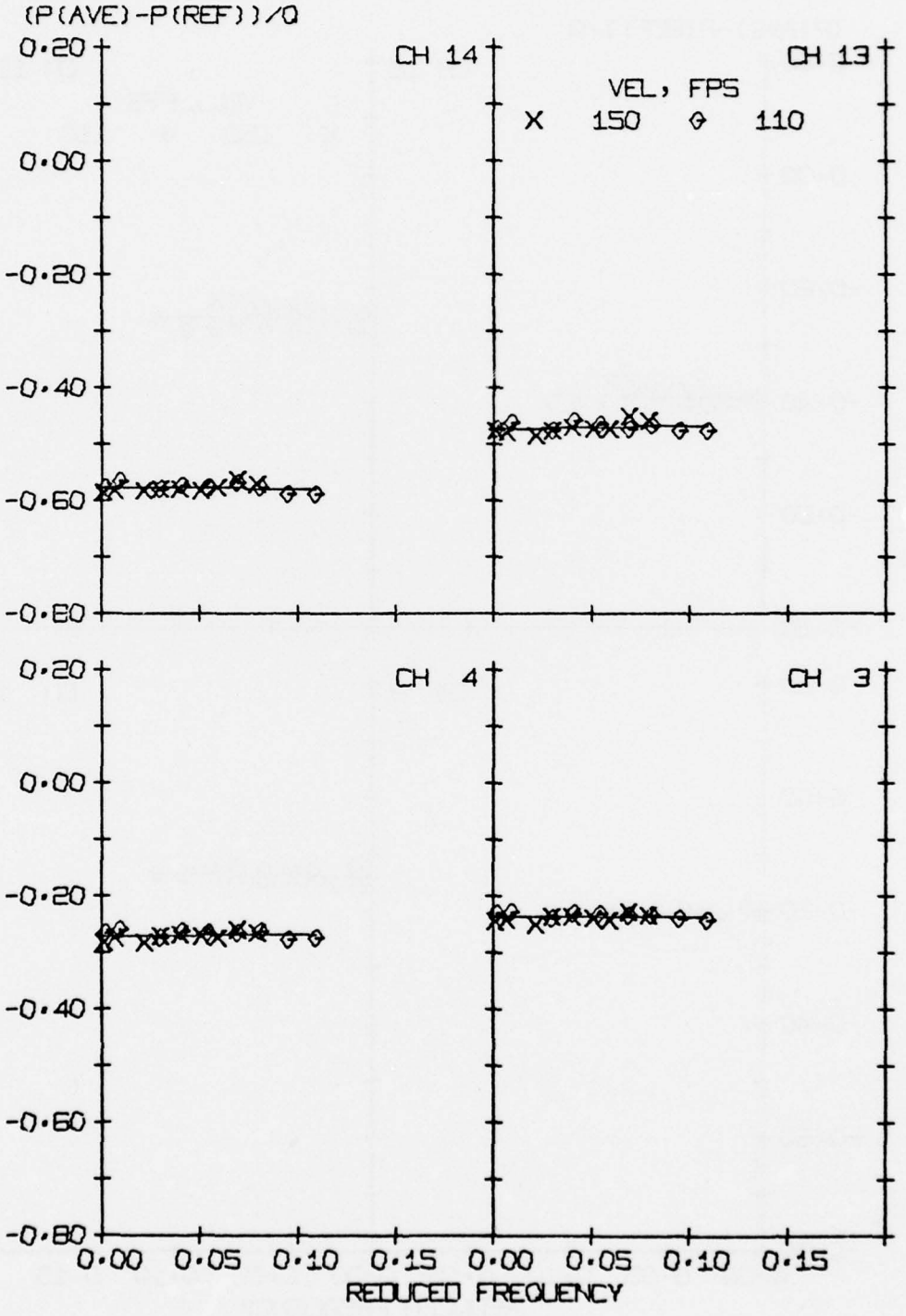

Figure 164. Normalized average pressure versus f_t, Group 4, α_m = 12°

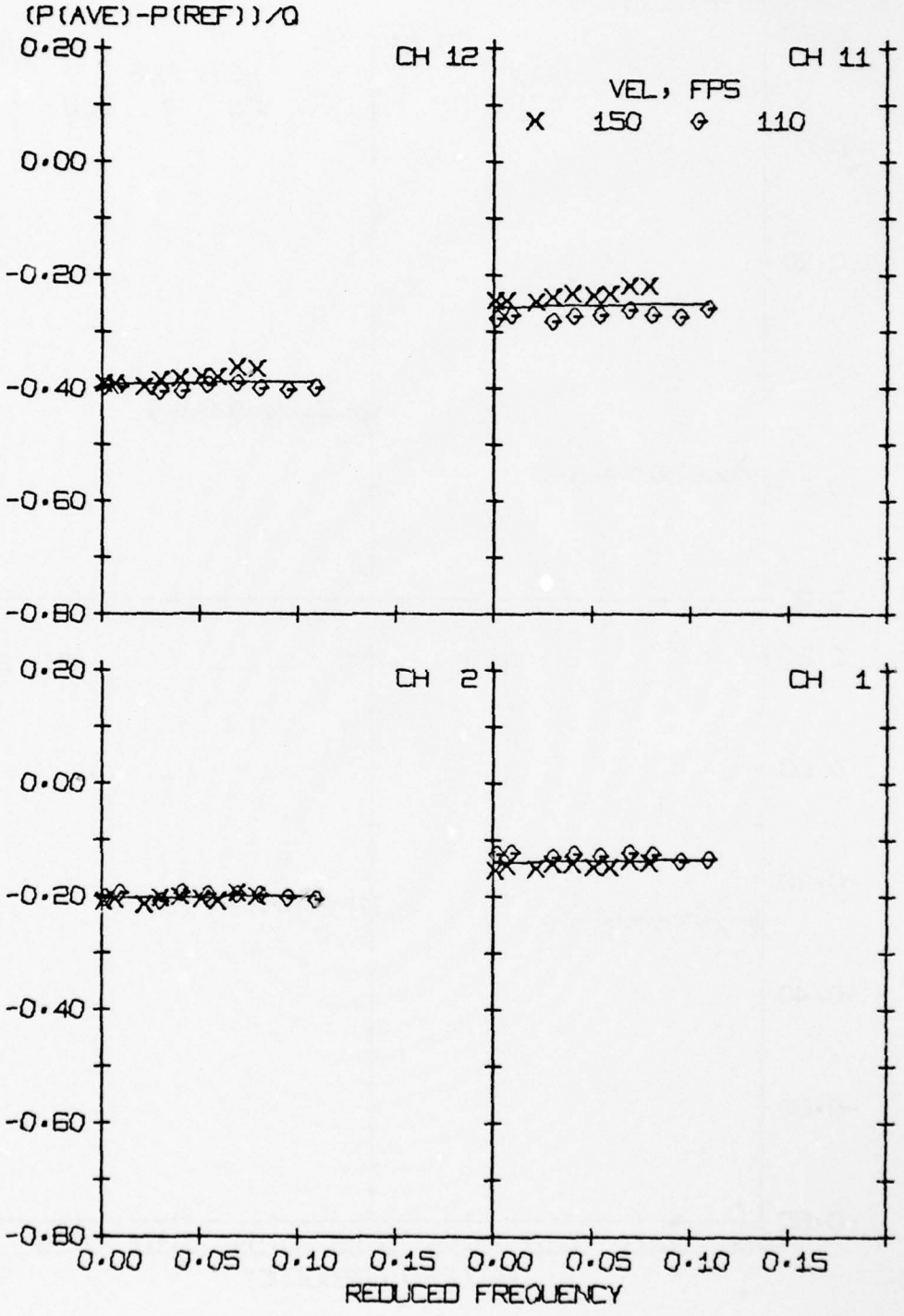

Figure 165. Normalized average pressure versus f_t, Group 5, α_m = 12°

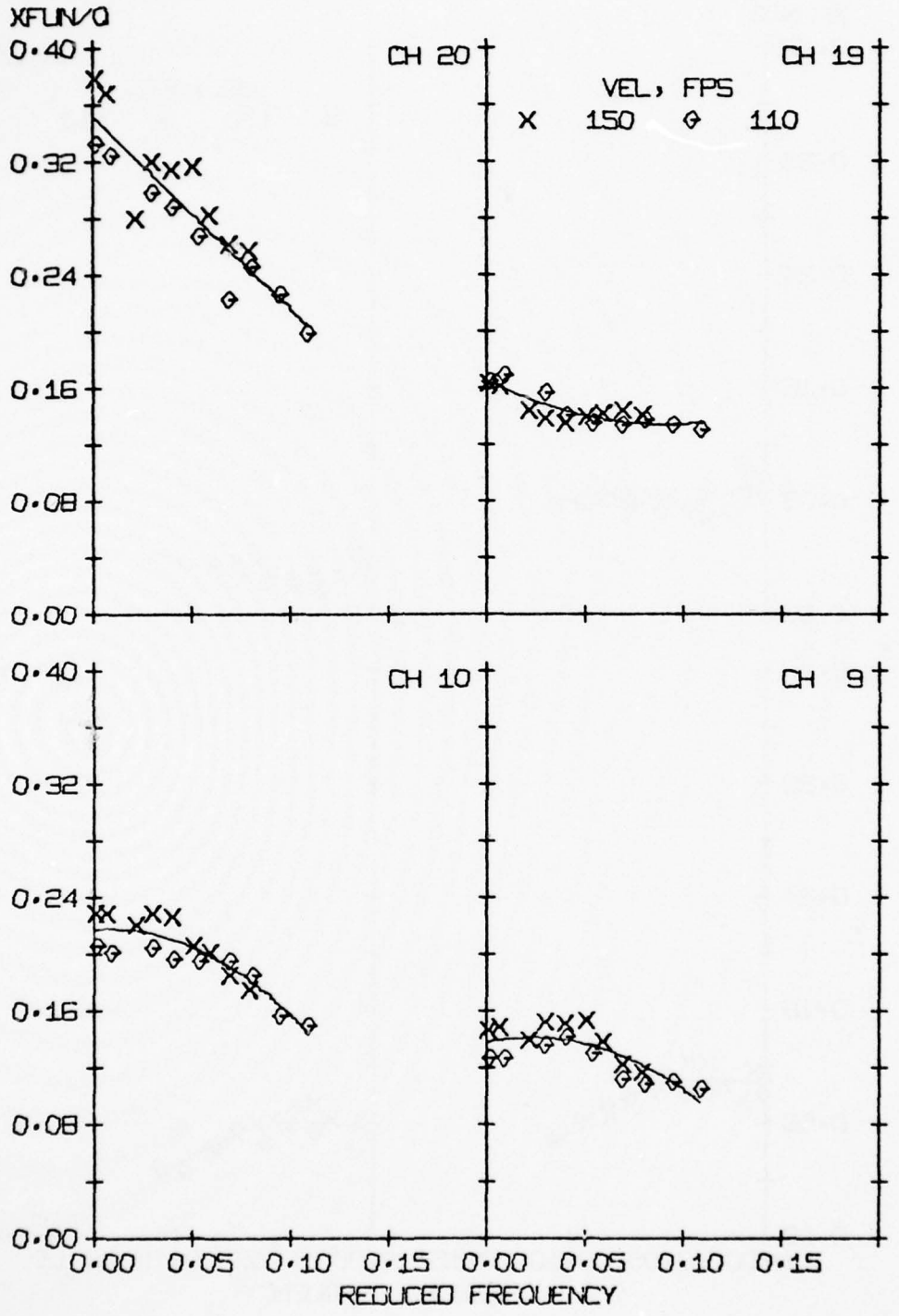

Figure 166. Normalized unsteady pressure versus f_t, Group 1, α_m = 12°

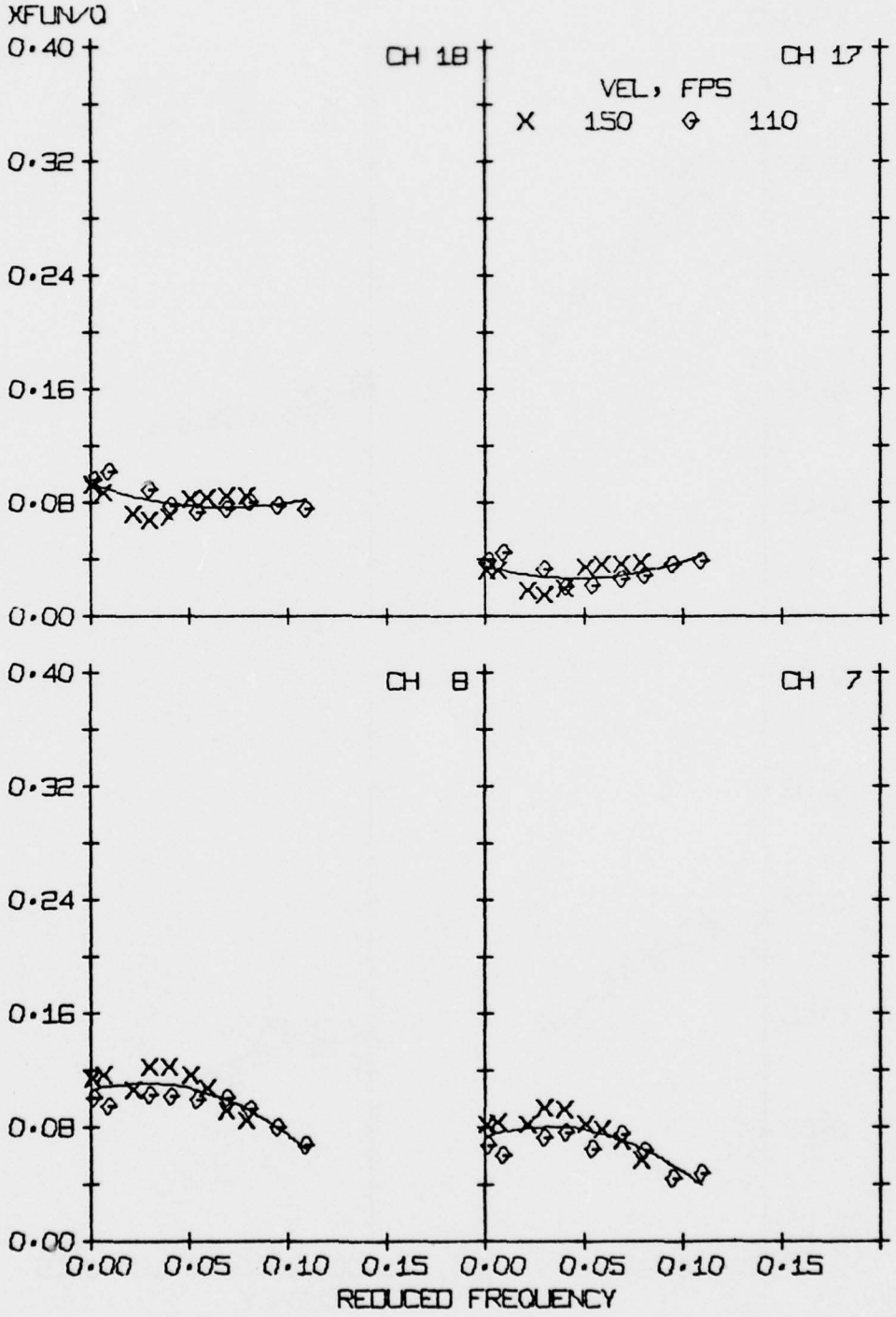

Figure 167. Normalized unsteady pressure versus f_t, Group 2, α_m = 12°

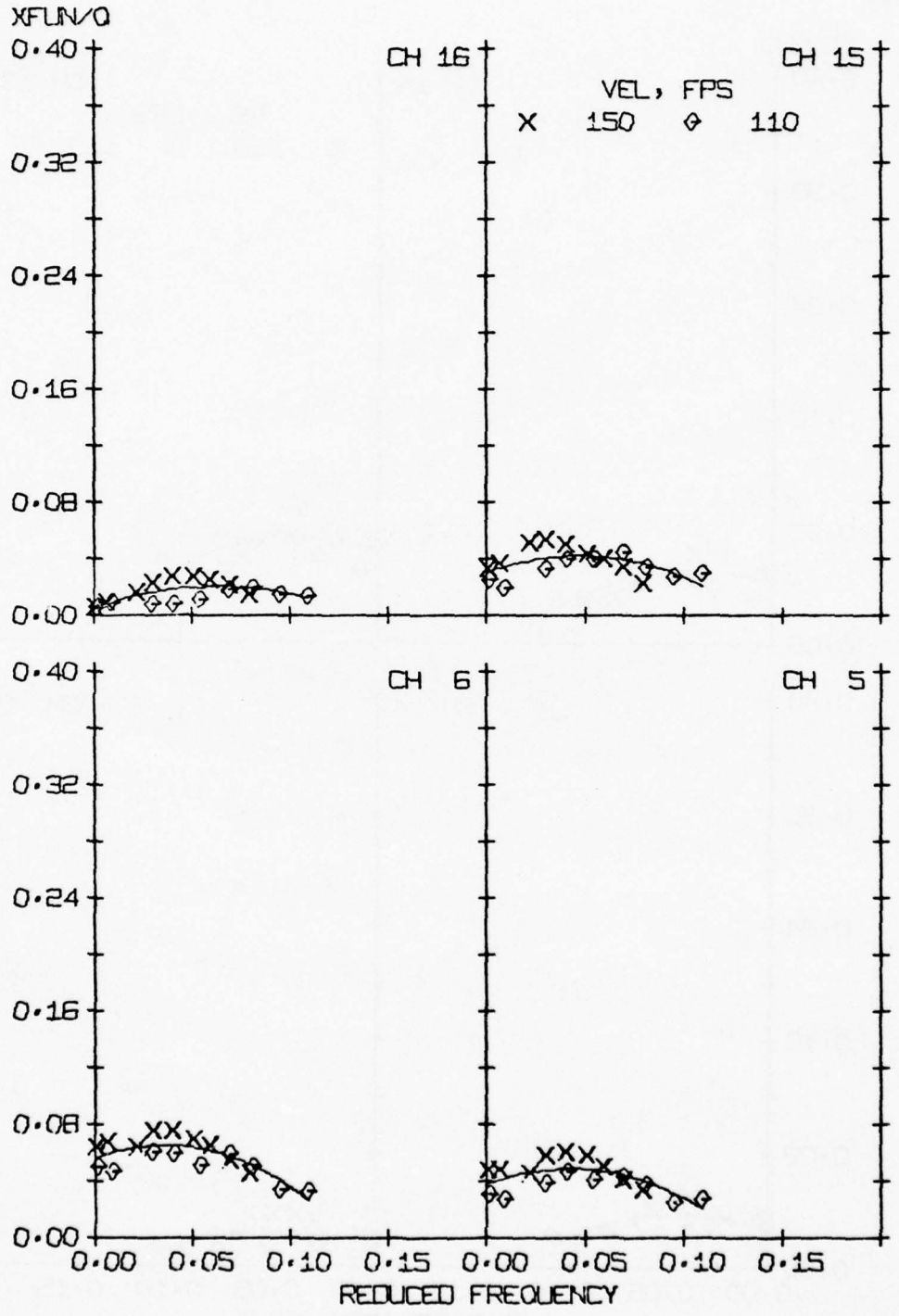

Figure 168. Normalized unsteady pressure versus f_t, Group 3, α_m = 12°

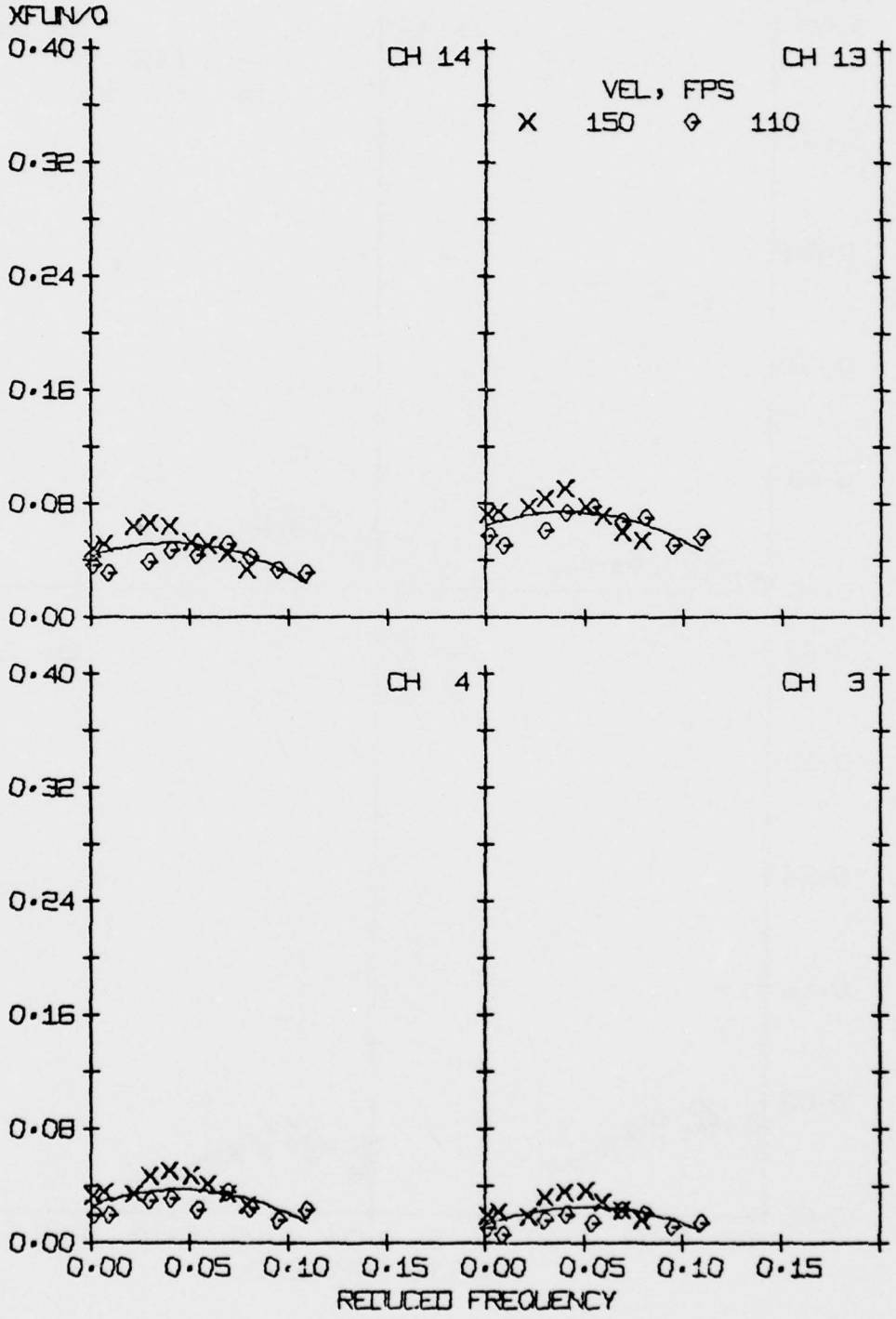

Figure 169. Normalized unsteady pressure versus f_t, Group 4, $\alpha_m \approx 12°$

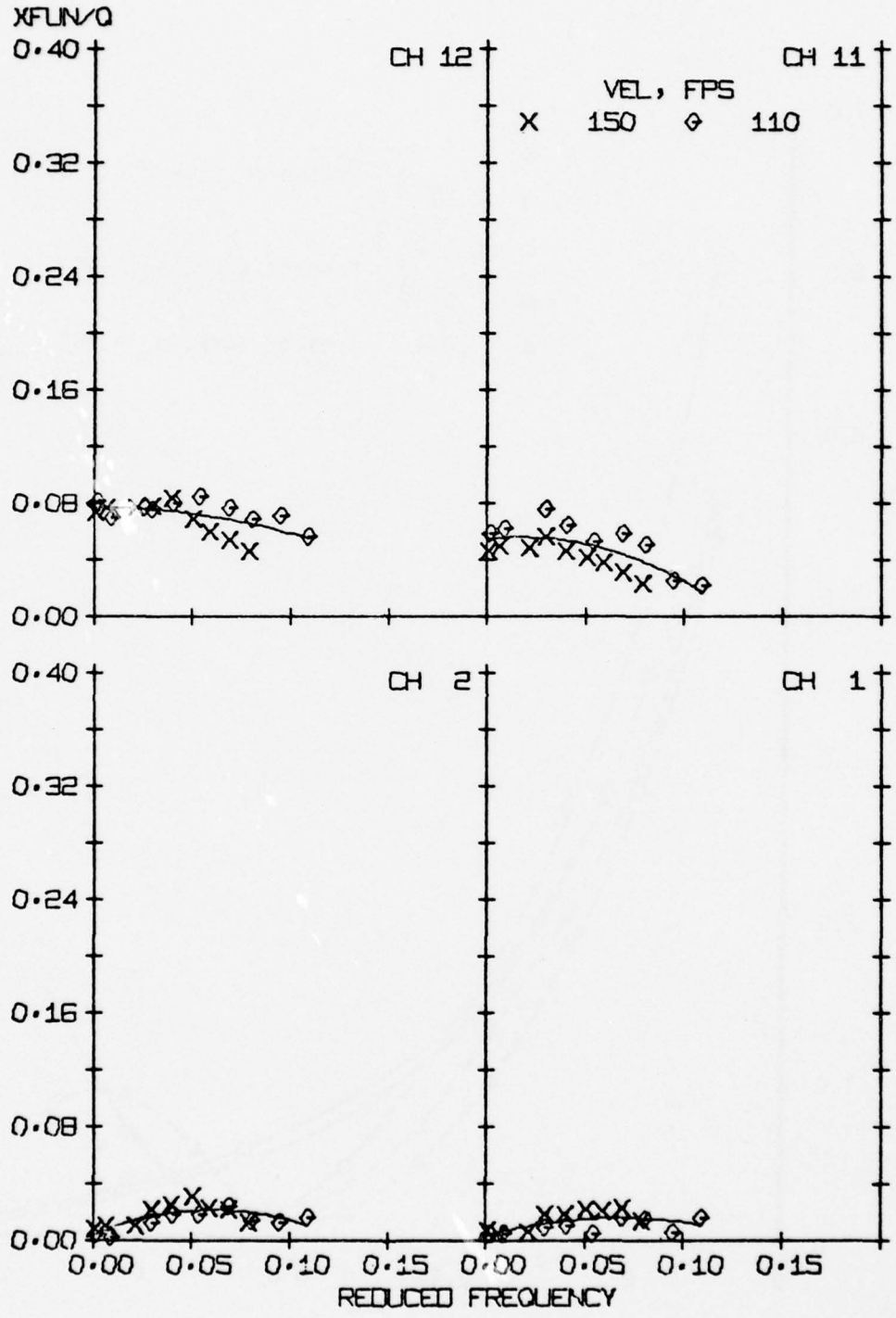

Figure 170. Normalized unsteady pressure versus f_t, Group 5, α_m = 12°

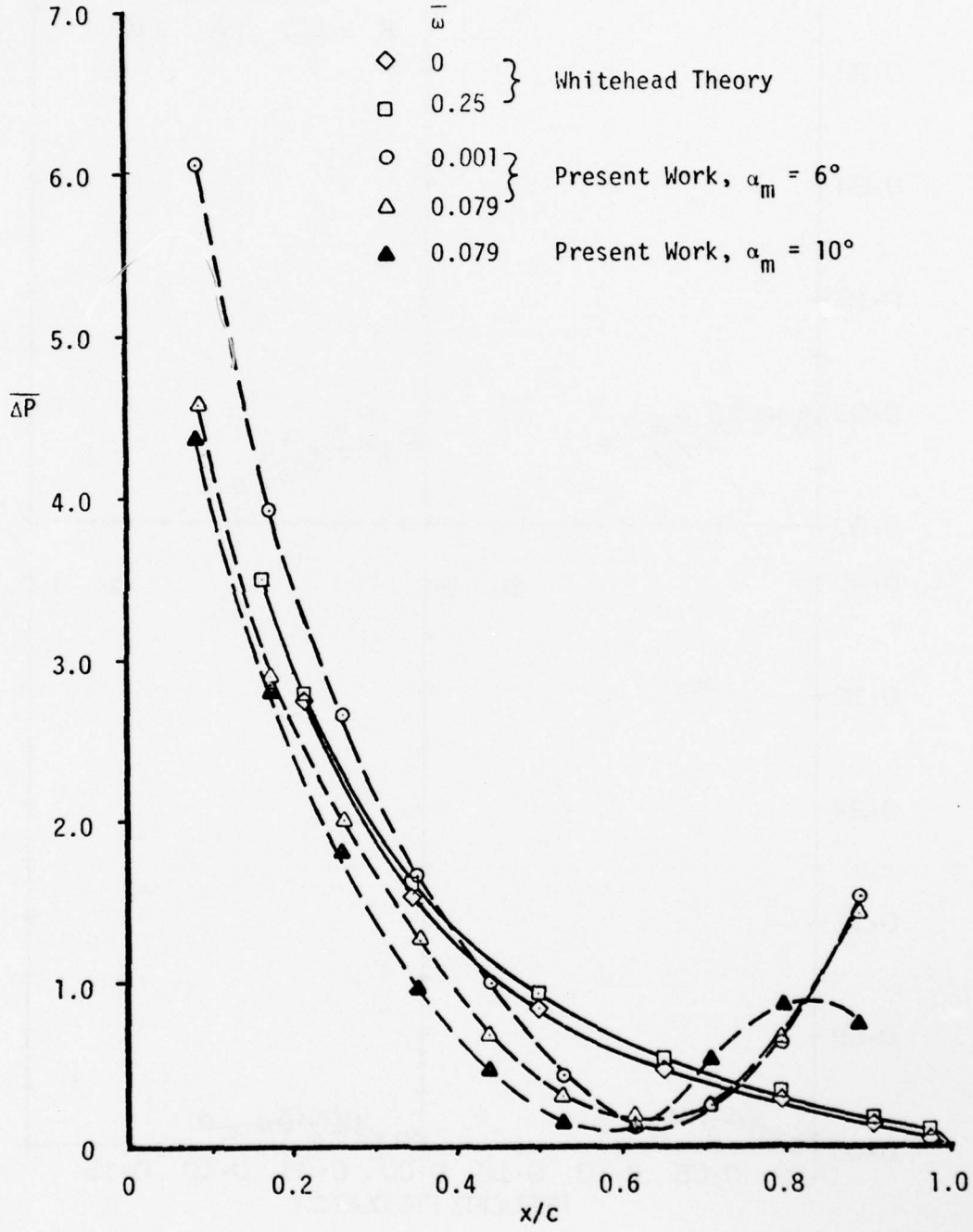

Figure 171. Comparison of experimental data with Whitehead theory

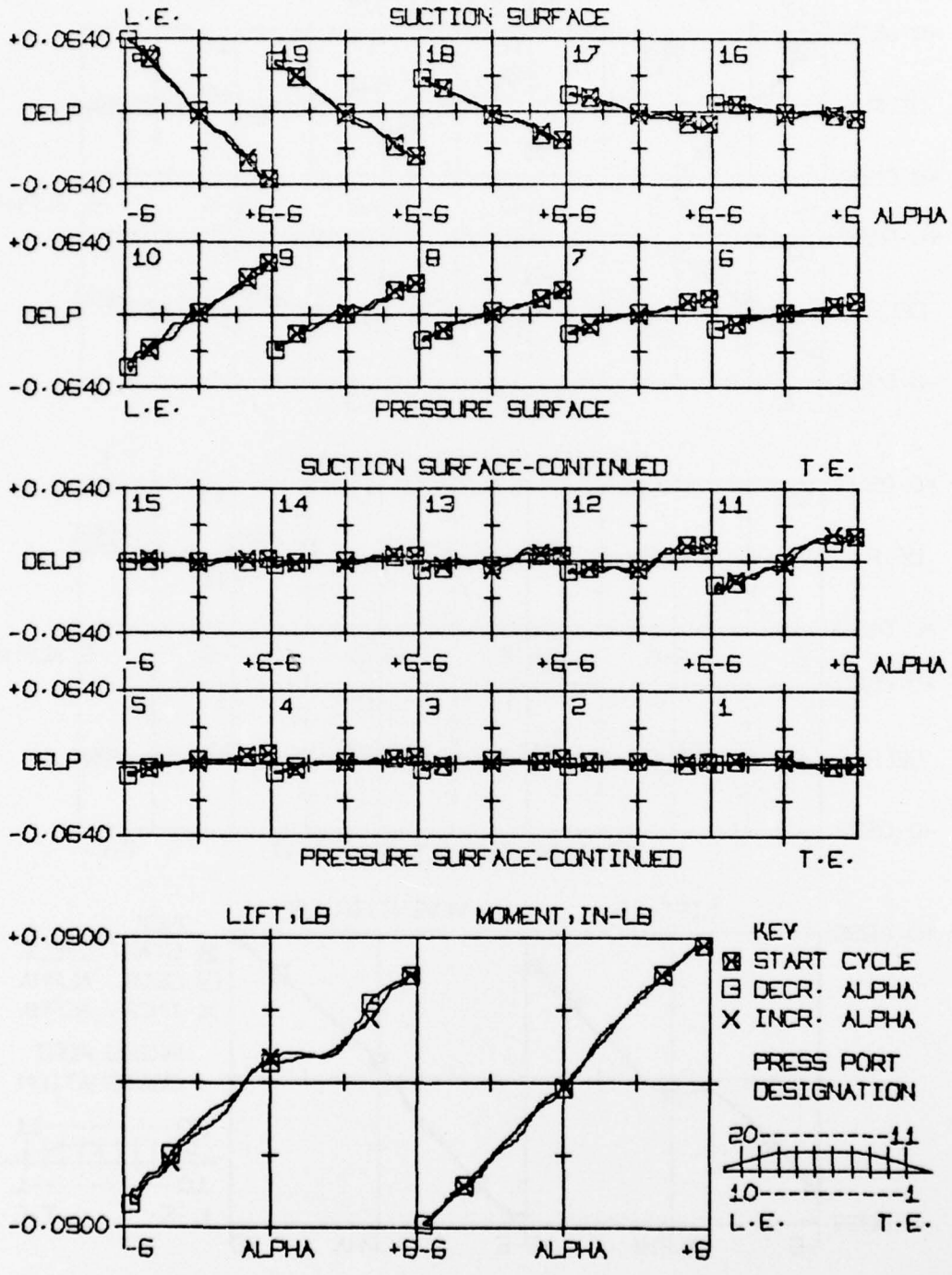

Figure 172. Pressure, lift, and moment hysteresis, Run 7020, α_m = 6°, V_N = 150 fps, f_t = 0.2 hz

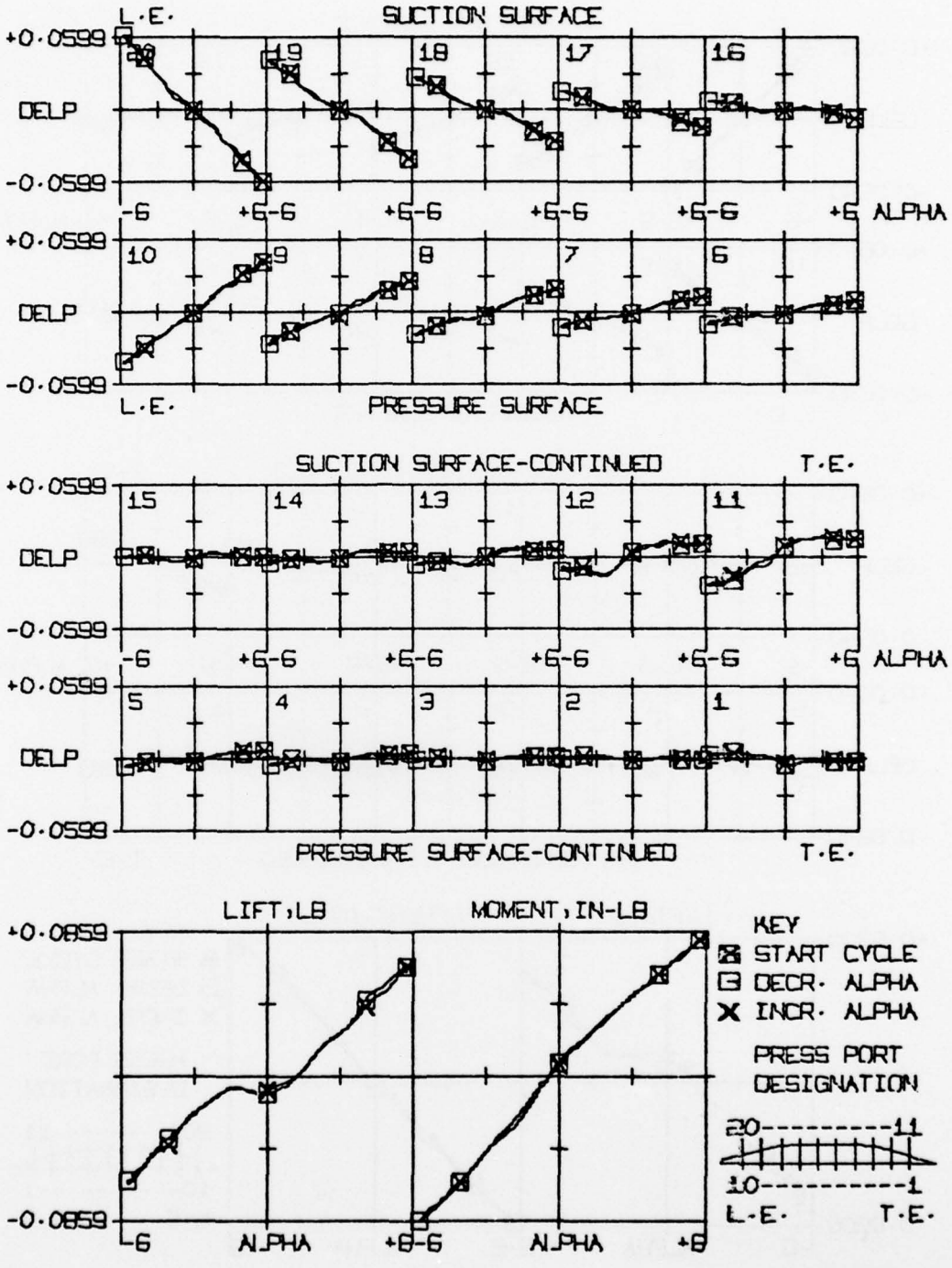

Figure 173. Pressure, lift, and moment hysteresis, Run 7220, α_m = 8°, V_N = 150 fps, f_t = 0.2 hz

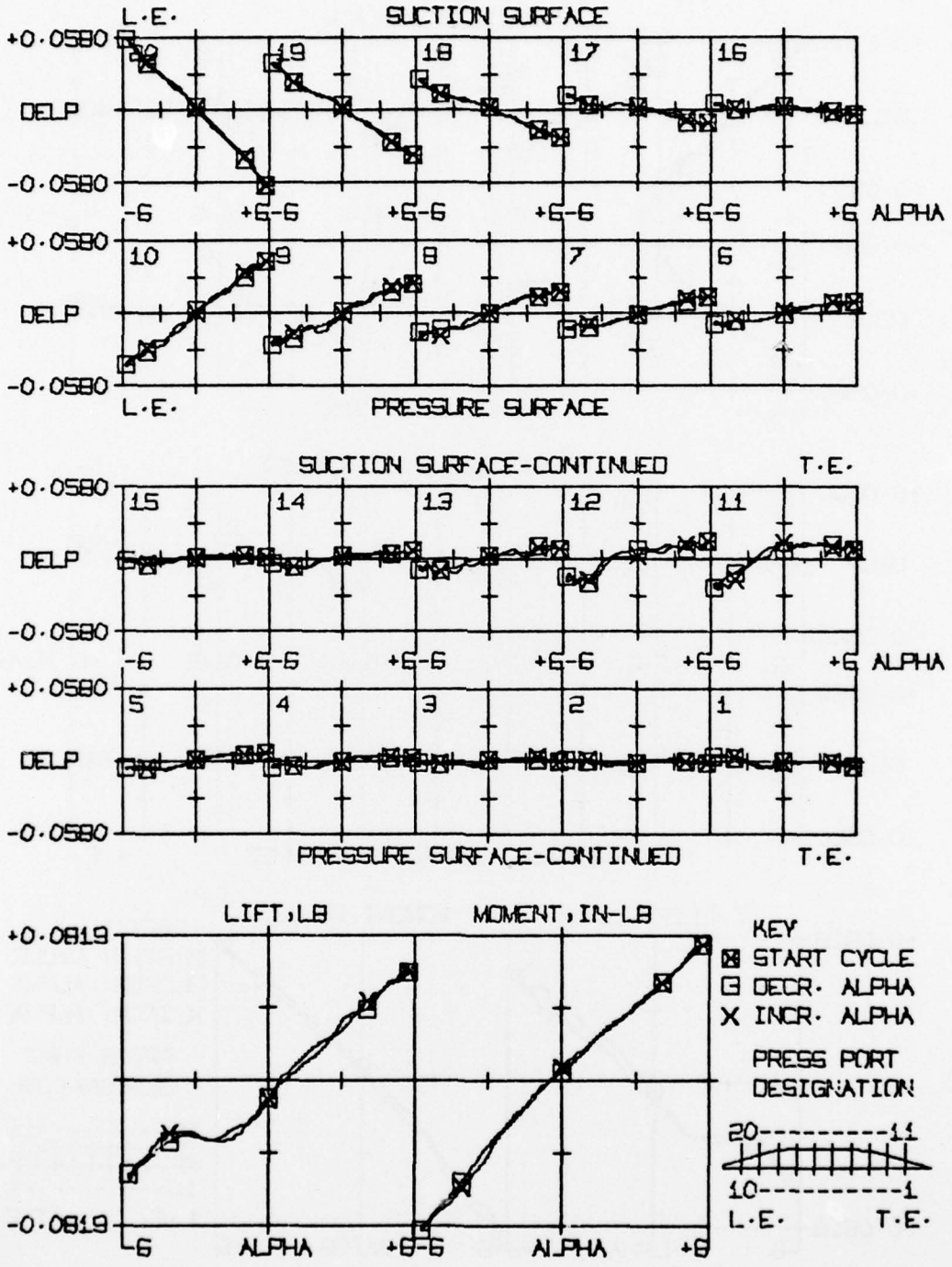

Figure 174. Pressure, lift, and moment hysteresis, Run 7490, α_m = 10°, V_N = 150 fps, f_t = 0.2 hz

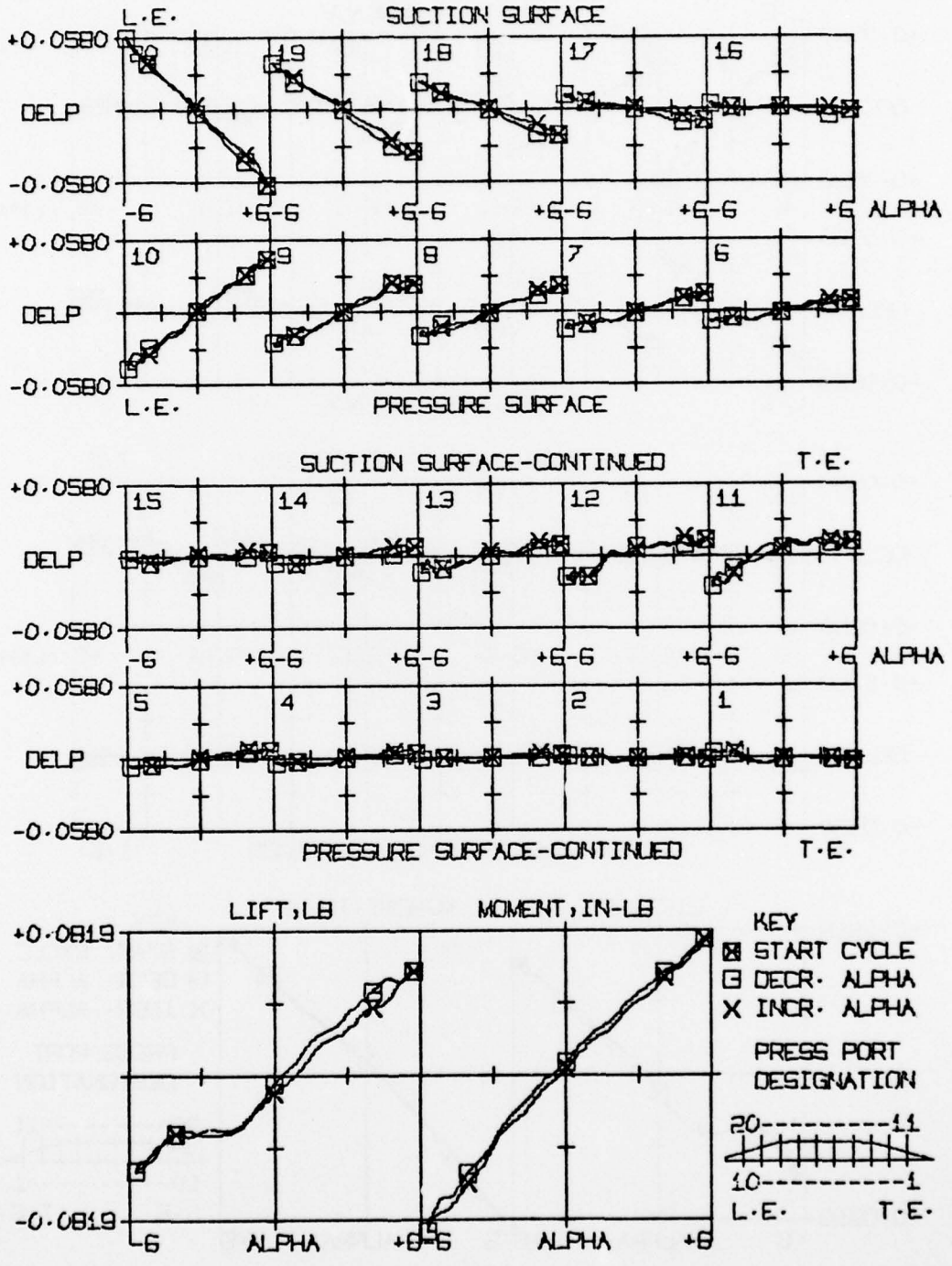

Figure 175. Pressure, lift, and moment hysteresis, Run 7500, α_m = 10°, V_N = 150 fps, f_t = 1.42 hz

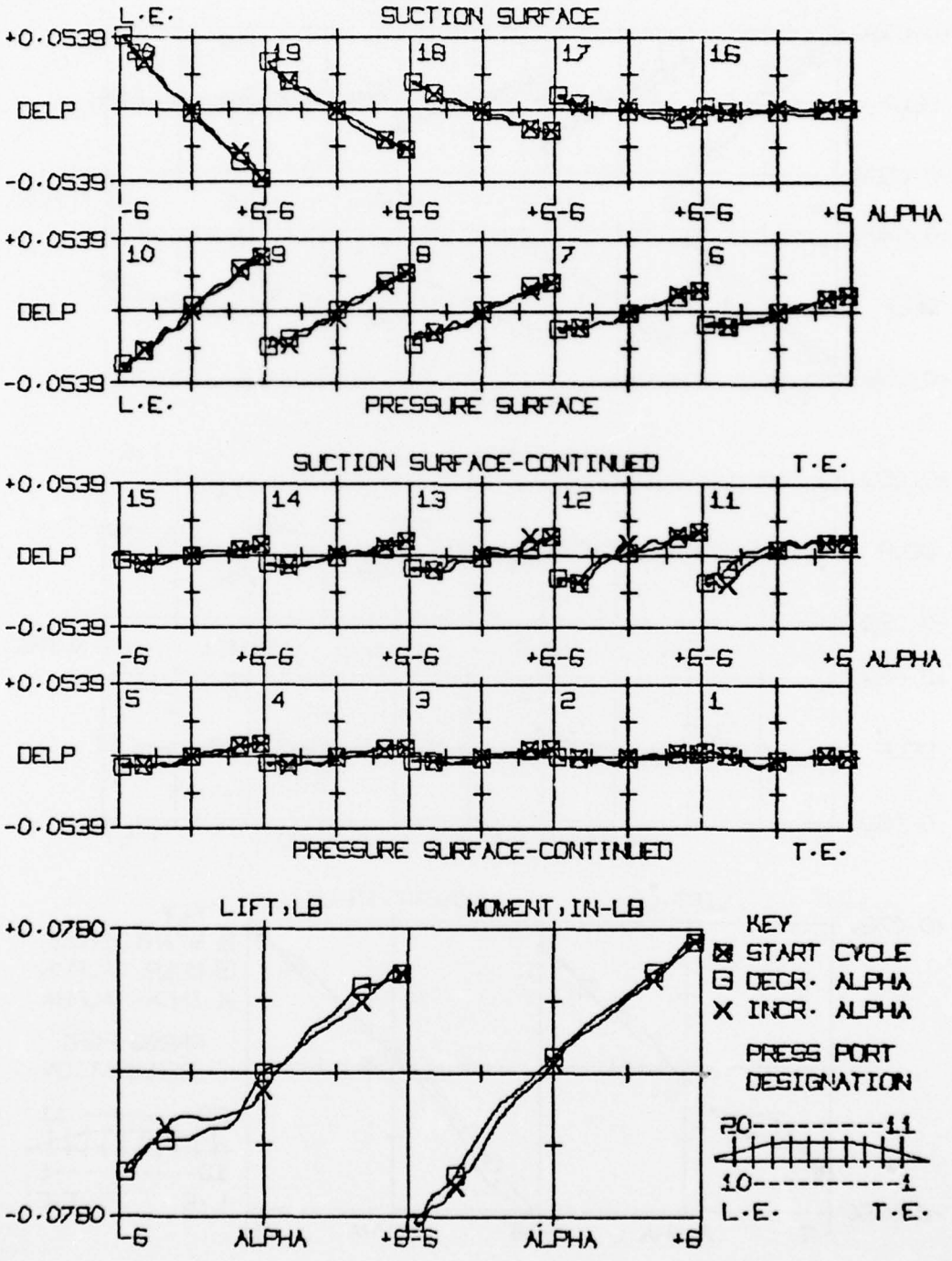

Figure 176. Pressure, lift, and moment hysteresis, Run 7510, $\alpha_m = 10°$, $V_N = 150$ fps, $f_t = 4.42$ hz

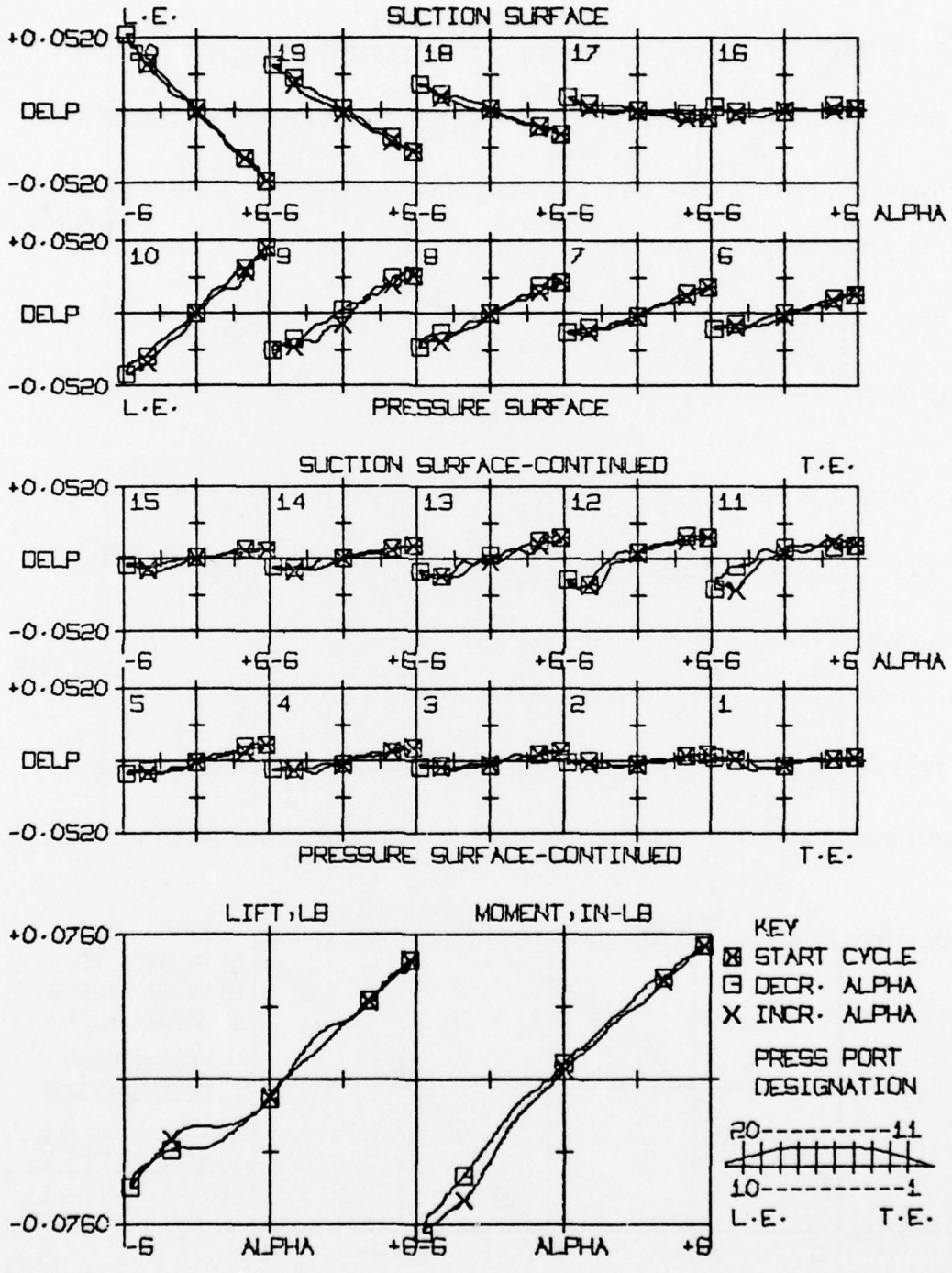

Figure 177. Pressure, lift, and moment hysteresis, Run 7520, α_m = 10°, V_N = 150 fps, f_t = 6.14 hz

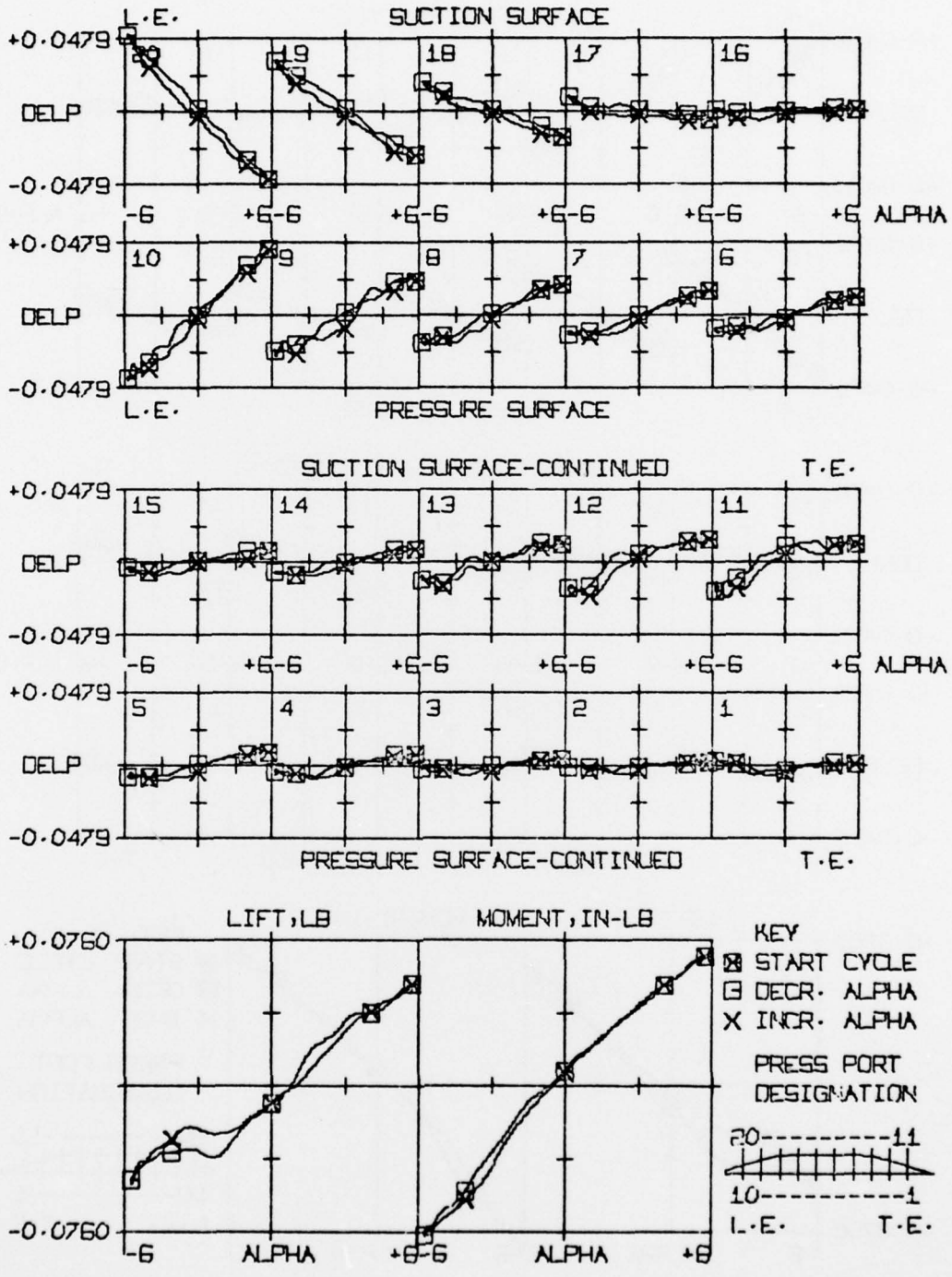

Figure 178. Pressure, lift, and moment hysteresis, Run 7530, α_m = 10°, V_N = 150 fps, f_t = 8.08 hz

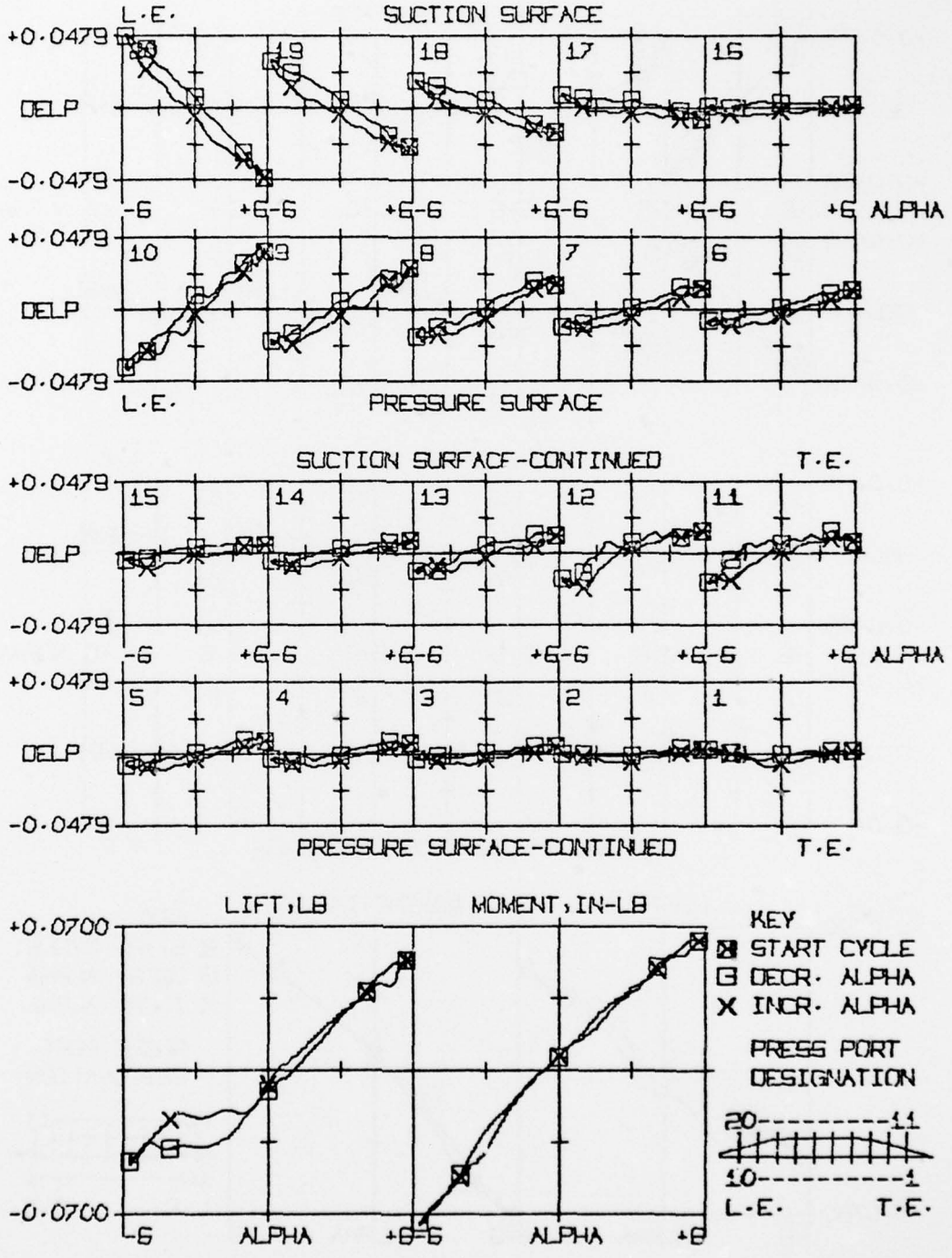

Figure 179. Pressure, lift, and moment hysteresis, Run 7540, α_m = 10°, V_N = 150 fps, f_t = 10.34 hz

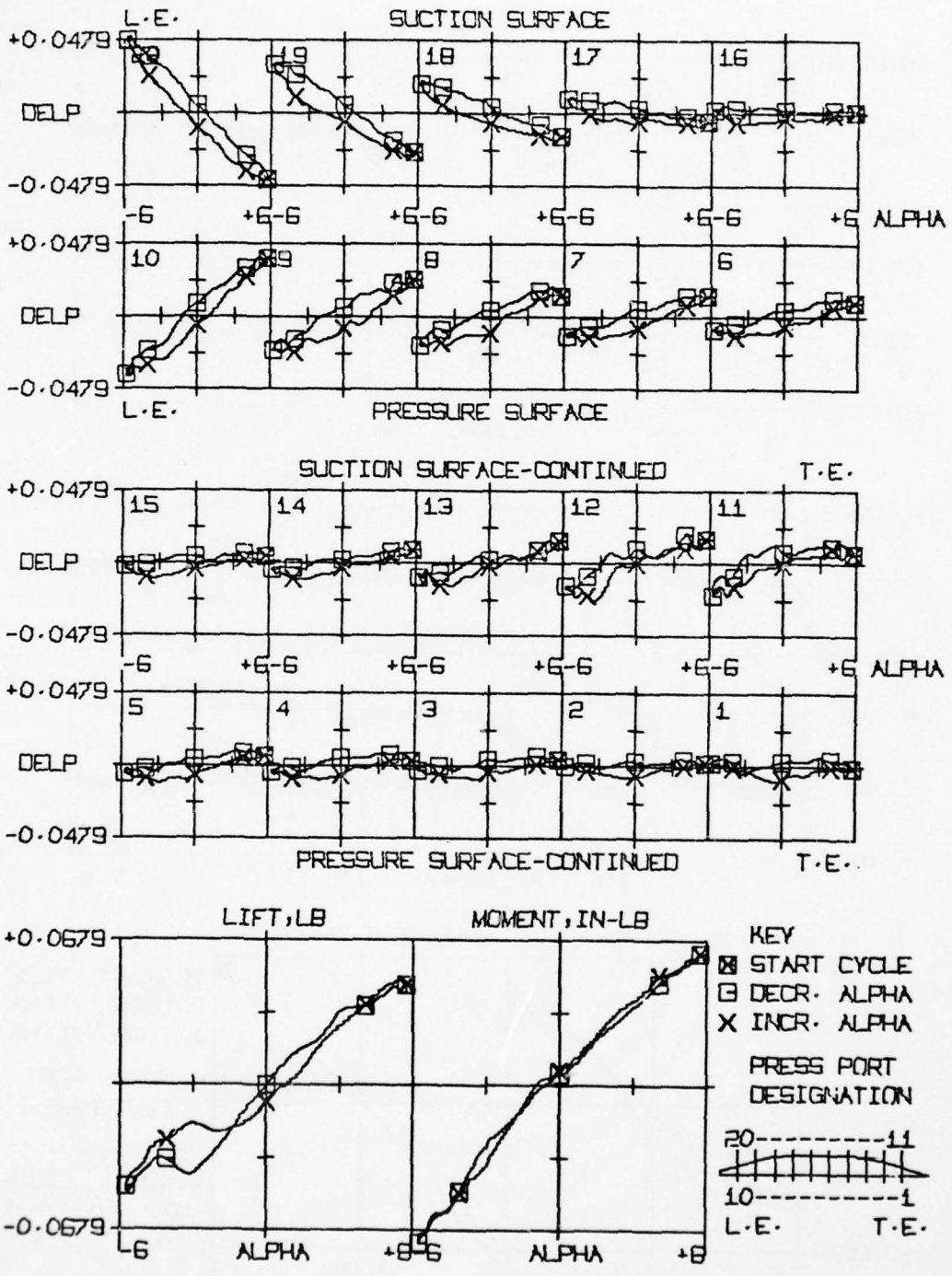

Figure 180. Pressure, lift, and moment hysteresis, Run 7550, $\alpha_m = 10°$, $V_N = 150$ fps, $f_t = 12.01$ hz

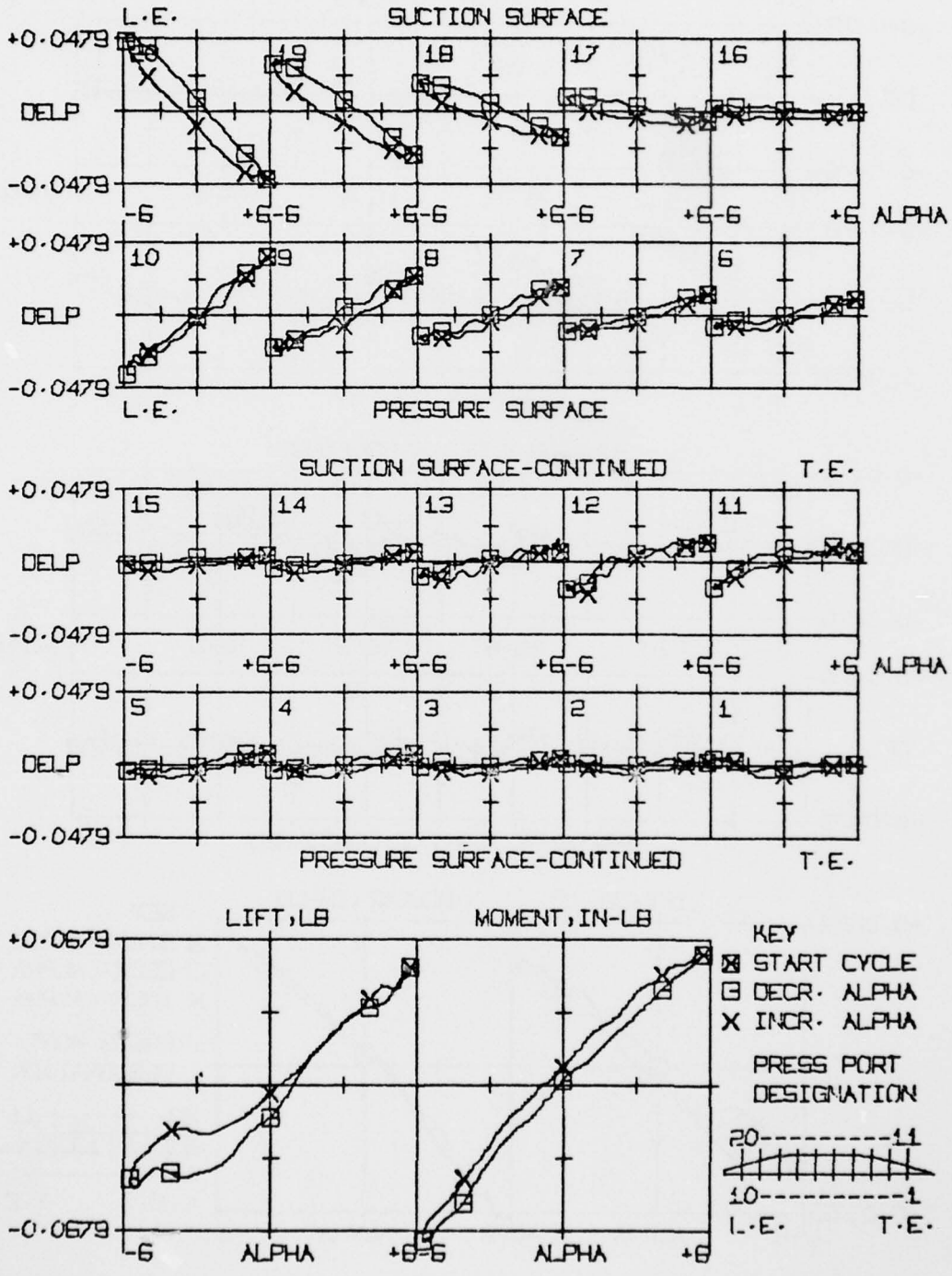

Figure 181. Pressure, lift, and moment hysteresis, Run 7560, α_m = 10°, V_N = 150 fps, f_t = 14.09 hz

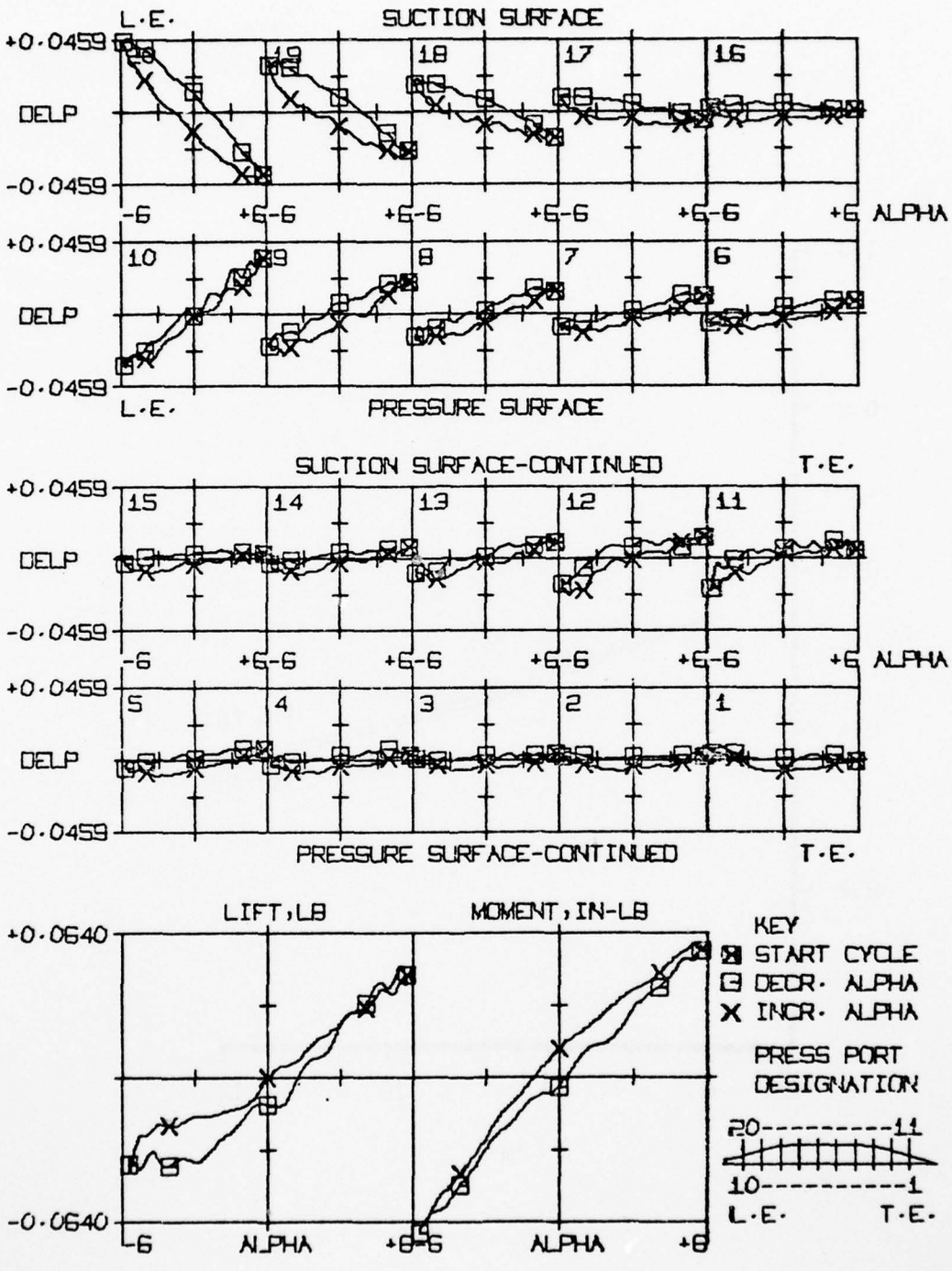

Figure 182. Pressure, lift, and moment hysteresis, Run 7570, α_m = 10°, V_N = 150 fps, f_t = 16.21 hz

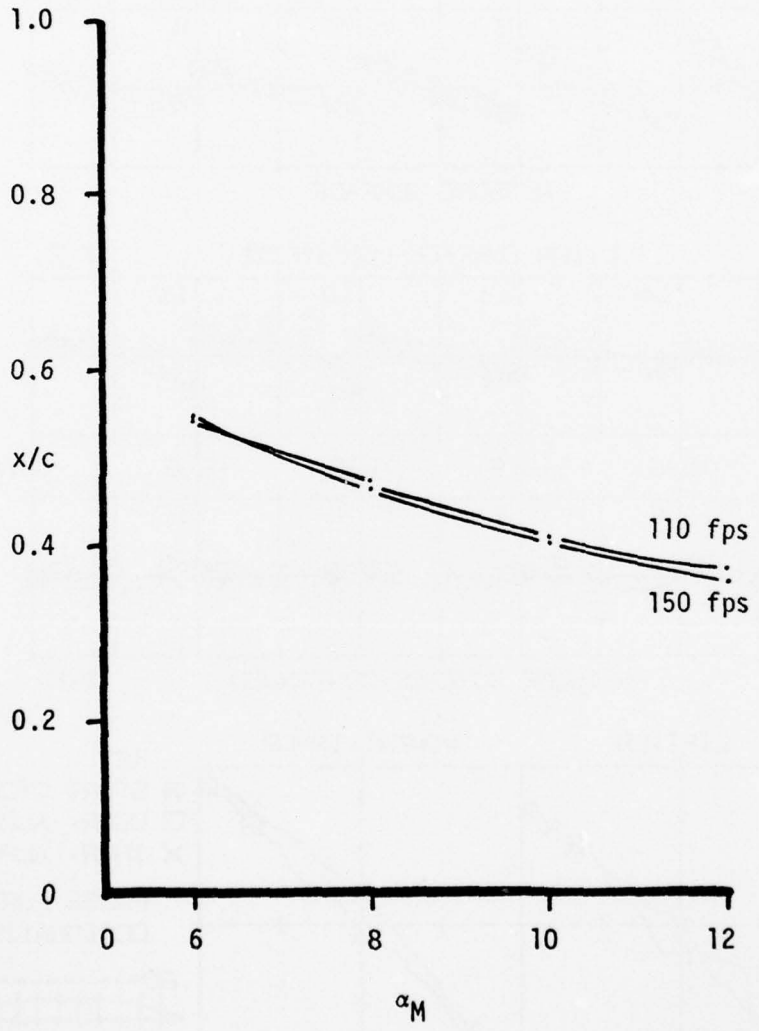

Figure 183. Time-average center of pressure versus angle of attack

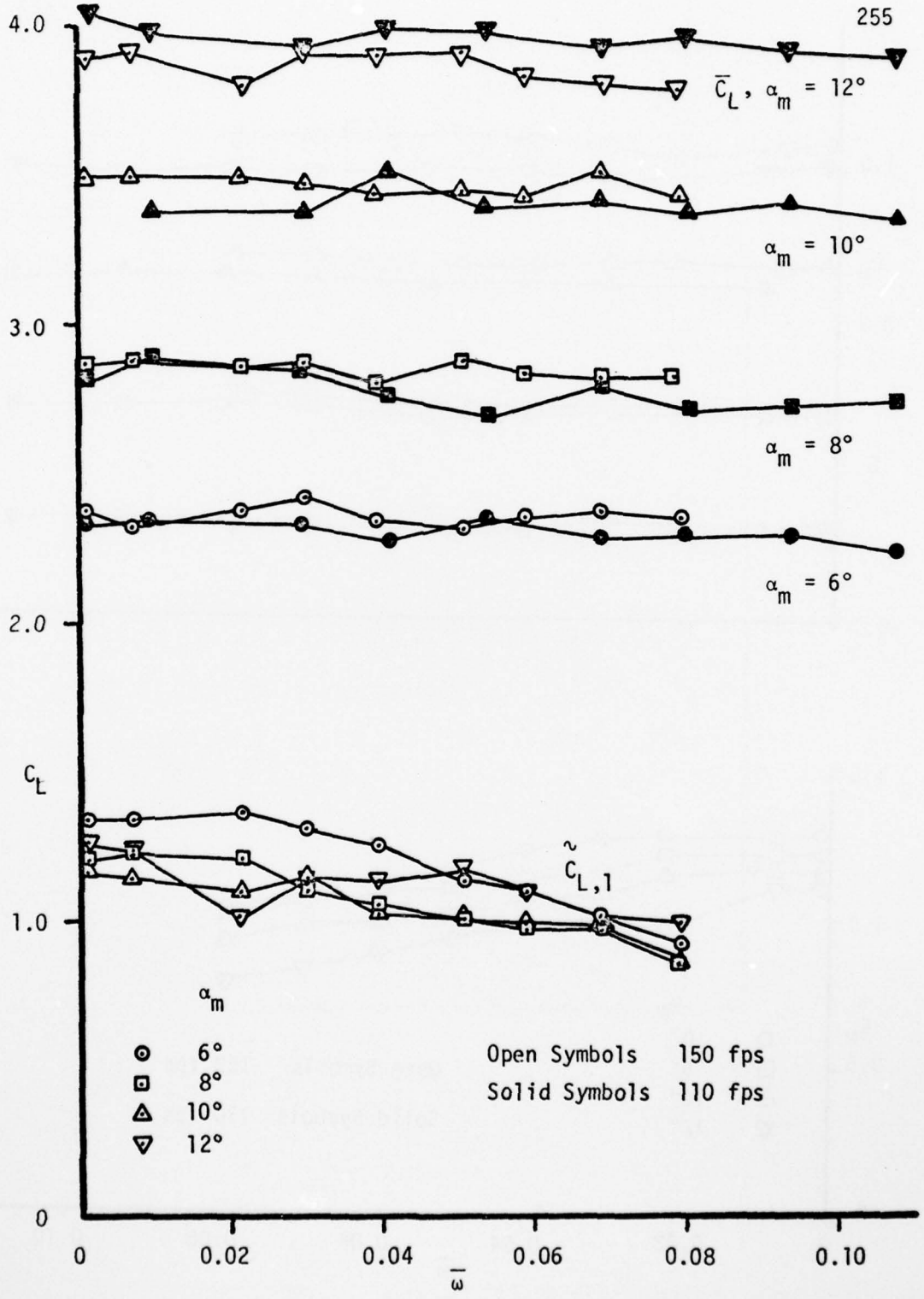

Figure 184. Lift coefficients versus reduced frequency

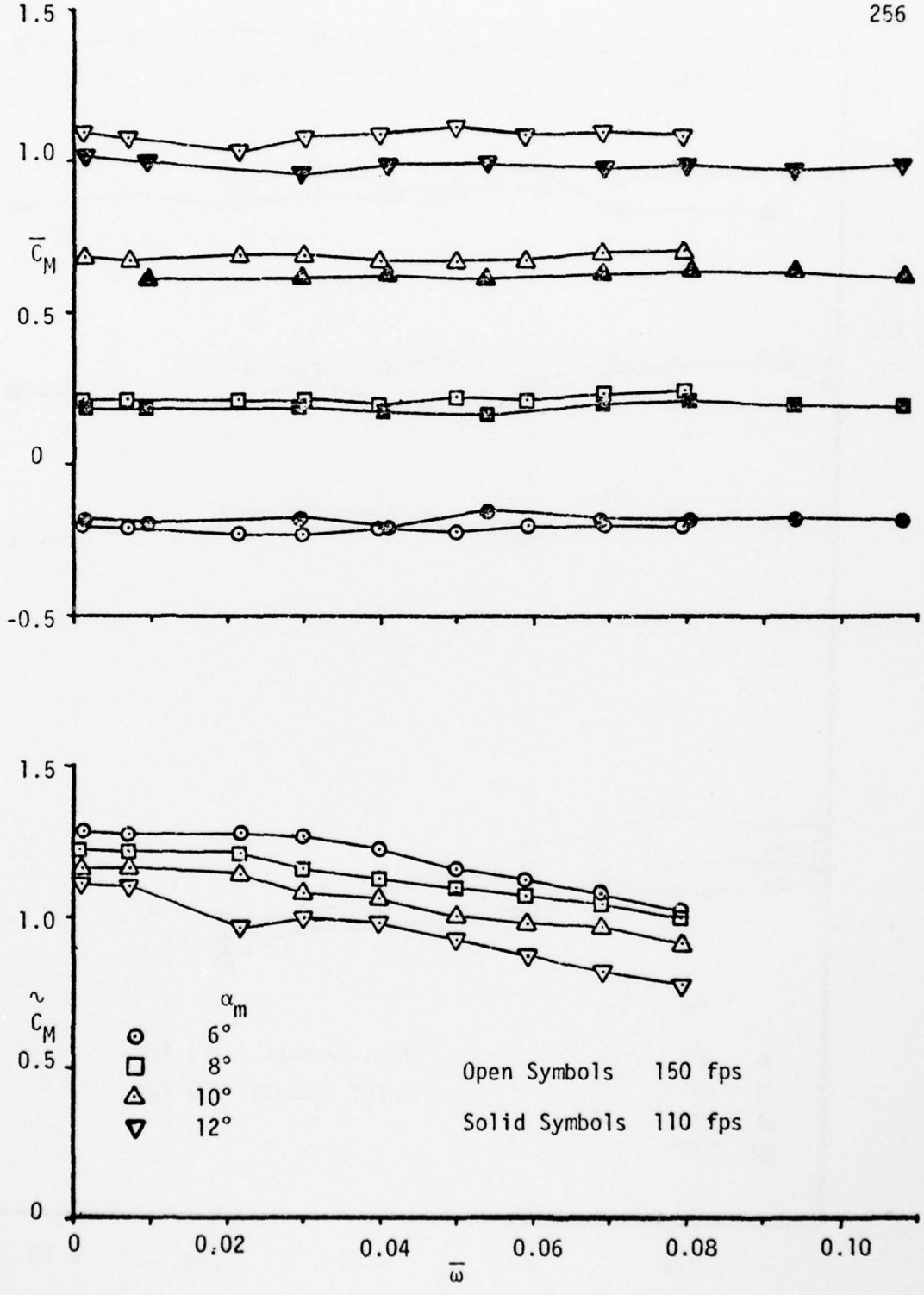

Figure 185. Moment coefficients versus reduced frequency

☆U.S.Government Printing Office: 1977 — 757-001/18